SANDIA REPORT

SAND2006-7508
Unlimited Release
Printed December 2006

Well-Characterized Open Pool Experiment Data and Analysis for Model Validation and Development

Thomas K. Blanchat, Vernon F. Nicolette, W. David Sundberg, Victor G. Figueroa

Prepared by
Sandia National Laboratories
Albuquerque, New Mexico 87185 and Livermore, California 94550

Sandia is a multiprogram laboratory operated by Sandia Corporation,
a Lockheed Martin Company, for the United States Department of Energy's
National Nuclear Security Administration under Contract DE-AC04-94AL85000.

Sandia National Laboratories

Issued by Sandia National Laboratories, operated for the United States Department of Energy by Sandia Corporation.

Available to DOE and DOE contractors from
U.S. Department of Energy
Office of Scientific and Technical Information
P.O. Box 62
Oak Ridge, TN 37831

Telephone: (865) 576-8401
Facsimile: (865) 576-5728
E-Mail: reports@adonis.osti.gov
Online ordering: http://www.osti.gov/bridge

Available to the public from
U.S. Department of Commerce
National Technical Information Service
5285 Port Royal Rd.
Springfield, VA 22161

Telephone: (800) 553-6847
Facsimile: (703) 605-6900
E-Mail: orders@ntis.fedworld.gov
Online order: http://www.ntis.gov/help/ordermethods.asp?loc=7-4-0#online

SAND2006-7508
Unlimited Release
Printed December 2006

Well-Characterized Open Pool Experiment Data and Analysis for Model Validation and Development

Thomas K. Blanchat, David Sundberg, and Alexander Brown
Fire Science and Technology Department
Sandia National Laboratories
P.O. Box 5800
Albuquerque, NM 87185-1914

Abstract

Four Well-Characterized Open Pool fires were conducted by Fire Science and Technology Department. The focus of the Well-Characterized Open Pool fire series was to provide environmental information for open pool fires on a physics first principal basis. The experiments measured the burning rate of liquid fuel in an open pool and the resultant heat flux to a weapon-sized object and the surrounding environment with well-characterized boundary and initial conditions. Results presented in this report include a general description of test observation (pre and post-test), wind measurements, fire plume topology, average fuel recession and heat release rates, and incident heat flux to the pool and to the calorimeters. As expected, results of the experiments show a strong correlation between wind conditions, fuel vaporization (mass loss) rate, and incident heat flux to the fuel and ground surface and calorimeters. Numerical fire simulations using both temporally- and spatially-dependant wind boundary conditions were performed using the Vulcan fire code. Comparisons of data to simulation predictions showed similar trends; however, simulation-predicted incident heat fluxes were lower than measured.

ACKNOWLEDGEMENTS

This report concludes a multi-year study of the data from a suite of unique fire experiments. The authors would like to thank the following individuals for their participation in this effort.

- Capt. La Kesha Stevenson Robinson (USAF), Nuclear Weapons Program Officer, Defense Threat Reduction Agency/CSNP for her oversight and guidance of the program.
- Sylvia Gomez, Manager of the Lurance Canyon Burn Site and Lead Technician; Dann Jernigan, Lead Technician; and the capable crew who prepared the site, assembled the experiment and instrumentation, and performed the experiments.
- Sandia meteorologist Gina Deola, who provided wind and weather predictions and set up the Sodar instrument.
- Alex Brown (SNL) and Carlos Lopez (SNL) for their technical review of this report.
- Charles C Allen, Northrop Grumman Information Technology, who performed the Optical Observations Analyses that is included as Appendix B of this report.

Left to right – Ahti Suo-Anttila, Chuck Allen, Bob Nichols, Sylvia Gomez, Gina Deola, Mike Toledo, Tom Blanchat, Bobby Strait, Dann Jernigan, Randy Foster, Richard Simpson, Armando Saenz.

This study was sponsored by the Department of Defense - DTRA (originally chartered by the Defense Nuclear Agency (DNA)), and was performed at Sandia National Laboratories.

This work was supported by the United States Department of Energy and was performed at Sandia National Laboratories. Sandia is a multiprogram laboratory operated by Sandia Corporation, a Lockheed Martin Company, for the United States Department of Energy under Contract No. DE-AC04-94AL85000.

Contents

Figures

Tables

This page intentionally left blank.

Executive Summary

This report is essentially a data package that contains temperature, heat flux, and ambient wind data for a series of outdoor-pool fire experiments conducted by Sandia National Laboratories (SNL) for the Defense Threat Reduction Agency (DTRA) (formerly the Defense Special Weapons Agency (DSWA)).

The focus of the Well-Characterized Open Pool fire series was to provide environmental information for open pool fires on a physics first principal basis. This series has provided data of sufficient quality for fire code validation data purposes. The experiments measured the burning rate of liquid fuel in an open pool and the resultant heat flux to a weapon-sized object and the surrounding environment with well-characterized boundary and initial conditions.

The scope of this work included preparation of the 26-ft diameter open pool fire test facility at Sandia's Lurance Canyon Burn Site (Burn Site), installing instrumentation, performing pre-test predictions of the expected environment, performing experiments, performing post-test predictions using the measured boundary conditions, and comparing the post-test predictions with the actual test results. All of these objectives were met.

This report describes four large-scale fire experiments that were conducted at the Sandia National Laboratory Lurance Canyon Burn Site in Albuquerque, NM. The fire experiments were conducted in a 26-foot diameter, outdoor pool fueled with JP8 over a period from September 8, 2003 to September 24, 2003. Experiment and hardware requirements, the test facility, instrumentation, and a complete description of each experiment are provided herein.

This report was written specifically with the end-user, the fire analyst, in mind. All of the experiment data is included on a CD ROM. Data and plots in Excel format provide a convenient interface for navigating the experiment data sets. Many of the figures in this report were made using this Excel program.

In addition to the numerical and graphical presentation of the data, animations of temperature and heat flux contour plots of particular sections of the fuel pool, terrain, and calorimeters were created to better visualize the fire insult (some animations are included on the CD). The CD ROM also contains some of the digitized movies from the video camera coverage of all the fires. The digitized movies can be viewed with a standalone MPEG viewer, such as Windows Media Player. The Excel program and the video media are intended to provide a user-friendly archival database in support of model validation efforts.

The continued development of the technology to provide validated fire physics models (e.g. VULCAN and FUEGO) will eventually lead to an ability to predict the threat posed by fires, the response of objects in fires, and confidence in those predictions. In turn, for specific cases of interest to DTRA, the basic understanding of fire physics can be used to develop threat reduction tools. These tools can be used to not only reduce the threats caused by fires, but to reduce the cost and time to complete future safety studies.

This page intentionally left blank.

1 Introduction

1.1 Background

The Department of Defense (DoD) requested the Defense Threat Reduction Agency (DTRA) to continue the development of capabilities for performing probabilistic Weapon System Safety Assessments (WSSA). In response, DTRA established a Fuel Fire Technology Base Program, the goal of which is to develop validated numerical tools to predict the thermal hazard posed by a fuel fire that results from an aircraft or ground transportation accident. Two types of tools are being developed to support this type of activity: (1) tools that model the detailed physics of the problem (e.g., fire field models); and (2) tools that model the dominant physical phenomena (e.g. the risk assessment compatible fire models (RACFMs)). RACFMs are tailored to be compatible with the methodology of a probabilistic WSSA.

To further support WSSA, DTRA also established a large-scale fire testing program to obtain experimental data to (1) develop and calibrate RACFMs, (2) validate and further develop fire field models, (3) assess the fire threat to actual systems of interest and, (4) provide archival data for future assessments. As part of the program, an extensive test series, listed in Table 1, involving outdoor pool fires has long been underway fulfilling the goals of the experiment program by investigating factors, such as wind interaction with large objects that influence the fire environment.

Table 1. WSSA Test Series

Test Series Number	Title	Purpose	Number of Tests
1	Free-fire	Obtain baseline fire data	2
2	Flat Plate	Assess thermal threat to near objects	3
3	Container	Response of shipping containers	2
4	Mock Fuselage	Data for a large cylinder in cross flow	8
5	C-141 Fuselage	Investigate complex changing geometry	1
6	Mock B52 Wing	Assess hazard posed to fuel tank and ALCM	
7	Mock B52 Bomb Bay	Assess the protection afforded by bomb bay doors	4

Test Series #1 served as a means of providing baseline fire data for the remainder of the test series. Limited thermocouple temperature and heat flux measurements within the continuous flame zone of free-fires (i.e. fires without large engulfed objects or

obstructions) were obtained in Test Series #1. Data were obtained in Test Series #1 for high (JP4) and low (JP8) volatility fuels burned under various wind conditions. Observations of fire-induced flow and postulation of the dominant mixing mechanisms in fires without objects were acquired during the course of these experiments [1]. Measurements of the distributions of the heat flux to the fuel pool [2], which determines the fuel burning rate, and differences in the temperature distribution in JP4- and JP8-fueled fires [3] were obtained for comparison with computational model predictions. The extent of the oxygen-starved interior was also estimated using data from this test series [4]. The data from these fires provided the basis for the first version of RACFMs developed by Sandia [5].

In the next test series (the Flat Plate Test Series), fire data were acquired under several wind conditions for the case of a large flat plate located adjacent to the fuel pool. Since the fire environment adjacent (within 3-5 optical paths) to an object determines the thermal threat (i.e. the heat flux) to the actual system, the region adjacent to the flat plate was heavily instrumented. Sparse instrumentation was used elsewhere for global characterization of the fire environment. In addition to supplying data that directly support the goals of the test program [6], the importance of object-induced turbulence (in the form of a secondary flame zone attached to the plate surface) and radiative coupling was discovered during this test series [7].

In the following test series (the Container Test Series), actual weapon shipping containers, instrumented mock-ups, and weapon container-sized calorimeters were subjected to two different fire environments. The majority of the containers and calorimeters were positioned on the leeward side of a large, open pool since the highest heat fluxes were observed in that region during previous tests. One actual container was positioned outside of the fuel pool at a standoff distance from the fire. In the vicinity of the containers, the flame zone was again heavily instrumented. Sparse instrumentation was used for global fire characterization.

The Mock Fuselage Test Series was used to obtain fire environment data for the class of problems where a large cylinder is subjected to a fire. This series was performed in support of WSSA needs related to the air transport of weapons. Various wind conditions; including winds normal to the axis of the mock fuselage (generating the flow pattern consistent with a cylinder in cross-flow) were addressed. The same measurement philosophy (i.e. high resolution near the object and decreased resolution elsewhere throughout the flame zone) was applied in this test series. Based on enhancements to the knowledge base from the previous tests, new measurements including pressure measurements on the surface of the mock fuselage and radiative heat flux to targets outside of the continuous flame zone were added during this test series. In addition to satisfying the goals of the overall test program [8], this test series (in two cases) illustrated the ability of object-induced turbulence to generate heat fluxes over a factor of 2 greater than commonly expected values for large hydrocarbon pool fires [9].

In the next test series, the fore section of an actual C-141 fuselage was subjected to wind conditions similar to those producing significant object-induced turbulence effects in the

mock fuselage test series. Fire environment instrumentation similar to the Mock Fuselage Test Series was employed. Measurements were also included to characterize the fire-induced response of a C-141 and to assist in assessing the thermal protection afforded the cargo by the fuselage [10].

As demonstrated by the Mock Fuselage and subsequent C141 Test Series, the use of fire-survivable, mock-up test fixture in a series of tests provides characterization of the fire environment (including the heat flux boundary condition for the system of interest) for fixed system geometry over a range of environmental conditions. The actual response of the system of interest in a specific fire environment can be investigated by using the actual system in a test performed under environmental conditions that resemble, as closely as possible, one of the tests performed in the mock-up test series. The system response and changes in the geometry (melting, structural degradation, etc.) due to exposure of the actual system can then be assessed and correlated with the fire environment measurements from the corresponding test in the mock-up series. These "system-level" tests therefore provide measurements of the actual system response, an assessment of the changes in the system due to fire exposure and, to a limited extent, the influence of these changes on the fire environment. A new test fixture is required for each system-level test. In the event that the cost of acquiring such test fixtures and transporting them to the fire test facility becomes prohibitive, another option is to examine the response of the system using analysis or separate tests (such as those involving radiant heating) which provide the same thermal insult (i.e. the same boundary condition) as measured in the mock-up tests.

Attention was next focused on the thermal hazard posed by a fire to the wing of an aircraft. A series of JP8 fire tests was performed containing a mock B52 aircraft wing. In addition to satisfying the general objectives of the test program, specific data were acquired which allow assessment of the hazard posed to the fuel tank of a B52 aircraft and the thermal hazard posed to the pylon-mounted Air Launched Cruise Missile (ALCM) structure during an engulfing fuel fire. Ignition and full-scale flame spread rates on thick (i.e. > 1 in.) JP8 fuel layers were also measured as needed to allow improved assessment of fire growth and propagation. Previous low volatility (JP8) tests had focused on characterizing the fire after initial fire growth and therefore small amounts of accelerant (gasoline) were used to increase the rate of flame spread over the fuel pool. The cost of acquiring, transporting, and configuring an actual B52 wing for a systems-level test was prohibitive and therefore the results of the mock series will serve as the suite of credible boundary conditions for analyses of the actual system.

The Mock B52 Bomb Bay Test Series consisted of subjecting a mock-up B52 aircraft section (including the fuselage region encompassing the bomb bay, and one wing) to a specified series of fire conditions [11]. Attention was focused on the fire environment with ALCMs in the bomb bay. The details of these measurements were designed to provide increased resolution, and thus improved characterization, in regions of interest (typically locations of high heat fluxes or large gradients) based on trends observed in the data from the previous tests. Due to the complexity of the test fixture geometry, a priori speculation of the fire environment was notably more difficult in this test series than

previous endeavors. Scoping simulations of the expected fire environment for two different wind conditions were therefore performed using the VULCAN fire field model. The results of these calculations were used to define test environmental conditions and instrumentation requirements and locations.

The completion of the Mock B52 Bomb Bay Test Series completed that portion of the large-scale fire testing program in support of the WSSAs. A few physics and data voids remained after the completion of the Mock B52 Bomb Bay Test Series – i.e., heat flux to weapon sized calorimeters (e.g., 12-18 in diameter) in low and mid-velocity winds, heat flux external to the fire, and heat flux to the fuel surface. (A "calorimeter" is an instrumented device suitable for estimating heat flux, and approximates the shape of the test item of interest.)

The focus of the Well-Characterized Open Pool fire series was to provide environmental information for open pool fires on a physics first principal basis. This series has provided data of sufficient quality for fire code validation data purposes. The experiments measured the burning rate of liquid fuel in an open pool and the resultant heat flux to a weapon-sized object and the surrounding environment with well-characterized boundary and initial conditions.

The scope of this work included preparation of the 26-ft diameter open pool fire test facility at Sandia's Lurance Canyon Burn Site (Burn Site), installing instrumentation, performing pre-test predictions of the expected environment, performing experiments, performing post-test predictions using the measured boundary conditions, and comparing the post-test predictions with the actual test results.

The continued development of the technology to provide validated fire physics models (e.g. VULCAN and FUEGO) will eventually lead to an ability to predict the threat posed by fires, the response of objects in fires, and confidence in those predictions. In turn, for specific cases of interest to DTRA, the basic understanding of fire physics can be used to develop threat reduction tools. These tools can be used to not only reduce the threats caused by fires, but to reduce the cost and time to complete future safety studies.

1.2 Program Requirements and Deliverables

The VULCAN/FUEGO Fire Modeling Program produces fire-modeling tools with the capability to confidently predict the thermal response of objects involved in fuel fires. This work is expected to complete the DTRA model development effort known as VULCAN as applied to hydrocarbon fuel fire scenarios. The math models in VULCAN are being used to develop the next generation code FUEGO (part of the ASC program). The program has the following requirements and deliverables:

1. Complete fabrication of a 26-foot diameter open pool to lie inside a 30 ft x 60 ft (nominal) open pool burn facility;
2. Complete instrumentation fabrication; install in open pool;

3. Perform (iteratively) two experiments to provide boundary and initial conditions, heat flux and temperature data in calm and windy conditions at various locations in and external to the open pool fire for discovery and comparison with VULCAN results.
4. Perform (iteratively) two experiments to obtain boundary and initial conditions, heat flux and temperature, for VULCAN comparison using weapon-sized calorimeters in the pool;
5. Analyze data from the four experiments described above and provide the data to DTRA and to the builders of Risk Assessment Compatibility Fire Models (RACFMs), Isis, or other DOD related fire models;
6. Complete four post-test VULCAN simulations for comparison with the four experiments above; and
7. Produce an Experiment / VULCAN model comparison assessment final report. The Final Report will include a description of the work accomplished, areas of concern that need to be further investigated, and any computer code comparisons. It will also include description of data updates provided to the builders of RACFMs, VULCAN model results, experimental data, and comparisons between the VULCAN model and the experimental data.

1.3 Test Goals, Objectives and Deliverables

1.3.1 Test Goals

The overall goal of these experiments is to study the effects of a JP-8 fire environment on weapon-sized objects in varying winds and to obtain supporting experimental data for ongoing fire physics model development (e.g., VULCAN and FUEGO).

1.3.2 Test Objectives

The objectives of the tests are to:

1. Determine incident heat flux to weapon sized calorimeters at various locations in the fire under calm and windy conditions;
2. Gather data on the heat flux to the fuel surface with a higher resolution than previously obtained;
3. Gather heat flux data close to but external to the pool to better understand the threat posed by the fire;
4. Gather data regarding wind speed, direction and wind fluctuations from ground level to 5 m above the ground to provide better boundary conditions to associate with data for model inputs; and
5. Gather data on heat flux to the lee side fire in high winds to compare with “flame drag” correlations and VULCAN predictions.

1.3.3 Test Deliverables

The deliverables of the tests are to:

1. Configure the 26-ft diameter open pool at Sandia National Laboratories (SNL) Lurance Canyon Burn site for a series of four (4) fire experiments;
2. Build and calibrate all diagnostic test fixtures;
3. Measure spatial and temporal distributions of the incoming wind temperature to the test facility from four towers each containing three 3-D ultrasonic anemometers;
4. Measure spatial and temporal variation of the heat flux within the pool using 25 Sandia-designed Heat Flux Gauges (HFGs) placed at the pool center and at approximately 1/4R, 1/2R, and 3/4R from the center of a circle whose center is concentric with that of the pool, at 45° intervals;
5. Measure spatial and temporal variation of the heat flux external to the pool using 24 Sandia-designed Heat Flux Gauges (HFGs) (or equivalent heat flux gauge) placed at approximately 1R, 1.5R, and 2R from the center of a circle whose center is concentric with that of the pool, at 45° intervals – spacing may change based on test conditions (wind vs. no wind);
6. Measure spatial and temporal variation of the heat flux to two (2) weapon-sized calorimeters (12 inch diameter x 16 inch long) placed near the pool center and at approximately 1/2R, 1 m above the pool;
7. Measure spatial and temporal variation of the heat flux to one (1) large calorimeter (4 ft diameter x 15 ft long) placed on the lee-side edge of the pool, 1 ft above the ground plane;
8. Measure spatial and temporal variation of the heat flux to one weapon sized calorimeter (12 inch diameter x 6 ft long) placed above and beyond the large calorimeter (exact location to be determined based on pre-test simulations and may vary between tests);
9. Measure the fuel recession rate;
10. Provide digital, color photographs of the facility, instrumentation, and test setup and conduct;
11. Provide VHS camera coverage of the facility, instrumentation, and test setup and conduct;
12. Provide limited pre-test predictions of the fire environment using the VULCAN fire physics code;
13. Provide post-test predictions of the fire environment using the VULCAN fire physics code and the actual test conditions; and
14. Analyze and validate all data taken, compare experimental data and VULCAN predictions, and write final report.

A series of four experiments were conducted with two different wind conditions. Two tests were conducted with calorimeters external to the pool and two tests were conducted without calorimeters. All tests were conducted at the same location within the test facility.

2 Experimental Matrix and Test Conditions

2.1 Experimental Matrix

The experimental configurations for the four experiments are given in Table 2:

Table 2. Experiment Configurations

Experiment	Description	Purpose
1	Calm (0-5 mph) winds, pool with no large objects, 25 heat flux gauges inside pool, 24 heat flux gauges external to pool, four wind speed and direction towers each with 2-3 measurements stations from 0-5 m off the surface, three small calorimeters at three radial locations TBD off the fuel surface.	Obtain data on heat flux to pool surface, at ground level external to the pool, and to small calorimeters inside fire in calm winds.
2	Same as for Experiment #1 except for medium to high winds (5-15 mph).	Obtain data on heat flux to pool surface, at ground level external to the pool, and to small calorimeters inside fire in medium to high winds.
3	Same as Experiments #1 and #2, except with two calorimeters on the pool edge. Study heat flux to calorimeters in most stressing wind conditions, perpendicular to wind direction, calm winds.	Obtain heat flux data to weapon sized calorimeters in wind speeds chosen from Experiments #1 & #2, with the calorimeters perpendicular to the wind direction.
4	Same as for Experiment #3, except for medium to high winds.	Same as for Experiment #3 except for higher winds

2.2 Test Conditions

Experiments #1 & #2 provide a baseline for the setup and were performed with the same physical layout but under differing wind conditions. Experiment #1 provided data under calm (0-5 mph) wind conditions, typical of most past qualification experiments. Experiment #2 provided data under medium (5-15 mph) wind conditions, more typical of the conditions that will generate higher heat fluxes.

Experiments #3 & #4 provided heat flux data to large calorimeters (i.e., "systems" sized calorimeters) perpendicular to the wind direction. They also provided data on heat flux to the pool, to the exterior, wind speed and fluctuations, etc. These last two experiments contained no large objects to minimize object-induced turbulence.

2.3 Pretest Fire Modeling

Pre-test computer simulations have been performed using the fire physics code VULCAN. VULCAN is a finite difference, 3-dimensional transient FORTRAN computer code that uses the Reynolds Averaged Navier-Stokes (RANS) formulation. In this formulation, results are generated at each cell and stored at each time step at pre-defined locations, called "history cells." Temperature, incident heat flux, gas velocity and many other parameters are saved at the history cells. These are averaged over a short time period (e.g., 2 seconds) and plotted via a post-processor.

Table 3. Pre-test VULCAN Simulations

Simulation Name	Wind Condition (mph)	Obstacle	Zones i,j,k	X (m)	Y (m)	Z (m)
noobsw0tec.plt	0	no	62,62,38	-50 to 50	-50 to 50	0 to 54
noobsw5tec.plt	5	no	62,62,38	-50 to 50	-50 to 50	0 to 54
noobsw10tec.plt	10	no	78,62,38	-50 to 60	-50 to 50	0 to 54
obsz0w0tec.plt	0	yes	91,76,45	-50 to 60	-50 to 50	0 to 54
obsz0w5tec.plt	5	yes	91,76,45	-50 to 60	-50 to 50	0 to 54
obsz0w10tec.plt	10	yes	91,76,45	-50 to 60	-50 to 50	0 to 54

Pre-test results were used to explore the formation of fire environments and the resultant heat flux to objects under various wind conditions. Pre-test results were also used for instrumentation selection and object placement in the experiments. The actual test results for measured initial and boundary conditions were used for post-test calculations. Table 3 shows the conditions used for the six pre-test simulations. The obstacle is the 4 ft diameter calorimeter, with center plane 1 ft outside the edge of the pool, on the downwind side. There are no small calorimeters in the model. The computational grid was identical for all the runs with the obstacle. The no wind and 5 mph wind cases (no obstacle) use the same grid and the 10 mph case (no obstacle) uses a slightly different grid. The number of zones (or cells) and the dimensions of the grid are also given in Table 3.

Figures 1-12 present the results of the pre-test simulations. Figures 1-6 present gas temperature at the pool centerline. Figure 7-12 present the heat flux to the cells near the ground plane (0.5 ft above the ground for the no-obstacle case and 0.75 ft above the ground for the obstacle case due to the different grids).

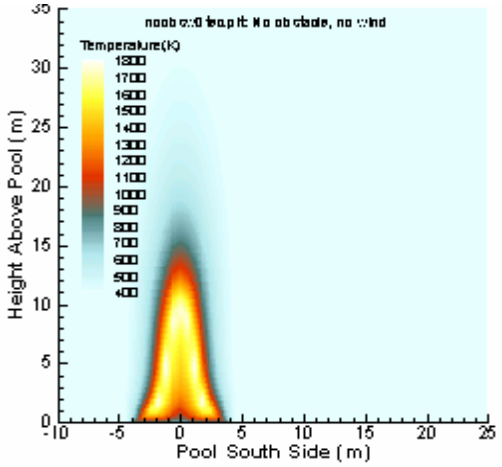

Figure 1. Pretest sim, temperature, 0 mph, no obstacle.

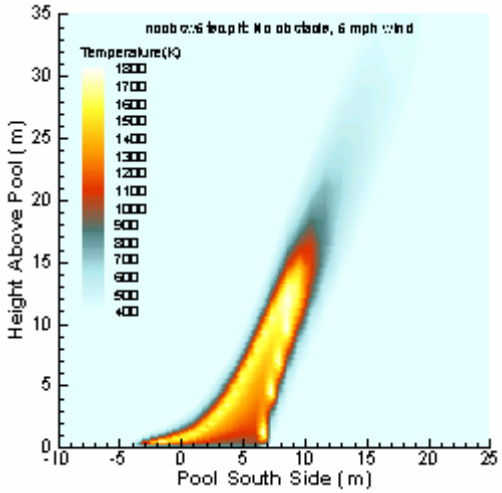

Figure 2. Pretest sim, temperature, 5 mph, no obstacle.

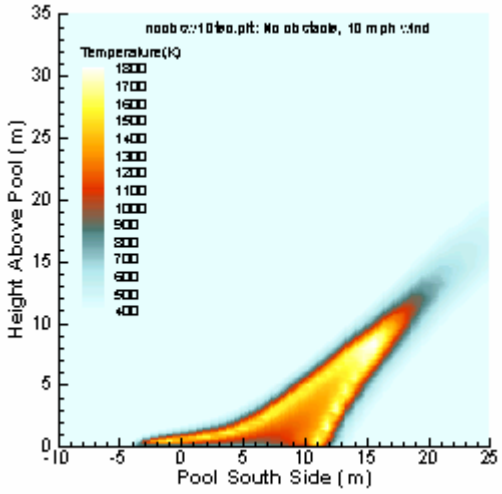

Figure 3. Pretest sim, temperature, 10 mph, no obstacle

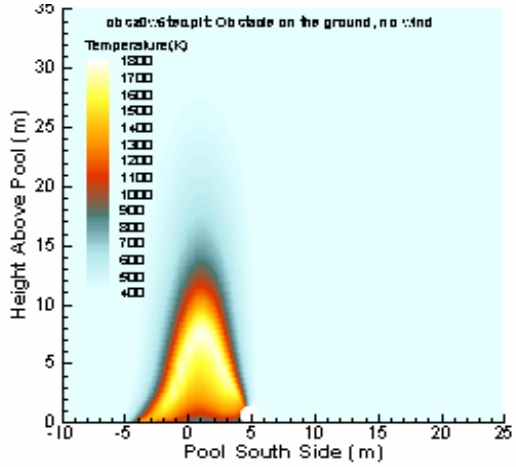

Figure 4. Pretest sim, temperature, 0 mph, w/obstacle.

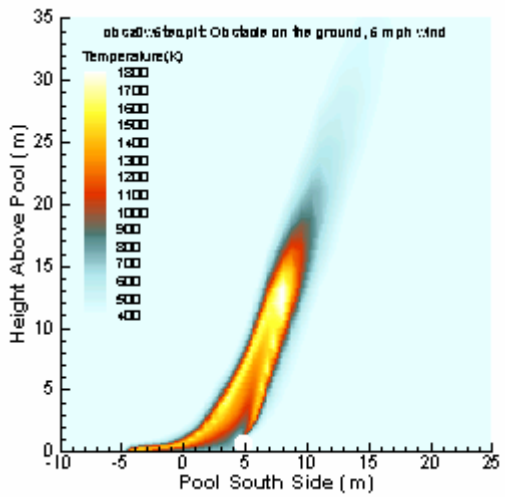

Figure 5. Pretest sim, temperature, 5 mph, w/obstacle.

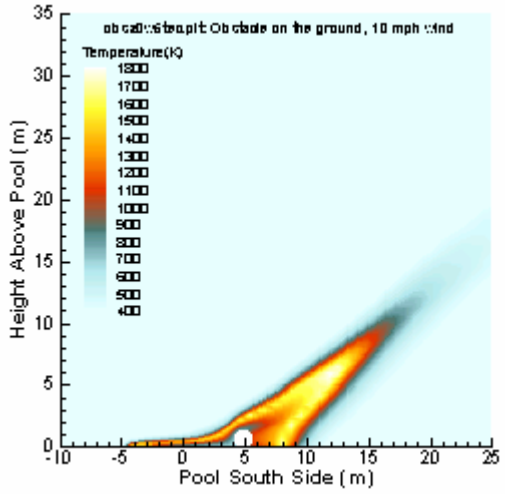

Figure 6. Pretest sim, temperature, 10 mph, w/obstacle.

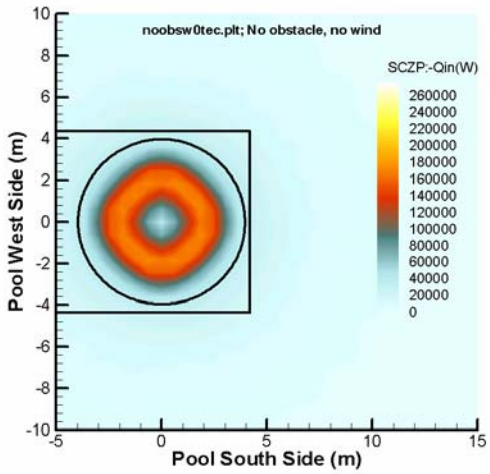

Figure 7. Pretest sim, heat flux, 0 mph, no obstacle.

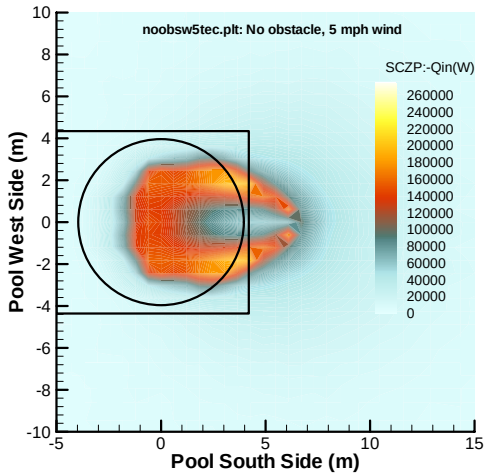

Figure 8. Pretest sim, heat flux, 5 mph, no obstacle.

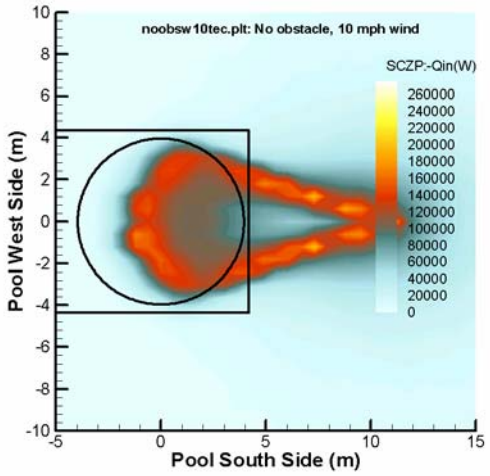

Figure 9. Pretest sim, heat flux, 10 mph, no obstacle.

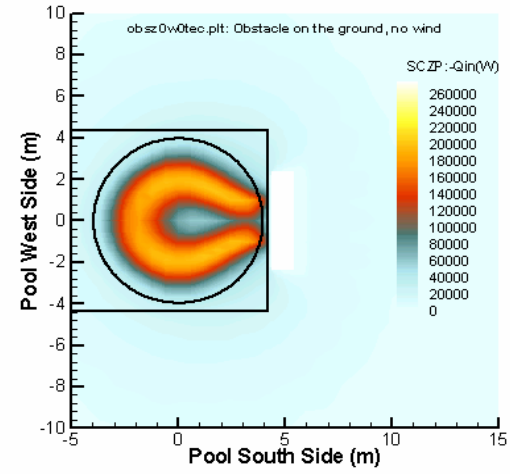

Figure 10. Pretest sim, heat flux, 0 mph, w/obstacle.

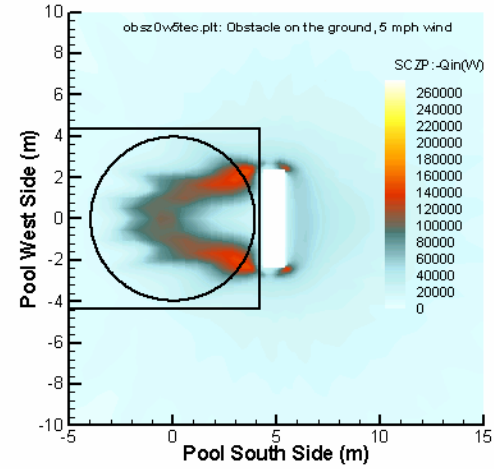

Figure 11. Pretest sim, heat flux, 5 mph, w/obstacle.

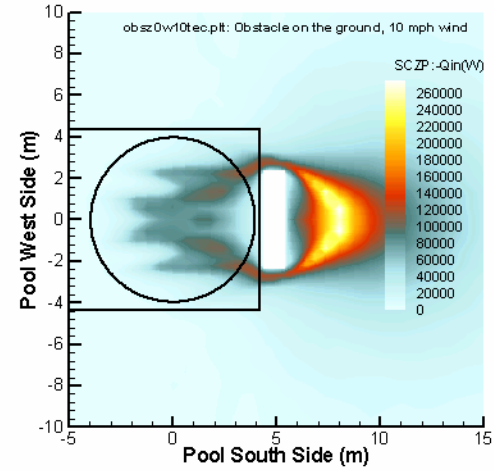

Figure 12. Pretest sim, heat flux, 10 mph, w/obstacle.

The fuel consumption rate is fundamental in determining the heat release rate (HRR) and hence the fire environment. The vaporization process from a pool of fuel is not yet fully understood. As such, this process is likely to be the weak point in pretest fire modeling. Various sub-models ranging from empirical correlations to detailed heat transfer calculations exist. Fuel consumption data, heat flux to the pool, and pool temperatures from this test series may be used to evaluate the different sub-models and contribute to the empirical correlation database. Fuel consumption can be deduced from the time history response of a pool thermocouple array deployed to sense fuel level.

The following empirical correlation for HRR (in MW units) as a function of pool dimensional characteristics has been developed from historical test data [12] and a functional form suggested by Drysdale [13]. The functional form of the fuel surface regression rate based on physical reasoning is

$$\dot{r} = \frac{C_1}{D} + C_2 + C_3 \cdot \left(1 - e^{-C_4 \cdot D}\right) \quad \text{mm/min}$$

where a best fit to historical data for pools ranging from 0.3-18 m (1-60 ft) in diameter (D) gives

$C_1 = 0$ m^2/min
$C_2 = 0.409$ mm/min
$C_3 = 4.103$ mm/min
$C_4 = 0.38423$ 1/m

The mass flow rate per unit area is

$$\dot{m}'' = \frac{\dot{r}}{1000 mm/m \cdot 60 s/\min} \cdot \rho_{fuel} \quad \text{kg/(sec m}^2\text{)}$$

where ρ_{fuel} = 808 kg/m^3.

The total heat release rate is

$$HRR = \dot{m}'' \cdot \Delta H_c \cdot A_{pool}$$

where the heat of combustion ΔH_c = 43.2 MJ/kg. A_{pool} is the surface area of the pool in m^2. For the 26 ft (7.92 m) pool in this test, the correlation yields

$\dot{r}$ = 4.32 mm/min
$\dot{m}''$ = 0.058 kg/(m^2 sec)
A_{pool} = 49.3 m^2
HRR = 124 MW

These values are used in experimental design and instrumentation selection.

This page intentionally left blank.

3 Experimental Instrumentation

This section describes the experimental setup for the Well-Characterized Open Pool Test Series. The tests were performed in a 26 ft. diameter, outdoor-pool fire test facility located at Sandia National Laboratories Lurance Canyon Burn Site. All tests utilize JP8 fuel. Figure 13 is a photograph showing the pre-test fueling of the pool for Test 1.

Figure 13. 26-ft diameter open pool with heat flux instrumentation.

3.1 Test Hardware and Instrumentation

Four calorimeters and 49 Sandia Heat Flux Gauges (HFGs) mounted both inside and outside the fire were used to measure object, pool, and surrounding terrain incident heat flux. Four weather stations collecting wind data were located about 95 feet from the pool centerline (upwind to the pool). The wind sensors were placed at 2, 5, and 10 meters above the ground at each of the stations. Wind conditions were measured relative to magnetic north and recorded at approximately 1 sample per second. The overall test layout, with locations of calorimeters, cameras, and weather stations, are as indicated in Figure 14.

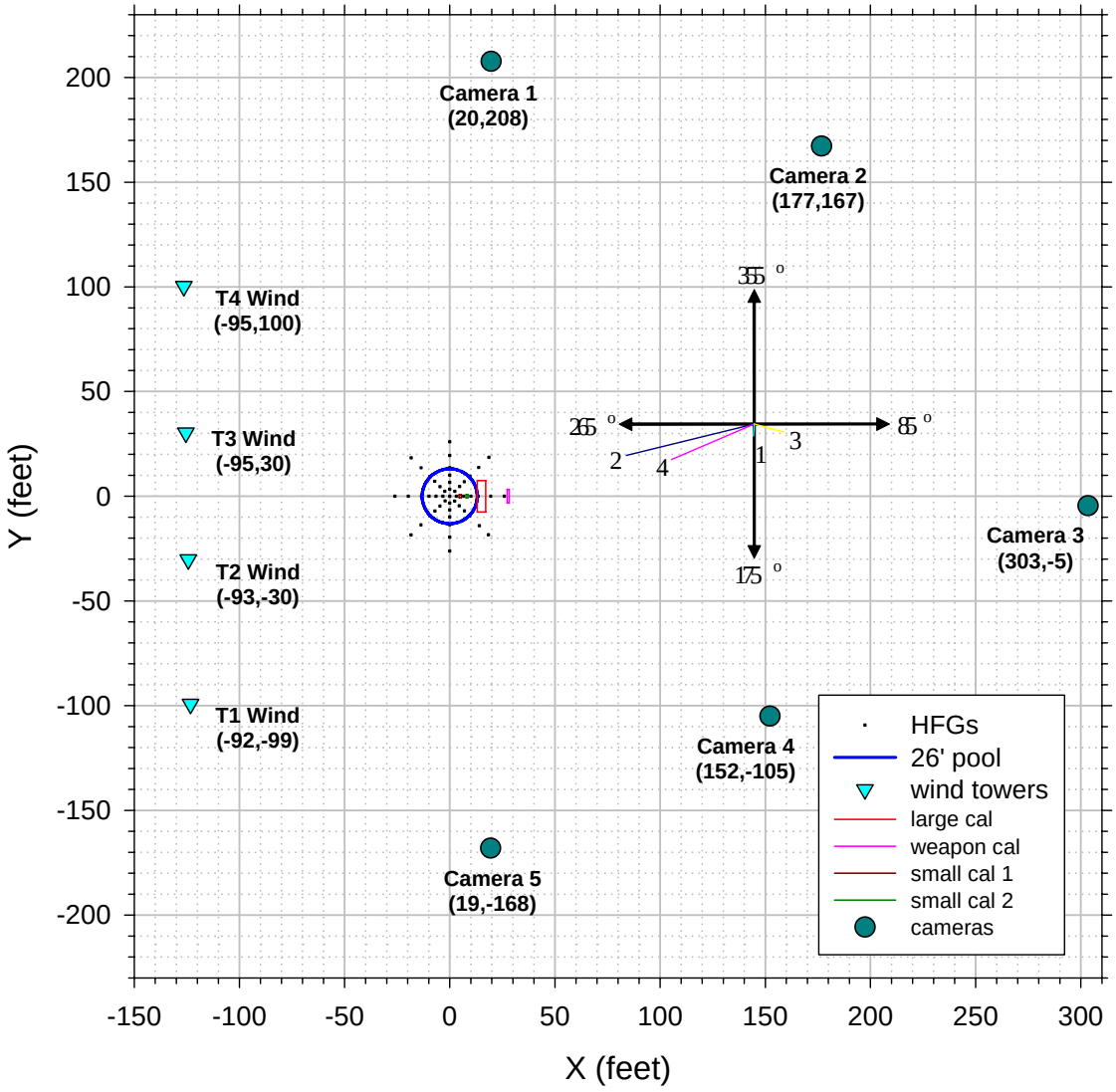

Figure 14. Overall layout of the test, note prevailing wind from 265°.

All calorimeters were positioned such that prevailing winds were normal to the calorimeters. The large calorimeter was positioned at the lee side (edge) of the open pool. This position was chosen in part based on previous results from the mock fuselage test series where the presence of a cylinder at the lee side of a wind-swept flame zone had a pronounced effect on the fire as compared to fires without engulfed objects.

Figure 14 also provides a wind rose based on the test layout to the prevailing wind (from 265°). The average wind vector (from direction) and wind magnitude (length of vector) are graphically shown for each test.

The fuel pool was fitted with a thermocouple array (or comb) at the pool south end to measure in-depth temperatures in the fuel during the burn. The response of the in-depth thermocouples can be used to deduce the fuel consumption rate. The comb contained 30 thermocouples (0.5-

inch spacing). At the start of the fire, the top 2 or 3 fuel comb thermocouples would reside above the fuel surface (typically 12 thermocouples would reside in the fuel layer (about 6 inches, assuming 2200 gallons (nominal) of JP-8).

Except where indicated, all temperature measurements utilized type K thermocouples, 0.063-inch diameter, Inconel sheathed, ultra-pure MgO insulated, with ungrounded junctions. The type K thermocouple has an operating range from 0°C to 1250°C that encompassed expected temperature levels. The 0.063-inch diameter has proven best for field use. Smaller diameters are too fragile and larger diameters are too unwieldy. The Inconel sheath has been found to withstand the fire environment where other materials such as 304 stainless steel have not. Ultra-pure MgO insulation is required to avoid thermal shunting, an insidious problem that appears in long thermocouples routed through multiple zones of high and low temperature [14,15]. The use of ungrounded junctions with grounded sheathing minimizes electrical noise prevalent in thermocouple circuitry. The response time of these thermocouples in a fire is expected to be on the order of a few seconds. A detailed description of the devices can be found in the Omega Catalog [16], however, equivalent thermocouples are available from several manufacturers including Thermoelectric, Watlow Gordon, and Omega.

The maximum type-K thermocouple error using the manufacturer calibration is ±9.4°C at 1250°C. It is possible in some cases for considerable temperature measurement error to occur [17]. This error is caused by thermal shunting (the creation of false junctions due to TC insulation breakdown) in overheated sheath and insulation sections in the assembly. The locations of the thermocouples have an uncertainty of approximately 0.1 m (4”).

Appendix A provides a succinct listing of all instruments, including the name, data file designator, description, and location referenced to zero (pool centerline, fuel surface). The locations of the pool and ground surface thermocouples (used in the SNL HFGs) have an uncertainty of approximately 0.1 m (4”).

The following sections describe the construction of the test hardware and the instrumentation used to obtain the necessary data as described in section 2.1. The test hardware consists of three assemblies: the two small calorimeters, the large transportation calorimeter, and the weapon calorimeter.

3.2 Fuel Surface and Terrain Heat Flux Measurements

The rate of liquid fuel vaporization is among the most important variables to be predicted in the simulation of fire environments. The fuel vaporization, or burn rate, determines the amount of fuel available for combustion within the flame zone and also defines the duration of the fire. Data acquired from earlier test series in this program indicate that the rate of fuel vaporization rate becomes constant with time shortly after ignition, but varies over the surface of the fuel pool. This spatial variation may be induced by non-uniform fuel surface heat flux and thermal transport within the fuel.

Spatial and temporal distribution of heat near the fuel pool surface were acquired in this test series to support the assessment and further development of fuel vaporization sub-models for fire field models. Hemispherical heat fluxes gauges (HFG), designed by SNL, were used to measure the heat flux near the fuel surface and the surrounding terrain.

As illustrated in Figure 15, forty-nine single-sided, upward facing, HFGs were used to measure the spatial distribution of incident heat flux to the fuel pool surface and the terrain surrounding the pool. The spatial distribution of heat flux was used to deduce the overall size of the fuel vapor dome and to infer the distribution of fuel vaporization from the surface of the liquid.

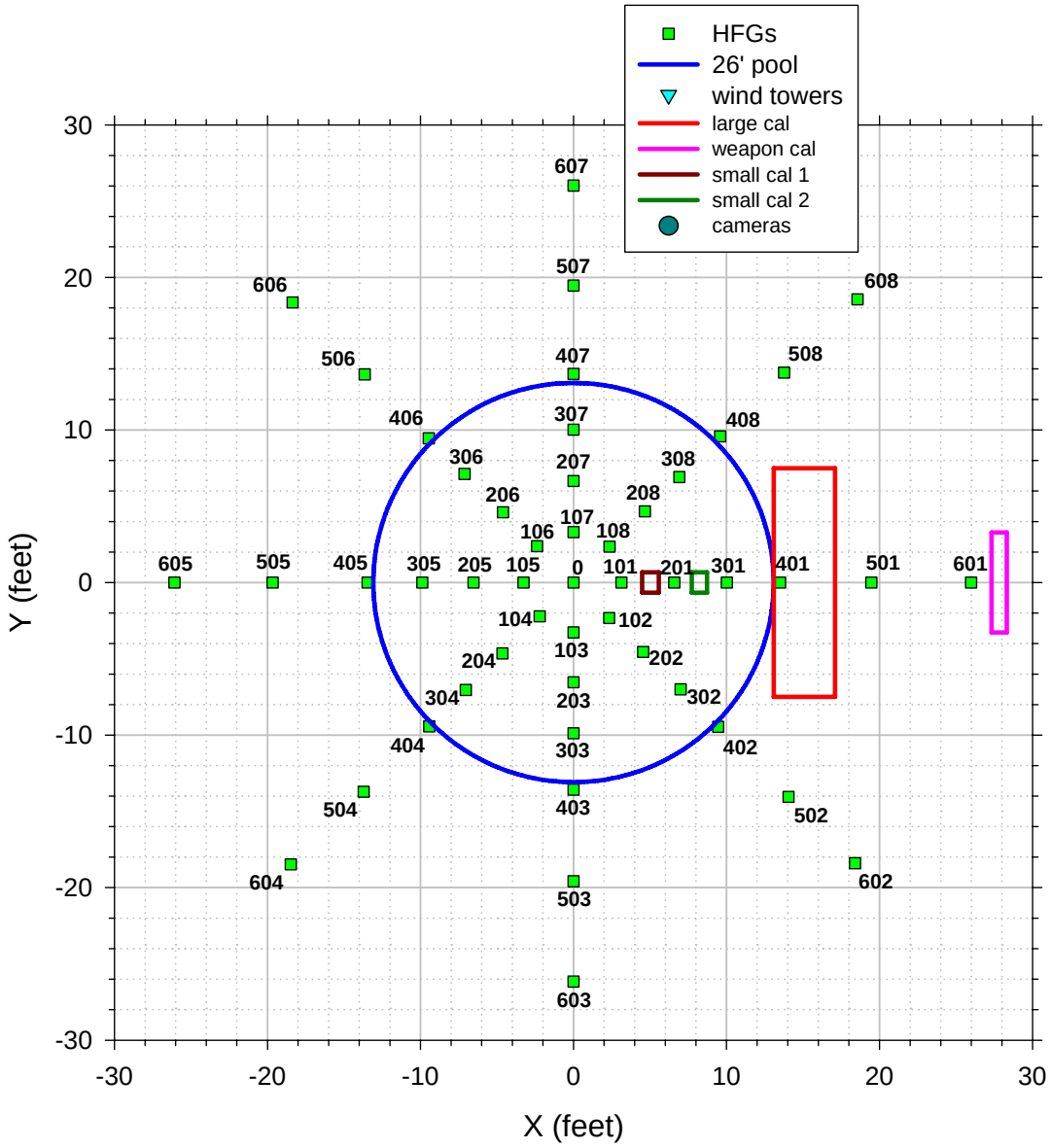

Figure 15. Instrument designators and location of HFGs.

The single-sided HFGs were constructed according to SNL drawing R45065 [18]. HFGs located within the fuel pool are mounted to a square base plate. Stands attached to the corners of the base plate were used to level the pool gauges and to position the gauge sensor surface approximately 6 inches above the ground plane surface (approximately 7 inches above the fuel surface). The HFGs located outside the pool were also located such that the sensing surface of the gauge was 6 inches above the ground plane.

The HFG is primarily a thin metal plate with one side facing the fire environment and the other side insulated. The metal plate responds to the heat flux from the half space in front of the exposed face. If it is assumed the plate is in thermal equilibrium with a radiation-dominated environment, the plate temperature can: 1) be converted to an incident flux characteristic of the half space, or 2) be interpreted as an effective temperature of the half space. The plate temperature is measured using a thermocouple attached to the insulated face of the metal plate.

The response time of the HFG has been experimentally determined to be on the order of about 60 seconds. Experimental analyses have determined that applying a simple thermal response model to the SNL HFG data yields calculates incident heat fluxes to within about 5% of measured values, provided the input flux is steady. However, the early time results may be in considerable error. All HFG temperature data were processed posttest to provide an estimate of the instantaneous incident heat flux. Details of the construction and the performance of the gauge, the thermal response model used to reduce the HFG data, and the uncertainty analysis of the thermal response model are described in the SNL HFG report [18].

Fifteen Gardon heat flux gauges were also placed in the surrounding terrain adjacent to HFGs on the leeward side of the pool (i.e., on the bottom right and top-right quadrants of Figure 15).

3.3 Small Calorimeters

Two Sandia-designed calorimeters were placed within the pool approximately 6-7 inches (from the calorimeter bottom) above the ground plane surface (5.75 inches for calorimeter 1, 7 inches for calorimeter 2). Figure 16 shows a sketch of a typical calorimeter. Each calorimeter is a stainless steel (SS) cylinder 12 inches in outside diameter, 16 inches long, with 1/8 in wall thickness and ¼ in thick SS end caps. TCs were spot welded to the inner surface of each of four (4) disc-like cutouts every 90 degrees. These disc cutouts are located 8 inches from each end and in the center of each end cap. Also included are four TCs 1 inch from the inside wall adjacent to each wall TC. These TCs provide an additional boundary condition to calculate heat flux. Lastly, a single TC was positioned at the very center of the inside of the calorimeter to check for shunting and noise. The inside is packed with multiple layers of 1-inch thick ceramic fiber (Kaowool, 8lbs/cu.ft.) insulation. End plates were bolted to the cylinder ends. All external surfaces were painted black using Pyromark 2500 to provide a known emissivity (0.86 ± 0.09) [19]. Figure 17a shows one on the small calorimeters in place for the first test (with insulated thermocouple bundle). Figure 17b shows the location of TCs. The top-right view shows the end cap TCs looking at the calorimeter from the west side of the pool. The #1 small calorimeter was located 4.98 ft from pool centerline and 0.48 ft above the ground plane. The #2 small calorimeter was located 8.23 ft from pool centerline and 0.58 ft above the ground plane.

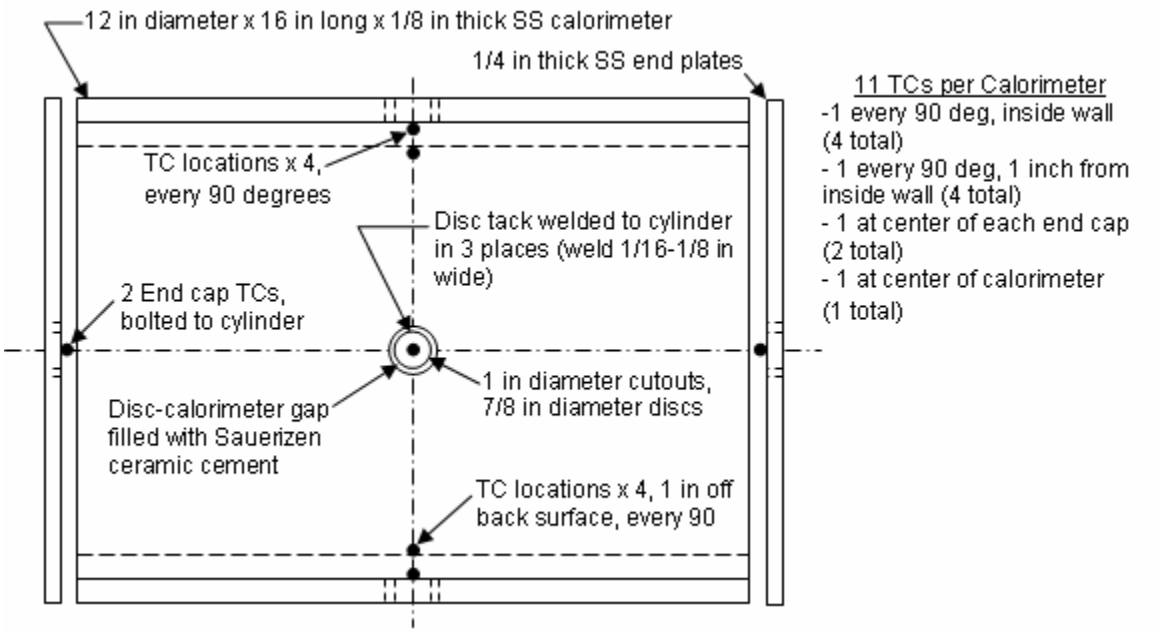

Figure 16. The small calorimeter assembly.

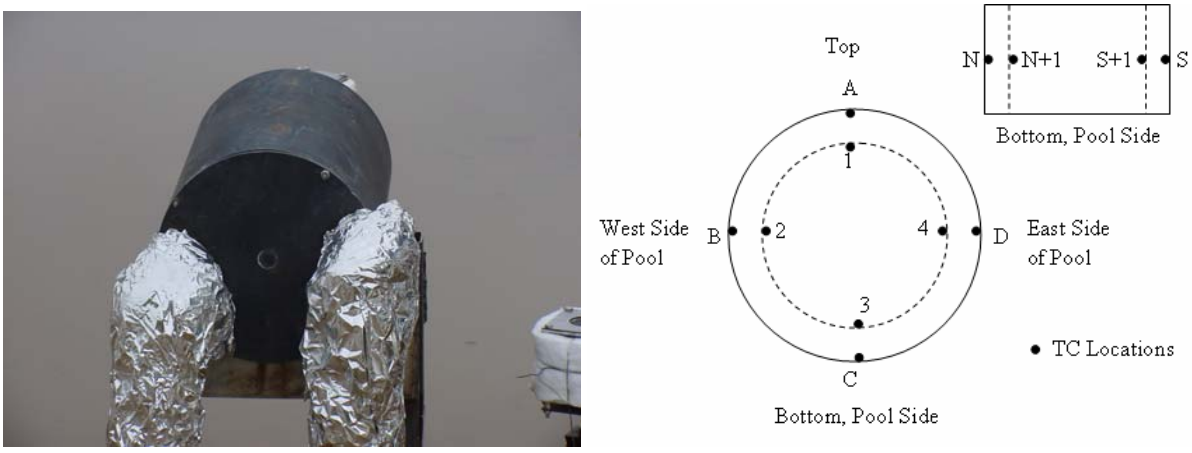

(a) (b)

Figure 17. Small calorimeter (a) mounted above the pool surface and (b) TC locations.

3.4 Large "Transportation-Sized" Calorimeter

A large calorimeter, similar in size and shape to a truck sized waste transportation container, simulating a bluff body obstruction was placed on the lee side of the pool surface, 13.0 ft from pool centerline and 3 ft above the ground plane. The carbon-steel calorimeter is a 1.22 m diameter, 4.57 m long, 2.54 cm wall thickness (4 ft diameter, 15 ft long, 1 inch wall thickness) with an end cap (1 inch thick) welded to one end, and an end cap bolted to the other end. The calorimeter has a mass of 3860 kg (8500 lb weight).

Sixty-three (63) thermocouples are attached to inside surfaces (tacked down with thin metallic strips), the wires exit through a notch in the bottom of the bolt-on end cap. Figure 18 shows the locations of the thermocouples. All of the thermocouples (with the exception of the 200 series) are covered with a 3-inch thick, 3-inch diameter pad of ceramic fiber insulation. For the 200 series, two thermocouples are used (one thermocouple is tacked to the inside surface with the second thermocouple directly opposite the first, separated by a 1-inch thick, 3-inch diameter pad of ceramic fiber insulation). Figure 19 shows the inside of the calorimeter with the insulation pads over the thermocouples. All external surfaces were painted black using Pyromark 2500 to provide a known emissivity (0.86 ± 0.09) [19].

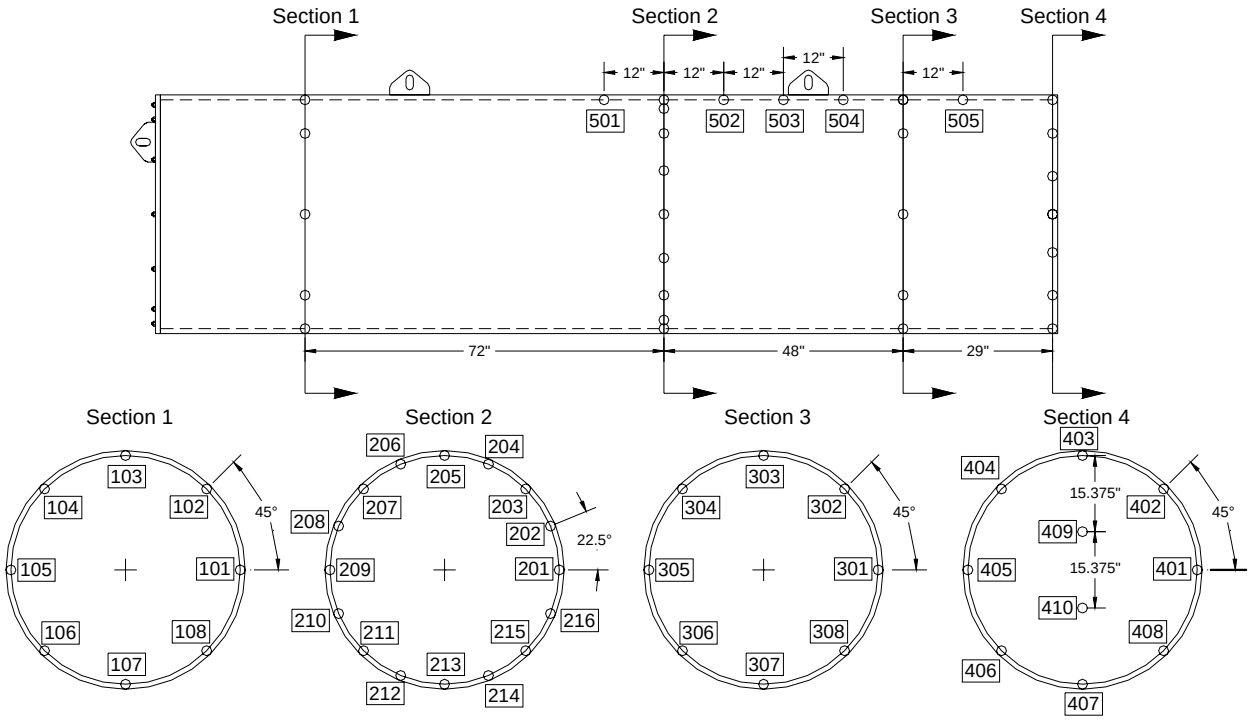

Figure 18. Large calorimeter thermocouple locations and ID numbers.

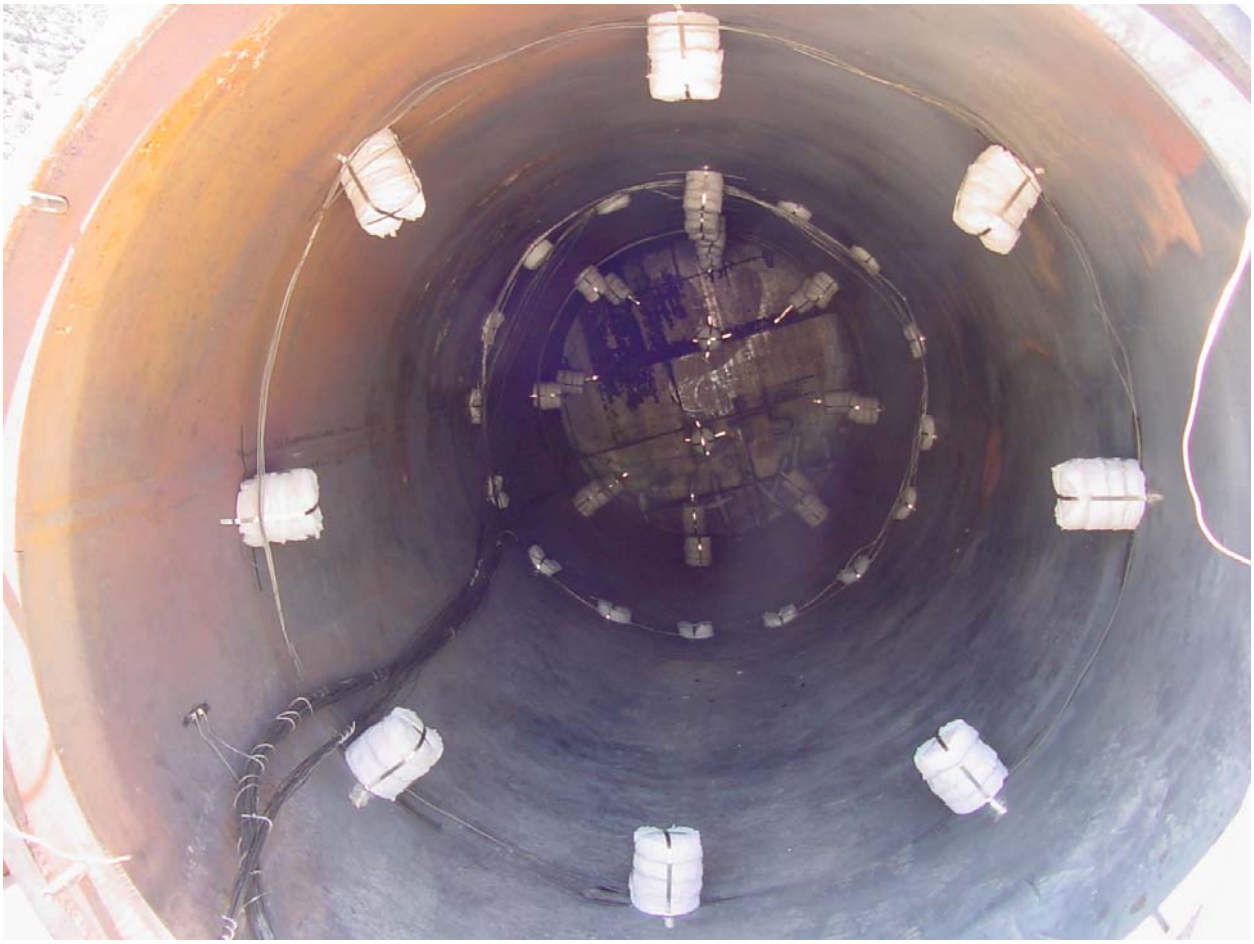

Figure 19. Insulation pads for thermocouples inside the large calorimeter.

3.5 Medium "Weapon-Sized" Calorimeter

The weapon calorimeter is constructed of 0.125 inch thick 304 stainless steel (see Figure 20). It has an outer diameter of 12 inches, and is 2 m long. It was located 27.75 ft from pool centerline and 1 ft above the ground plane. There are 8 circumferential measurement stations. Measurement station 1 faces due East with the rest sequentially numbered in a counterclockwise direction when facing North (see Figure 21).

Each station consists of a square coupon and a Gardon heat flux gauge. The coupons are 0.125" thick and are fitted with an intrinsic thermocouple on the internal surface. A layer of 1" thick ceramic fiber insulation covered the thermocouple. Another thermocouple (attached to .040" stainless shim stock) was directly opposite and separated from the coupon thermocouple by a layer of 1" thick ceramic fiber insulation. The rest of the volume was filled with ceramic fiber insulation.

The steel coupons with intrinsic thermocouples attached to the calorimeter have proved to be robust and viable. For calibration purposes, circular holes have been machined into the calorimeter body about 1-2 diameters to the side of the coupons in order to internally mount a circumferential array of eight water-cooled Gardon gauges. The calorimeter's modification has been designed and fabricated to allow in-situ calibration of each individual coupon. Figure 22 shows the coupons being calibrated with a radiant heat assembly. The calorimeter body (center section) has been painted with Pyromark 2500 to provide a known emissivity.

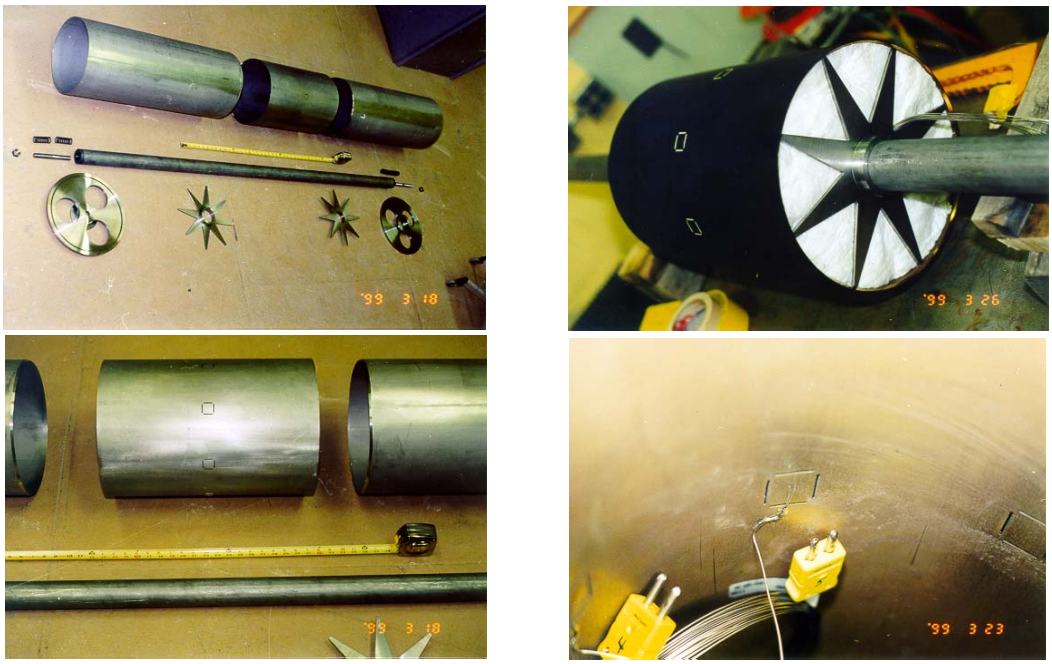

Weapon calorimeter construction and assembly

Figure 20. Modification of the weapon calorimeter to mount internal Gardon gages.

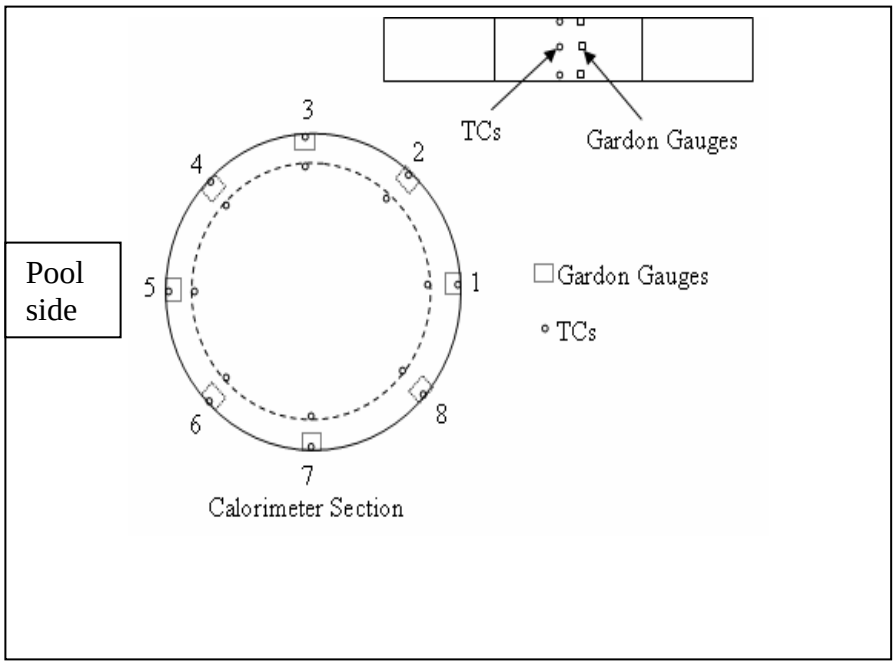

Figure 21. Medium (Weapon) calorimeter TC locations.

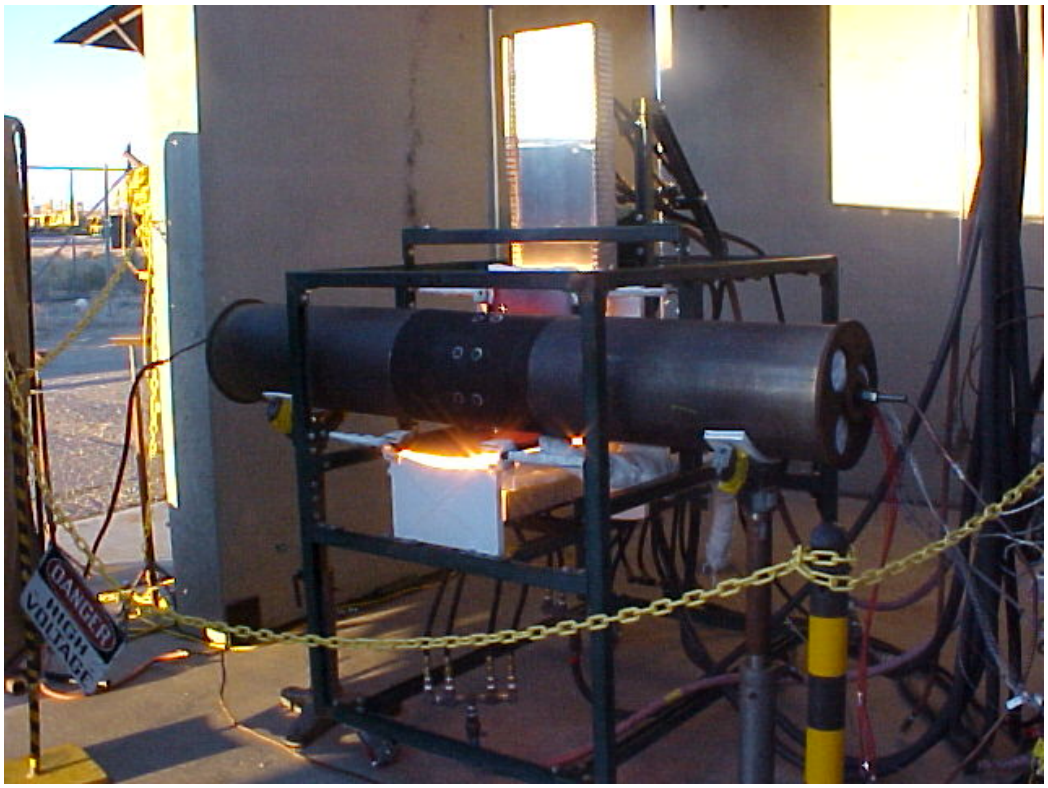

Figure 22. Weapon calorimeter with 8 Gardons during in-situ calibration.

3.6 Measurement of Wind Speed and Direction

Wind speed and direction were measured sufficiently far from the boundary of the pool to reduce the influence of air entrained by the fire plume from the surrounding environment and mitigate the potential effects of radiant heat from the fire. Measurements were performed approximately 95 ft. upwind of the leading edge of the pool at four locations. At all locations, the measurements were made at elevations of 2 m, 5 m, and 10 m above the ground surface.

This approach provides estimates of boundary conditions needed to define the conditions associated with the data. Wind measurements were conducted using the YOUNG 81000 Ultrasonic Anemometer. The 81000 measures wind velocity based on the transit time of ultrasonic signals sent between the transducers. Depending on its orientation and magnitude, airflow alters the sonic signal transit time. By measuring the transit time in each direction along all three paths, the three dimensional wind velocity and speed of sound may be calculated. From speed of sound, sonic temperature is derived. The speed of sound and sonic temperature is corrected for crosswind effects. The 81000 has the following specifications:

WIND SPEED Range: 0 to 40 m/s (0 to 90 mph)
Resolution: 0.01 m/s
Threshold: 0.01 m/s
Accuracy: ±1% rms ±0.05 m/s (0 to 30 m/s)
±3% rms (30 to 40 m/s)

WIND DIRECTION Azimuth Range: 0.0 to 359.9 degrees
Elevation Range: ±60.0 degrees
Resolution: 0.1 degree
Accuracy: ±2° (1 to 30 m/s)
±5° (30 to 40 m/s)

SPEED OF SOUND Range: 300 to 360 m/s
Resolution: 0.01 m/s
Accuracy: ±0.1% rms ±0.05 m/s (0 to 30 m/s wind)

SONIC TEMPERATURE Range: -50 to +50 Cº
Resolution: 0.01 Cº
Accuracy: ± 2 Cº (0 to 30 m/s wind)

GENERAL Air sample column: 10 cm high X 10 cm diameter
Air sample path: 15 cm
Internal sample rate: 160 Hz
Output sample rate: 4 to 32 Hz (selectable).

The tower locations and the position of the US anemometers on each tower are shown in Figure 23 and Figure 24. Photos of the anemometer and towers placed in position are given in Figure 25 to Figure 28.

Additional wind measurements were made using vane-type gauges. The gauges were calibrated within the stated accuracy of the instruments prior to each test and a consistency check was performed to ensure that gauges provide the same indication of speed and direction when placed in the same location.

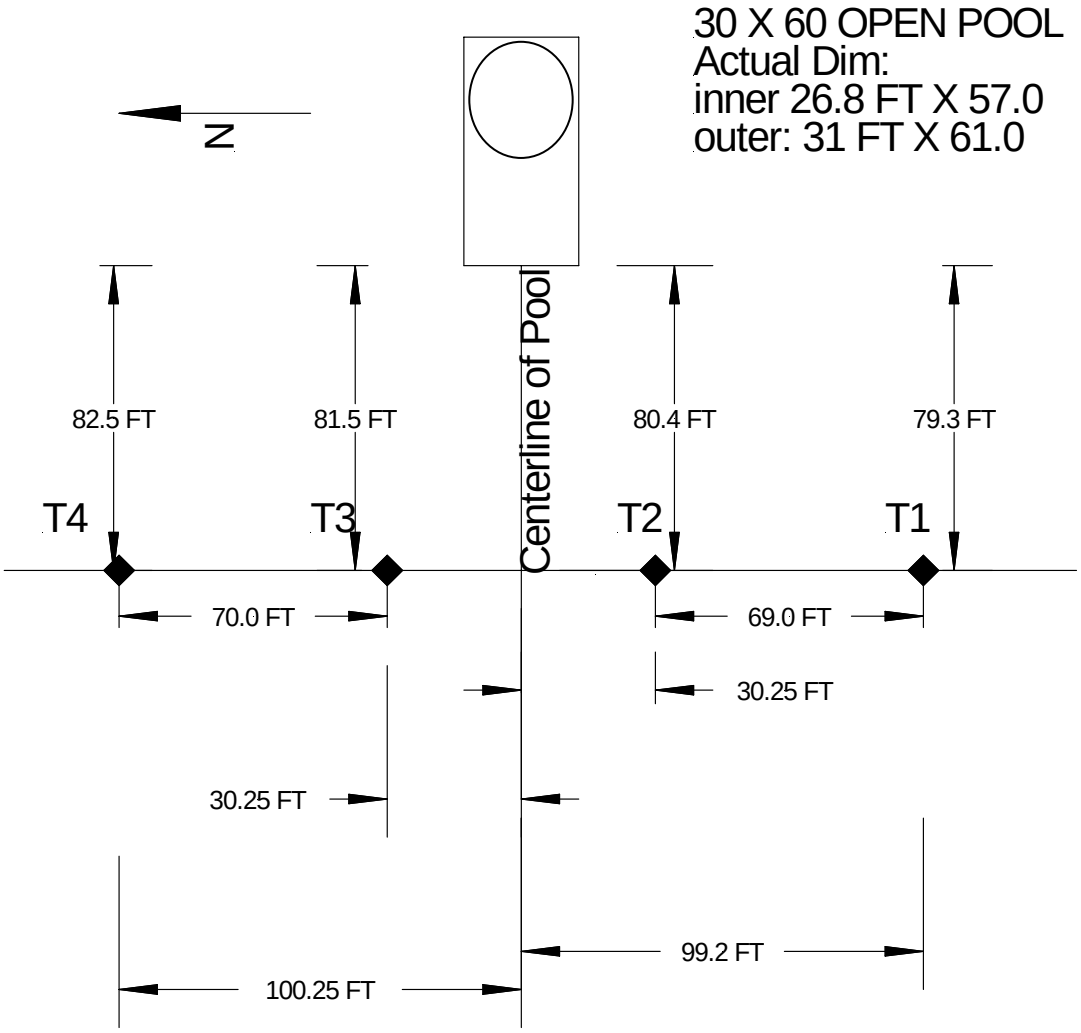

Figure 23. Location of the wind towers relative to the pool.

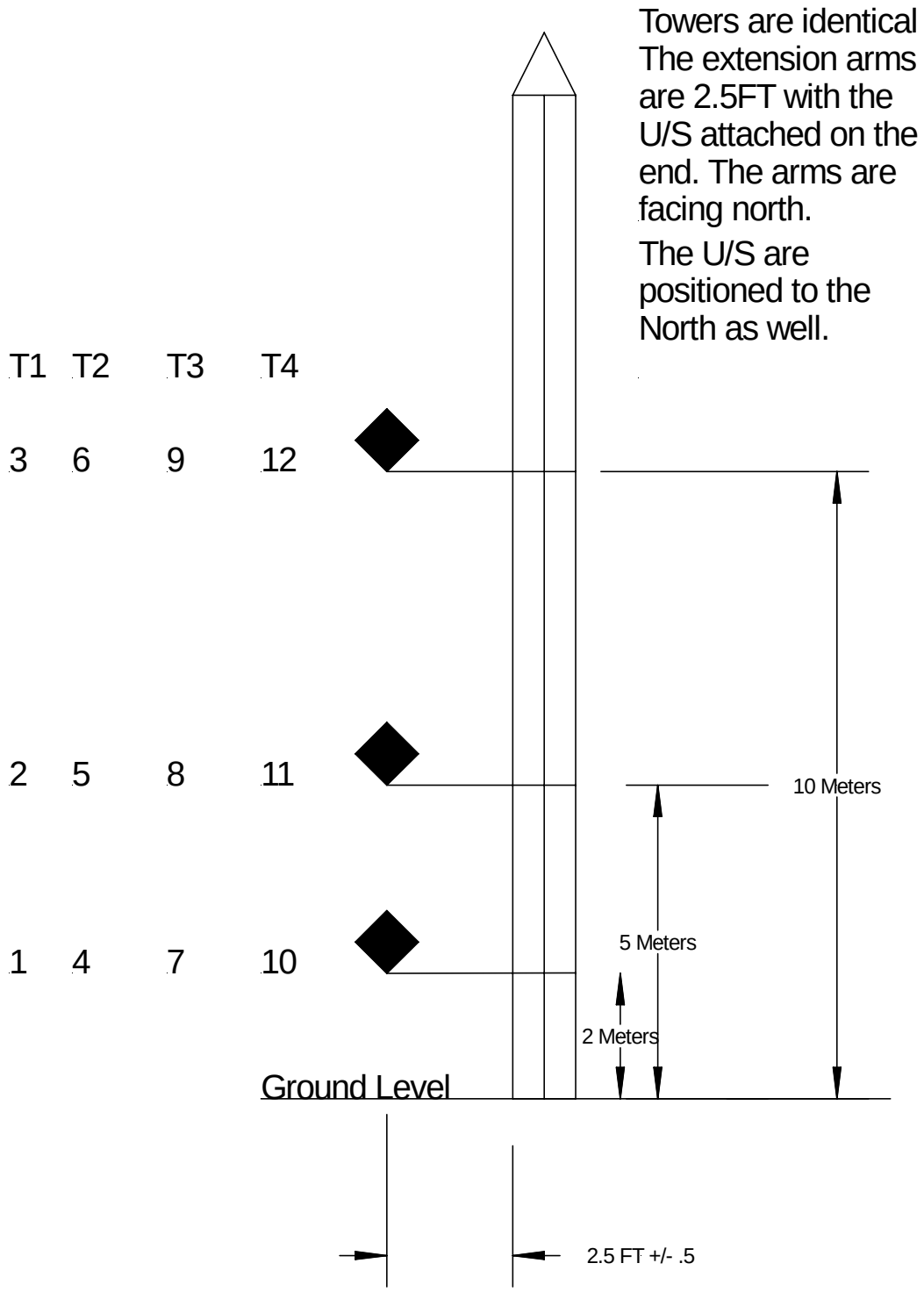

Figure 24. Location and identification of the US wind anemometers on each tower.

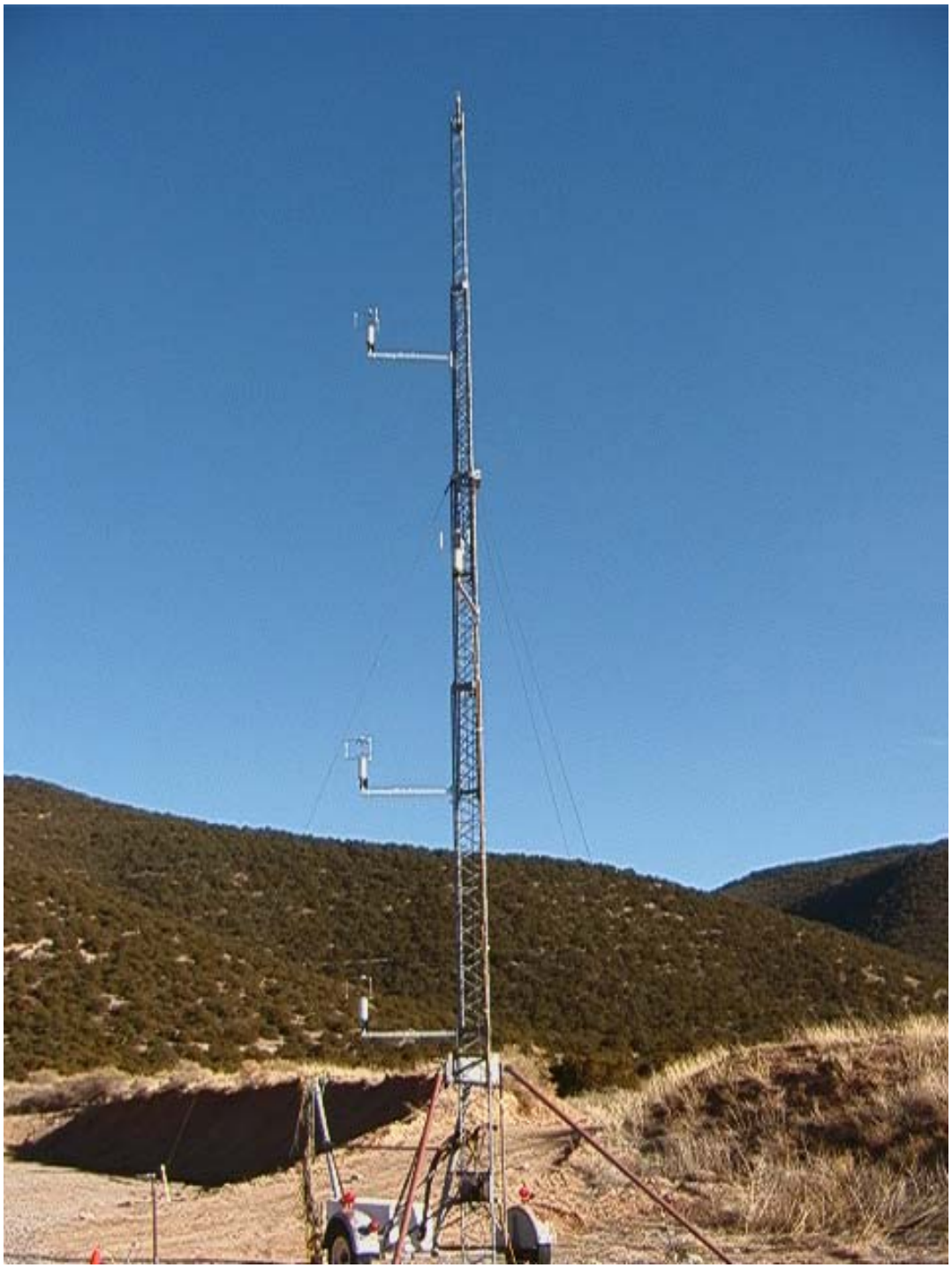

Figure 25. Tower with 3 ultrasonic anemometers.

Figure 26. Close-up of the Young 81000 ultrasonic anemometer.

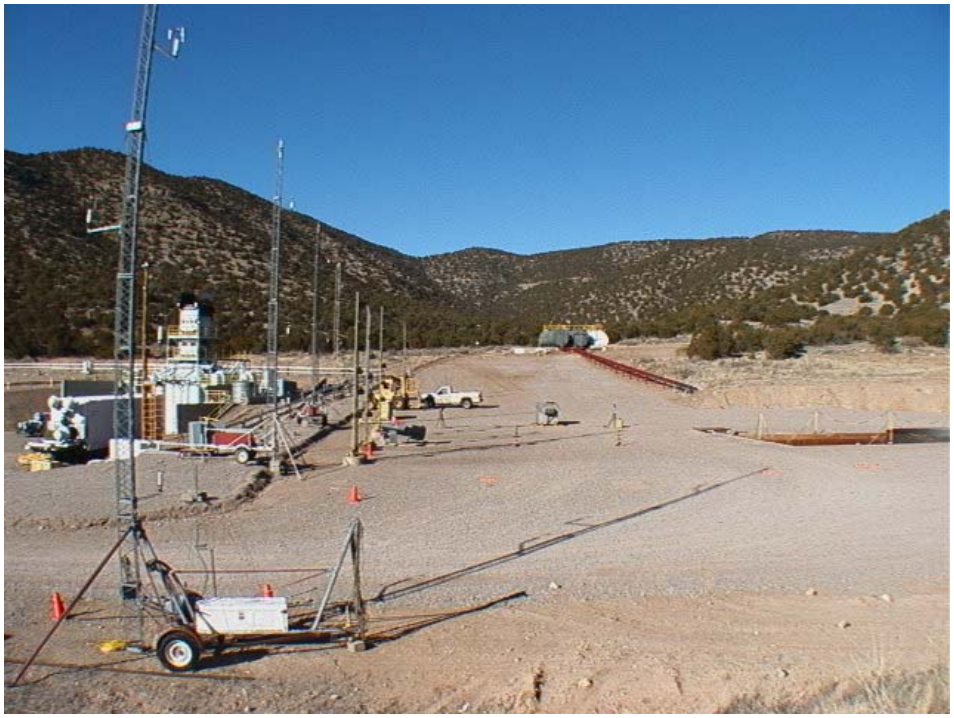

Figure 27. View of the wind tower array looking south to north.

Figure 28. View of the wind tower array looking east to west.

3.7 Fuel Recession Measurements

Fuel recession rates were measured with a differential pressure gage. The differential pressure transducer was attached to the pool to measure fuel depth in fractions of an inch of water. Note that it was necessary to route the low-pressure line to a point above the pan surface to reduce the cyclic pressure pulse due to the flame "puffing". This measurement provided fuel consumption as a function of time, and yielded data for determining burn rates under different conditions.

3.8 Fuel Temperature

The fuel temperature was measured using a TC "rake". The fuel rake can also be used to determine fuel recession, based on a time-of-arrival analysis, a technique used and proven many times in previous experiments. Fuel temperature affects the burn rate and thus becomes an important parameter to measure. The fuel pool used one vertically mounted thermocouple rake containing 30 thermocouples to measure the fuel temperature and gradient.

Figure 29 shows a typical fuel rake. For the open pool tests, thirty type-K, 1/16-inch diameter, inconel sheathed thermocouples were mounted on a steel pedestal. Thermocouple spacing was set to 0.5 inches.

Figure 29. Fine-wire TC array for fuel temperature/regression measurements.

3.9 Photometric Coverage

Video camera coverage of the fire was provided at five locations. The vertical field of view for the cameras extended from the pool surface to an elevation of approximately 180 ft. above the pool surface. As appropriate, the vertical field of view of all the cameras could be adjusted during the test to encompass the entire height of the continuous flame zone. Camera 1, 2, 3, 4 and 5 were located 310°, 15°, 100°, 170° and 190° clockwise with respect to the wind direction axis shown in Figure 14.

3.10 Data Acquisition

The data acquisition system is capable of acquiring temperature, pressure, and wind vane data. A summary of the data required to support this test is given in the Table 4, List of Instruments Table. The integrity of all channels was evaluated prior to the test. Data were sampled simultaneously for all channels, at a rate of one sample per second.

3.11 Fuel Addition and Ignition

Ignition of the fuel was accomplished using the "blowtorch". The blowtorch consists of an ASME pressure vessel holding about one liter of JP-8, an automotive fuel pump, a jet engine fuel nozzle, and an oil-fired boiler 3000-V spark gap. A fire set controls both the fuel pump and the spark gap. The fuel pump forces pressurized JP-8 into the nozzle and the JP-8 is then ignited by the spark gap and sprayed across the pool. The blowtorch is a safe and effective tool to ignite the

entire surface quite rapidly and uniformly. Figure 30 shows the fuel pump, fuel reservoir, valve, pressure gauge, and fire set.

Figure 30. Fuel igniter setup.

3.12 Summary of Instrumentation

Shows instrumentation used for the 4-experiments. Note the Gardon heat flux gauges were only used in Test 1. A total of 223 measurement points were used in these experiments.

Table 4. Instrumentation Summary.

Measurement Sensor Type	No. of Locations	Sensors per Location	Total No. of Sensors
Fuel Surface HFGs (TCs)	25	1	25 TCs
Ground Surface HFGs (TCs)	24	1	24 TCs
Ground Surface HFGs (Gardon) (only on Test 1)	15	1	15 GHFGs
Fuel Temperature & Recession (TCs)	1	30	30 TCs
Wind (Ultrasonic)	4	3	12 USs
Fuel Recession (DP)	1	1	1 DP
Small Calorimeter Heat Flux (TCs)	2	12	24 TCs
Medium (Weapon) Calorimeter Heat Flux (TCs)	1	16	16 TCs
Medium (Weapon) Calorimeter Heat Flux (Gardon)	1	8	8 GHFGs
Large Calorimeter Heat Flux (TCs)	1	63	63 TCs
Video Cameras	5	1	5 VCs
Total			223
Thermocouples			182
Gardon Gauges			23
Wind Sensors			12
Pressure			1
Video			5

This page intentionally left blank.

4 Experimental Results

4.1 Overview

A series of well-characterized open pool fire tests was performed during the month of September, 2003. The focus of these fire tests was to provide environmental information for open pool fires on a physics first principal basis. Results presented here include a general description of test observation (pre and post-test), wind measurements, fire plume topology, average fuel recession and heat release rates, and incident heat flux to the pool and to the calorimeters. Average wind conditions are given and were used to identify quasi-steady periods. Heat flux contour plots were generated for quasi-steady periods for the pool and for the large calorimeter.

4.2 Data Archive

All of the experiment data presented in this report are provided on CD ROM. The raw data includes wind speed and direction plots from ultrasonic wind measurement stations, thermocouple and fuel recession data. Other post-processed data are also included and include post-processed fuel recession data and 1- and 2-dimensional post-process heat flux data and plots obtained from thermocouples. The ignition time was selected to be the zero time for all plots. Ambient and initial conditions can be obtained form the first few minutes of each plot.

All of the photographs taken during the experiments before and after the test are included with the raw data in the data archive. Some of the movies from video cameras were digitized and are also included with the raw data in the data archive. The movies can be viewed with MPEG views, such as Windows Media Player. Observations from video records are included in the discussion of results.

4.3 Summary of Test Observations

Notes were taken during and after each test. These notes provided a summary of test observations.

4.3.1 Test 1

Test 1 was initiated at 7:53 AM on September 8, 2003. Figure 31 shows images of the experiment setup prior to ignition of fuel in Test 1. The test was performed using approximately

2207 gallons of JP8 aviation fuel. The fuel was floated on 30" of water (see Figure 31a), which was used as a level. Ignition was accomplished by using an electrically ignited blowtorch located between the south and south west side of the pool (see Figure 31a). Test 1 included the large calorimeter (see Figure 31b)

Wind conditions were nearly calm in Test 1. Wind speeds were approximately 2 mph on average, well within the desired wind speed (0-5 mph, see Table 2). Figure 32. shows the fire plume from the various directions. As depicted in Figure 32a, the fire plume was approximately normal to the ground during most of the test. Changes in wind direction tipped the plume slightly in various directions and caused the east edge of the plume to lean towards or away from the large calorimeter from time to time as shown in Figure 32b and Figure 32c.

Figure 33a shows the soot outline on the ground. Soot coverage is limited to the area near the pool due to the relatively calm wind conditions. Accumulation of soot is slightly more severe on the south side of the pool, but not enough to suggest the plume's preferential direction.

Instruments were inspected before and after Test 1. A thin layer of soot coated many of the Sandia heat flux gauges located inside the pool (see Figure 33b) after the test. Several Gardon gauges placed adjacent to HFGs in the surrounding terrain on the leeward side of the pool (401, 402, 403, and 507 in Figure 15) exceeded their maximum output 300 to 600 seconds into the test, hence no test data is reported.

Signals from the small calorimeter thermocouples failed about 25 minutes into the test; inspection of the small calorimeters determined thermal damage of the thermocouple extension wires.

(a) (b)

Figure 31. Experiment setup for Test 1.
(a) view from west side, (b) view from the east side.

(a)

(b)

(c)

Figure 32. Fire plume during Test 1
(a) fully developed fire plume viewed from southwest; (b) close up of fire plume when east edge of pool was away from the large calorimeter; and (c) close up of fire plume when east edge of pool made contact with the large calorimeter

(a)

(b)

Figure 33. Post test images of Test 1.

Melting of the extension wires (placed within insulated stainless-steel tube) had occurred at the location between the calorimeter exit and the water level. These wires were replaced with new ones in Test 2. Table 5 shows the approximate time at which TCs failed. TC locations are shown in Figure 17b. In the large calorimeter, three TCs failed from the start (214, 304 and 406 in Figure 18) and one TC (inner 213 in Figure 18) failed after 1045 seconds. These TCs were not replaced in subsequent tests. Lastly, Gardon gauge 7 in the medium (weapon) calorimeter was found to be inoperative from the beginning of the test (and was not replaced in subsequent tests).

Table 5. Time to Failure of the Small Calorimeter Thermocouple in Test 1.

TC Location	Small Calorimeter: West (s)	Small Calorimeter: East (s)
N	1923	1570
N+1	1911	1570
S	2149	1795
S+1	1860	1871
A	2091	1780
B	2140	1800
C	2154	1748
D	1882	1902
1	2112	1075
2	2179	1748
3	1904	1748
4	1930	1780

4.3.2 Test 2

Test 2 was initiated at 1:42 PM on September 16, 2003. Test 2 setup was the same as Test 1 (see Figure 31). The test was performed using approximately 2207 gallons of JP8 aviation fuel. The fuel was floated on 30" of water in the 26 foot diameter circular pit. Ignition was accomplished by using an electrically ignited blowtorch located between the south and south west side of the pool.

Wind speeds were higher in Test 2, approximately 12.5 mph on average and right on target with the desired wind speed (5-15 mph, see Table 2). Figure 34a and b shows the fire plume from the south and southeast direction. As depicted, the fire plume tilted significantly from the ground normal (> 45°) in the wind direction during most of the test. As a result, the fire plume covered the large calorimeter and the weapon calorimeter during most of the test. The fire plume swayed between the northeast and southeast as the wind changed direction. This caused portions of the north side of the large calorimeter to protrude from the inside of the plume as observed in Figure 34c and d from time to time.

Figure 35 shows post test images of Test 2. The soot outline on the ground indicates the extent of the fire plume coverage over the adjacent terrain and shows the predominant plume direction

was toward the east side of the pool. The soot footprint extends approximately half a diameter from the edge of the pool in the direction toward the weapon calorimeter.

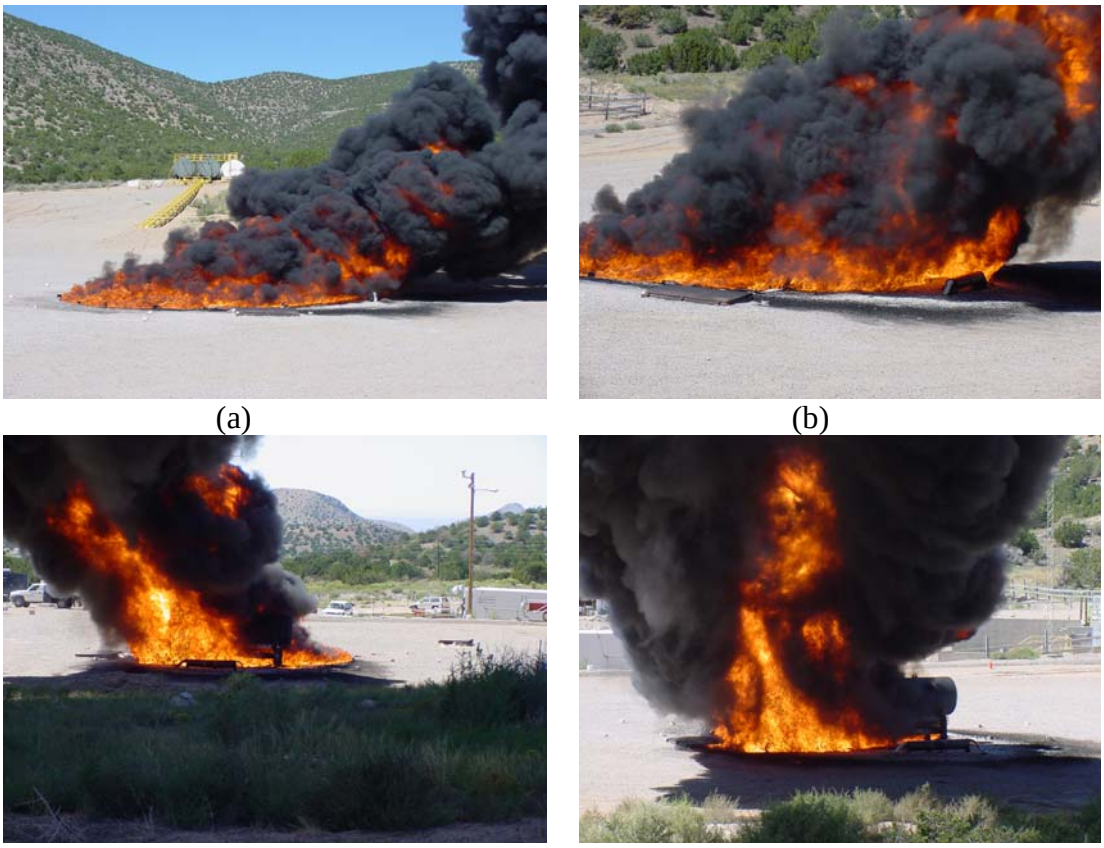

(a) (b)

(c) (d)

Figure 34. Fire plume during Test 2.
(a) fire viewed form the south; (b) fully engulfed large calorimeter; (c) fire plume flowing under the large calorimeter viewed from west; (d) fire plume flowing under the large calorimeter viewed from south.

(a) (b)

Figure 35. Soot footprint left after Test 2.

Instruments were inspected after Test 2. Several Sandia heat flux gauges failed due to TC extension wires being exposed to extreme heat during the wind-driven high heat flux environment, (see Table 6). All but one were located on the terrain on the east half of the pool. The center gauge inside the pool failed shortly after ignition. Also, all but four Gardon heat flux gauges failed due to gauges and wiring being exposed to extreme heat. Gardon gauges adjacent to the pool were not replaced in subsequent tests.

Inspection of the small calorimeter data show a number of thermocouple failures. Some instrumentation lines located on the lee side of the pool melted (see Figure 36). Extension wires were also melted on the southeast side of the pool.

Table 7 shows the approximate time at which small calorimeter TCs failed. TC labels correspond to the locations shown in Figure 17. In Test 3, calorimeter thermocouples were replaced with longer thermocouples and extension wires were eliminated. In the large calorimeter, two additional thermocouples (107 and 402 on the surface) failed in addition to those that failed in Test 1 (214, 304, 406 on the surface and 213 in the interior).

Table 6. Time to Failure of the Sandia HFG in Test 2.

TC Location	Time (s)
403	1139
501	642
507	495
508	440
601	1603
607	519
608	654

(a) (b)

Figure 36. Small calorimeter TC wires failed after exposure to fire.

Table 7. Time to Failure of the Small Calorimeter TCs in Test 2.

Location	Small Calorimeter: West (s)	Small Calorimeter: East (s)
N	1923	1570
N+1	1911	1570
S	2149	1795
S+1	1860	1871
A	2091	1780
B	2140	1800
C	2154	1748
D	1882	1902
1	2112	1075
2	2179	1748
3	1904	1748
4	1930	1780

4.3.3 Test 3

Test 3 was initiated at 7:10 AM on September 24, 2003. Figure 37 shows images of the experiment setup prior to ignition of fuel in Test 3. Test 3 did not include the large calorimeter. The test was performed using approximately 2207 gallons of JP8 aviation fuel floated on 30 inches of water. The fuel raised the level of the pool to 36 inches (1 inch below the ground plane). Ignition was accomplished by using an electrically ignited blowtorch located between the south and south west side of the pool.

Wind conditions were relatively calm in Test 3. Wind speeds were approximately 3.7 mph on average, within the target wind speed (0-5 mph, see Table 2). Figure 38 shows the fire plume from the north and northeast direction. The fire plume remained close to the vertical position with respect to the ground during most of the test.

Figure 37. Experiment setup for Test 3

Figure 39 shows post test images of Test 3. The soot outline on the ground indicates the extent of the fire plume coverage over the adjacent terrain and shows the plume direction was toward the northwest side of the pool. The outline suggests wind direction was predominantly from the southeast.

Again, after the test instruments were inspected to detect any flaws. Only two TCs failed in the small calorimeters (TC S and TC N, both in the west calorimeter).

(a) (b)

Figure 38. Fire plume during Test 3.
(a) view from northwest and (b) view from northeast.

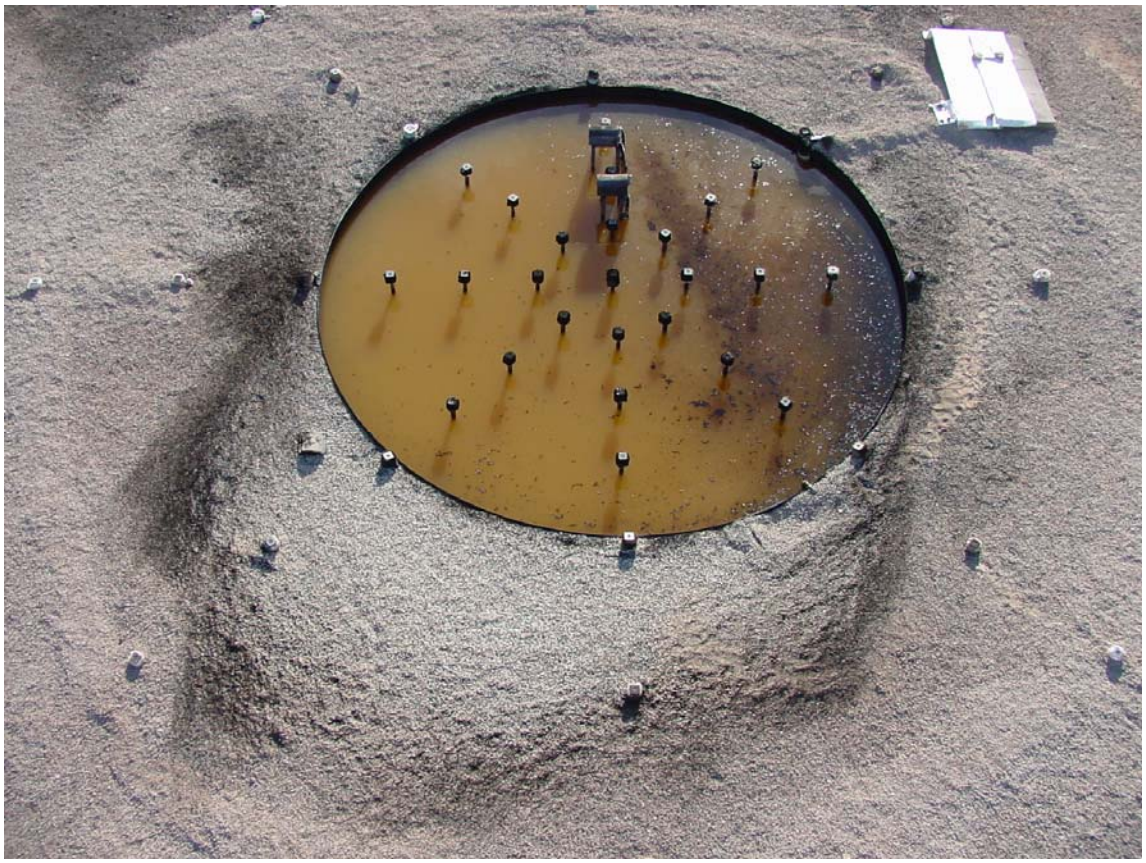

Figure 39. Soot footprint left after Test 3.

4.3.4 Test 4

Test 4 was initiated at 1:42:00 PM on September 24, 2003. Test 4 setup was the same as Test 3 (see Figure 37). The test was performed using approximately 2207 gallons of JP8 aviation fuel. The fuel was floated on 30 inches of water. Ignition was accomplished by using an electrically ignited blowtorch located between the south and south west side of the pool.

Wind speeds were higher in Test 4 than in Test 3, approximately 8.5 mph on average, within the desired wind speed (5-15 mph). Figure 40 shows the fire plume from the south and southeast direction. As depicted in this figure, the fire plume was tilted significantly from the ground normal during most of the test. The fire plume seemed to sway from northeast to the east during most of the test.

Figure 41 shows post-test image taken after Test 4 from the west side of the pool. The soot outline on the ground indicates the extent of the fire plume coverage over the adjacent terrain and shows the plume direction was toward the east side of the pool as expected from predominant wind direction.

(a) (b)

Figure 40. Fire plume during Test 4
(a) view from south and (b) view form southeast.

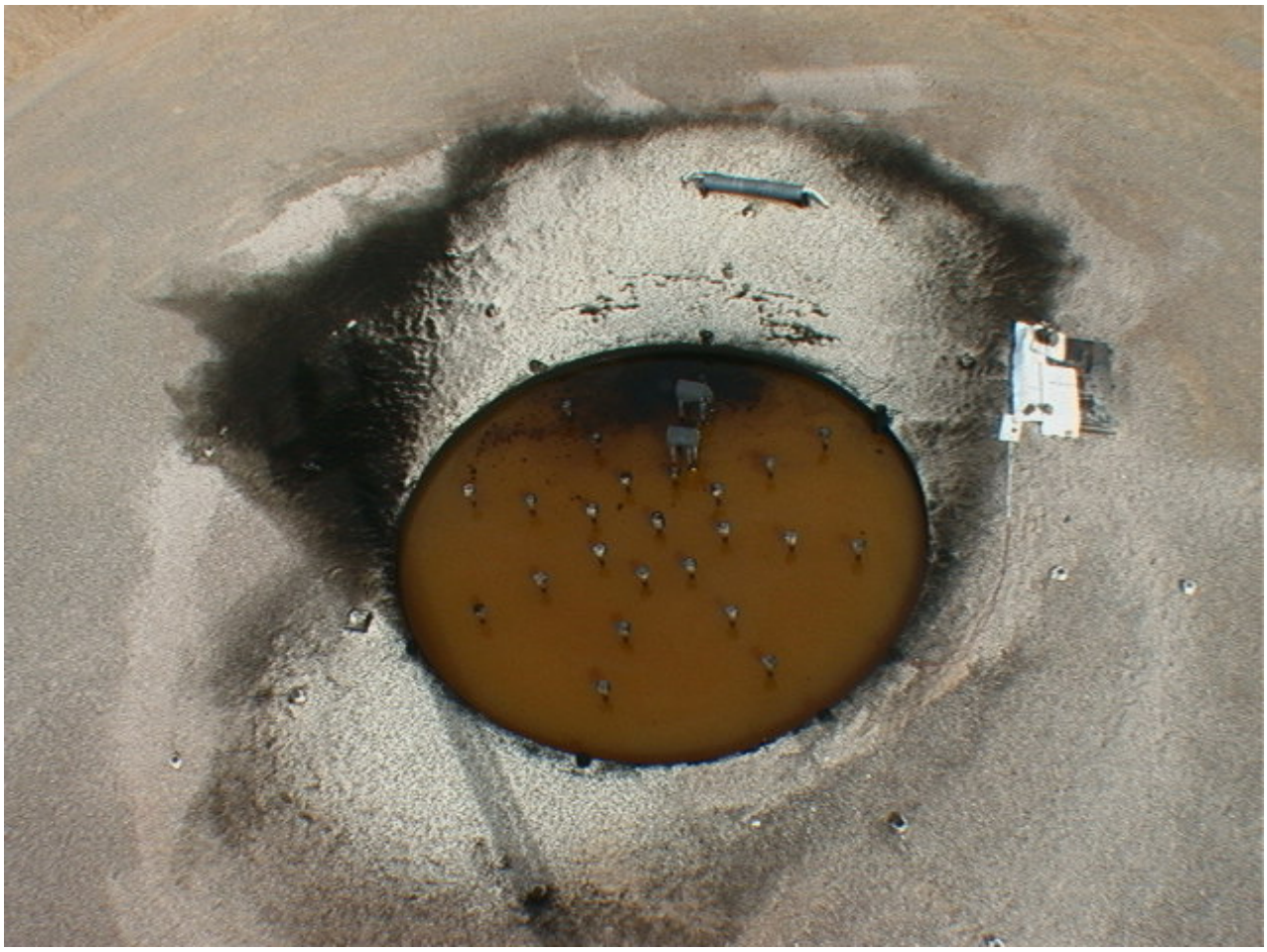

Figure 41. Soot footprint left after Test 4.

4.4 Wind Measurements

The target wind conditions for the Well-Characterized Open Pool Fire Test Series ranged from calm (less than 5 mph or 2.25 m/s) to medium (between 5 and 15 mph, or 2.25 and 6.7 m/s). This section presents wind measurements collected with ultrasonic wind sensors. The wind conditions were defined by the speed and direction of prevailing winds at test facility. Wind directions are specified in terms direction of wind vector, where axis perpendicular to the large calorimeter is 85°. Description of wind direction in the text is also given relative to true north (355°), east (85°), south (175°) and east (265°). So for example, if the wind direction is 220°, the wind is moving from southwest to northeast.

Measurements were performed approximately 95 ft. upwind of the leading edge of the pool at four locations. At all locations, the measurements were made at elevations of 2 m, 5 m, and 10 m above the ground surface. As expected, wind data generally showed an increase in wind speed with increasing elevation due to the effects of boundary layer near the ground level.

Wind measurements were also recorded with vane-type wind gauges. These data were used to verify data collected with ultrasonic wind measurement sensors, but are not presented here. In general, wind speed and wind direction measurements obtained with wind birds were consistent with ultrasonic wind measurements. Wind measurements obtained from wind birds had higher variability than wind measurements obtained from ultrasonic wind sensors (due to their reduced sensitivity and longer time response, especially at the lower wind speeds).

Since the measurements acquired at the highest elevations are least subjected to the boundary layer and other topography effects, an average of the four measurements obtained from the highest elevations (10 m) is taken as representative of the wind conditions in each test. Figures in the four summary sections that follow display average wind speed and direction data for the highest elevations from time of ignition throughout the duration of the test. A small coordinate system is drawn in each figure to assist the reader in locating wind directions. The circle and the rectangle in the coordinate system drawing depict the pool and the large calorimeter, respectively.

The following algorithms were used to calculate the resultant wind vectors from the three wind components (U, V, W). S is the resultant wind velocity (m/s) and AZ is the resultant wind azimuth angle (degrees). Note ATAN2 is a special trigonometric function for 4-quadrant applications.

$$S = \sqrt{\left(U^2 + V^2 + W^2\right)}$$

$$AZ = \left[ATAN2\left(V, U\right) * 180 / \pi + 180\right]$$

4.4.1 Test 1

Figure 42 shows the wind variations throughout the testing period. Test 1 was classified as a low wind speed test. Wind speeds remained relatively constant throughout the test except for a peak at 1700 where the speed increased to approximately 1.7 m/s. The average wind speed during Test 1 was 0.85 m/s. The standard deviation of the wind speed over the entire test period was ±0.27 m/s.

The average wind direction during the test was 178.5° (south). The wind direction however varied significantly for the majority of the test. The standard deviation over the entire test period was ±76.6°, the largest of any test. During the first 700 seconds after ignition, the wind blew predominantly from the southeast (145°). During this period, wind speed on average remained slightly lower than during the rest of the test. During the period between 700 and 1350 seconds, the predominant wind direction changed first from south-southeast (145°) to west-northwest (285°), then back to south-southeast (145°) for a short period of time before changing to west (270°), and finally changing to east-southeast (110°) near the end of this period. During this period of time, wind speeds remained relatively constant and near the average (0.85 m/s). During the period between 1350 and 2700 seconds, the predominant wind direction changed from east-southeast (110°) to northwest (300°) and then slowly to the east (90°). Note that during the early part of this period, wind speeds were significantly higher than the average speed. During this period, wind directions were out of north (355°) on extreme conditions. Recall that in Test 1, soot accumulation on the ground was most significant in the south-southwest side of the pool, consistent with the period which saw significantly higher wind speed in this direction.

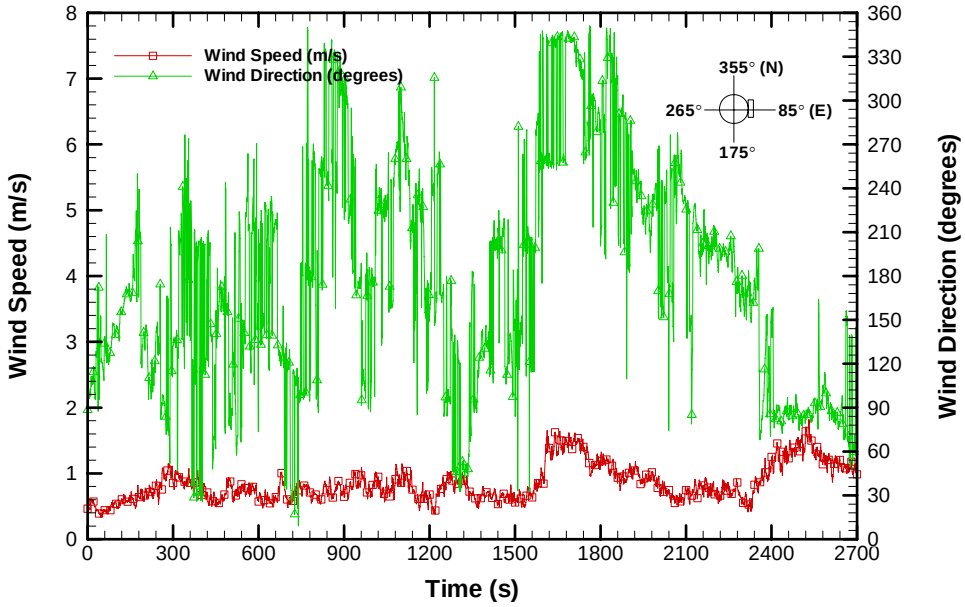

Figure 42. Wind conditions in Test 1

4.4.2 Test 2

Figure 43 shows the wind variations throughout the testing period. Test 2 was classified as a high wind speed tests. The average wind speed during the test was 5.76 m/s. Wind speed variability was more significant than in Test 1. The standard deviation of the wind speed over the entire test period was ±1.72 m/s. During the first 1650 seconds of test, wind speeds remained relatively constant except for a dip at the beginning of the test (2.0 m/s). After 1650 seconds, long term wind fluctuations cause the wind speed to slowly decrease to approximately 2.0 m/s and then to suddenly increase to approximately 7 m/s before slowly decreasing again down to 2 m/s.

The wind direction was constant for the majority of the test. The average wind direction during the test was 246.9° (southwest). The standard deviation of wind direction was ±15.0°. Since wind speeds were significantly higher, the large tilt of the fire plume produced a greater heat flux to the large and medium calorimeter. It was expected that even small variation in wind direction would have a significant impact on the heat flux to the large calorimeter.

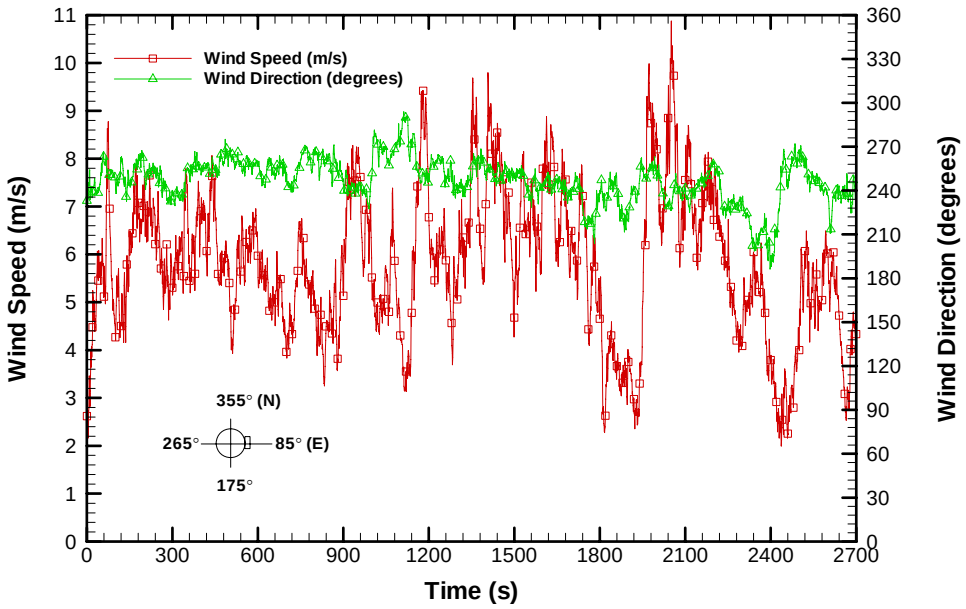

Figure 43. Wind conditions in Test 2

4.4.3 Test 3

Figure 44 shows the wind variations throughout the testing period. Test 3 was classified as a low wind speed test. Wind speeds remained relatively constant throughout the test except for dip at approximately 670 seconds when the speed fell to 1 m/s. Wind speed seemed to decrease slowly

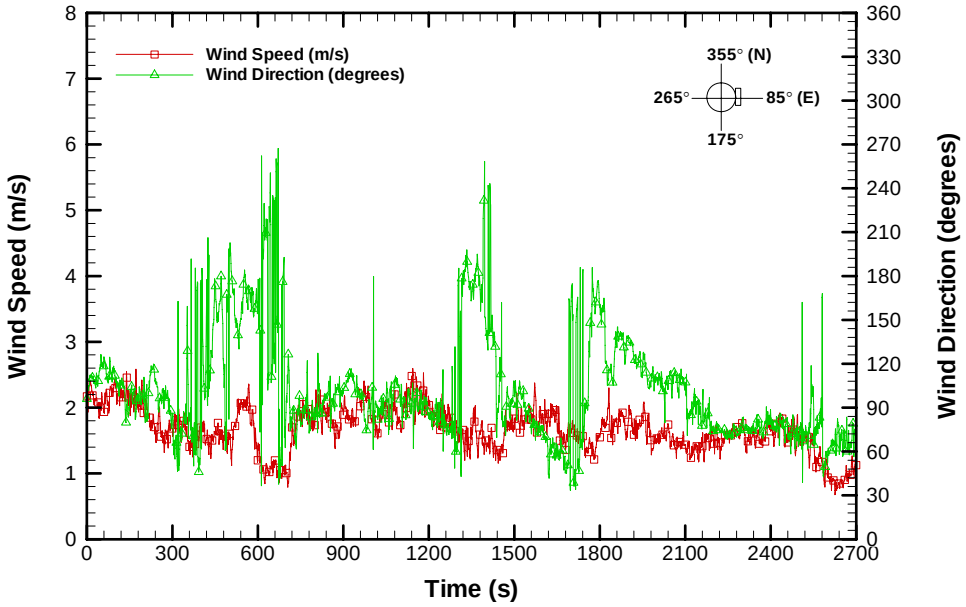

Figure 44. Wind conditions in Test 3

during the test. The average wind speed during Test 1 was 1.66 m/s over the entire test period and the standard deviation of wind speed was ±0.34 m/s.

The average wind direction during the test was 102.6°. As in Test 1, wind direction varied significantly, but only at irregular intervals. The standard deviation over the entire test period was ±36.8°, the second largest of any test. During the first 300 seconds after ignition, the wind blew predominantly from the east (90°). After 300 seconds, the predominant wind direction changed abruptly to the south (175°) and remained there for approximately 300 seconds before changing suddenly back to east (90°). Winds remained out of the east until about 1300 seconds. At approximately 1300 seconds, the predominant wind directions changed abruptly to south-southwest (185°) and remained there for approximately the next 50 seconds. Wind direction then began to change slowly to the east-northeast (60°) until 1750 seconds, at which time the wind direction changed abruptly back to the south (175°). Wind direction then began to change slowly back to the east-northeast (70°).

4.4.4 Test 4

Figure 45 shows the wind variations throughout the testing period. Test 4 was classified as a high wind speed test. Except for a dip at 200 seconds followed by a spike at 300 seconds, wind

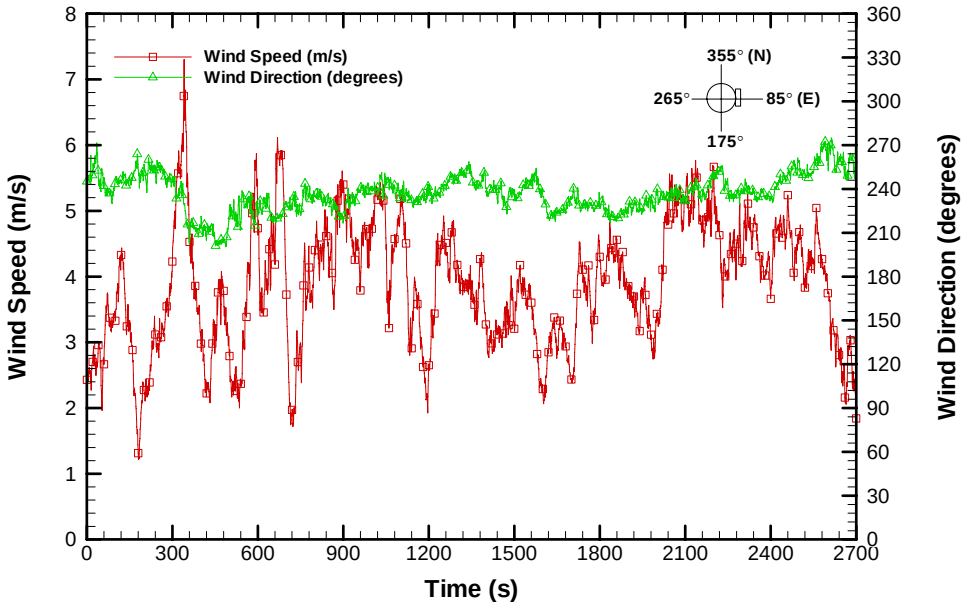

Figure 45. Wind conditions in Test 4

speeds remained relatively constant throughout the test. The average wind speed during Test 4 was 3.83 m/s. As in Test 2, wind speed variability was significantly higher than in lower speed test (Test 1 and Test 3). The standard deviation of the wind speed over the entire test period was ±0.97 m/s.

The wind direction was constant for the majority of the test. The average wind direction during the test was 246.9° (southwest). The standard deviation of wind direction was ±12.7°. Since wind speeds were significantly higher, the fire plume titled significantly affecting heat flux to the medium calorimeter. As in Test 2, it was expected that even small variation in wind direction would have a significant impact on the heat flux to the medium calorimeter.

4.4.5 Boundary Layer Wind Measurements

A model VT-1 sodar, developed by Atmospheric Research and Technologies, was used to sample and summarize lower boundary layer winds. The VT-1 sodar can be used to measure lower boundary layer winds through a maximum of 300 meters above ground level (AGL), depending on the atmospheric conditions of the sampled environment. During neutral atmospheric conditions and periods of low relative humidity (below 25%), maximum height for which valid data can be acquired will be reduced, and few valid samples will be obtained above 150 meters in the SNL/NM environment. The nominal frequency of the VT-1 sodar is 4504 Hz.

Theory of Operation:
The VT-1 sodar works by sending acoustic pulses at defined time intervals, and directions on and off a vertical axis; and listening and measuring the amplitude and frequency of the returned signal. One vertical and two off-vertical pulses are used to gather information about the

atmospheric environment. The returned signals from all three pulses and geometric calculations are used to develop vertical velocities and the vertical profiles of the horizontal wind speeds and directions.

Test Support:
To support the open pool tests, the SODAR was operated to transmit a pulse at approximately 1.23 second time intervals, sequencing a pulse for each beam axis, resulting in approximately 16 samples along each axis each minute. The maximum height possible with these temporal settings and the software limited data bins was 150 meters. The system was operated to average information at 5 minute intervals for the first test, and 4 minute intervals for the rest of the tests. While these time intervals are longer than an optimum averaging interval to assist with time simulations, 4 minutes was the shortest interval that was used to assure high quality data with good statistical representation.

Under light and variable wind conditions it is common to see calculated mean directions shift and meander across the 360 degree compass over time. This can be seen in test 1 and 3 when speeds are near or below 1 meter/second. Low wind speeds and meandering directions are also characteristic as nocturnal winds mix out and change to daytime type wind patterns. This is a common feature of the wind in the vicinity of SNL/NM and, for these tests, the burn site in particular.

Figures 46-53 give the Sodar measured wind direction and speed in the four tests.

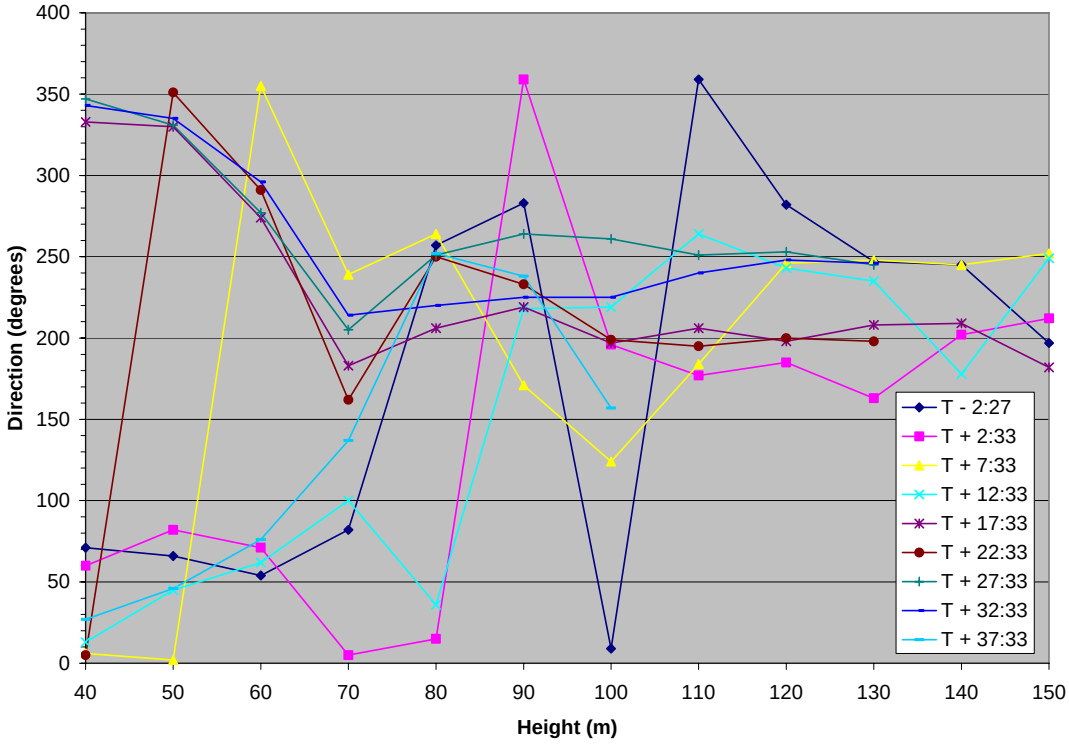

Figure 46. Sodar measured wind direction in Test 1

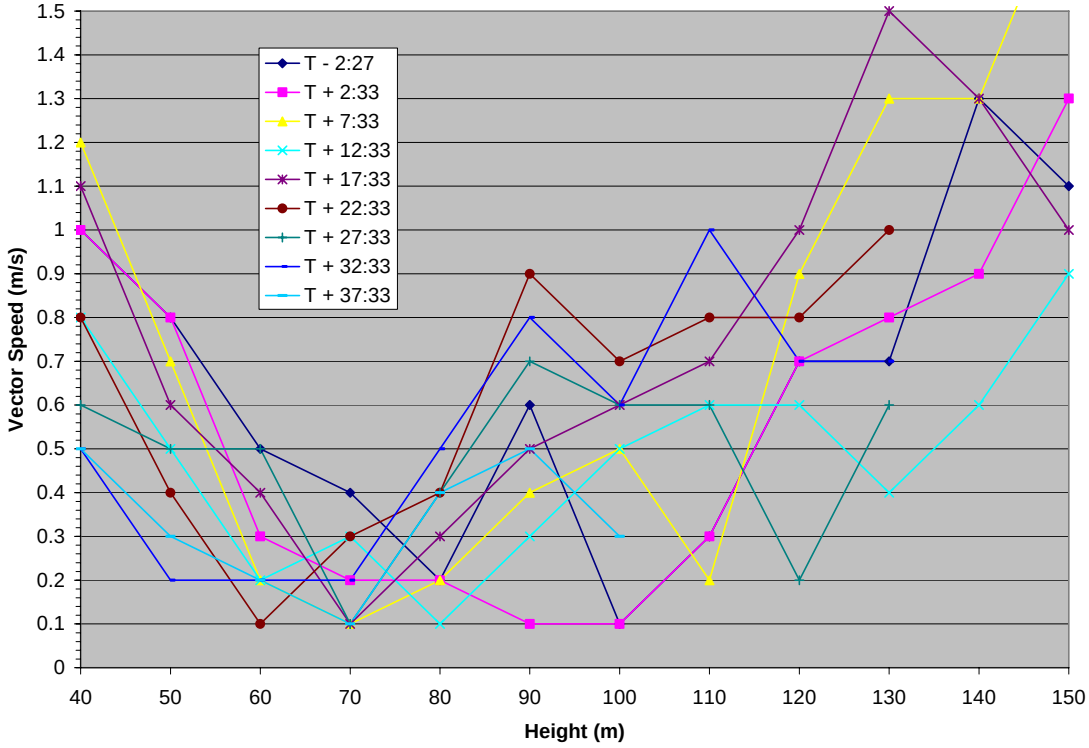

Figure 47. Sodar measured wind speed in Test 1

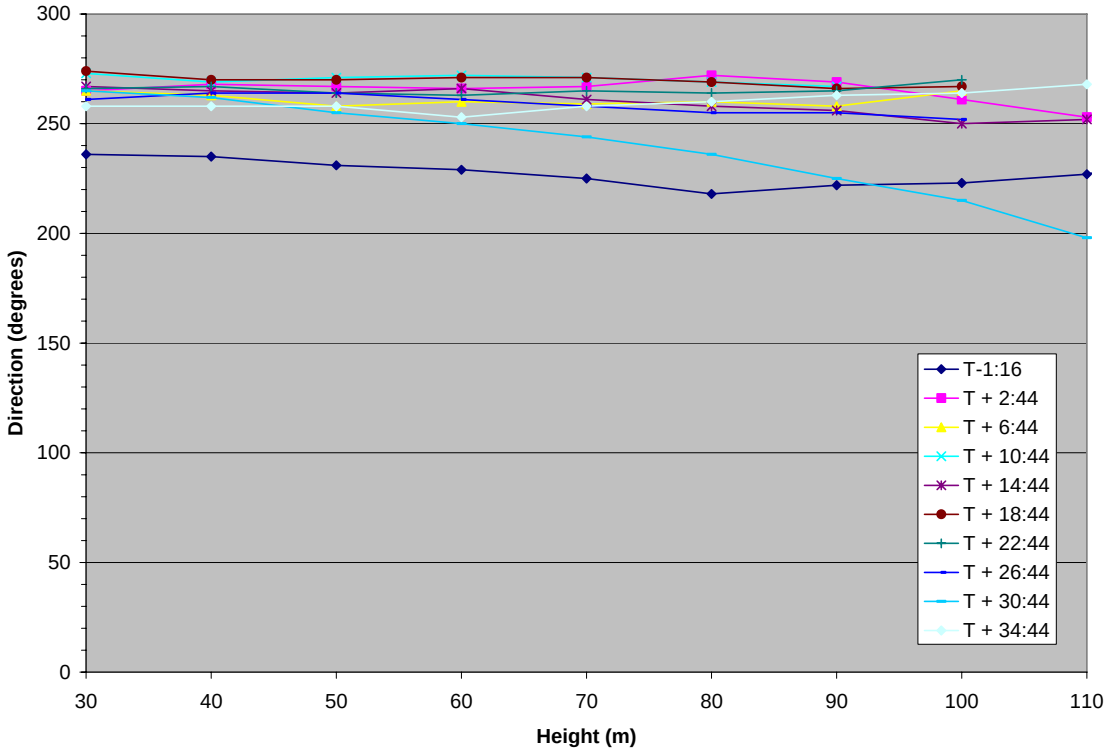

Figure 48. Sodar measured wind direction in Test 2

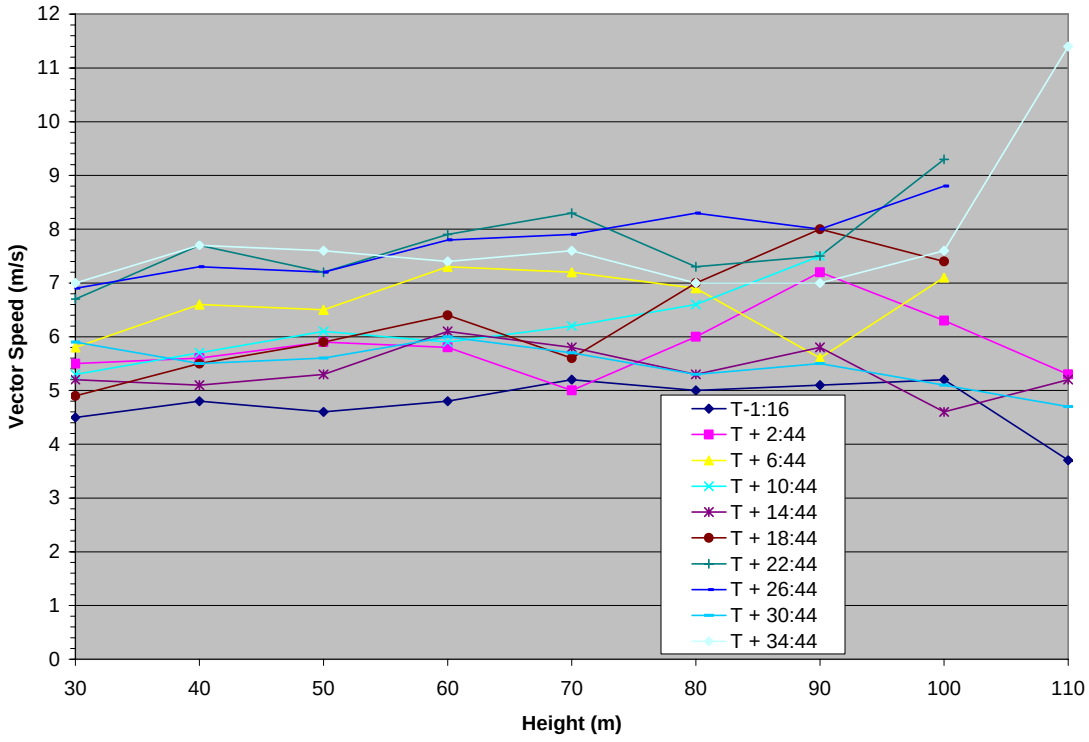

Figure 49. Sodar measured wind speed in Test 2

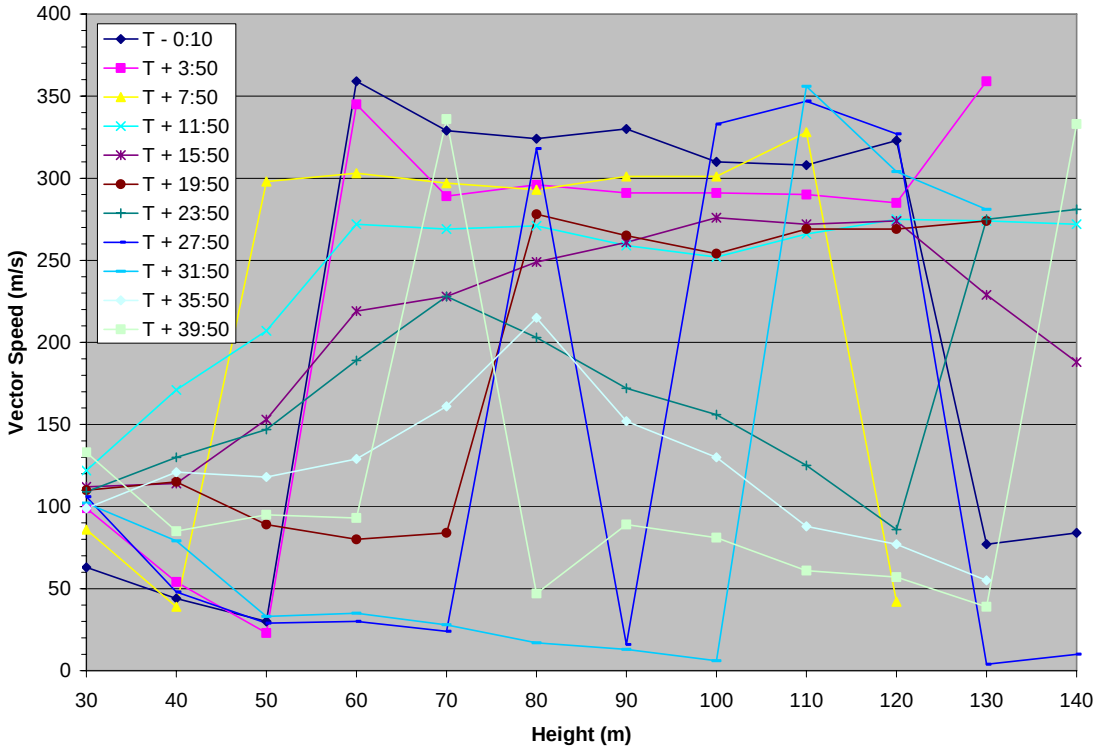

Figure 50. Sodar measured wind direction in Test 3

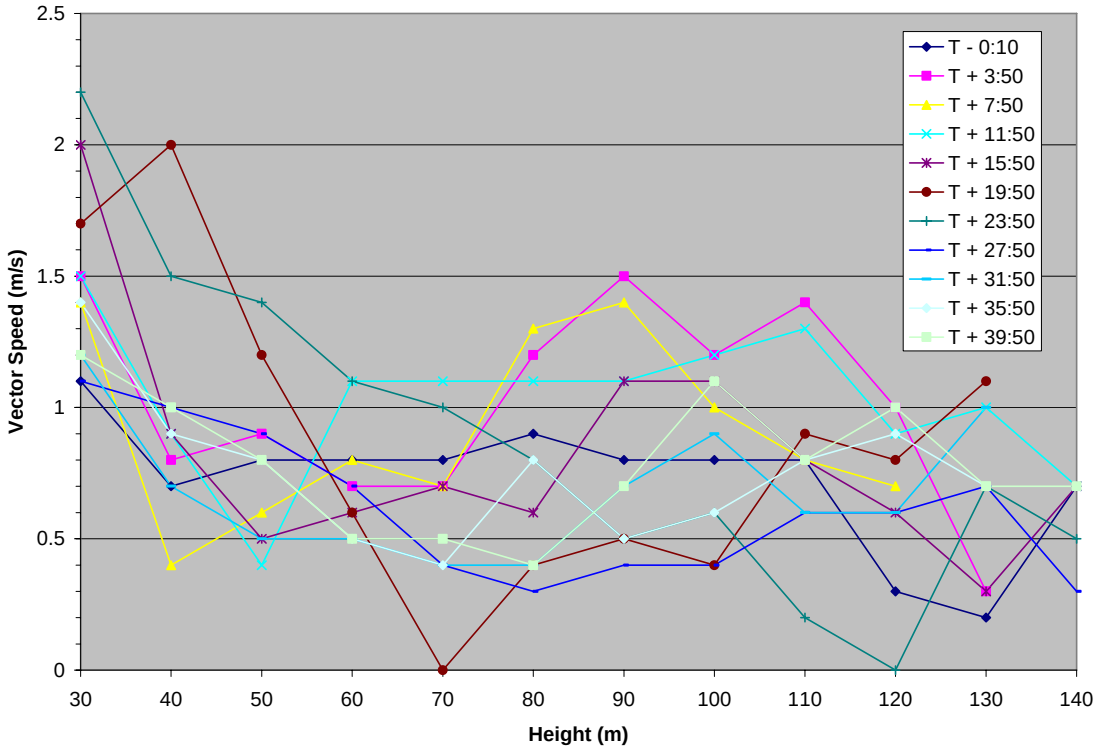

Figure 51. Sodar measured wind speed in Test 3

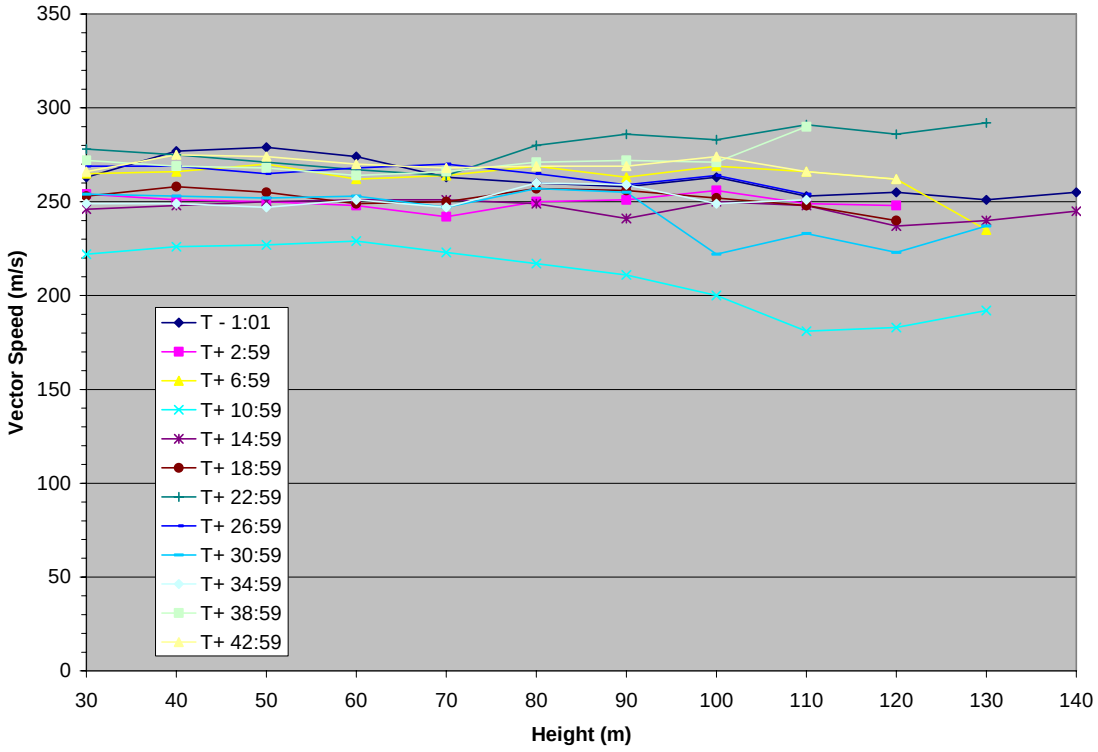

Figure 52. Sodar measured wind direction in Test 4

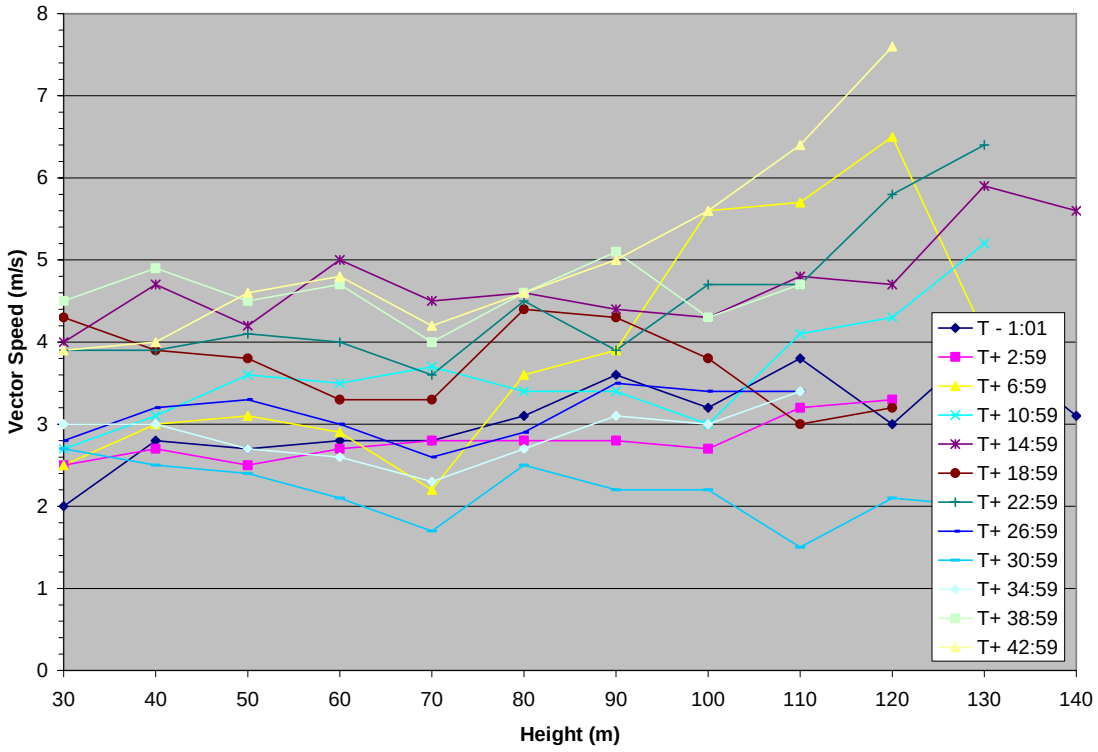

Figure 53. Sodar measured wind speed in Test 4

4.4.6 Summary of Wind Conditions

Wind speeds were averaged at each location and across all four locations. Table 8 shows average wind speeds recorded at each tower location (arithmetic mean of the three US anemometers) for each test for t = 0-2700 s. With the exception of Test 3, wind speeds measured by ultrasonic wind sensors in Towers 1 and 4 were higher than wind speeds measured by Towers 3 and 4.

Figure 54 shows wind speed profiles for the test series. The average data presented is the arithmetic mean of the four US anemometers located at the same height on each tower. Wind speed typically increased with elevation and the increases in wind speed were more significant for higher wind speed tests.

Table 9 summarizes average wind speeds and wind directions at the 10 m height (computed from t = 0-2700 s) in the test series. As expected, highest wind speeds were observed in Test 2 and Test 4 and were right on target with desired velocities. Note the standard deviation of wind speed for Test 2 and Test 4 are larger than in Test 1 and Test 3. This is expected since wind gusts are stronger at higher wind speeds.

Table 8. Average Wind Speed of Each Tower for Each Test.

Tower	Test 1 Speed (m/s)	Test 2 Speed (m/s)	Test 3 Speed (m/s)	Test 4 Speed (m/s)
1	0.85	4.99	1.83	3.41
2	0.61	4.01	1.47	2.67
3	0.55	4.15	1.15	2.47
4	0.89	5.95	1.26	3.60

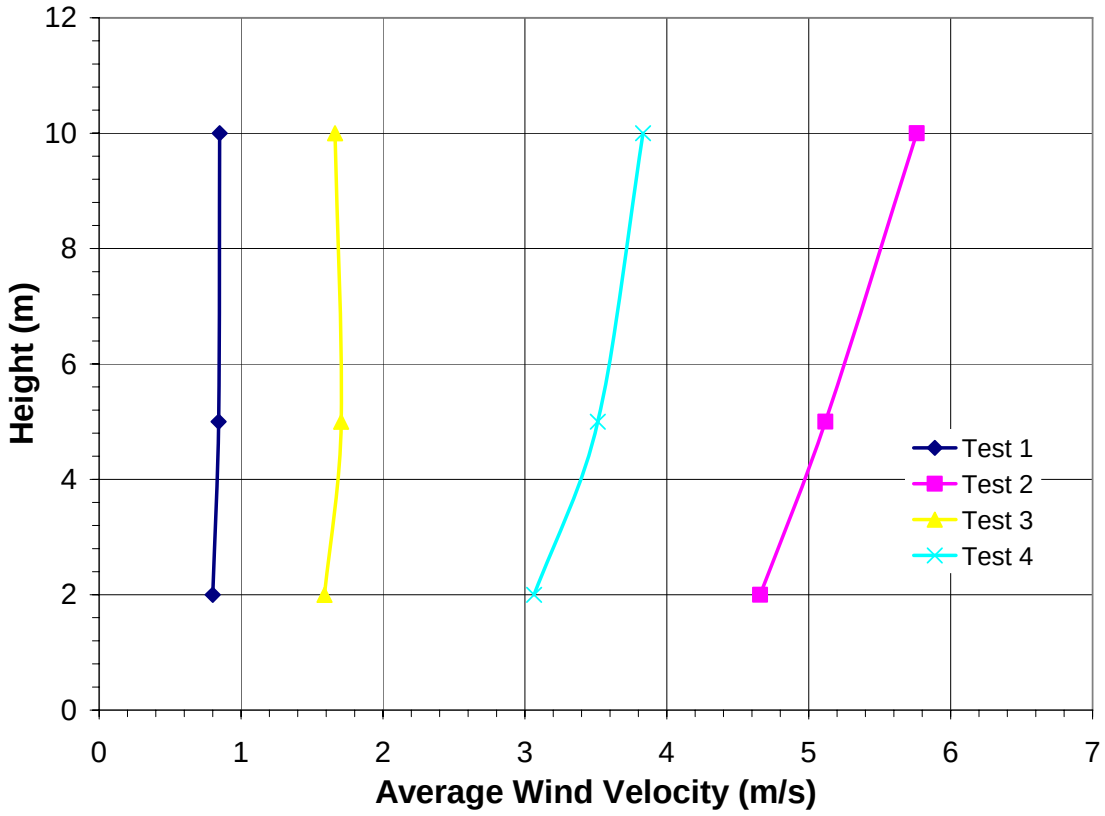

Figure 54. Wind velocity profiles for the Test Series.

Table 9. Average Wind Conditions at 10-m in each Test..

Test	Wind Speeds (m/s)		Wind Direction (degrees)	
	Mean	Standard Deviation	Mean	Standard Deviation
1	0.85	±0.27	178.5	±76.6
2	5.76	±1.52	246.9	±15.0
3	1.66	±0.34	102.6	±36.8
4	3.83	±0.97	237.0	±12.7

In general, the standard deviation of the wind speed is between 20 to 30% of the corresponding average wind speed. Table 9 also summarizes the standard deviation of wind direction in the test series. Standard deviation of wind direction for Test 1 and Test 3 were two to three times larger than in Test 2 and Test 4. It is speculated that at higher wind speeds the direction of average wind speed has the most impact on the wind direction measurement, while at lower wind speeds the chaotic behavior of small wind gusts contribute most to wind direction.

Figure 55 shows predominant wind vectors for all four tests. The length of the vectors is proportional to the wind speed and angle is given in terms of true north. Again, the circle and

the rectangle depict the pool and the large calorimeter, respectively. In general, winds were out of the south, southwest and southeast.

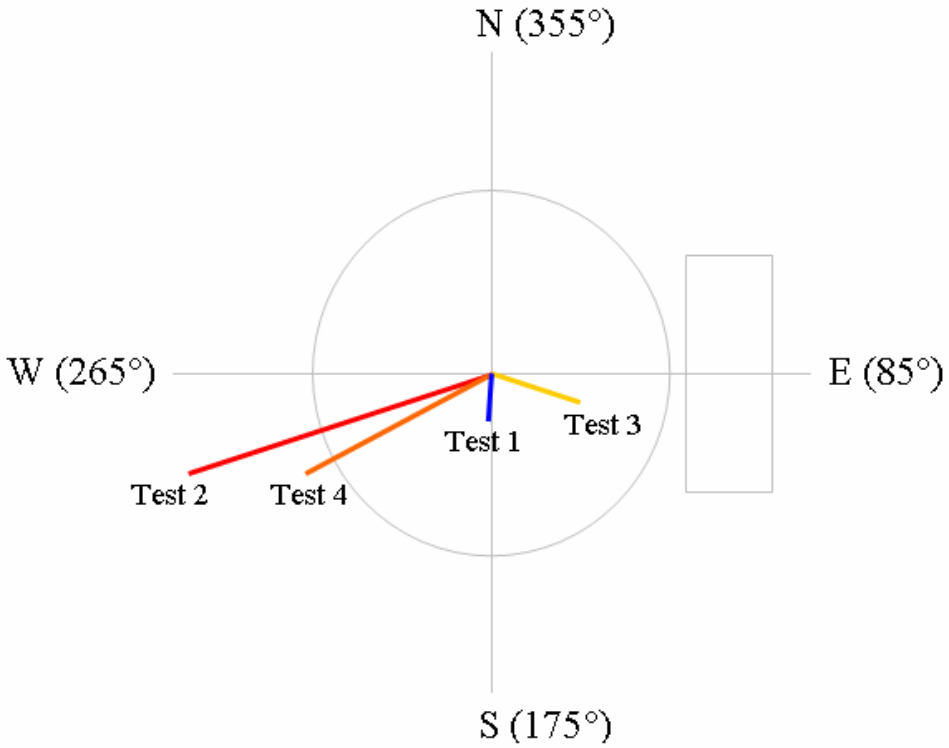

Figure 55. Predominant wind direction in the test series

In general, fire data are characterized by rapid changes due to interaction of instrumentation with turbulent winds outside the plume and flame sheets inside the fire plume. Periods of quasi-steady behavior were identified using the following criteria:

- initial heat flux transients stabilized
- no major changes in fire plume geometry observed in video record
- wind speed close to mean value of test (within 1σ)
- wind direction close to mean value of test (within 1σ)
- constant oscillation about a mean value

Wind data were averaged over this period. Table 10 shows statistics for wind data during quasi-steady behavior. Note that quasi-steady periods are 60 seconds. For larger periods it was difficult to meet criteria outlined above.

Table 10. Wind Conditions During Quasi-Steady Time Period (60 s).

Test	Time After Ignition (s)	Wind Speeds (m/s)		Wind Direction (degrees)	
		Mean	Standard Deviation	Mean	Standard Deviation
1	545-605	0.71	±0.04	175.3	±11.6
2	560-620	6.12	±0.44	257.4	±3.4
3	815-875	1.83	±0.18	94.2	±9.8
4	770-830	4.27	±0.35	247.1	±6.1

4.5 Flame Topology

A portion of the instrumentation consisted of five video cameras placed between 200 and 300 feet North, Northeast, East, Southeast and South of the pool. These cameras were used to study the fire plume topology. In order to get quantitative measurements from the images, each camera had two fiducials in the field of view (FOV). The fiducials were two-foot square markers with an alternating black and white square pattern in them. They were placed approximately 30-feet away from the cameras and separated so that they were in the lower left and right corners of the FOV of the camera. The cameras, fiducials, and various points of interest around the test site were surveyed and recorded.

The cameras recorded images in standard 480 x 512 pixel US format at 30 frames per second. The automated spark to start the fire was placed so each camera could see the ignition that provided the start time hack for each camera. Post processing the video files (the first 15 minutes of each test) electronically transformed each frame of every camera to a JPEG format. Additionally, a digital movie was created for each camera in a MPEG format. Fire and plume structure of interest were defined by reviewing the movies and calculating the time to the scene of interest. Fire plume structure sizes were determined from triangulation with two cameras. Estimates of the timing for certain changes in the fire plume were obtained from the movies.

Appendix B describes the fire plume topology analysis process and results of the four tests in more detail. Recall Tests 1 and 3 were conducted with minimal wind. Test 3 had a little more wind than Test1 and was more variable. Tests 2 and 4 had stiff winds, but Test 4 had motion out of several directions over the course of the test. This caused the plume to blow over the top of several cameras (2, 3 and 4) (NE, E, and SE). That in turn caused the analysis to use different sets of cameras to obtain the measurements.

The resultant maximum vertical height of the visible flame plume (i.e., glow) and the maximum distance from the pool center to the farthest glow point is given in Figure 56.

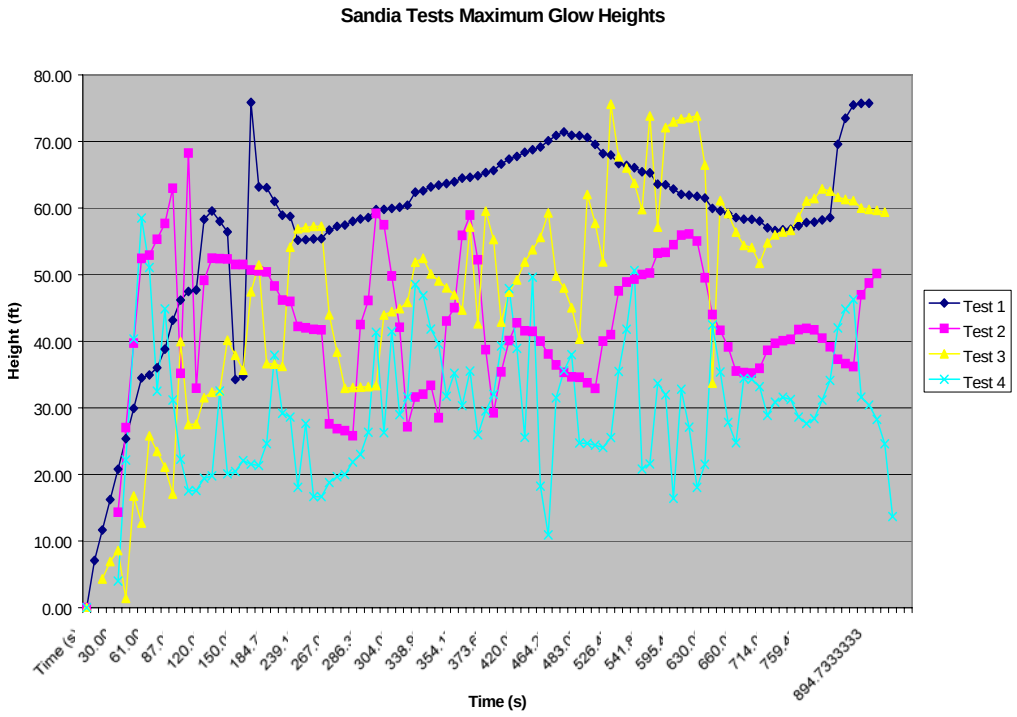

(a)

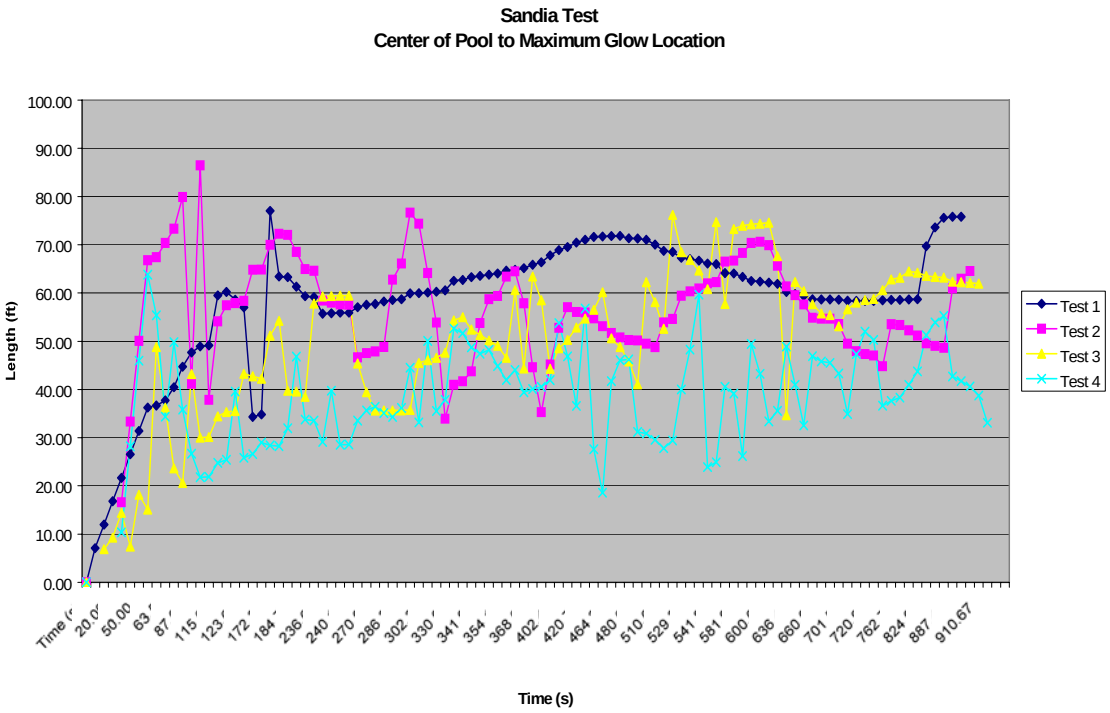

(b)

Figure 56. Flame characteristic dimensions.
(a) maximum glow heights, and (b) maximum distance from pool center to farthest glow

Tests 1 and 3 have about the same heights and maximum distance from the pool center over time (approximately 60-70 ft). Both maximum height and distance from center of the pool are fairly constant due to the relatively calm wind condition).

The maximum heights in Tests 2 and 4 varied from 30 to 50 feet depending on the intensity of the wind. The plume lengths (maximum distance from pool center) in Test 2 vary from 40 to 80 ft whereas in Test 4 the plume lengths vary from 30 to 50 ft.

4.6 Fuel Recession Rates and Heat Release Rates (HRR)

One thermocouple array and differential pressure gauge were used to measure the fuel recession rate. The fuel recession rate can be used to obtain estimates of fuel mass loss rate, average fuel vapor velocity and heat release rate from the pool.

The thermocouple array monitors the temperature of the fuel and the water underneath the fuel. Data from the thermocouple array were reduced and are presented here in the form of line plots. Figure 49 shows fuel temperatures starting from the top thermocouple (Rake 30) and displaying results for only the first seven even thermocouples in the array. Data shown begins at the time of ignition and extends approximately the end of the test (Figure 57a and 57d) or just prior to the time the thermocouples began to fail (Figure 57b and 57c).

Fuel temperatures recorded during the test by thermocouple array in the fuel pool ranged from approximately ambient temperature to 850°C. In Test 2, maximum temperatures were approximately 625°C, significantly lower than in all other tests. The lower temperatures are due to the location of the array (southwest corner, near the pool edge) and the wind speed and direction moving the flame plume significantly to the opposite side of the pool.

As the fire burned, the temperature of the thermocouples increased beginning with the top thermocouple. The top thermocouples were initially located just below the top surface; typically a few seconds elapsed after ignition before these thermocouples attained their maximum temperature. In all other measurements, thermocouple temperatures increased gradually and level off momentarily around 220°C. This leveling off in temperature suggests a phase change was occurring (i.e. vaporization) [20]. Thermocouple temperatures continued to increase until the thermocouples emerged from the fuel surface into the vapor dome.

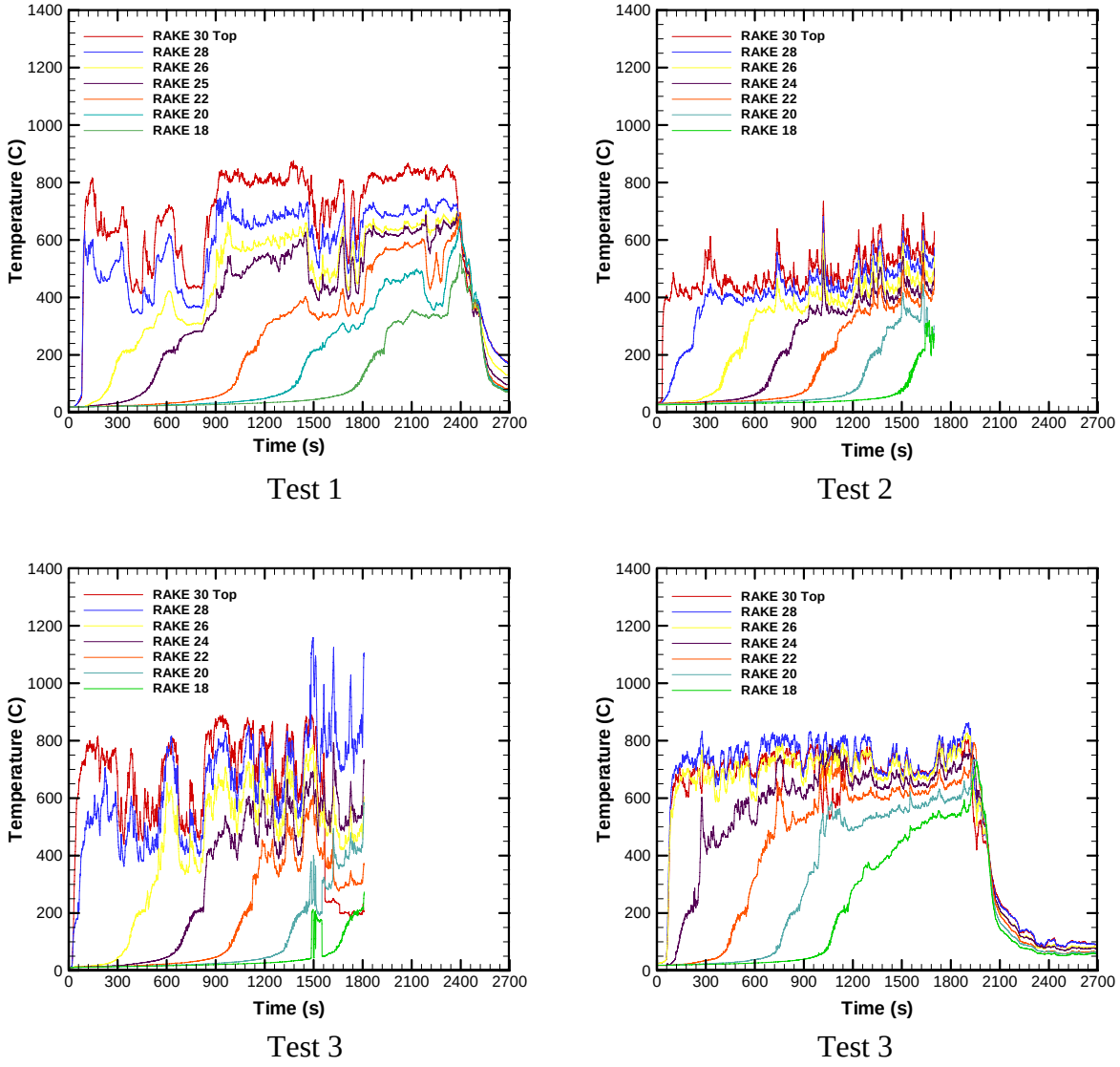

Figure 57. Fuel temperatures obtained using the thermocouple rake array.

Fuel recession rates for the liquid fuel in the pool were calculated from the temperature history of the thermocouple array. The fuel recession rate is calculated by dividing the thermocouple spacing (0.5 inches) by the time it took the thermocouple to reached 150°C between successive thermocouples. Fuel recession rates for the liquid fuel in the pool were also obtained from differential pressure (DP) gauge measurements. The DP gauge gives a measurement that when scaled by the specific gravity of the JP8 fuel (0.8) gives the height of the fuel layer. Table 11 shows fuel recession rates obtained from thermocouple array and from DP measurements (DP data was unreliable in Test 1).

Table 11. Pool Fuel Recession Rate.

	Test 1 Recession (mm/min)	Test 2 Recession (mm/min)	Test 3 Recession (mm/min)	Test 4 Recession (mm/min)
DP	NA	5.17	4.53	5.02
TC array	4.32	5.28	4.64	5.03

In general, fuel recession rates obtained using fuel temperature measurements and DP measurements are in good agreement. Note that is takes about 5 minutes before a steady state fuel regression occurs over the full pool The fuel recession rates ranged between 4.32 mm/in (Test 1) and 5.28 mm/in (Test 2). These estimates are consistent with what is typically observed in large pool fires [12, 13]. Figure 58 shows a scatter plot of fuel recession rates vs. average wind speeds for each of the test. The dash line suggests a linear correlation between these two parameters for these test series, but a quadratic relation cannot be discarded.

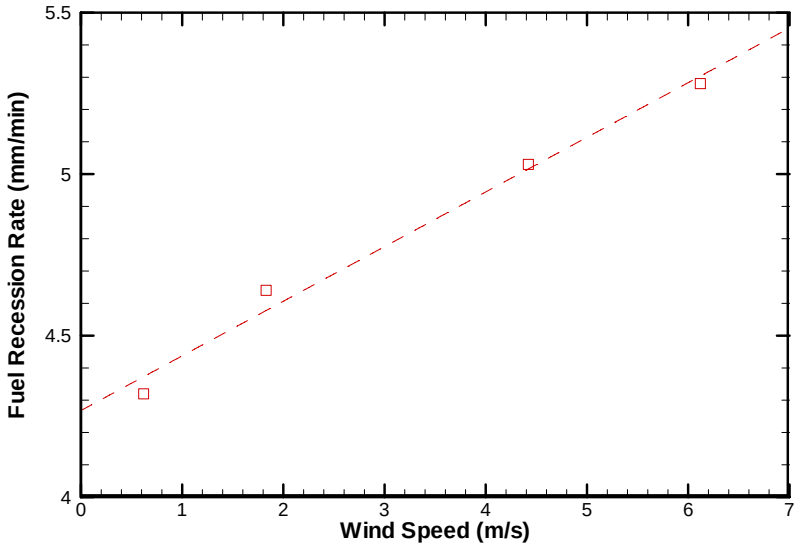

Figure 58. Correlation of average wind and fuel recession rate.

The mass loss rate of liquid fuel from the surface of the pool fire determines the amount of fuel for burning. Mass loss rates were calculated by multiplying the fuel recession rate by the pan area and the fuel density (refer to Section 2.3 for parameter values). The heat release rate was then by multiplying the mass loss rate by the JP-8 fuel heat of combustion. Table 12 presents the mass loss rate and the heat release rate for these test series.

Table 12. Mass Loss Rate and Heat Release Rate.

Test	Mass Loss Rate (kg/m^2-s)	Heat Release Rate (MW)
1	0.058	124
2	0.071	151
3	0.062	132
4	0.067	143

4.7 Fuel Pool and Surrounding Terrain Heat Fluxes

Knowledge of spatially-resolved heat transfer to the surface of the pool is necessary to develop and validate pool fire models. Fuel is vaporized as a result of heat transfer to the pool surface. Fuel vaporization rates in turn determine the potential heat released to the environment.

HFG data from the fuel surface were post-processed to obtain spatially-resolved estimates of heat transfer to the surface of the pool. As illustrated in Figure 15, forty-nine single-sided, upward facing, HFGs were used to measure the spatial distribution of incident heat flux to the fuel pool surface and the terrain surrounding the pool. The HFG is primarily a thin metal plate with one side facing the fire environment and the other side insulated. Type-K thermocouples were mounted on the inside insulated steel surface. The temperature data and the thermal model and methodology for SNL HFG [18] were used to obtain the incident heat flux to the surface of the pool and surrounding terrain.

The heat balance on the heated surface of an idealized one-dimensional heat flux gage can be summarized by the following equation:

$$\alpha\, q_{surf}(t) = \varepsilon\, q_{rad}(t) + q_{steel}(t) + q_{insul}(t) + q_{conv}(t)$$

where $q_{surf}(t)$ is the heat flux incident to the HFG heated plate, $q_{rad}(t)$ represents the heat re-radiated from the surface of the plate, $q_{steel}(t)$ is the heat stored in the plate, $q_{insul}(t)$ is the heat loss to the insulating material (Kaowool), and $q_{conv}(t)$ is the convective heat loss. The absorptivity (α) and the emissivity (ε) are assumed equal to 0.9.

The convective heat component of the incident heat flux, $q_{conv}(t)$, was not considered in the data reduction. This component can be estimated using convection coefficient correlations, the HFG plate temperature and the free stream gas temperature. Far from the fire, in the terrain surrounding the pool, the convection coefficient over a flat horizontal plate is expected to be less than 30 W/m^2-K. This value is based on: (1) a free stream air velocity of 5 m/s (maximum velocity 2 m from ground in Test 2) and a temperature of 500°C (mean of ambient and HFG TC temperature), (2) convection coefficient correlations for forced convection of air over a flat plate, and (3) assuming turbulent flow over the entire HFG plate. The convection coefficient will be much lower for calm wind conditions (e.g., Test 1). Inside large pool fires, vertical gas velocities typically ranged from 5-10 m/s between 2 and 10 m above the pool, and gas temperatures range between 1300K and 1700K depending on wind conditions [21]. Based on this velocity and temperature range, the convection coefficient over a flat horizontal plate is also expected to be less than 30 W/m^2-K. The temperature of the plate can be assumed to be the temperature of the HFG thermocouple.

The convective heat component can be estimated using the convective coefficients and temperature estimates cited above. However, since the level of uncertainty in these estimates is high due to lack of free stream gas velocity and gas temperature measurements, the convection heat transfer was treated as an uncertainty of incident heat flux calculations. Uncertainty

estimates for HFG measurements are given in [21] and include uncertainty due to lack of knowledge of convective heat transfer coefficient, free stream gas temperature, and plate temperature. For typical large pool fires, incident heat flux measurement uncertainty is approximately ±42% of the calculated incident heat flux. This estimate was obtained using large pool fire experiment data and is only valid for steady-state conditions. For transient conditions, the uncertainty is expected to be higher.

4.7.1 General Trends

Figure 59 shows spatially-averaged incident heat fluxes obtained from the pool and terrain HFGs. In all four tests the averaged incident heat fluxes across the pool reached steady-state conditions at approximately 100 seconds after ignition. Burnout occurred sometime after 1900 seconds. The low wind test conditions in Test 1 and 3 produced lower fuel burn rates that prolonged the fire.

In general, Figure 59 shows there is a slight increase in the averaged incident heat flux during the time period between 200 and burnout in all tests. This increase in incident heat flux has been observed in previous experiments [20] and is believed to be related to the slight increase in burn rate time as test progress. Note also that spatially-averaged heat incident fluxes were consistently higher in high wind test, i.e., Test 2 and Test 4. This was expected since high wind conditions generally result in higher fuel vaporization rates, and thus high incident heat flux feedback to the pool. Standard deviations (1σ) for the spatially-averaged incident heat fluxes are also shown in Figure 59 for all tests and give an indication of extreme variations in incident heat flux across the pool.

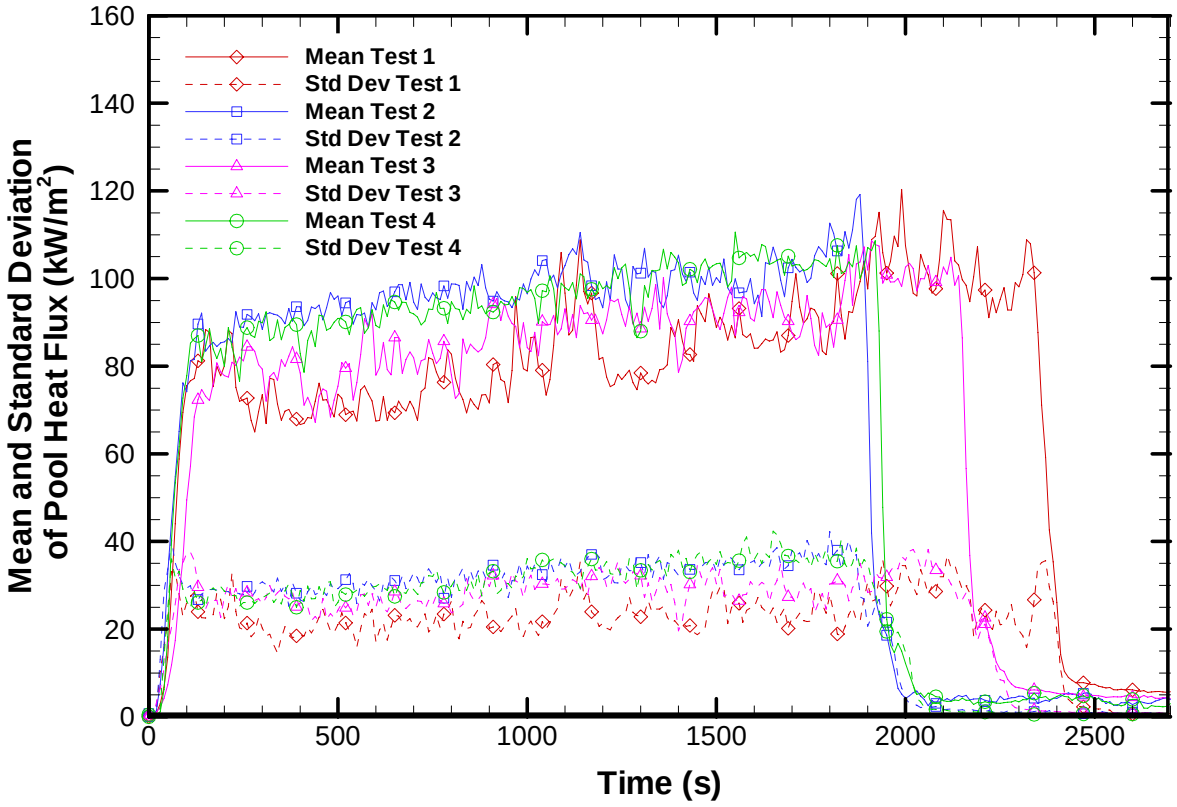

Figure 59. Spatially-averaged incident heat fluxes obtained from pool HFG measurements.

4.7.2 Incident Heat Flux Spatial Distribution

The spatially-averaged incident heat fluxes shown in Figure 59 fail to give an indication of the spatial distribution of incident heat flux across the surface of the pool and surrounding terrain. Contour animations were generated to study incident heat flux spatial variations across the pool and terrain for all tests from ignition to burnout. Figures 60 to 63 present contour plots of incident heat flux to the surface of the pool and surrounding terrain for each of the tests at increments of 200 seconds, starting from 100 seconds and ending at 2300 seconds, are shown in the following pages (left to right, then top to bottom). Corresponding wind speed and wind direction information are given in each plot to facilitate interpretation of results.

As expected, incident heat fluxes were largest inside the pool. The notable exception is Test 2 and Test 4 where significantly higher heat fluxes were observed from time to time on surrounding terrain on the leeward side of the pool. In Test 2, maximum incident heat fluxes in the terrain near the weapon calorimeter reached 150 kW/m^2. In general, heat fluxes near the edge of the pool were less than expected. Gauges located in regions near the edge of the pool usually measure low heat fluxes due to lack of an optically thick flame and the influence of the

relatively cool environment near the edge of the fire [8]. On the upwind side, gauges measure much lower heat fluxes. In Test 2 and Test 4, some HFGs on the leeward side of the pool failed; yielding a potential for interpolation error in the incident heat flux distributions of the spatial distribution of incident heat flux across the pool surface and surrounding terrain. Data from obviously failed HFGs were not used during spatial interpolation. Also, there are some "sharp" gradients in the contour plots. These non-physical gradients are due to linear interpolation between data points.

In single column vertical pool fires, eddies formed on the exterior of the flame zone and near the toe of the fuel pool define the mixing of air across the fire plume. These eddies grow in size due to increasing effects of density gradients and travel up the plume. Very little air is entrained into the interior of the fire plume until these eddies are sufficiently large in size and the flame has necked due to momentum from external air. Accordingly, an oxygen starved interior region exists near the fuel surface in the interior of the fire [4]. This is clearly observed in the contour plots of Test 1. Recall that in Test 1 winds were relatively calm and the plume was near vertical during most of the test. In Figure 60, regions near the center receive little heat feedback to the pool due to poor combustion, while regions near the edge of the pool receive significantly more heat feedback due to eddies that form near the edges of the plume, which enhance combustion. In general, the extent and location of the oxygen starved region is expected to change with the size of the pool and wind conditions [4]. Previous test show that with slightly higher wind speeds (~ 1.2 m/s), the extent of the oxygen starved region is much smaller and pushed slightly upward [4].

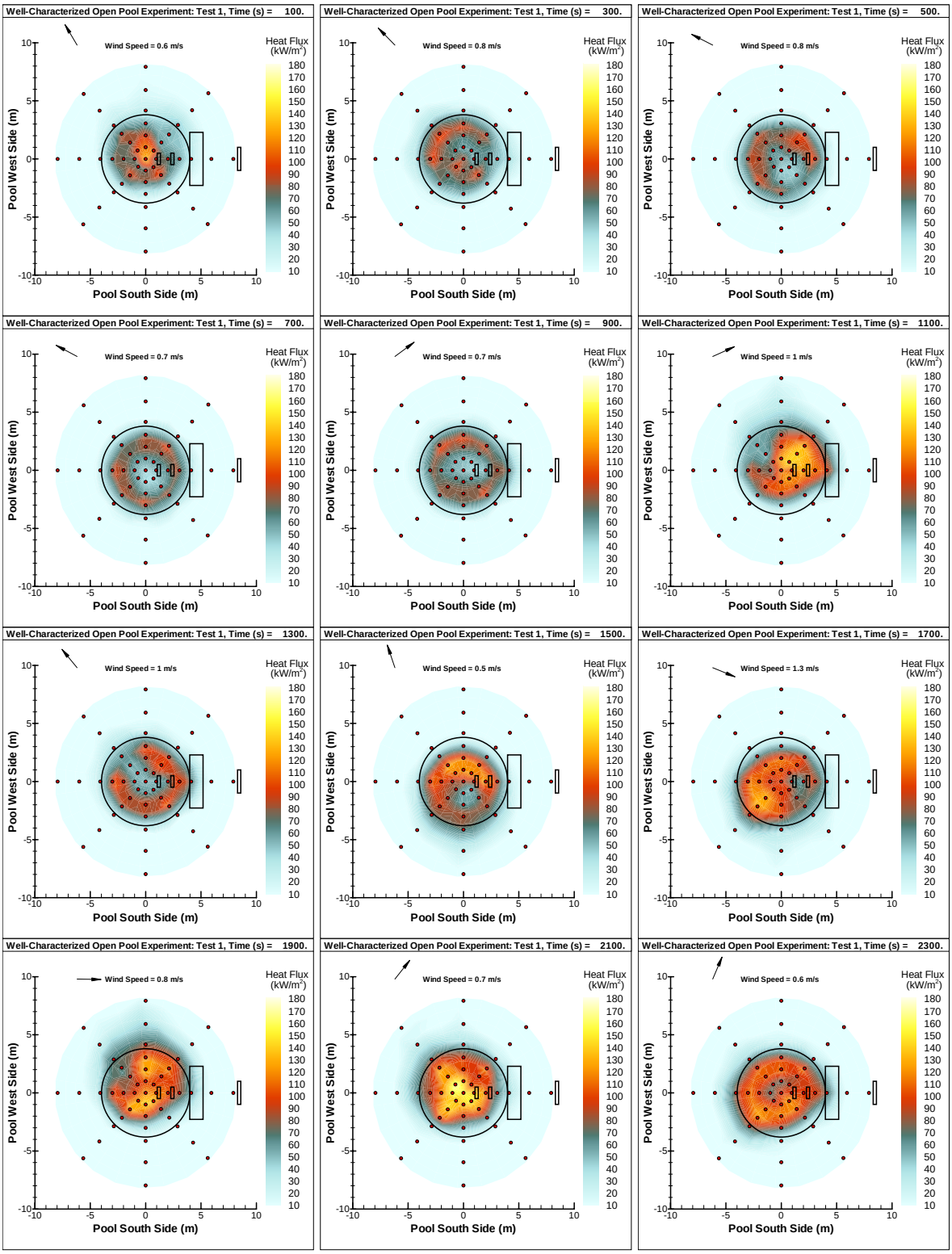

Figure 60. Incident heat flux to the surface of the pool and surrounding terrain for Test 1

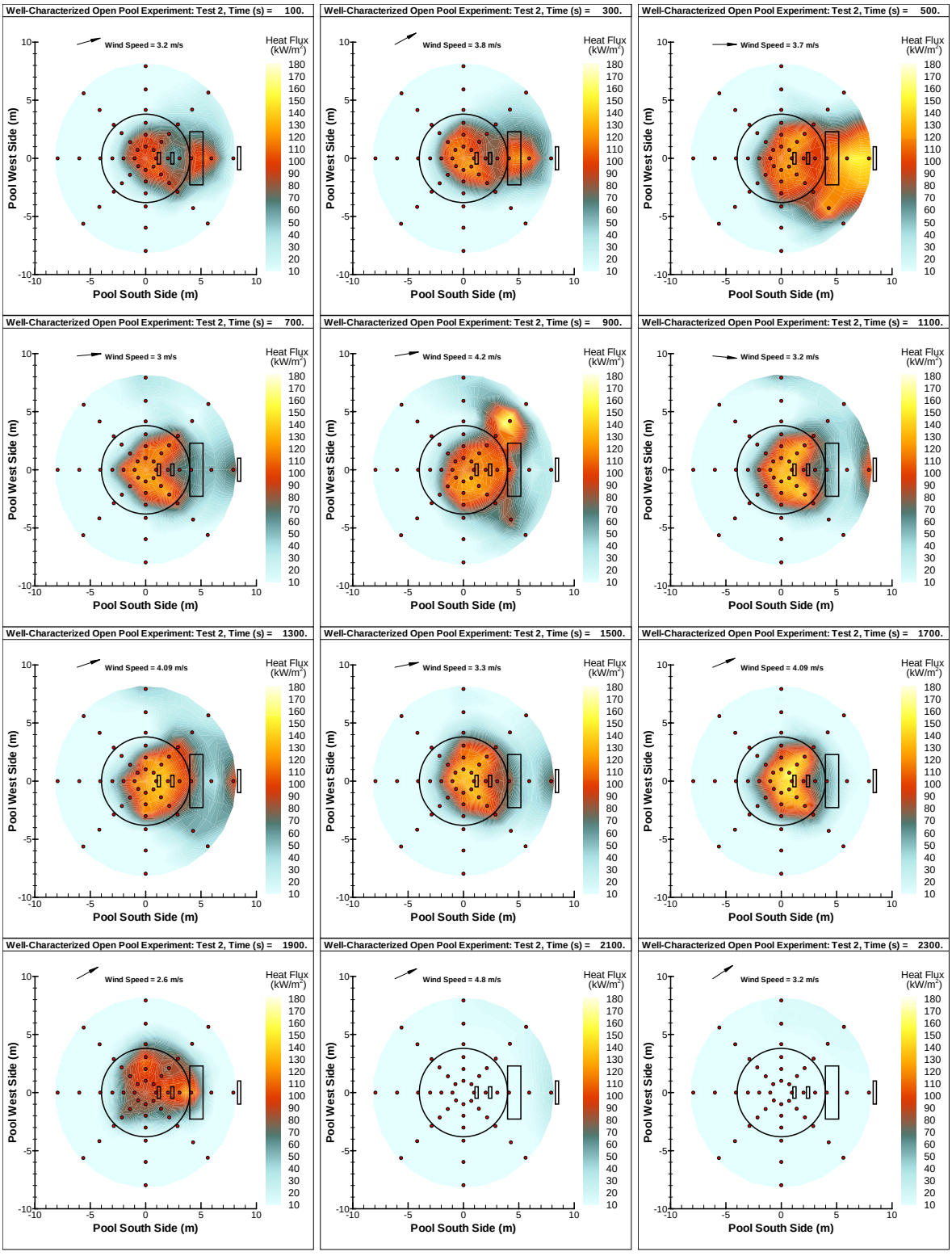

Figure 61. Incident heat flux to the surface of the pool and surrounding terrain for Test 2

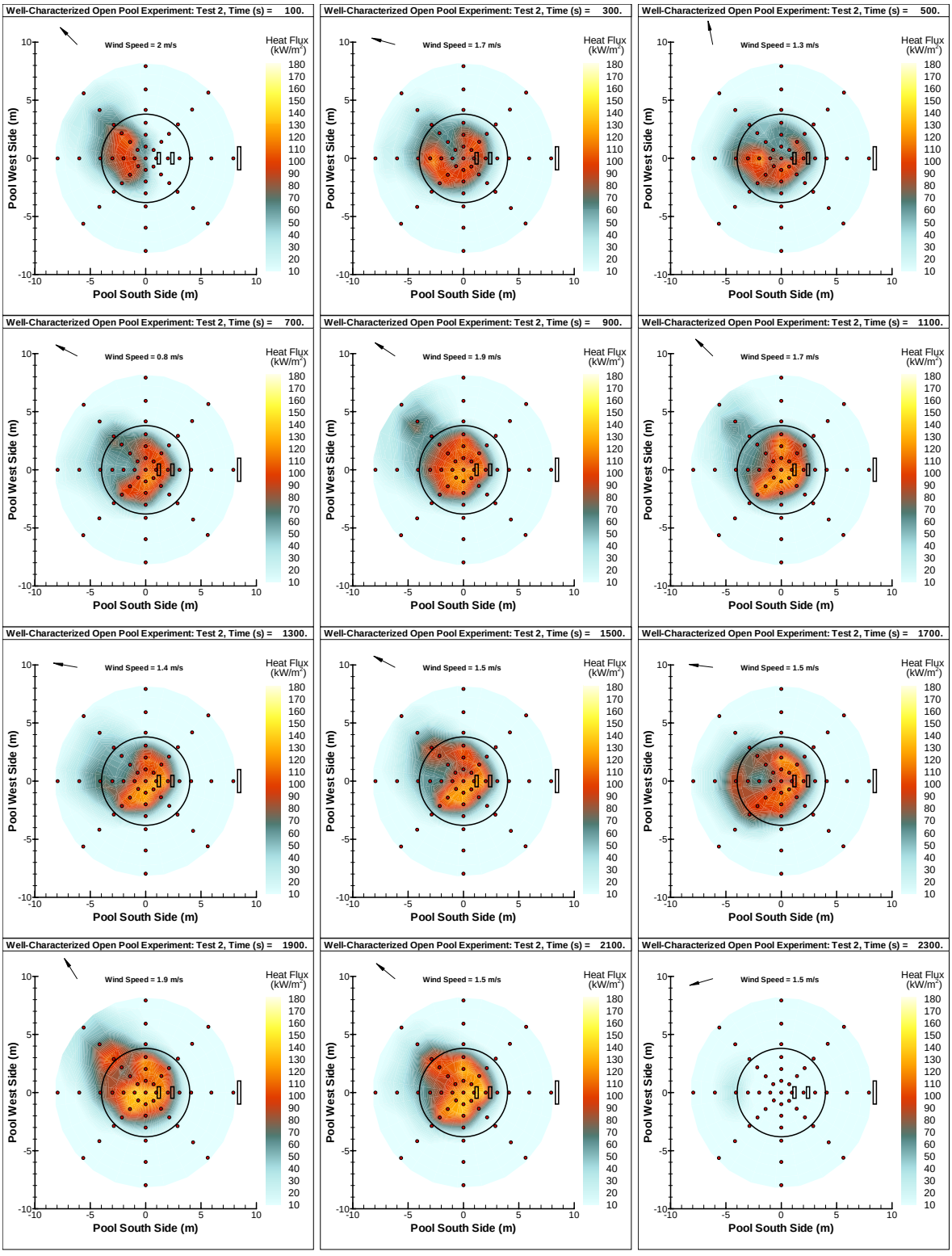

Figure 62. Incident heat flux to the surface of the pool and surrounding terrain for Test 3.

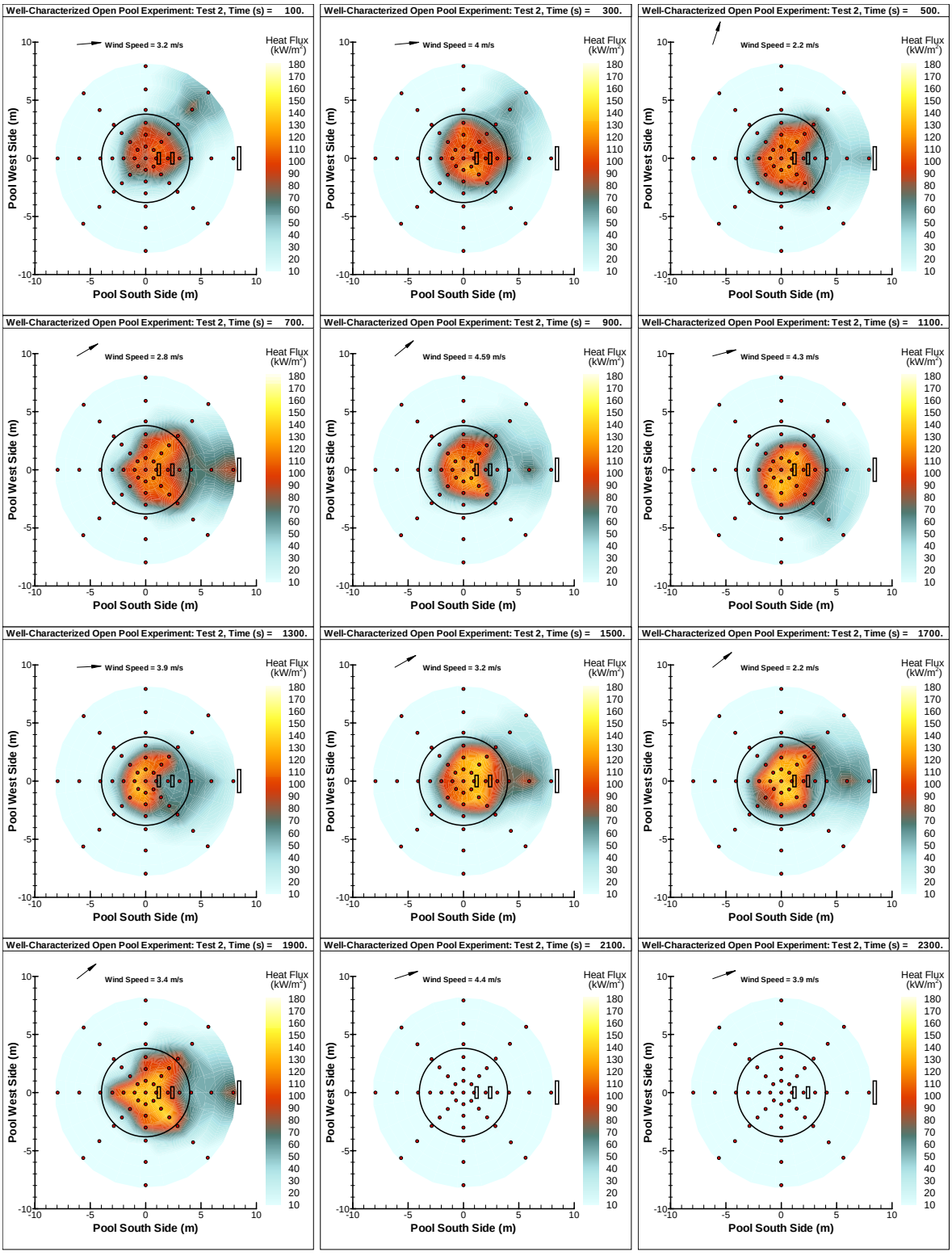

Figure 63. Incident heat flux to the surface of the pool and surrounding terrain for Test 4.

In Test 2, 3 and 4, crosswinds tilted the plume away from the ground normal. This is evident in Figure 61 through 63 where high incident heat flux regions are generally biased toward the leeward side of the pool. In general, the reduced heat flux (possibly oxygen starved) region is missing from the center region of contour plots in these figures. Instead, in some contour plots there are subtle discontinuities in the incident heat flux regions (e.g., Figure 61 at 100 seconds), and in others the incident heat flux region takes on a U-shape geometry. In crosswinds, rotational structures are formed on the leeward side of the plume and are different from the upwind side structure. On the upwind side, rotational structures are similar to those found in single column, vertical pool fires. On the leeward side, the rotation of the structures is axial. Relatively cool air entrained in these structures may cool some of the gauges located on the leeward side and give rise to the subtle discontinuities in the heat flux regions and/or the U-shaped heat flux regions observed in some of the plots.

Characterization of oxygen starved region is an important aspect of fire phenomenology since the extent of the oxygen starved region will strongly influence heat feedback to the pool, which in turn, influences fuel vaporization. It has been suggested that non-uniform incident heat flux distributions, in conjunction with the presence of an oxygen-starved region in the interior of the plume may slow the fuel vaporization rates [4].

4.7.3 Quasi-Steady Heat Flux

Fire data are characterized by rapid changes in heat flux due to interaction of heat flux gages with turbulent flame sheets in the fire and turbulent winds in the surrounding terrain. In order to spatially characterize the fire environment, heat flux data were also averaged over a period of quasi-steady behavior typical of the overall behavior of the fire during the entire test. Periods of quasi-steady behavior were identified in Table 10.

Contour plots of incident heat fluxes averaged over the quasi-steady periods are shown in Figure 64. The extent of high heat flux regions increased in size due to the averaging effect.

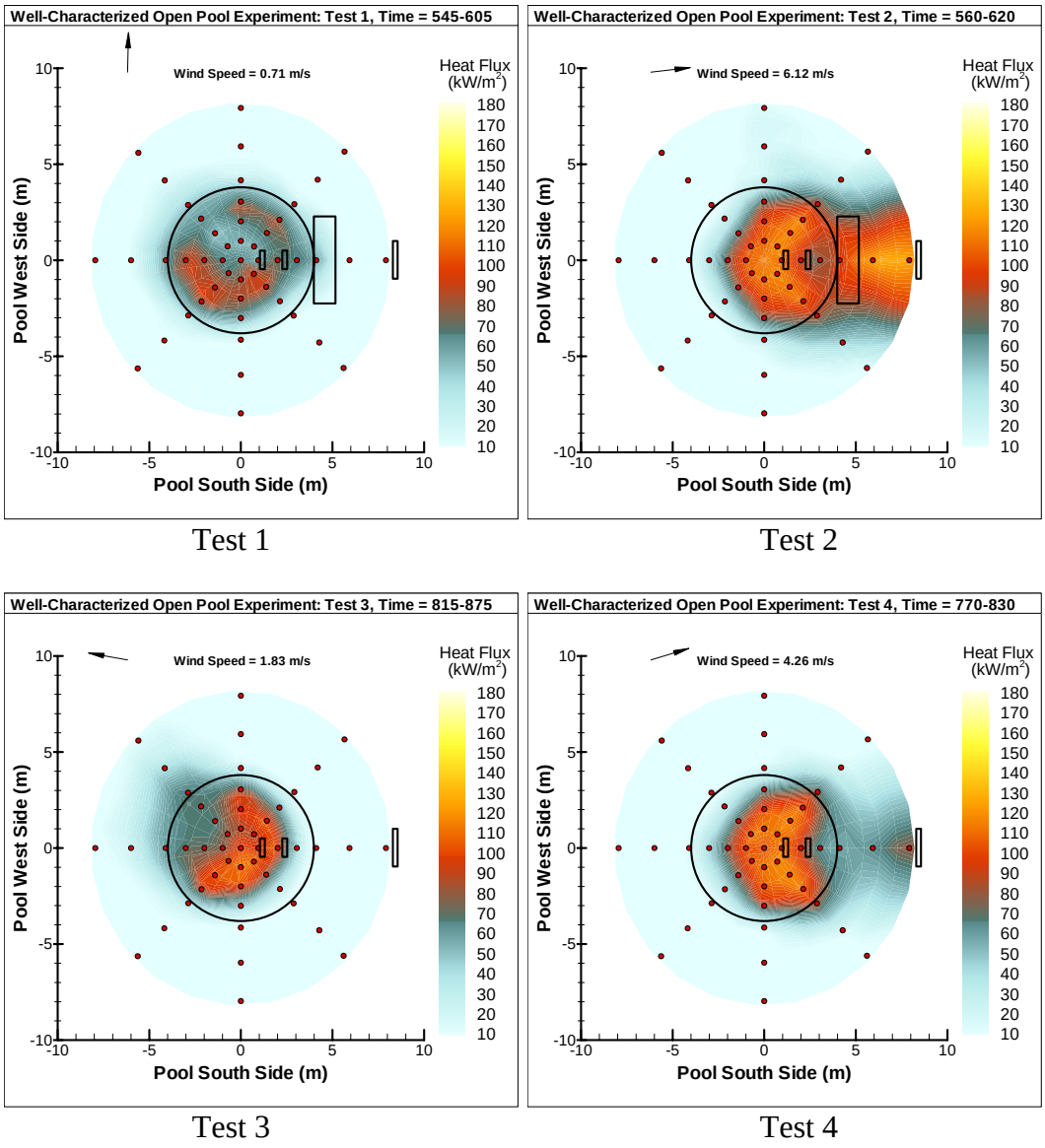

Figure 64. Quasi-steady incident heat flux to the pool and terrain.

4.8 Calorimeter- Heat Fluxes

Data from calorimeter thermocouples were reduced to obtain time- and spatially-resolved estimates of heat transfer to the surface of calorimeters. Thermocouple locations in the small, large and medium (weapon) calorimeters are shown in Figures 17b, 18, and 21, respectively. With the exception of the large calorimeter, a limited number of thermocouples were used in the

small and medium size calorimeters. Cost and robustness dictated the number of thermocouples used in these calorimeters.

The thermal model and methodology for SNL HFG [18] were used to obtain the incident heat flux to the surface of calorimeters, using the appropriate thickness of the calorimeter and material property data. The convective heat component of the incident heat flux, $q_{conv}(t)$, was not considered in the data reduction. Instead, it was treated as an uncertainty of the measurement. Again, for typical large pool fires, incident heat flux measurement uncertainty is approximately ±42% of the calculated incident heat flux. This estimate was obtained using large pool fire data and is only valid for steady-state conditions. For transient conditions, the uncertainty is expected to be higher.

4.8.1 Small Calorimeter Heat Flux

Two Sandia-designed calorimeters were placed within and above the pool approximately 6-7 inches (from the calorimeter bottom) above the ground plane surface (5.75 inches for calorimeter 1, 7 inches for calorimeter 2). Figure 16 shows a sketch of a typical calorimeter. Calorimeter 1 (east cal) was approximately 4.75 feet east of the center of the pool and calorimeter 2 (west cal) was approximately 3.25 feet east of calorimeter 1 (see Figure 15). TCs were spot welded to the inner surface of the calorimeters every 90 degrees from each other as shown in Figure 17b. TCs were also spot welded to the ends of the calorimeter as shown in the top right view of Figure 17b.

Since very few TCs were used in the small calorimeters, plots of spatial distribution of heat fluxes on the skin of these calorimeters were not generated. Instead, heat flux time series plots were generated to analyze incident heat flux to both calorimeters. In Figure 65-66 and Figure 68-69, the labels in the legend correspond to labels shown in Figure 17b. Calorimeter 1 is the west (W Pool Cal) calorimeter and calorimeter 2 is the east (E Pool Cal) calorimeter. As described in Section 4.3, TCs mounted to the calorimeters failed during the tests. Only those temperatures when the TCs were fully operational are plottedFigure 65. In general, incident heat flux reached stable values 100 seconds after ignition. This is consistent with results shown in the previous section.

4.8.1.1 Test 1

Figure 65 shows incident heat flux histories for calorimeter 1 and 2 for Test 1. For both calorimeter 1 and 2, incident heat fluxes were consistently lowest on the bottom and highest on top side of the side of the calorimeters. On the top of calorimeter 1, heat fluxes near 150 kW/m^2 were measured consistently through the test duration; on the bottom, heat fluxes rose from 25 kW/m^2 to approximately 100 kW/m^2 near the end of the test. Heat fluxes on the east and west side of the calorimeter 1 were less predictable, varying significantly from the heat fluxes measured on the top and bottom. Heats fluxes as high as 130 kW/m^2 and as low as 50 kW/m^2 were consistently measured on the top and bottom of calorimeter 2, respectively. Heat fluxes measured on the east side of calorimeter 2 followed closely heat fluxes measured on the top of

calorimeter 2. Heat fluxes on the west side vary significantly, but remained consistently between those observed on the top and bottom.

Heat fluxes on the sides of calorimeter 1 and 2 were consistent with circumferentially measured incident heat fluxes.

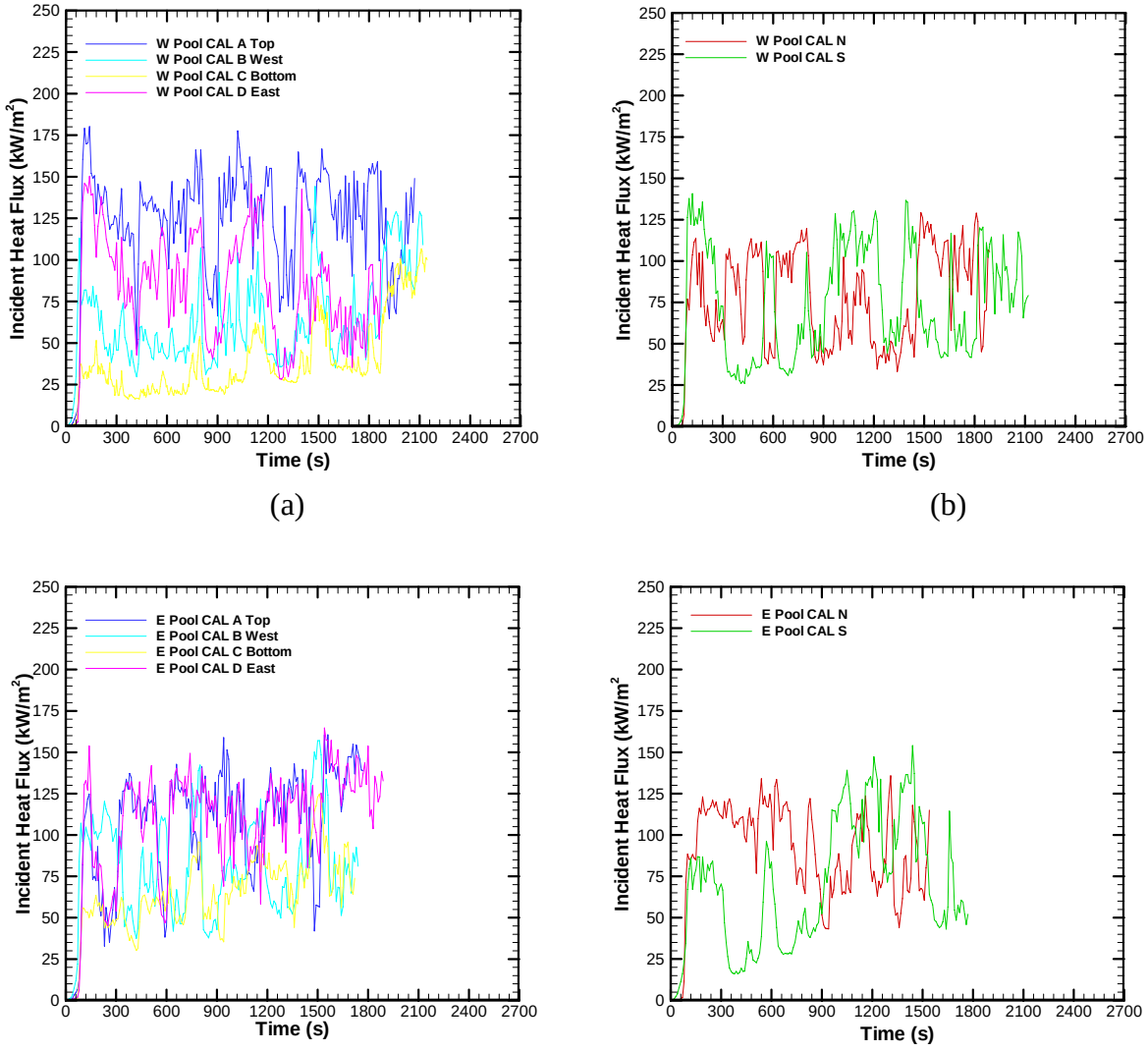

Figure 65. Incident heat flux to the surface of the calorimeter of Test 1.
(a) circumferential heat fluxes on calorimeter 1, (b) heat flux on sides of calorimeter 1, (c) circumferential heat fluxes on calorimeter 2, (d) heat flux on ends of calorimeter 2

4.8.1.2 Test 2

Figure 66 shows incident heat flux histories for calorimeter 1 and 2 for Test 2. In Test 2, TCs on the top of calorimeter 1 failed from the start of the test, so no data is presented from the top of calorimeter 1 in Figure 66a.

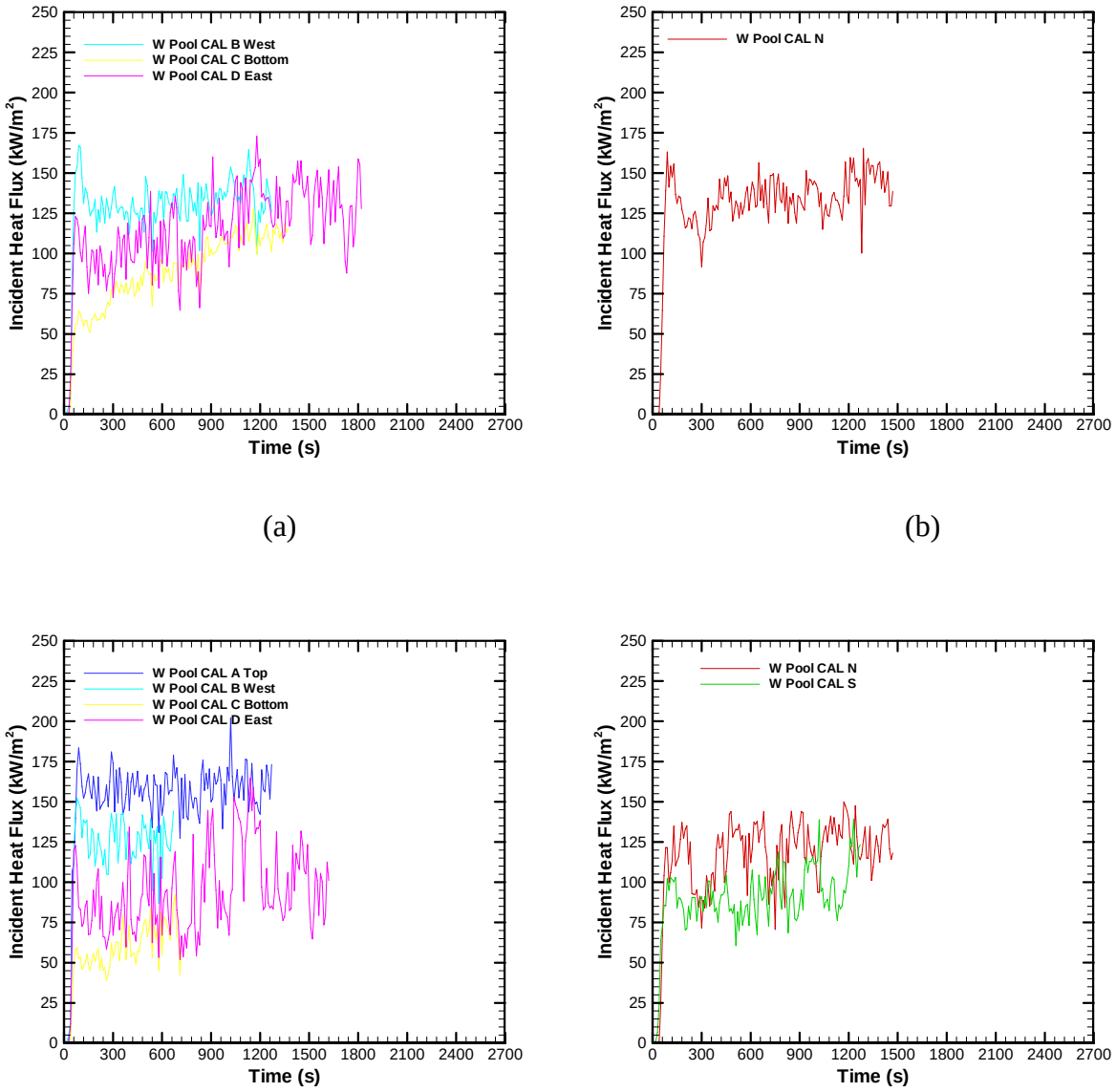

Figure 66. Incident heat flux to the surface of the calorimeter of Test 2.
(a) circumferential heat fluxes on calorimeter 1, (b) heat flux on sides of calorimeter 1,
(c) circumferential heat fluxes on calorimeter 2, (d) heat flux on ends of calorimeter 2

Initially heat fluxes to the west and bottom of calorimeter 1 were highest and lowest respectively. However, as time progress, heat flux to the bottom and east side of circumferential sides seemed to asymptotically approach heat flux values on the west side (150 kW/m^2). In contrast, in calorimeter 2, heat fluxes to each side of the calorimeter remained flat and distinct from each other through time. Note however that larger variations were observed on the east side as compared to other locations in this calorimeter. Heat fluxes on the top and on the west side of calorimeter 2 reached values 160 kW/m^2 and 125 kW/m^2, respectively.

In both calorimeter 1 and 2, incident heat flux magnitudes on the north and south sides of the calorimeter were about equal with those on the circumferential side. On calorimeter 2, heat fluxes on the north end of the calorimeter were slightly higher than heat fluxes on the south end.

4.8.1.3 Test 3

In Test 3, crosswinds were predominantly from east to west. Photographs of test showed the top part of calorimeter 2 protruding out of the flame zone (see Figure 67). This may explain some of the trends observed in Figure 68c.

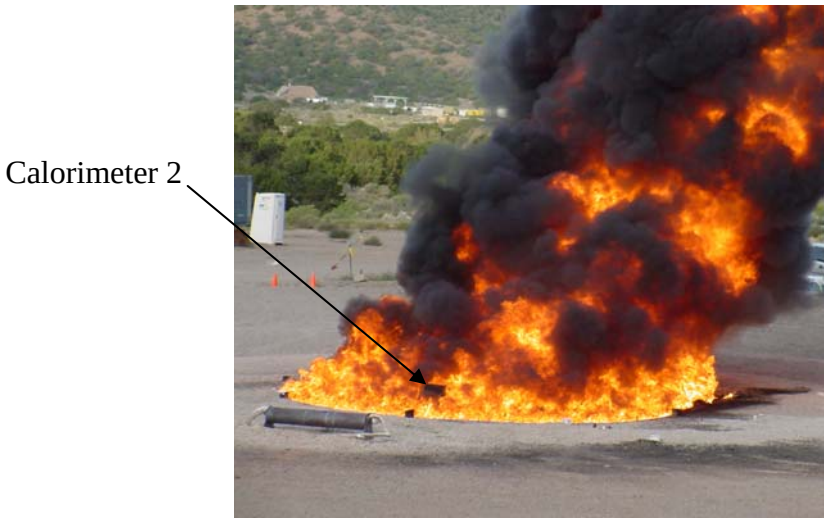

Figure 67. Calorimeter 2 protruding from flames in Test 3.

Figure 68 shows incident heat flux histories for calorimeter 1 and 2 for Test 3. As in Test 2, incident heat fluxes on calorimeter 1 were more uniform from location to location. Heat fluxes on the bottom of calorimeter 1 are lowest initially but quickly rise to the level measured on top, east and west side. In calorimeter 2, heat fluxes to each side of the calorimeter remained flat and even more distinct through time than in Test 2. Heat fluxes measured on the top are not consistently the highest for this calorimeter. Instead, heat fluxes on the west side of calorimeter are significantly higher than at other locations on the circumference of calorimeter 2. Note also that heat fluxes on the ends of calorimeter are also consistently higher than heat fluxes on the top, bottom and east side of calorimeter 2.

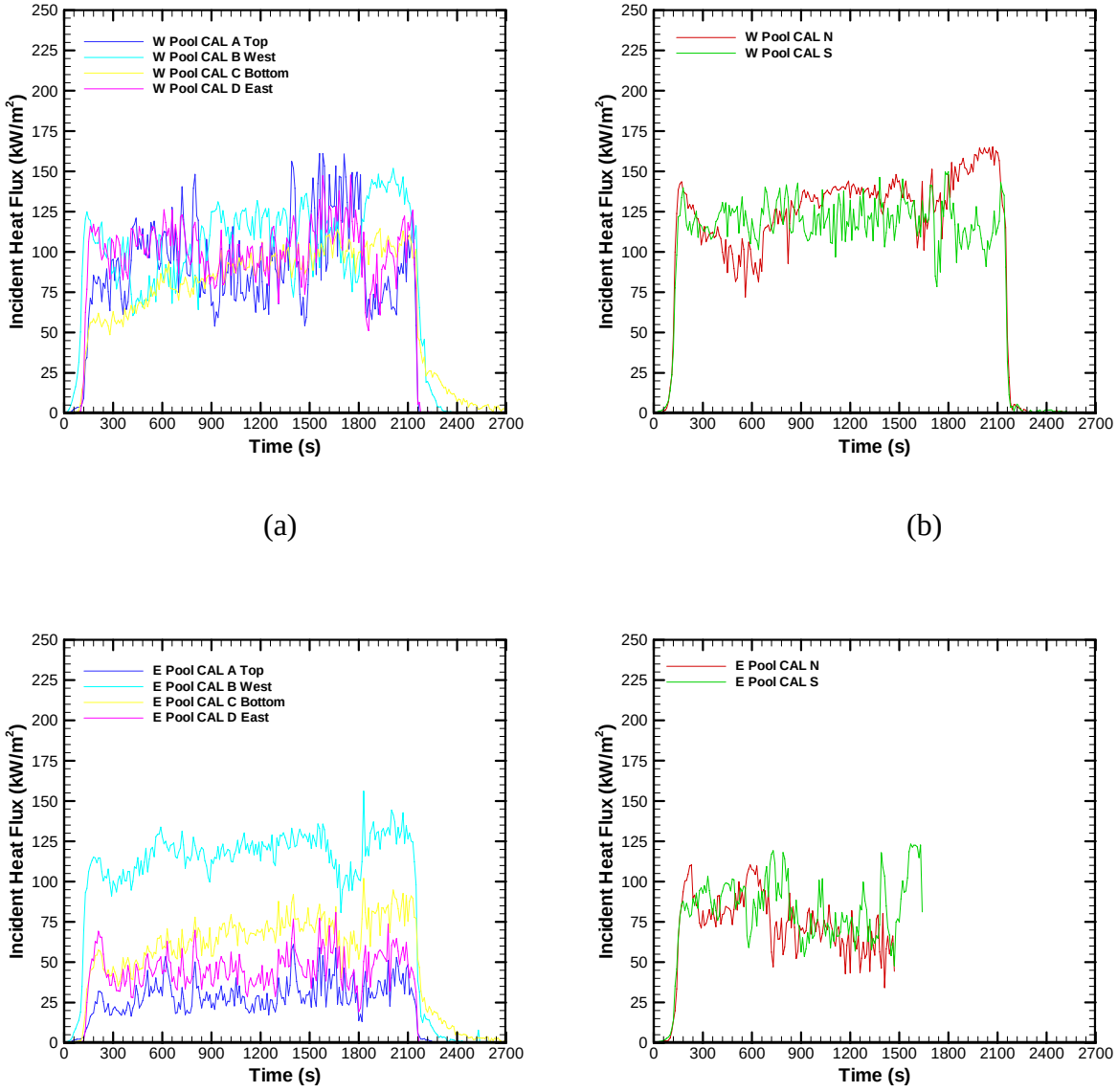

Figure 68. Incident heat flux to the surface of the calorimeter of Test 3.
(a) circumferential heat fluxes on calorimeter 1, (b) heat flux on sides of calorimeter 1,
(c) circumferential heat fluxes on calorimeter 2, (d) heat flux on ends of calorimeter 2

4.8.1.4 Test 4

Figure 69 shows incident heat flux histories for calorimeter 1 and 2 for Test 4. As in Test 1 and 2, heat fluxes were consistently highest on the top of calorimeters. In calorimeter 1, heat fluxes to the top of calorimeter were approximately 150 kW/m^2 initially, but increased with time and reached 175 kW/m^2 near the end of the test. With the exception of heat fluxes on the east side, similar rising trends were observed at all other locations. Also, very little differences in heat fluxes were observed between the north and south end of calorimeter 1. Steady-state incident heat flux to the top of the calorimeter 2 was approximately 150 kW/m^2.

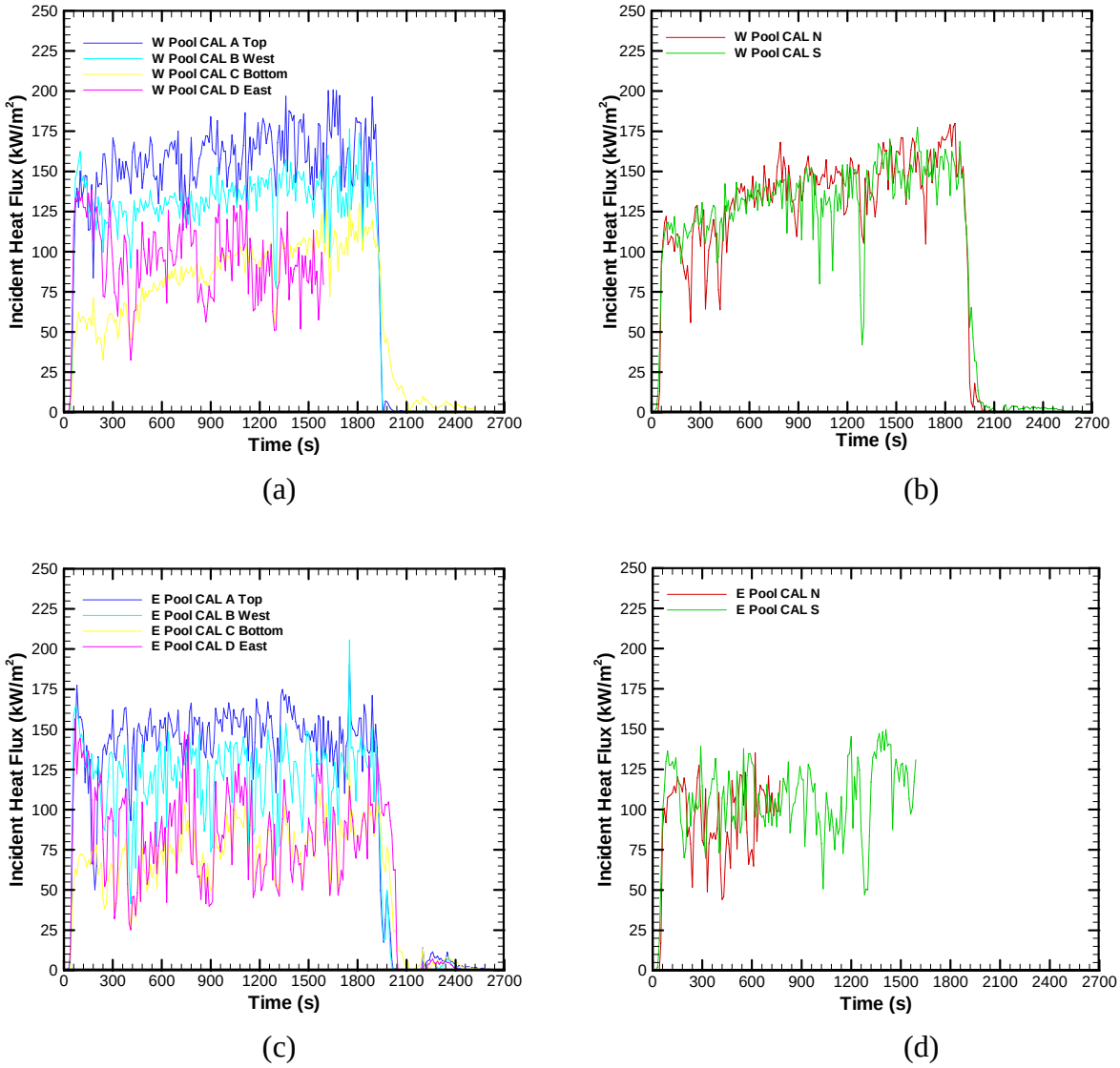

Figure 69. Incident heat flux to the surface of the calorimeter of Test 4. (a) circumferential heat fluxes on calorimeter 1, (b) heat flux on sides of calorimeter 1, (c) circumferential heat fluxes on calorimeter 2, (d) heat flux on ends of calorimeter 2.

4.8.2 Large Calorimeter-Heat Fluxes

A large carbon-steel calorimeter simulating a bluff body obstruction was placed on the lee side of the pool surface in Test 1 and Test 2. The calorimeter was 1.2 m in diameter, 4.5 m in length, and had a wall thickness of 2.54 cm (4 ft diameter, 15 ft long, 1 inch wall thickness). Sixty-three (63) thermocouples were attached to inside surfaces (tacked down with thin metallic strips). Figure 18 shows the locations of the thermocouples.

Since a significant number of TCs were used on the circumferential surface of the large calorimeters, contour animations showing the spatial distribution of heat fluxes on the skin of this calorimeter were generated and were used to study incident heat flux time variations across circumferential skin of this calorimeter. Figure 70 and 63 show contour plots of incident heat flux on the circumferential surface of the large calorimeter at various times during Test 1 and Test 2. Although not complete, these plots are representative of the type of data obtained from Test 1 and Test 2. In these plots the time sequence goes from the upper left to the lower right corner of the page. Corresponding wind speed and wind direction information are given in each plot to facilitate interpretation of results.

In Figure 70 and 63, the x-axis corresponds to the circumferential angle. The center of the x-axis (zero) corresponds to the top of the calorimeter; the extreme ends of the x-axis correspond to the bottom of the calorimeter. Angles -90 and +90 correspond to the west and east sides of the calorimeter respectively. The y-axis corresponds to the longitudinal axis of the calorimeter. The center of the y-axis (zero) is the center of the calorimeter. It is aligned with the center of the pool. The positive and negative ends of the y-axis correspond to the north and south facing ends of the calorimeter.

Contours extend from the north end to approximately 0.8 m (2.6 ft) from the south end of the calorimeter. As shown in Figure 18, not enough TCs were placed on the south end of the calorimeter to obtain meaningful results from spatial interpolation in this section of the calorimeter. There are some “sharp” gradients in the contour plots. These non-physical gradients are due to linear interpolation between data points. Realize also there may be as much as ±42% uncertainty in the incident heat flux measurements shown in these plots due to the method used to reduce the TC data.

Figure 70 shows contour plots of incident heat flux to the surface of the large calorimeter for Test 1 at increments of 200 seconds, starting from 100 seconds and ending at 2300 seconds. In general incident heat fluxes to large calorimeter were less than 80 kW/m^2. As expected, the largest heat fluxes were observed on the west side of the calorimeter, the closest surface to the pool. Also, as expected maximum heat fluxes occurred when crosswinds were blowing from west to east.

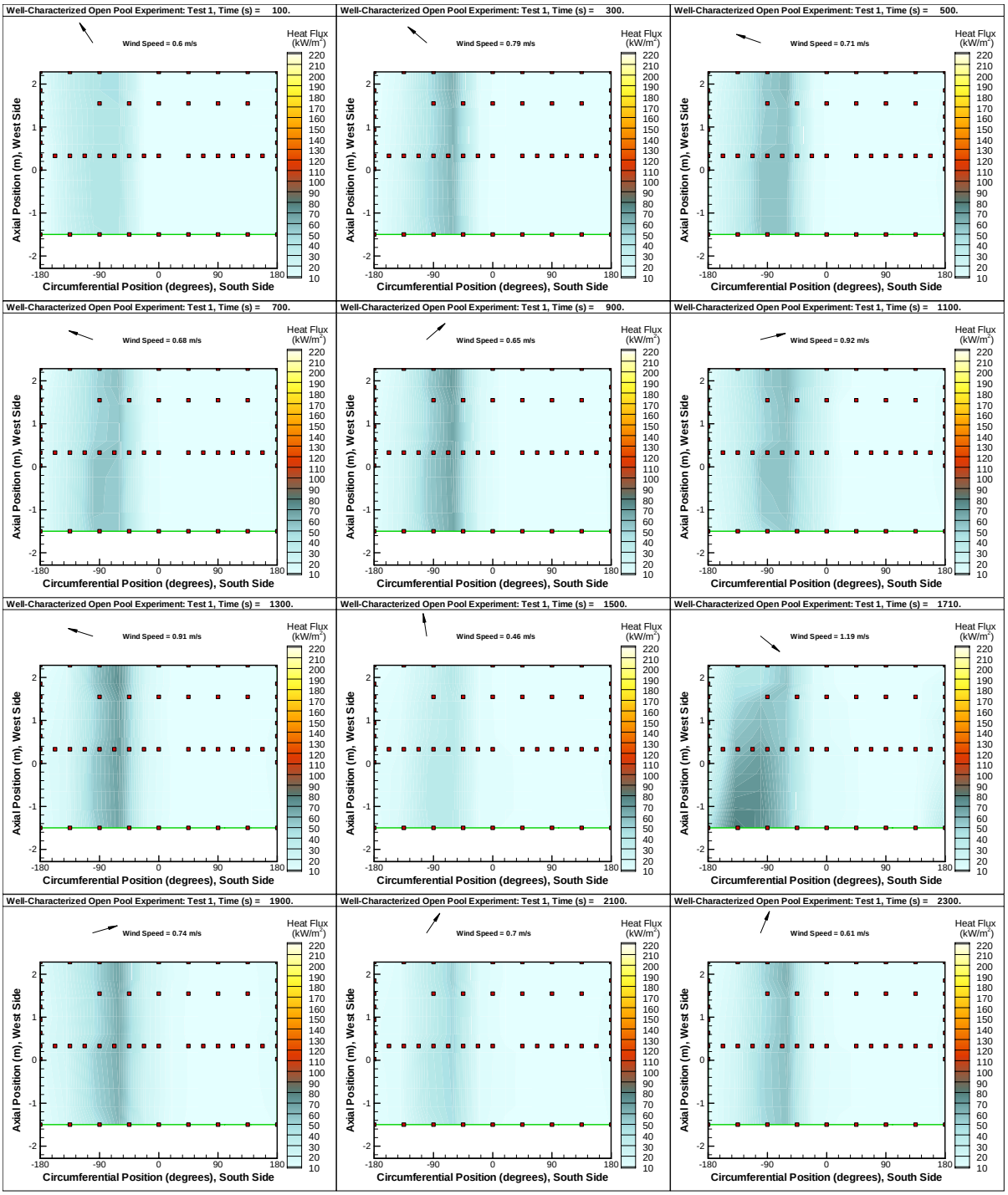

Figure 70. Spatial distribution of incident heat flux to the large calorimeter during Test 1.

Figure 71 shows contour plots of incident heat flux to the surface of the large calorimeter for Test 2 at increments of 100 seconds, starting from 100 seconds and ending at 800 seconds. A number of TCs malfunctioned after 800 seconds, so no contour plots were generated beyond 800 seconds.

In Test 2, incident heat fluxes to the large calorimeter were largest on the top and east sides of the calorimeter. Movies of contour plots showed heat fluxes reached maximum values on the east side of calorimeter (~210 kW/m^2). The large heat fluxes on the windward side of the large calorimeter are due to increase fuel/air mixing in the wake from interaction of wind with the calorimeter.

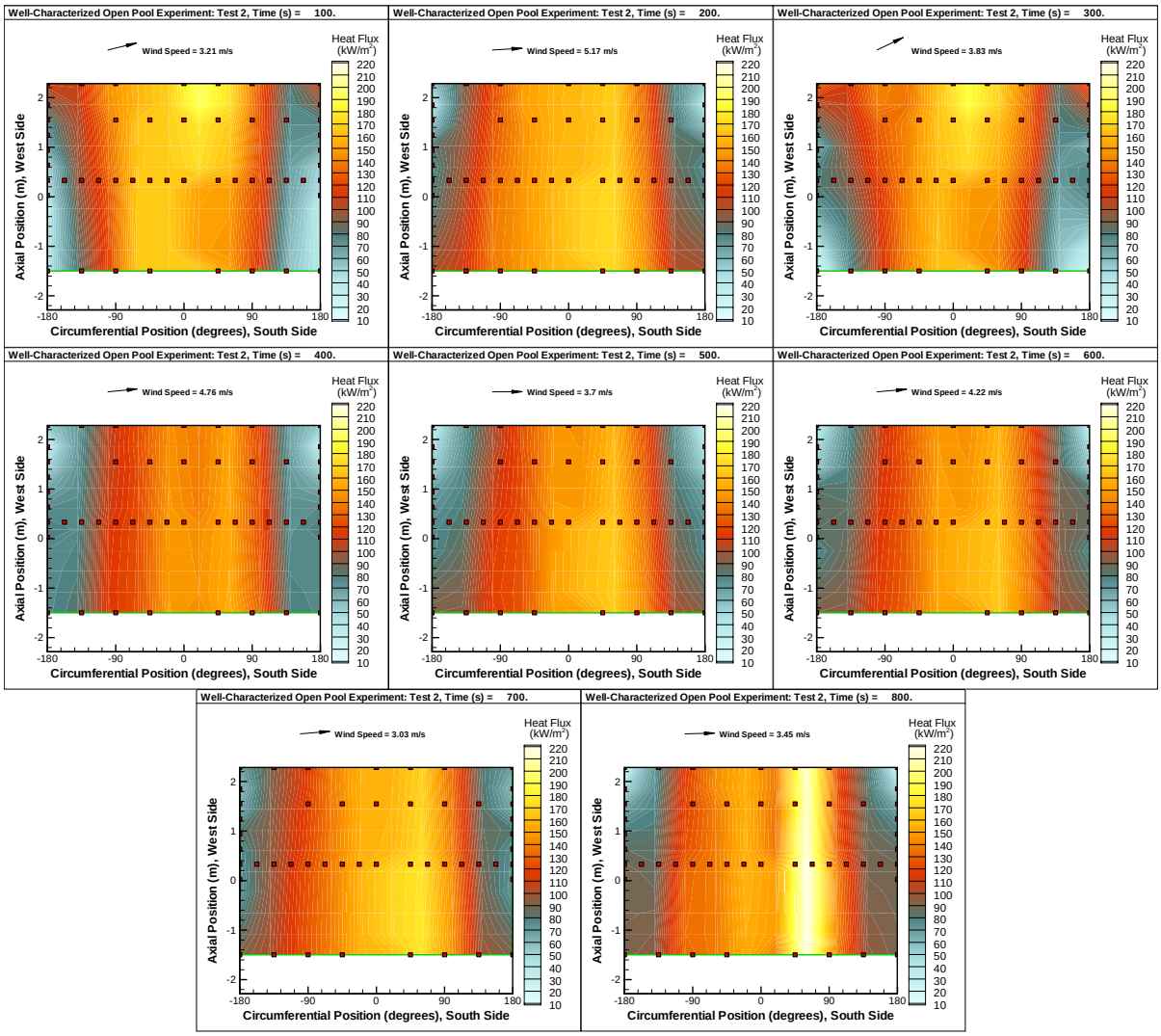

Figure 71. Spatial distribution of incident heat flux to the large calorimeter during Test 2.

4.8.3 Medium (Weapon) Calorimeter-Heat Fluxes

A medium calorimeter simulating a weapon was placed on the windward side of the large calorimeter (approximately 10.75 ft separation distance). The weapon calorimeter is constructed of 0.125 inch thick 304 stainless steel (see Figure 20). It has an outer diameter of 12 inches, and is 2 m long. There were 8 circumferential measurement stations. Measurement station 1 faced due East with the rest sequentially numbered in a counterclockwise direction (see Figure 21).

Since very few TCs were used in the medium calorimeters, spatial distribution of heat fluxes on the skin of the medium calorimeters were not generated. Instead, heat flux time series plots were generated to analyze incident heat flux to both calorimeters (see Figure 72). In Figure 72, the labels in the legend correspond to labels shown in Figure 21.

As expected, incident heat fluxes to the medium calorimeter were small for Test 1 and 3, and large for Test 2 and 4. For Test 1 and 2, the fire plume remained close to the ground normal; hence, heat flux to the medium calorimeter was dominated by radiation from the fire plume and was not significant due to the fire-calorimeter distance. In contrast, in Test 2 and 4, strong crosswinds tilted the fire plume in the direction of the medium calorimeter. The fire plume covered the calorimeter or lingered near the calorimeter as shown in Figures 34 and 40. As Figure 72 shows, incident heat fluxes reached 200 and 250 kW/m^2 in Test 2 and 4 respectively.

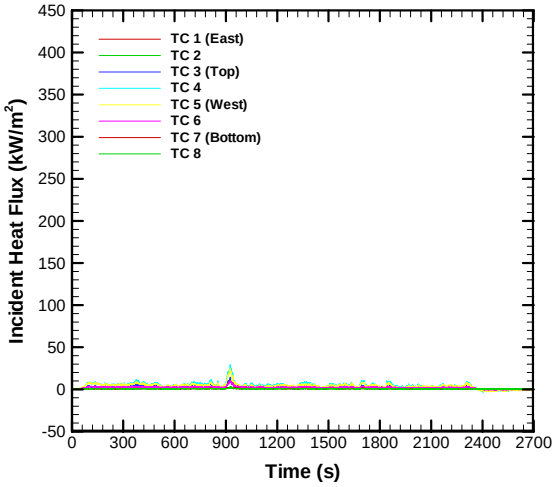

Test 1

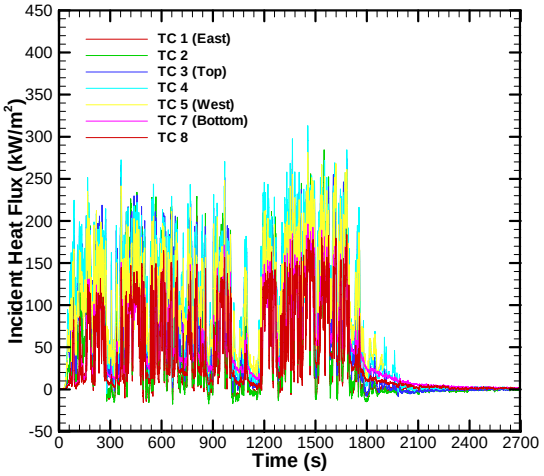

Test 2

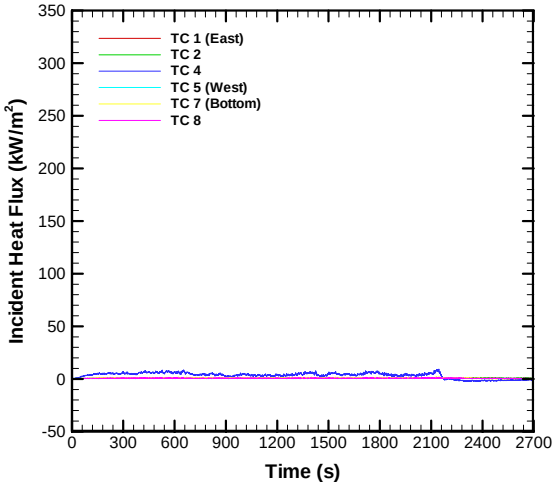

Test 3

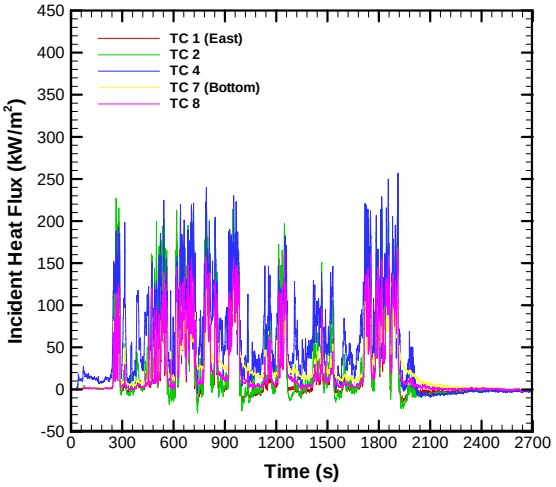

Test 4

Figure 72. Incident heat fluxes to medium (weapon) calorimeter.

5 Simulation Predictions

Numerical fire simulations were performed using the Vulcan fire code. Vulcan utilizes the Kameleon fire model [22] and solves the conservation equations on a structured 3-dimensional Cartesian grid. The conservation equations are discretized using first and second-ordered finite difference scheme. In Vulcan, turbulence can be modeled using the standard k-e model or a LES formulation; for this study, the k-e models was used. Combustion is modeled using the Magnussen Eddy Combustion Concept [23], thermal radiation is modeled using the Discrete Transfer Method [24], and soot formation is modeled using the two step process proposed in [25]. Eddy viscosity near solid walls and convective heat transfer to solid surfaces are calculated using the logarithmic wall function.

Four calculations were performed each corresponding to one of the experiments in the test series. The origin of the xyz axes for the simulations is vertically at ground level and horizontally at the center of the pool. x is positive to the east, y is positive to the north, and z is positive up. The pool surface is 0.1 m below ground level. The ground is treated as completely level.

The computational domain was 137 m ($-62 \leq x \leq 75$) x 124 m ($-62 \leq y \leq 62$) x 88.9 m ($-0.1 \leq z \leq 88.8$) in length and had 107, 93 and 55 grid cells in the x, y, and z direction, respectively. The pool and calorimeter model details and dimensions (Figures 73-75) were kept as close as possible to corresponding dimensions used in the experiments. Special cells were added to the model to simulate the heat flux gauges (HFGs) used in the pool and surrounding terrain during the experiments. They were placed at the same xy-location and height as HFGs in the experiments. History cells were specified in Vulcan to extract detail time information (e.g., incident heat flux) at specific locations in the domain.

A variable wind boundary was applied in the Vulcan simulations, based on the measured wind for each test. The input to Vulcan is a wind value at a height h of 10 m, which is then varied with height by a power law distribution, e.g.,

$$wind(h) = wind(10m)\left(\frac{h}{10m}\right)^{0.117}.$$

The input values were a running time average over 10 s of the wind measurements at the 10 m locations on the four towers. On the vertical boundaries of the Vulcan model, if there is an inward component of wind, that boundary is treated as a velocity boundary. Otherwise, that boundary is treated as a constant pressure boundary. Note that in the calm wind tests (Test 1 and 3), winds measured downwind from the pool fire are applied on the upwind edge for the simulation.

Wind boundary conditions were varied with time in the simulation runs according to the following rule:

$$BC_x = \begin{cases} \text{U(t), V(t)} & \text{on - x boundary if a component of the wind is from west; on + x boundary otherwise} \\ \text{P = constant} & \text{pressure on opposite boundary of U, V} \end{cases}$$

$$BC_y = \begin{cases} \text{U(t), V(t)} & \text{on - y boundary if a component of the wind is from south; on + y boundary otherwise} \\ \text{P = constant} & \text{pressure on opposite boundary of U, V} \end{cases}$$

The fuel pool was treated as a time varying, spatially uniform, input flux boundary of fuel vapor, where the fuel vapor flux vs. time is from the experimental data. Fuel properties for JP8 were used for fuel.

Simulations were run out to approximately 10 minutes. Numerical results of simulations are shown in Figure 80 through 71.

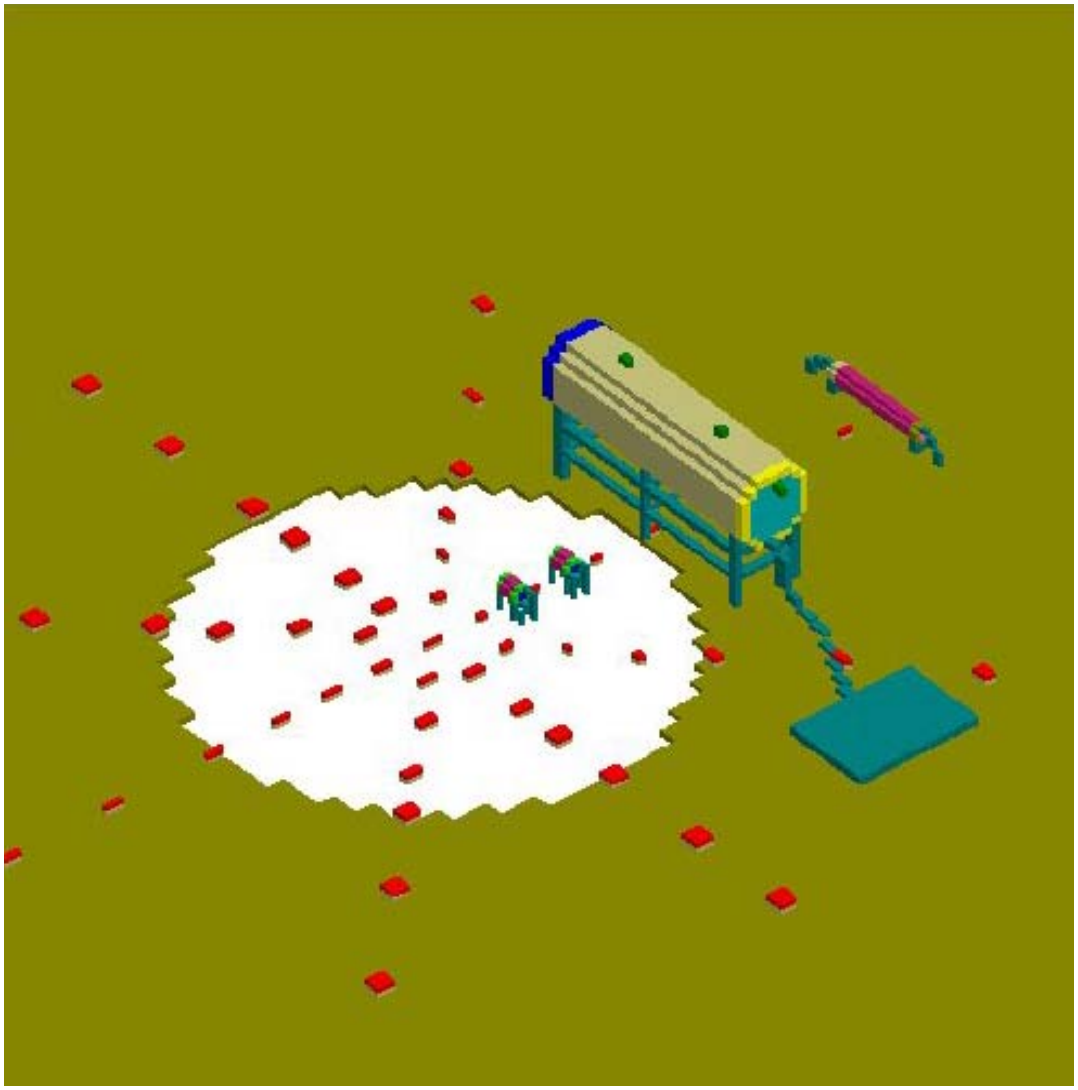

Figure 73. Simulation model in the vicinity of the fuel pool with the large calorimeter.

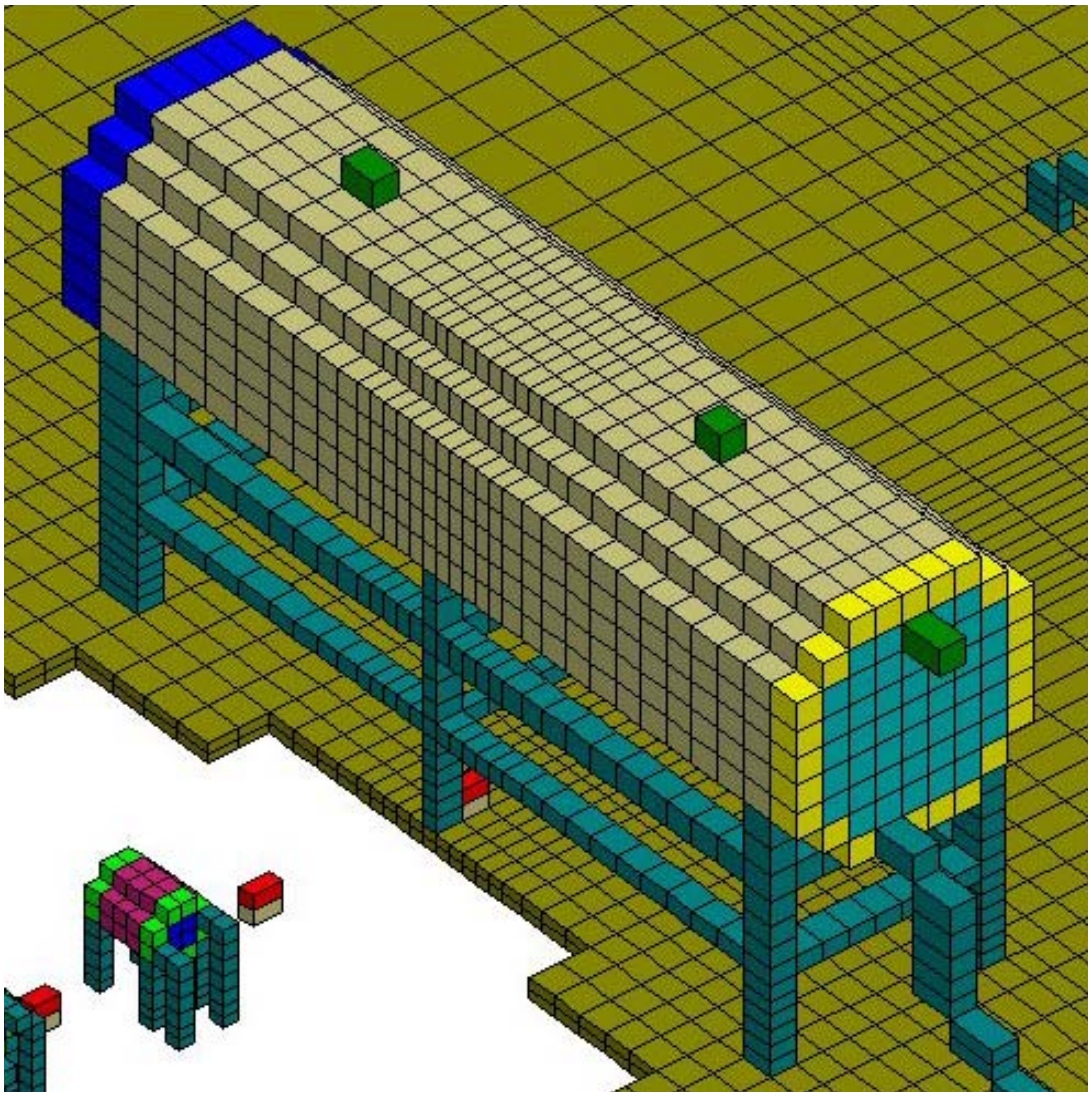

Figure 74. Simulation model detail of the large calorimeter.

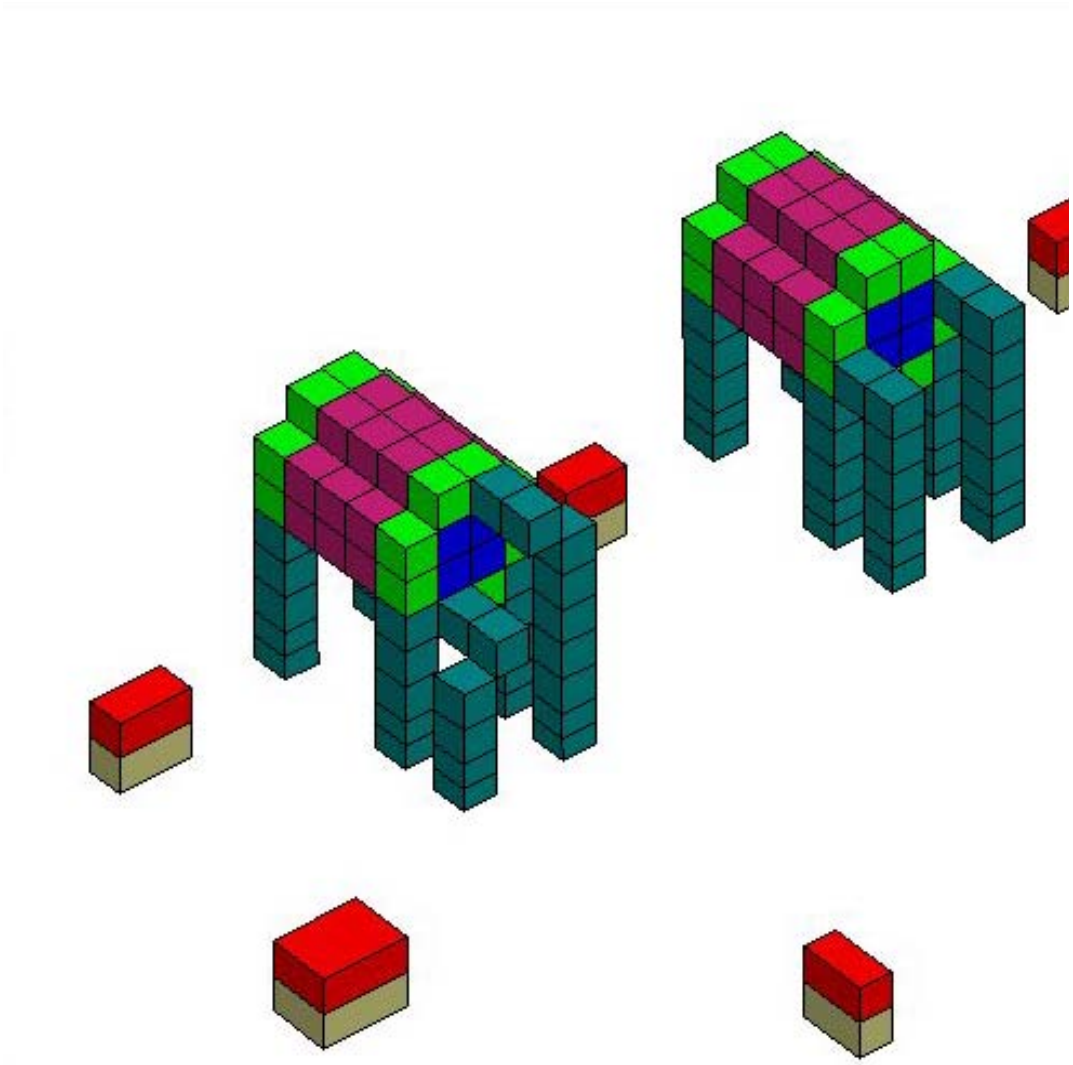

Figure 75. Simulation model detail of the small calorimeters.

Figures 76 through 79 show predicted flame topology at 200 s, 300 s, 400 s, and 500 s in the four experiments. Results shown in these plots are representative of general trends.

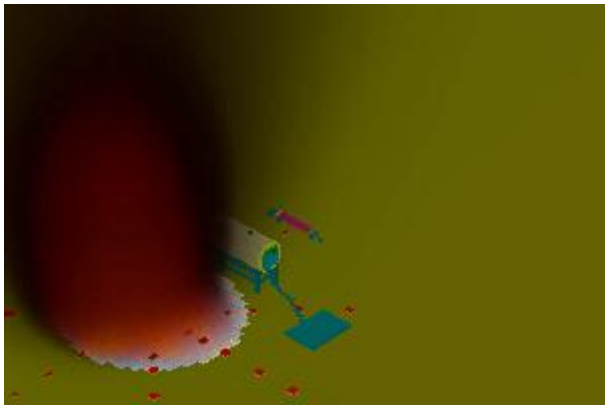

200 s

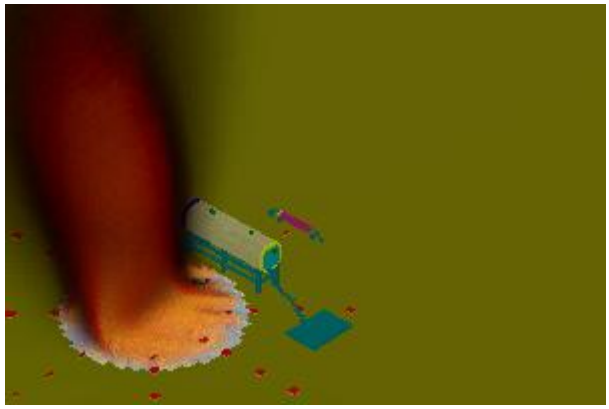

300 s

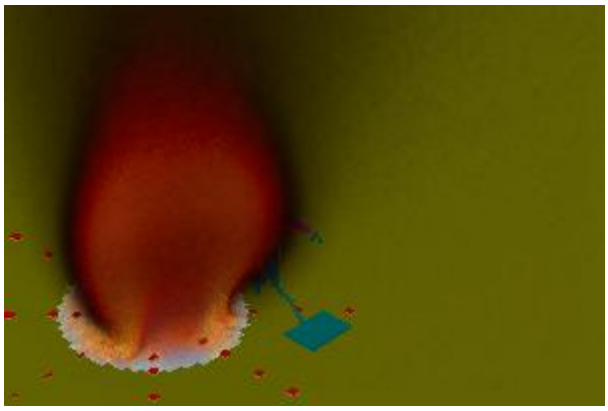

400 s

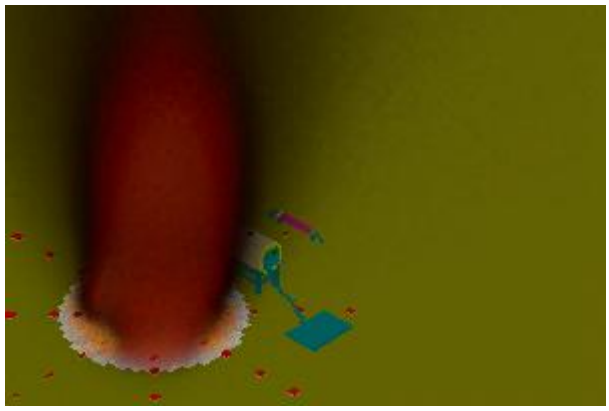

500 s

Figure 76. Predicted flame topology in the Test 1 simulation.

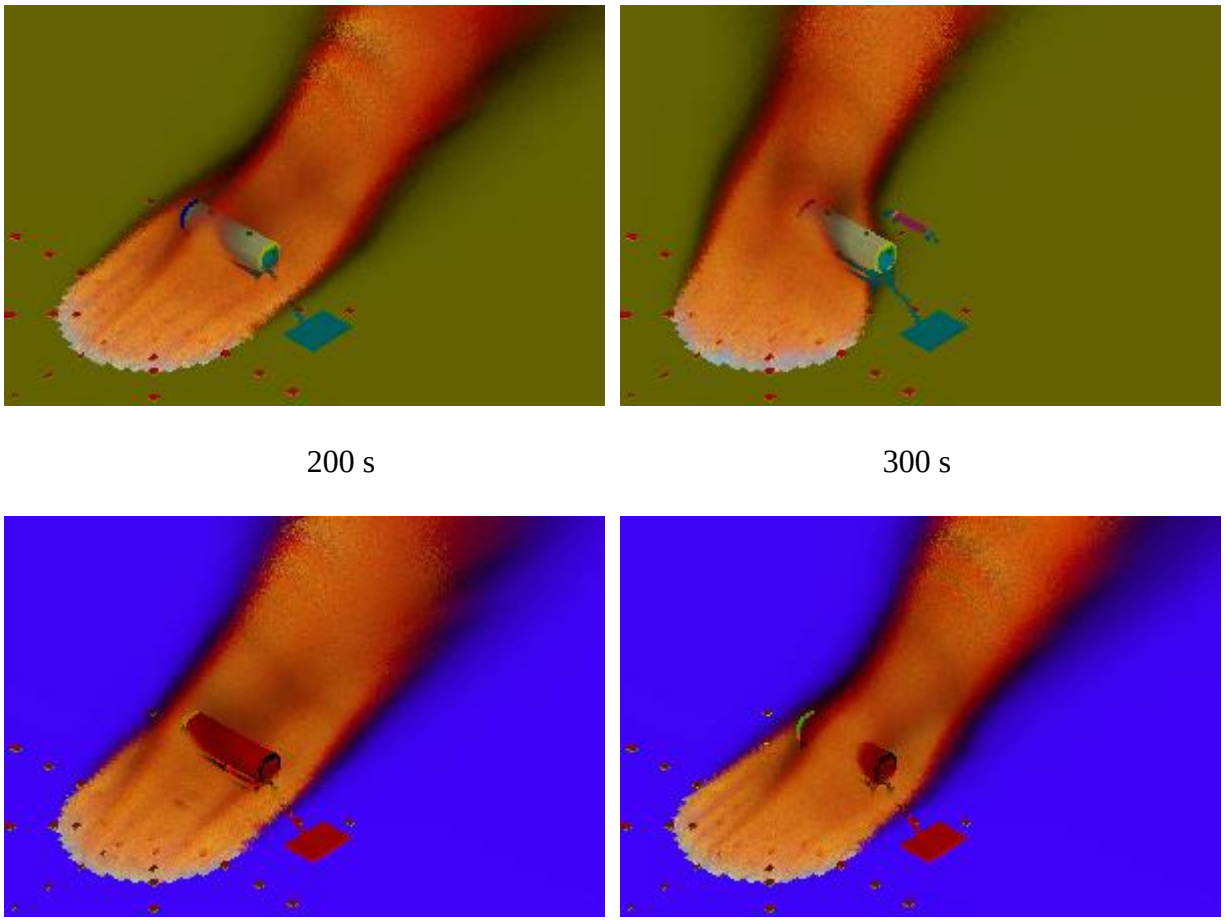

Figure 77. Predicted flame topology in the Test 2 simulation.

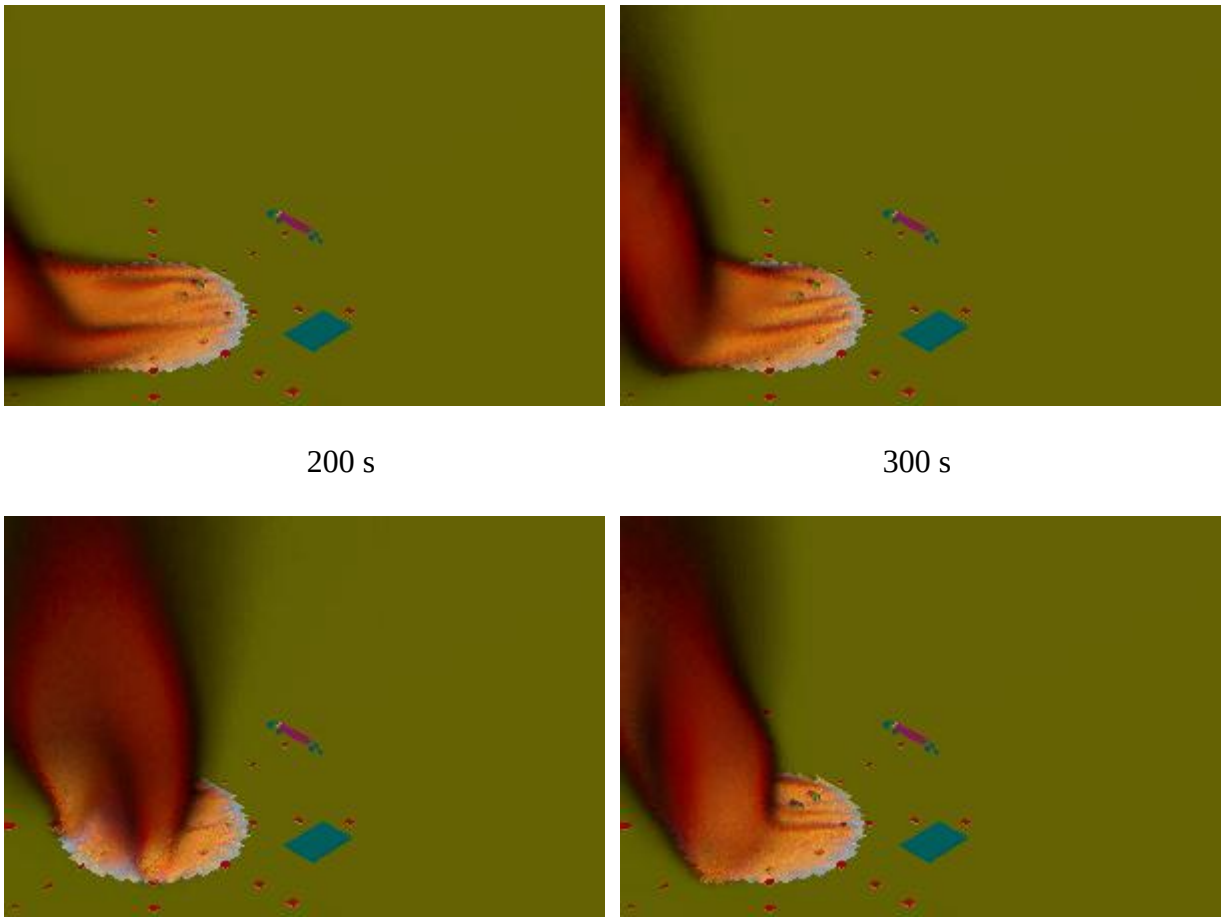

200 s 300 s

400 s 500 s

Figure 78. Predicted flame topology in the Test 3 simulation.

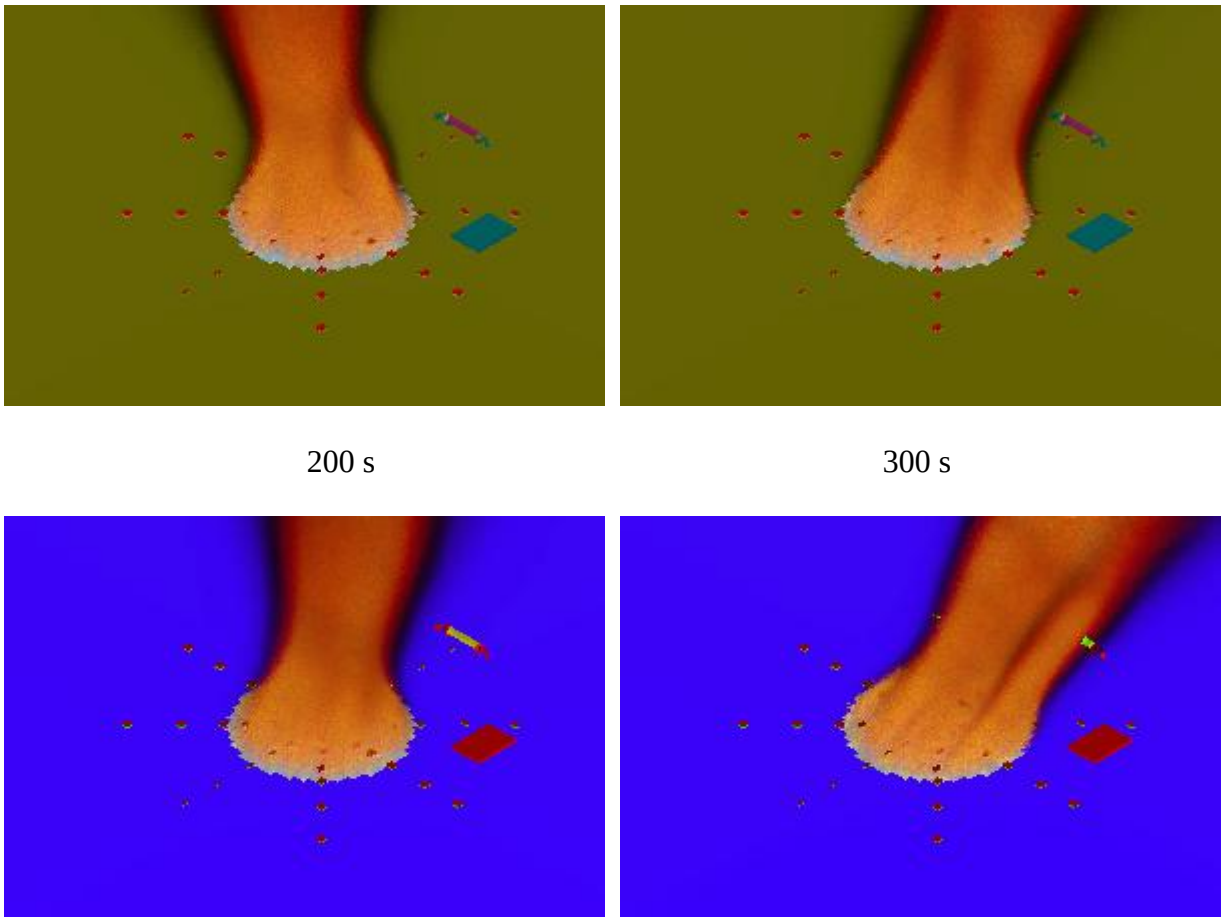

Figure 79. Predicted flame topology in the Test 4 simulation.

Figure 80 through 83 show predicted incident heat fluxes over the pool surface. Results shown in these plots are representative of general trends. Movies of simulations show significant puffing during the first 100 seconds of simulation time and were interpreted to be effects of numerical instability early on. For this reason, only results between 200 and 500 seconds are shown for each simulation run. In general, predicted incident heat fluxes to the pool and terrain are 20 to 40% lower than in experiments. Results for Test 1 simulation show low incident heat fluxes in the center of the pool characteristic of an oxygen starved interior. As observed in the experiment results, predicted incident heat fluxes on the windward side are relatively low far from the edge of the pool.

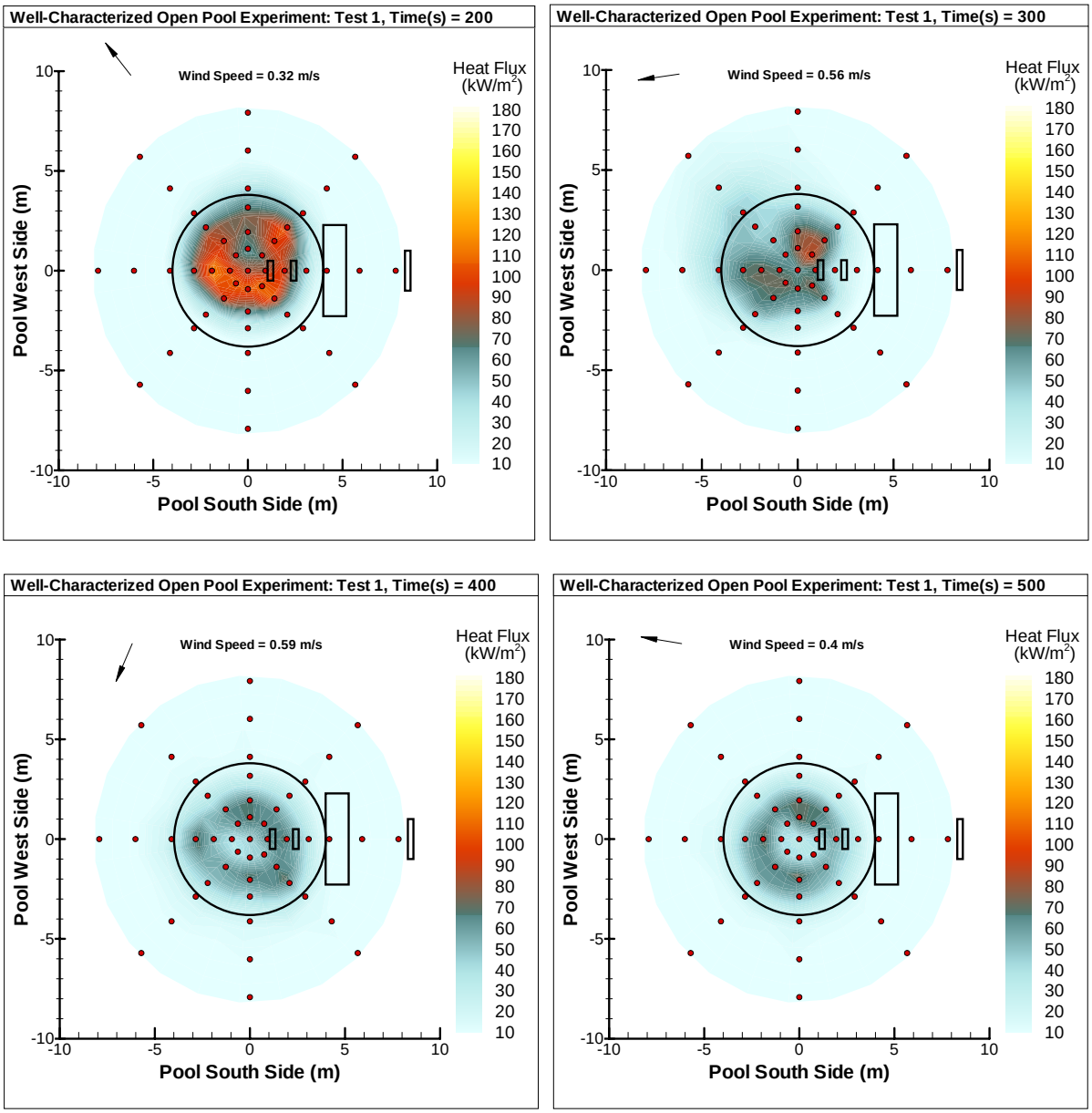

Figure 80. Predicted incident heat fluxes over the pool and terrain surface for Test 1.

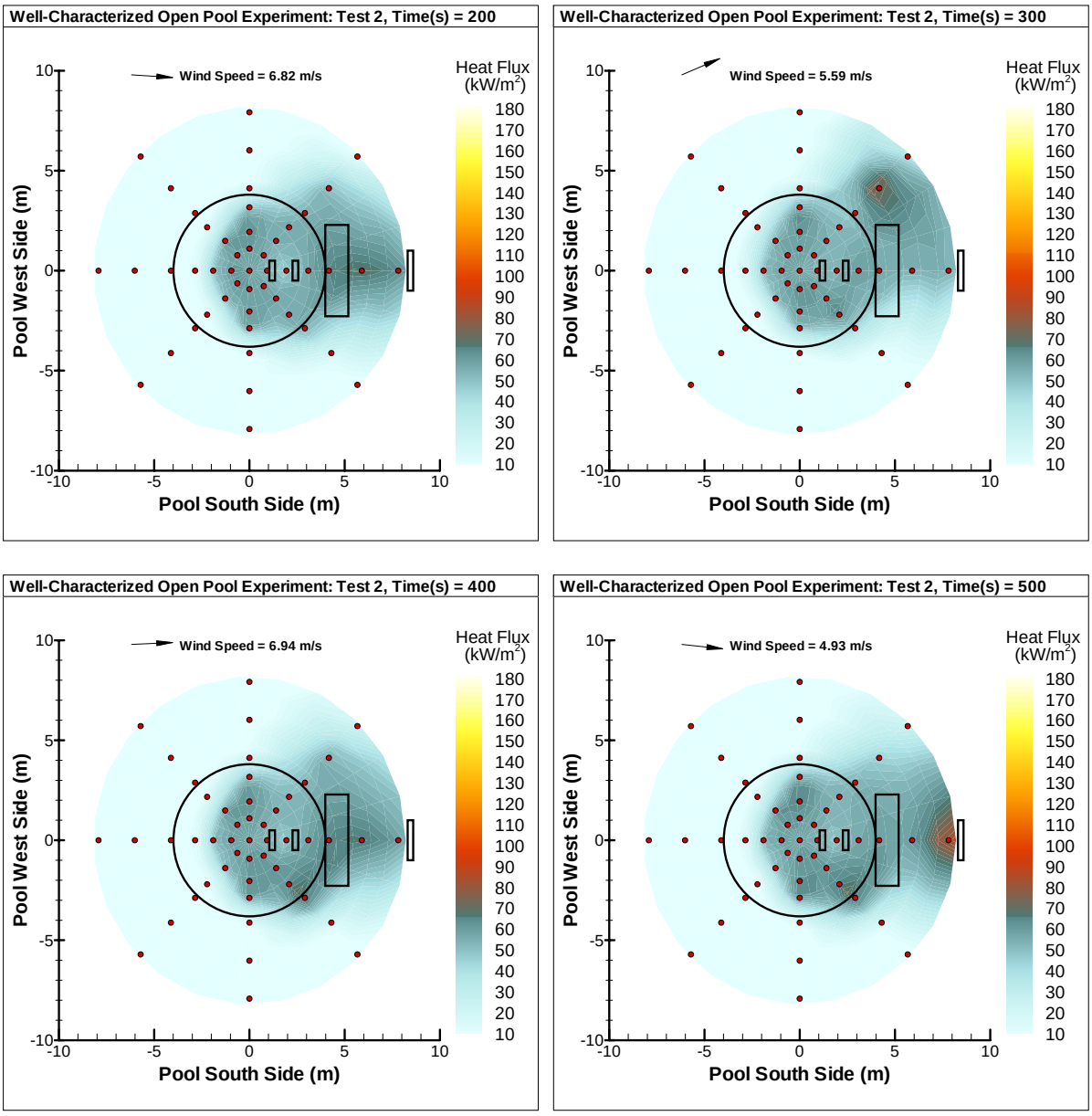

Figure 81. Predicted incident heat fluxes over the pool and terrain surface for Test 2.

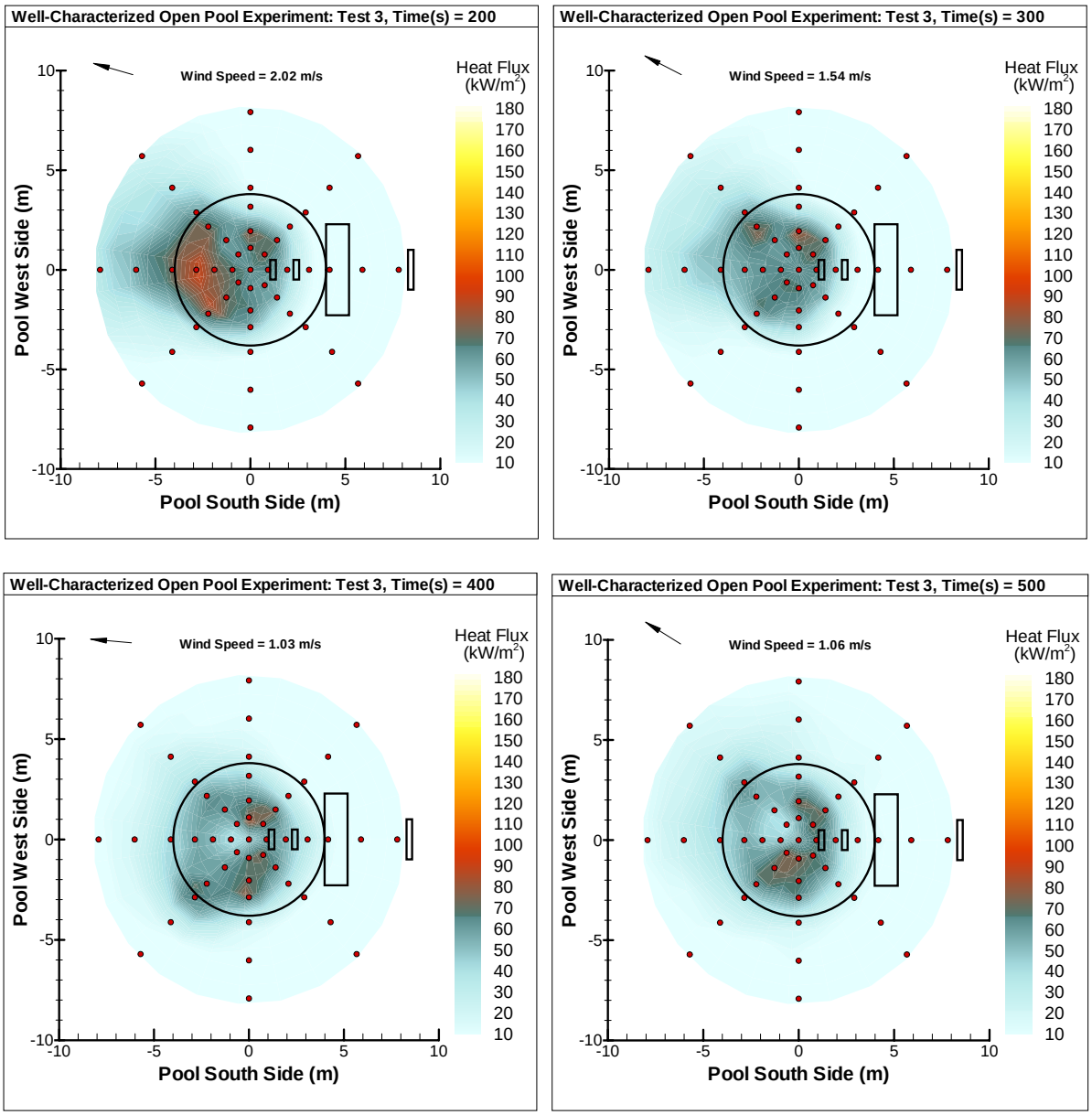

Figure 82. Predicted incident heat fluxes over the pool and terrain surface for Test 3.

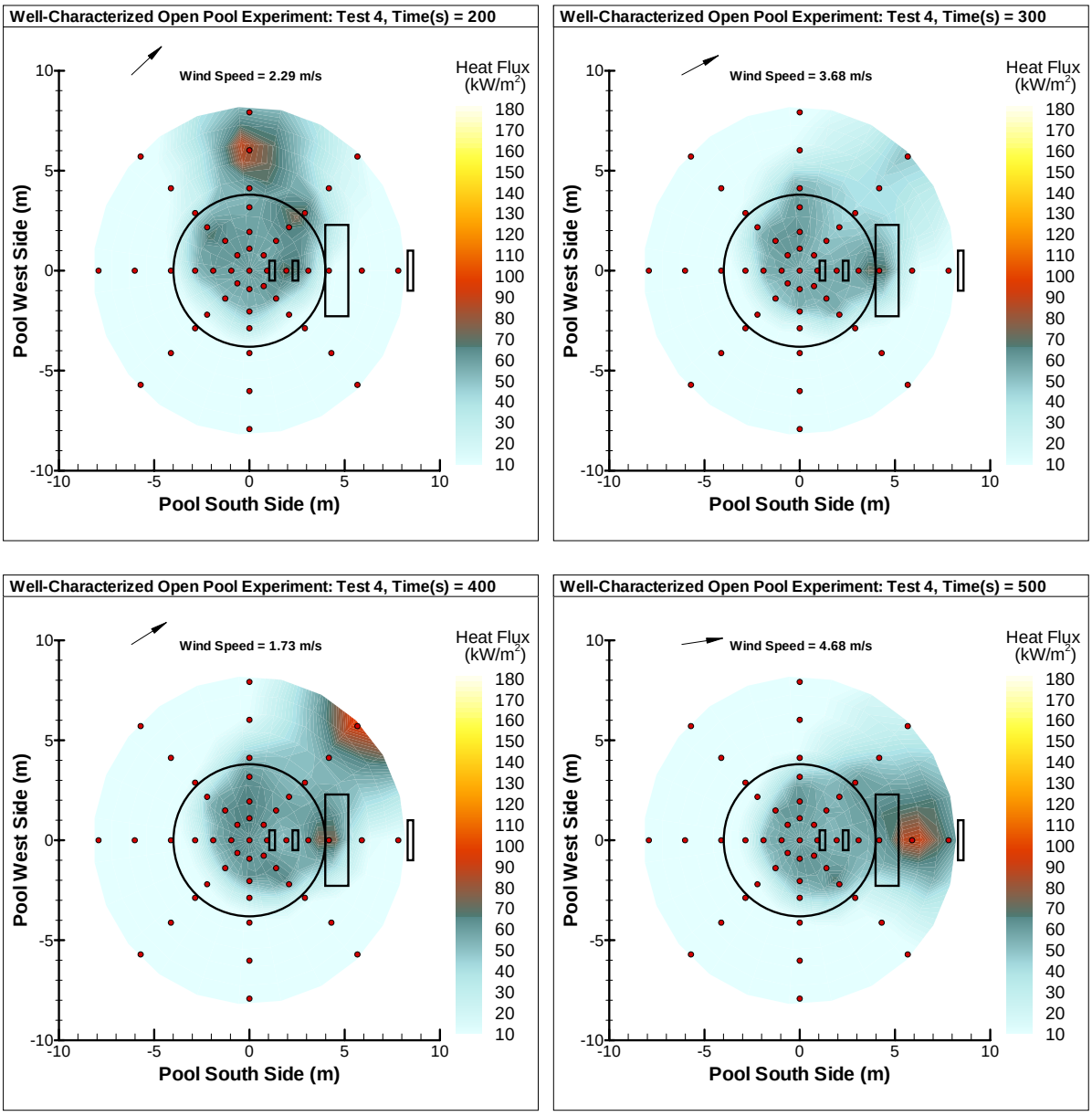

Figure 83. Predicted incident heat fluxes over the pool and terrain surface for Test 4.

Figures 84 and 85 shows predicted incident heat fluxes to the circumference of the large calorimeter in Test 1 and Test 2, respectively. The heat fluxes appear discontinuous because of the Cartesian coordinate system used in Vulcan that allows only horizontal or vertical surfaces. In some areas, vertical and horizontal surfaces are adjacent. Also, areas that are contact surfaces for supports show zero heat flux. Predicted incident heat fluxes to the large calorimeter are approximately 20% lower than measured heat fluxes. In Figure 84, the highest heat fluxes are observed on the west of the large calorimeter. In contrast, in Figure 85, the highest heat fluxes are observed on the bottom of the large calorimeter. Results of Test 2 simulations show the wind having a significantly higher impact on the plume tilt, essentially driving the plume under the large calorimeter for a substantial amount of time. These resulted in higher heat fluxes at or to the bottom of the calorimeter.

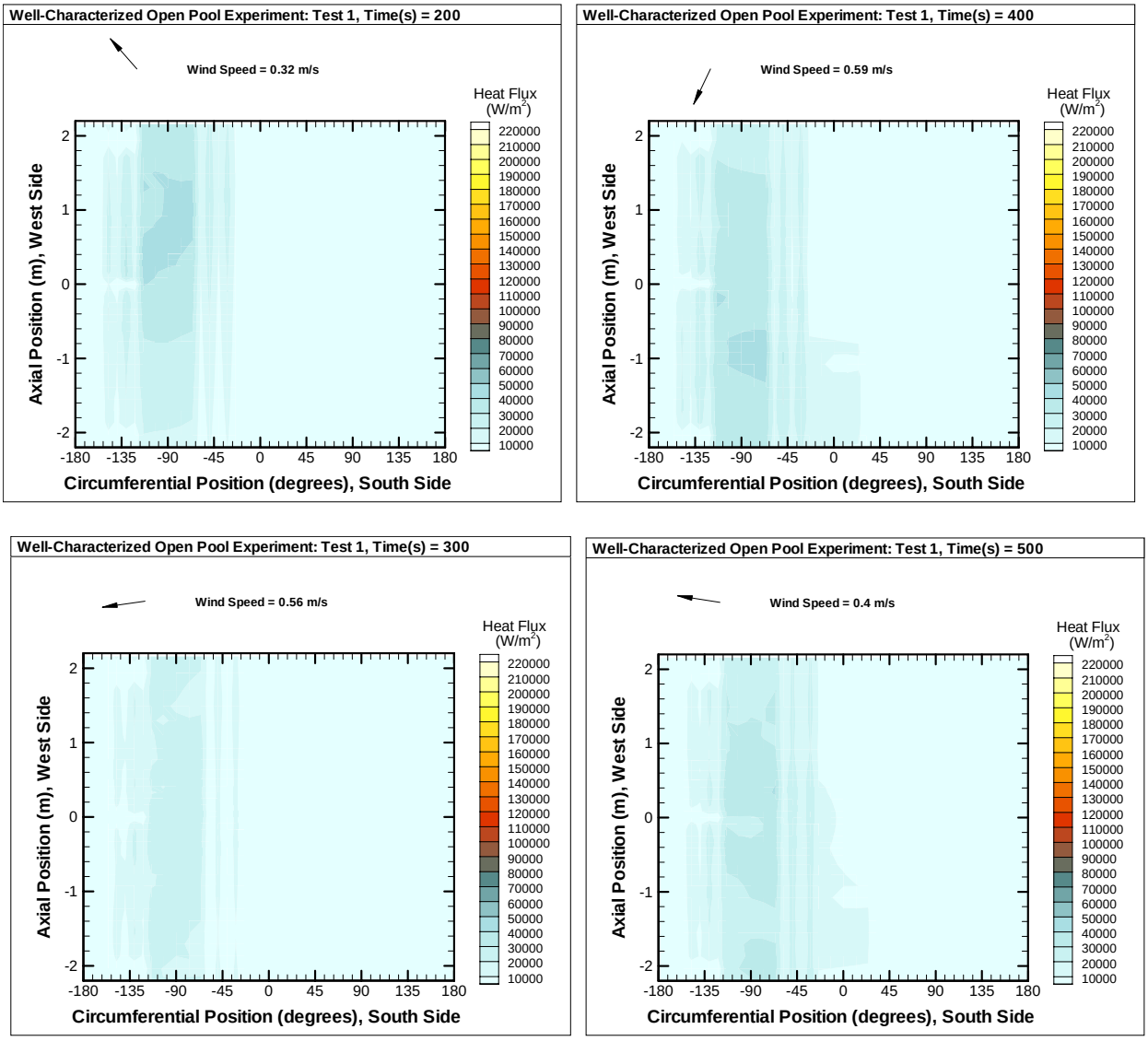

Figure 84. Predicted incident heat fluxes to the large calorimeter in Test 1.

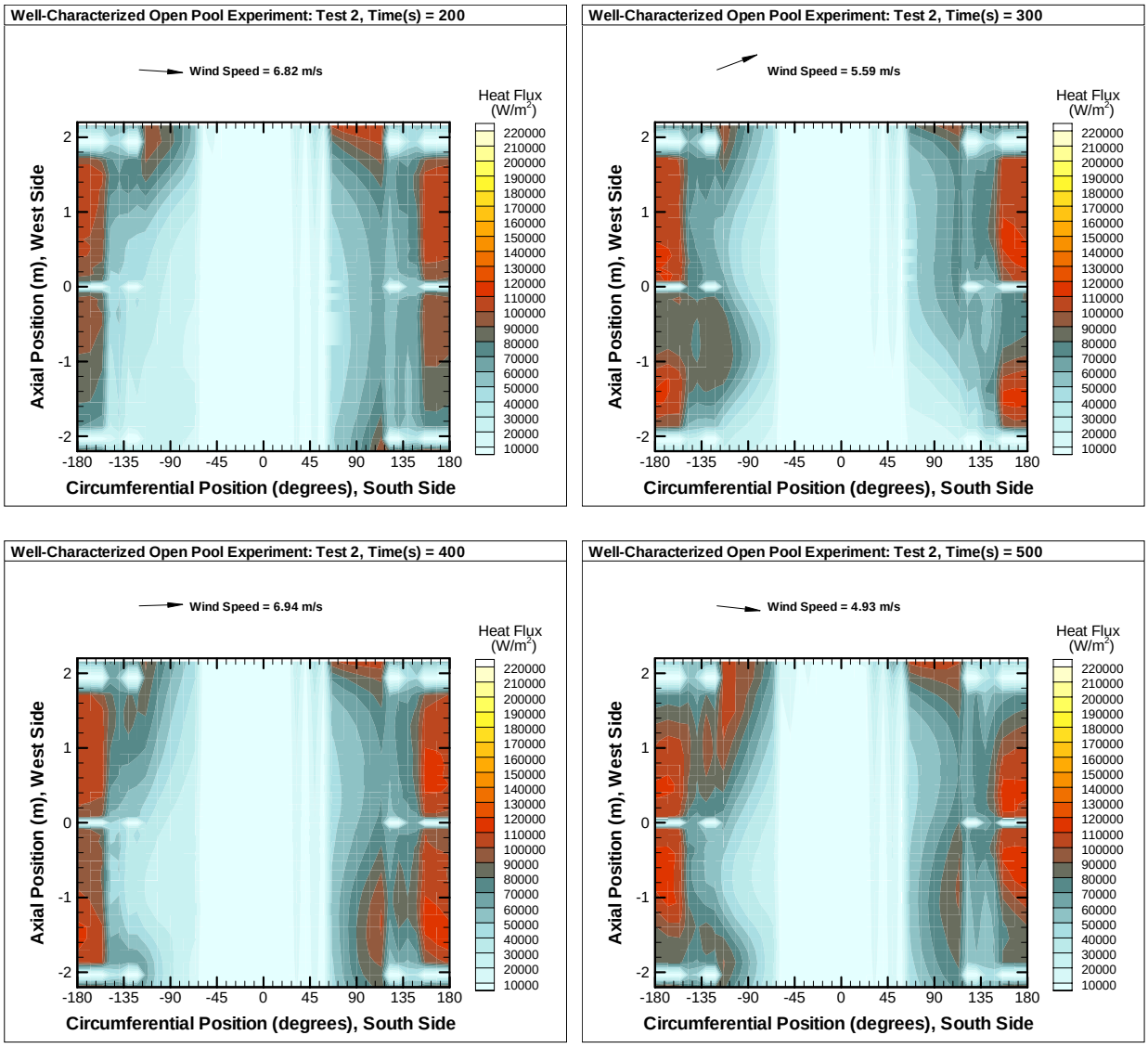

Figure 85. Predicted incident heat fluxes to the large calorimeter in Test 2.

Contour plots of heat fluxes on the skin of the weapon (medium) calorimeter were not generated. Instead, heat flux time series plots were generated to analyze incident heat flux to the medium calorimeters. Figure 86 shows predicted heat fluxes on the center of the calorimeter surface. The labels in the legend correspond to labels shown in Figure 21. As in previous results, average incident heat fluxes were about 20% lower than measured. Note that peak Vulcan heat flux results will be lower than the peak values observed in experiments. Vulcan solves the Reynolds average conservation equation; hence all results presented are averaged over time.

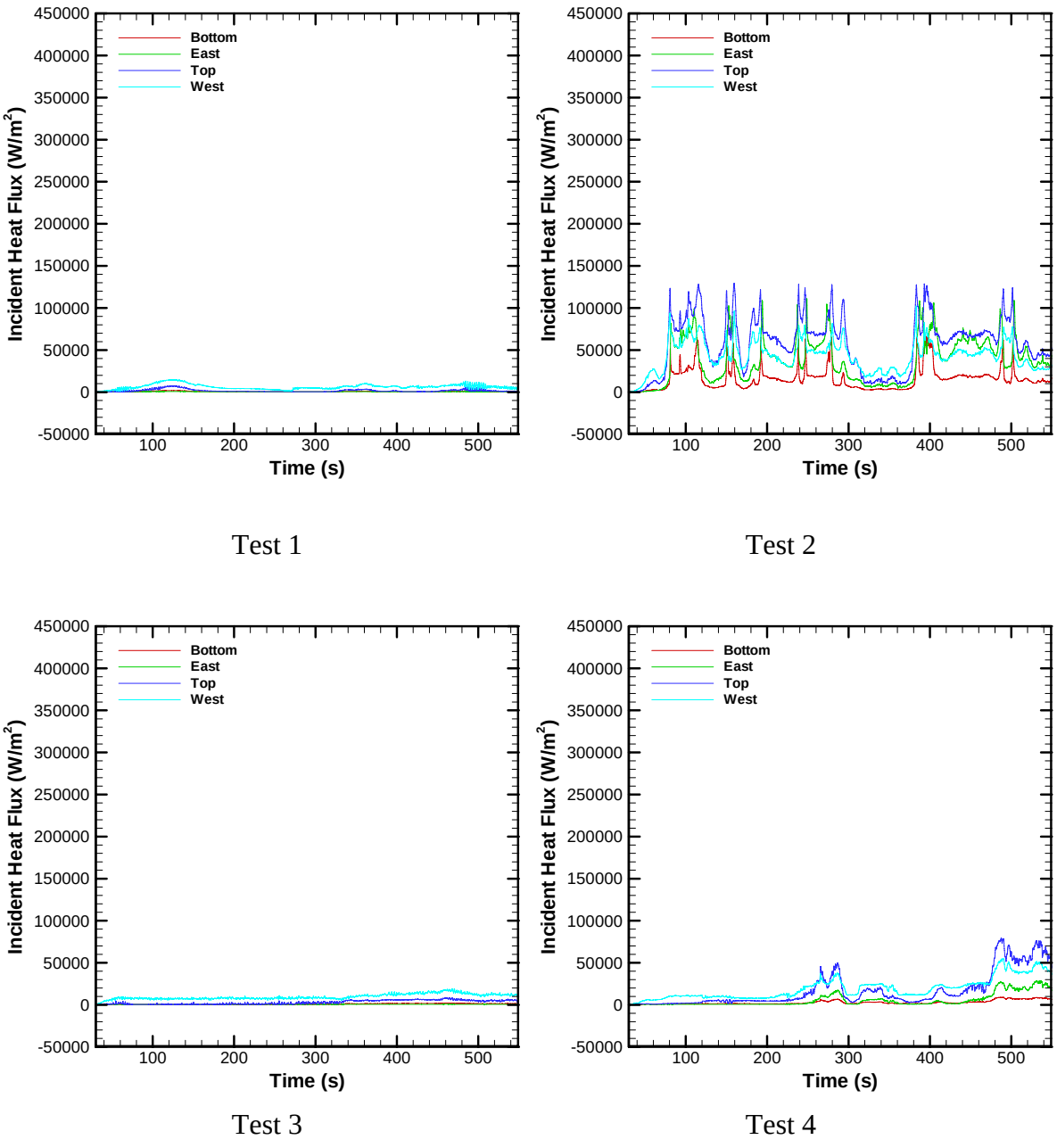

Figure 86. Predicted incident heat fluxes to weapon calorimeter.

Predicted flux values are lower than might be expected based on the experimental data. This elicited an investigation into the reason. Figure 87 shows a plot of maximum predicted soot mass fraction looking down on the fire at 655 seconds for Test 2 (The object outlined in the plot shows the position of the large calorimeter). For reference, a mass fraction of 0.04 corresponds roughly to a volume fraction of 20 ppm. Soot mass fraction varies almost linearly with soot volume fraction. Most of the predicted soot mass fractions fall more than an order of magnitude below this level. Soot is commonly found in high single-digit and double-digit volume fractions (ppm) in large fires of this nature. No soot measurements were taken as part of this test. It is postulated that the soot concentrations are under-predicted for this case, and other similar cases presented herein. This would explain the difference between the predicted and measured incident heat flux values.

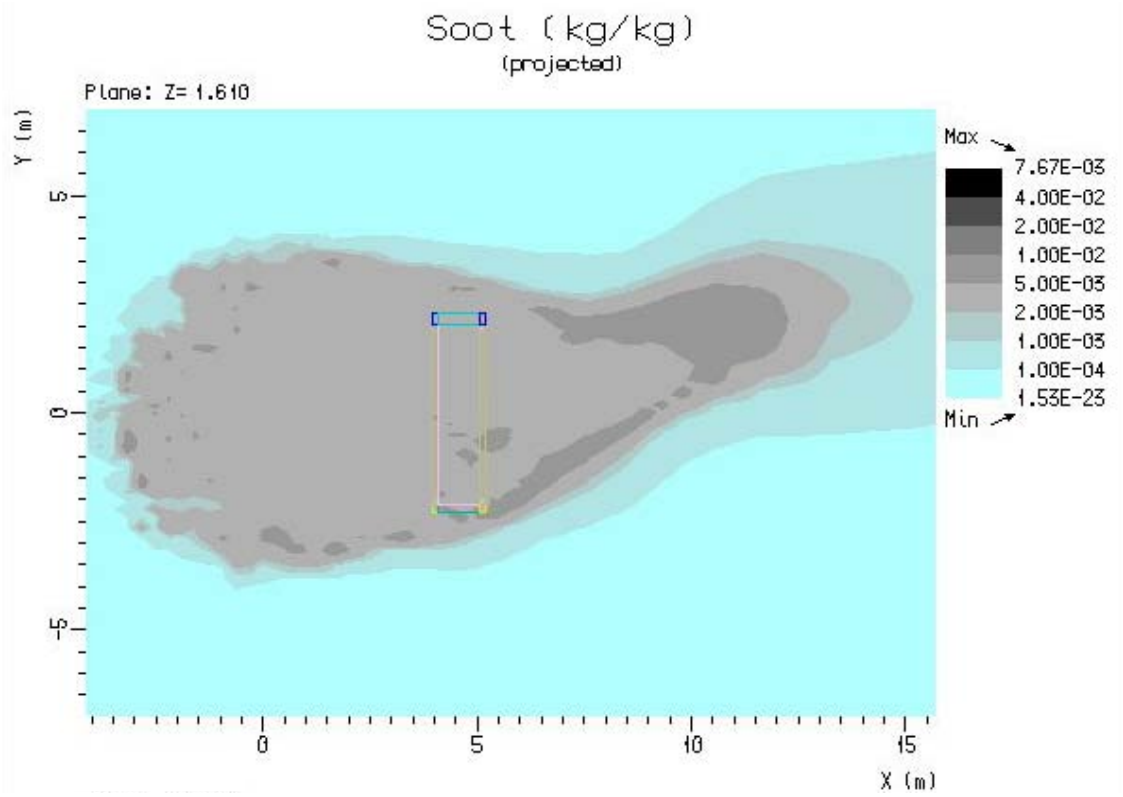

Figure 87. Predicted soot mass fraction at 655s in Test 2.

6 Conclusion

Four Well-Characterized Open Pool fire experiments were conducted by the Fire Science and Technology Department at Sandia National Laboratories. The focus of the Well-Characterized Open Pool fire series was to provide environmental information for open pool fires on a physics first principle basis. This series has provided data of sufficient quality for fire code validation data purposes. The experiments measured the burning rate of liquid fuel in an open pool and the resultant heat flux to a weapon-sized object and the surrounding environment with well-characterized boundary and initial conditions.

The scope of this work included preparation of the 26-ft diameter open pool fire test facility at Sandia's Lurance Canyon Burn Site (Burn Site), installing instrumentation, performing pre-test predictions of the expected environment, performing experiments, performing post-test predictions using the measured boundary conditions, and comparing the post-test predictions with the actual test results.

Results presented in this report included a general description of test observation (pre and post-test), wind measurements, fire plume topology, average fuel recession and heat release rates, and incident heat flux to the pool and to the calorimeters. Average wind conditions are given and were used to identify quasi-steady periods. Heat flux contour plots were generated for quasi-steady periods for the pool and for the large calorimeter.

Results of the experiments show a strong correlation between wind conditions and fuel mass vaporization rate and incident heat flux to the pool and calorimeters. The largest heat fluxes were observed on the large calorimeter and medium calorimeter when crosswinds were at the highest levels. When crosswind velocities were small, the incident heat flux to these calorimeters was much smaller. Results of experiments also showed incident heat flux to the pool is significantly affected by the orientation of the fire plume with respect to the ground normal. For strong crosswinds, the highest heat fluxes were observed on the downwind side of the pool. Significantly smaller incident heat fluxes were observed on the windward side of the pool. When crosswinds were small, the largest incident heat fluxes occurred around ½ the radius of the pool. Much lower heat fluxes were observed at or near the center of the pool, probably a result of an oxygen-starved interior.

Numerical fire simulations were performed using Vulcan fire code. Four calculations were performed, each corresponding to one of the experiments in the test series. These simulations were designed to replicate each of the experiments as close as possible, including the first time use of a time-varying spatially dependent wind boundary condition. Results showed similar trends as seen in the experiments. Incident heat fluxes were approximately 20% less than measured values.

References

1 Tieszen, S.R., V.F. Nicolette, L.A. Gritzo, J.K. Holen, D. Murray, and J.L. Moya, “Vortical Structures in Pool Fires: Observation, Speculation, and Simulation,” SAND96-2607, Sandia National Laboratories, Albuquerque, NM.

2 Gritzo, L.A., V.F. Nicolette, S.R. Tieszen, and J.L. Moya, “Heat Transfer to the Fuel Surface in Large Pool Fires,” Transport Phenomenon in Combustion, S.H. Chan, ed., Taylor and Francis, 1995

3 Nicolette, V.F., L.A. Gritzo, J.L. Moya, and S.R. Tieszen, “Comparison of Large JP4- and JP8-Fueled Pool Fires,” Proceedings of the International Conference on Fire Research and Engineering, Orlando, Florida, September 10-15, 1995, SFPE, Quincy, MA, 1995

4 Gritzo, L.A., W. Gill, and V.F. Nicolette, “Estimates of the Extent and Character of the Oxygen-Starved Interior in Large Pool Fires,” Very Large Scale Fires, ASTM STP 1336, N.R. Keltner, N.J. Alvares, and S.J. Grayson, Eds., American Society for Testing and Materials, 1998

5 Lopez, A.R., L.A. Gritzo, and M.P. Sherman, “Risk Assessment Compatible Fire Models (RACFMs),” SAND Report in Final Preparation. Sandia National Laboratories, Albuquerque, NM

6 Gritzo, L.A., and J.L. Moya, “Fire Characterization and Object Thermal Response for a Series of Tests with a Large Flat Plate Adjacent to Large JP4 Fuel Fire,” SAND97-0047, Sandia National Laboratories, Albuquerque, NM.

7 Gritzo, L.A., and V.F. Nicolette, “Coupling of Large Fire Phenomenon with Object Geometry and Object Thermal Response,” Submitted to Journal of Fire Sciences.

8 Suo-Anttila, J.W., and L.A. Gritzo, “Thermal Measurements from a Series of Tests with a Large Cylindrical Calorimeter on the Leeward Edge of a JP-8 Pool Fire in Cross-Flow,” SAND2001-1986, Sandia National Laboratories, Albuquerque, NM.

9 Gritzo, L.A., V.F. Nicolette, J.L. Moya, R.D. Skocypec, and D. Murray, “Wind-Induced Interaction of a Large Cylindrical Calorimeter and an Engulfing JP8 Pool Fire,” Proceedings of the Symposium on Thermal Sciences in Honor of Chancellor Chang-Lin Tien, Berkeley, CA, November 14, 1995.

10 Suo-Anttila, J.W., and L.A. Gritzo, “Thermal Measurements for a JP-8 Pool Fire in Cross-Flow with a C-141 Fuselage Section Located on the Leeward Edge,” SAND2001-0313, Sandia National Laboratories, Albuquerque, NM, February 2001.

11 Blanchat, T.K, and L. Manning, “Mock B52 Bomb Bay Fire Experiment Data and Analysis for Model Validation and Development,” SAND2002-0145, Sandia National Laboratories, Albuquerque, NM, January 2002.

12 Gill, W., Private communication, Sandia National Laboratories, Albuquerque, NM, July 1997.

13 Drysdale, D., An Introduction to Fire Dynamics (2nd Edition), John Wiley & Sons, New York, page 162, 1998.

14 Reed, R. P., “Improving the Dependability of Critical Thermocouple Thermometry for Fossil Fuel Gasifiers and Retorts,” SAND82-0341, Sandia National Laboratories, July 1982.

15 Acton, R.U., W. Gill, D. Sais, D. Schulze, and J.T. Nakos, "An Investigation of Temperature Measurement Methods in Annealing Reactor Pressure Vessels," SAND96-1179, Sandia National Laboratories, Albuquerque, NM.

16 Omega, “The Temperature Handbook Vol. 28,” Omega Engineering Inc., Stamford, CT, 1992.

17 Gill, W., and J.T. Nakos, “Temperature/Heat Flux Measurement Errors Caused by Thermocouple Shunt Impedance,” accepted by the Ad Hoc Committee on Heat Flux Measurement and Calibration for presentation at the session "Case Studies in Heat Flux Measurements - Successes and Problems" at the 1999 International Mechanical Engineering Congress and Exposition (IMECE), Nashville, TN, November 1999.

18 Blanchat, T.K., L.L. Humphries, and W. Gill, “Sandia Heat Flux Gauge Thermal Response and Uncertainty Models,” SAND2000-1111, Sandia National Laboratories, Albuquerque, NM, May 2000.

19 Nakos, J., J.M Suo-Antilla, and W. Gill, “Shroud boundary condition characterization experiments at the Radiant Heat Facility.”, SAND2004-5080, Sandia National Laboratories, Albuquerque, NM.

20 Brown, A.L. and T.K. Blanchat, “A Validation Quality Heat Flux Dataset for Large Pool Fires.”, Proceedings of HT2003, ASME Summer Heat Transfer Conference, July 23, 2003, Las Vegas, NV.

21 Nakos, J.T., “Uncertainty Analysis of Steady State Incident Heat Flux Measurements in Hydrocarbon Fuel Fires.”, Sandia National Laboratories, SAND2005-7144, 2005

22 Holen, J., M. Brstrom, and B.F. Magnussen, “Finite Difference Calculation of Pool Fires,” Proceedings of the 41st International Instrumentation Symposium, Denver, CO, May 7-11, 1995, pp. 1677-1683.

23 Magnussen, B.F., “The Eddy Dissipation Concept.”, Proceedings of Eleventh Task Leaders Meeting, IEA Working Group on Conservation in Combustion, Lund, Sweden, 1989.

24 Shah, N.G., “The Computation of Radiation Heat Transfer.” Ph.D. Thesis, University of London, Faculty of Engineering, 1979.

25 Tesner, P.A., T.D. Snegiriova, and V.G. Knorre, “Kinetics of Dispersed Carbon Formation.”, Combustion and Flame, Vol. 17, 1971, pp 253-260.

Appendix A List of Instruments

#	Name	Description	Position X (ft)	Position Y (ft)	Position Z (ft)
1	Pan SHFG 0	Pool Surface Heat Flux	0.00	0.00	0.50
2	Pan SHFG 101	Pool Surface Heat Flux	3.13	0.00	0.50
3	Pan SHFG 102	Pool Surface Heat Flux	2.33	-2.33	0.50
4	Pan SHFG 103	Pool Surface Heat Flux	0.00	-3.27	0.50
5	Pan SHFG 104	Pool Surface Heat Flux	-2.21	-2.21	0.50
6	Pan SHFG 105	Pool Surface Heat Flux	-3.27	0.00	0.50
7	Pan SHFG 106	Pool Surface Heat Flux	-2.39	2.39	0.50
8	Pan SHFG 107	Pool Surface Heat Flux	0.00	3.31	0.50
9	Pan SHFG 108	Pool Surface Heat Flux	2.36	2.36	0.50
10	Pan SHFG 201	Pool Surface Heat Flux	6.58	0.00	0.50
11	Pan SHFG 202	Pool Surface Heat Flux	4.55	-4.55	0.50
12	Pan SHFG 203	Pool Surface Heat Flux	0.00	-6.54	0.50
13	Pan SHFG 204	Pool Surface Heat Flux	-4.65	-4.65	0.50
14	Pan SHFG 205	Pool Surface Heat Flux	-6.54	0.00	0.50
15	Pan SHFG 206	Pool Surface Heat Flux	-4.61	4.61	0.50
16	Pan SHFG 207	Pool Surface Heat Flux	0.00	6.65	0.50
17	Pan SHFG 208	Pool Surface Heat Flux	4.66	4.66	0.50
18	Pan SHFG 301	Pool Surface Heat Flux	10.02	0.00	0.50
19	Pan SHFG 302	Pool Surface Heat Flux	7.00	-7.00	0.50
20	Pan SHFG 303	Pool Surface Heat Flux	0.00	-9.88	0.50
21	Pan SHFG 304	Pool Surface Heat Flux	-7.04	-7.04	0.50
22	Pan SHFG 305	Pool Surface Heat Flux	-9.88	0.00	0.50
23	Pan SHFG 306	Pool Surface Heat Flux	-7.12	7.12	0.50
24	Pan SHFG 307	Pool Surface Heat Flux	0.00	10.02	0.50
25	Pan SHFG 308	Pool Surface Heat Flux	6.91	6.91	0.50
26	1R SHFG 401	Terrain Surface Heat Flux	13.50	0.00	0.50
27	1R SHFG 402	Terrain Surface Heat Flux	9.46	-9.46	0.50
28	1R SHFG 403	Terrain Surface Heat Flux	0.00	-13.58	0.50
29	1R SHFG 404	Terrain Surface Heat Flux	-9.43	-9.43	0.50
30	1R SHFG 405	Terrain Surface Heat Flux	-13.46	0.00	0.50
31	1R SHFG 406	Terrain Surface Heat Flux	-9.46	9.46	0.50
32	1R SHFG 407	Terrain Surface Heat Flux	0.00	13.67	0.50
33	1R SHFG 408	Terrain Surface Heat Flux	9.58	9.58	0.50
34	1.5R SHFG 501	Terrain Surface Heat Flux	19.46	0.00	0.50
35	1.5R SHFG 502	Terrain Surface Heat Flux	14.05	-14.05	0.50
36	1.5R SHFG 503	Terrain Surface Heat Flux	0.00	-19.58	0.50
37	1.5R SHFG 504	Terrain Surface Heat Flux	-13.71	-13.71	0.50
38	1.5R SHFG 505	Terrain Surface Heat Flux	-19.67	0.00	0.50
39	1.5R SHFG 506	Terrain Surface Heat Flux	-13.64	13.64	0.50
40	1.5R SHFG 507	Terrain Surface Heat Flux	0.00	19.46	0.50
41	1.5R SHFG 508	Terrain Surface Heat Flux	13.76	13.76	0.50
42	2R SHFG 601	Terrain Surface Heat Flux	25.98	0.00	0.50
43	2R SHFG 602	Terrain Surface Heat Flux	18.40	-18.40	0.50
44	2R SHFG 603	Terrain Surface Heat Flux	0.00	-26.15	0.50
45	2R SHFG 604	Terrain Surface Heat Flux	-18.47	-18.47	0.50

46	2R SHFG 605	Terrain Surface Heat Flux	-26.08	0.00	0.50
47	2R SHFG 606	Terrain Surface Heat Flux	-18.36	18.36	0.50
48	2R SHFG 607	Terrain Surface Heat Flux	0.00	26.02	0.50
49	2R SHFG 608	Terrain Surface Heat Flux	18.56	18.56	0.50
50	#1 SM CAL N	Temperature	North	Intrinsic	4.98 ft from pool center
51	#1 SM CAL N+1	Temperature	North	Internal	0.48 ft above ground plane
52	#1 SM CAL S	Temperature	South	Intrinsic	Sec. 3.3
53	#1 SM CAL S+1	Temperature	South	Internal	
54	#1 SM CAL A	Temperature	Top	Intrinsic	
55	#1 SM CAL B	Temperature	West	Intrinsic	
56	#1 SM CAL C	Temperature	Bottom	Intrinsic	
57	#1 SM CAL D	Temperature	East	Intrinsic	
58	#1 SM CAL 1	Temperature	Top	Internal	
59	#1 SM CAL 2	Temperature	West	Internal	
60	#1 SM CAL 3	Temperature	Bottom	Internal	
61	#1 SM CAL 4	Temperature	East	Internal	
62	#2 SM CAL N	Temperature	North	Intrinsic	8.23 ft from pool center
63	#2 SM CAL N+1	Temperature	North	Internal	0.58 ft above ground plane
64	#2 SM CAL S	Temperature	South	Intrinsic	Sec. 3.3
65	#2 SM CAL S+1	Temperature	South	Internal	
66	#2 SM CAL A	Temperature	Top	Intrinsic	
67	#2 SM CAL B	Temperature	West	Intrinsic	
68	#2 SM CAL C	Temperature	Bottom	Intrinsic	
69	#2 SM CAL D	Temperature	East	Intrinsic	
70	#2 SM CAL 1	Temperature	Top	Internal	
71	#2 SM CAL 2	Temperature	West	Internal	
72	#2 SM CAL 3	Temperature	Bottom	Internal	
73	#2 SM CAL 4	Temperature	East	Internal	
74	B Cal Center	Temperature	Center	Internal	
75	C Cal Center	Temperature	Center	Internal	
76	Weapon Cal 1	Temperature	East Internal	27.75 ft from pool center	
77	Weapon Cal 2	Temperature	Internal	0.5 ft above ground plane	
78	Weapon Cal 3	Temperature	Top Internal	Sec. 3.5	
79	Weapon Cal 4	Temperature	Internal		
80	Weapon Cal 5	Temperature	West Internal		
81	Weapon Cal 6	Temperature	Internal		
82	Weapon Cal 7	Temperature	Bottom		

			Internal		
83	Weapon Cal 8	Temperature	Internal		
84	LG Cal 101	Temperature		13 ft from pool center	
85	LG Cal 102	Temperature		3 ft above ground plane	
86	LG Cal 103	Temperature		Sec. 3.4	
87	LG Cal 104	Temperature			
88	LG Cal 105	Temperature			
89	LG Cal 106	Temperature			
90	LG Cal 107	Temperature			
91	LG Cal 108	Temperature			
92	Ambient Bunker	Equipment Temperature			
93	LG Cal 201	Temperature			
94	LG Cal 202	Temperature			
95	LG Cal 203	Temperature			
96	LG Cal 204	Temperature			
97	LG Cal 205	Temperature			
98	LG Cal 206	Temperature			
99	LG Cal 207	Temperature			
100	LG Cal 208	Temperature			
101	LG Cal 209	Temperature			
102	LG Cal 210	Temperature			
103	LG Cal 211	Temperature			
104	LG Cal 212	Temperature			
105	LG Cal 213	Temperature			
106	LG Cal 214	Temperature			
107	LG Cal 215	Temperature			
108	LG Cal 216	Temperature			
109	LG Cal Inner 201	Temperature			
110	LG Cal Inner 202	Temperature			
111	LG Cal Inner 203	Temperature			
112	LG Cal Inner 204	Temperature			
113	LG Cal Inner 205	Temperature			
114	LG Cal Inner 206	Temperature			
115	LG Cal Inner 207	Temperature			
116	LG Cal Inner 208	Temperature			
117	LG Cal Inner 209	Temperature			
118	LG Cal Inner 210	Temperature			
119	LG Cal Inner 211	Temperature			
120	LG Cal Inner 212	Temperature			
121	LG Cal Inner 213	Temperature			
122	LG Cal Inner 214	Temperature			
123	LG Cal Inner 215	Temperature			
124	LG Cal Inner 216	Temperature			
125	LG Cal 301	Temperature			
126	LG Cal 302	Temperature			
127	LG Cal 303	Temperature			

128	LG Cal 304	Temperature			
129	LG Cal 305	Temperature			
130	LG Cal 306	Temperature			
131	LG Cal 307	Temperature			
132	LG Cal 308	Temperature			
133	LG Cal 401	Temperature			
134	LG Cal 402	Temperature			
135	LG Cal 403	Temperature			
136	LG Cal 404	Temperature			
137	LG Cal 405	Temperature			
138	LG Cal 406	Temperature			
139	LG Cal 407	Temperature			
140	LG Cal 408	Temperature			
141	LG Cal 409	Temperature			
142	LG Cal 410	Temperature			
143	LG Cal 501	Temperature			
144	LG Cal 502	Temperature			
145	LG Cal 503	Temperature			
146	LG Cal 504	Temperature			
147	LG Cal 505	Temperature			
148	FUEL RAKE 1	Recession and Temperature	Bottom TC	SE pool edge	
149	FUEL RAKE 2	Recession and Temperature			
150	FUEL RAKE 3	Recession and Temperature			
151	FUEL RAKE 4	Recession and Temperature			
152	FUEL RAKE 5	Recession and Temperature			
153	FUEL RAKE 6	Recession and Temperature			
154	FUEL RAKE 7	Recession and Temperature			
155	FUEL RAKE 8	Recession and Temperature			
156	FUEL RAKE 9	Recession and Temperature			
157	FUEL RAKE 10	Recession and Temperature			
158	FUEL RAKE 11	Recession and Temperature			
159	FUEL RAKE 12	Recession and Temperature			
160	FUEL RAKE 13	Recession and Temperature			
161	FUEL RAKE 14	Recession and Temperature			
162	FUEL RAKE 15	Recession and Temperature			
163	FUEL RAKE 16	Recession and Temperature			
164	FUEL RAKE 17	Recession and Temperature			
165	FUEL RAKE 18	Recession and Temperature			
166	FUEL RAKE 19	Recession and Temperature			
167	FUEL RAKE 20	Recession and Temperature			
168	FUEL RAKE 21	Recession and Temperature			
169	FUEL RAKE 22	Recession and Temperature			
170	FUEL RAKE 23	Recession and Temperature			
171	FUEL RAKE 24	Recession and Temperature			
172	FUEL RAKE 25	Recession and Temperature			
173	FUEL RAKE 26	Recession and Temperature			
174	FUEL RAKE 27	Recession and Temperature			
175	FUEL RAKE 28	Recession and Temperature			
176	FUEL RAKE 29	Recession and Temperature			
177	FUEL RAKE 30	Recession and Temperature	Top TC		

178	Fuel Rake Box temp	Equipment Temperature			
179	Weapon Cal 1	Temperature	East Intrinsic	27.75 ft from pool center	
180	Weapon Cal 2	Temperature	Intrinsic	0.5 ft above ground plane	
181	Weapon Cal 3	Temperature	Top Intrinsic	Sec. 3.5	
182	Weapon Cal 4	Temperature	Intrinsic		
183	Weapon Cal 5	Temperature	West Intrinsic		
184	Weapon Cal 6	Temperature	Intrinsic		
185	Weapon Cal 7	Temperature	Bottom Intrinsic		
186	Weapon Cal 8	Temperature	Intrinsic		
187	Gardon 1	Terrain Surface Heat Flux	Adjacent SHFG 407		
188	Gardon 2	Terrain Surface Heat Flux	Adjacent SHFG 408		
189	Gardon 3	Terrain Surface Heat Flux	Adjacent SHFG 401		
190	Gardon 4	Terrain Surface Heat Flux	Adjacent SHFG 402		
191	Gardon 5	Terrain Surface Heat Flux	Adjacent SHFG 403		
192	Gardon 6	Terrain Surface Heat Flux	Adjacent SHFG 407		
193	Gardon 7	Terrain Surface Heat Flux	Adjacent SHFG 408		
194	Gardon 8	Terrain Surface Heat Flux	Adjacent SHFG 501		
195	Gardon 9	Terrain Surface Heat Flux	Adjacent SHFG 502		
196	Gardon 10	Terrain Surface Heat Flux	Adjacent SHFG 503		
197	Gardon 11	Terrain Surface Heat Flux	Adjacent SHFG 507		
198	Gardon 12	Terrain Surface Heat Flux	Adjacent SHFG 508		
199	Gardon 13	Terrain Surface Heat Flux	Adjacent SHFG 601		
200	Gardon 14	Terrain Surface Heat Flux	Adjacent SHFG 602		
201	Gardon 15	Terrain Surface Heat Flux	Adjacent SHFG 603		
202	Weapon Gardon 1	Weapon Calorimeter Heat Flux	East Internal	27.75 ft from pool center	
203	Weapon Gardon 2	Weapon Calorimeter Heat Flux	Internal	0.5 ft above ground	

				plane	
204	Weapon Gardon 3	Weapon Calorimeter Heat Flux	Top Internal	Sec. 3.5	
205	Weapon Gardon 4	Weapon Calorimeter Heat Flux	Internal		
206	Weapon Gardon 5	Weapon Calorimeter Heat Flux	West Internal		
207	Weapon Gardon 6	Weapon Calorimeter Heat Flux	Internal		
208	Weapon Gardon 7	Weapon Calorimeter Heat Flux	Bottom Internal		
209	Weapon Gardon 8	Weapon Calorimeter Heat Flux	Internal		
210	D/P Setra	Recession (0-15 inches)		SE pool edge	
211	Igniter	Fuel Ignition		SE pool edge	
212	D/P Rosemount	Recession (0-25 inches)		SE pool edge	
213	Wind Tower 1	Ultrasonic Wind Measurements	-92	-99	6.56, 16.40, 32.81
214	Wind Tower 2	Ultrasonic Wind Measurements	-93	-30	6.56, 16.40, 32.81
215	Wind Tower 3	Ultrasonic Wind Measurements	-95	30	6.56, 16.40, 32.81
216	Wind Tower 4	Ultrasonic Wind Measurements	-95	100	6.56, 16.40, 32.81
217	Wind Bird	Vane-Type Wind Measurements	between Towers 3 and 4		
218	Camera 1	Flame Topology	20	208	17.7
219	Camera 2	Flame Topology	177	167	23.9
220	Camera 3	Flame Topology	303	-5	21.1
221	Camera 4	Flame Topology	152	-105	13.4
222	Camera 5	Flame Topology	19	-168	6.7

Appendix B Optical Observations of the Fall 2003 Sandia Open Pool Fire Tests

By Charles C Allen
Northrop Grumman Information Technology

Supporting
Sandia National Laboratory For the Defense Threat Reduction Agency
March 31, 2004

INTRODUCTION

In the fall of 2003 Sandia National Laboratories conducted four well instrumented aviation fuel open pool burn tests under two different metrological conditions and test setups. A portion of the instrumentation consisted of five video cameras placed between 200 and 300 feet North, Northeast, East, Southeast and South of the pool. The fire had enough fuel to burn approximately 20 minutes over which time all cameras operated nominally.

In order to get quantitative measurements from the images, each camera had two fiducials in the field of view (FOV). The fiducials were two-foot square markers with an alternating black and white square pattern in them. They were placed approximately 30-feet away from the cameras and separated so that they were in the lower left and right corners of the FOV of the camera. The cameras, fiducials, and various points of interest around the test site were surveyed and recorded.

The cameras took images in standard 480 x 512 pixel US format at 30 frames per second. The automated spark to start the fire was placed so each camera could see the ignition that provided the start time hack for each camera. For each test, each frame from each camera was converted to JPEG format (and stored on CDs) for post processing. In addition, a digital movie was produced in MPEG format (and stored on CDs). These electronic files were analyzed to define fire and plume structures of interest. Triangulation with two cameras was performed to calculate structure sizes. The movies were reviewed to estimate the timing for certain changes in the plume.

This report describes the process and results of the four tests. Approximately 100 image pairs were analyzed for each test. A select few are presented here (all of the images are included in the full Appendix on the attached CD).

The background is a quick tutorial on the functioning of a digitization process of a video camera and how calculations are made for tilt and field of view using the triangulation process in order to size and locate structure in an image. Following the background are the discussions of the optical analyses from each test.

BACKGROUND

Figure 1 shows the relative layout of a five-camera suite surrounding an open pool circular fire pit with a large calorimeter to the east and weather vanes to the west. Each camera has two fiducials in the field of view for calibration. All cameras were set to observe the automated fire lighting system on the SW edge of the pool to act as time synchronization.

In order to quantify structure in a FOV of a digitized image it is important to understand several concepts. A camera views a scene through its optics such that the image is placed onto a flat focal plane array that is perpendicular to the bore sight of the camera. The bore sight is a perpendicular line from the center of the focal plane outward. Therefore if the image is stored on a standard 480 vertical by 512 horizontal pixels the bore sight may be found on the image by locating the 240 by 256 pixel. The image far removed from this bore sight is subject to distortion, which must be corrected. Since the standard TV image is in a ratio of 3 vertical by 4 horizontal, typical pixels in the camera are not square. In fact they are in a ratio of 0.8 vertical by 1 horizontal, therefore using the image straight from the television screen, requires accounting for this ratio in order to get proper measurements.

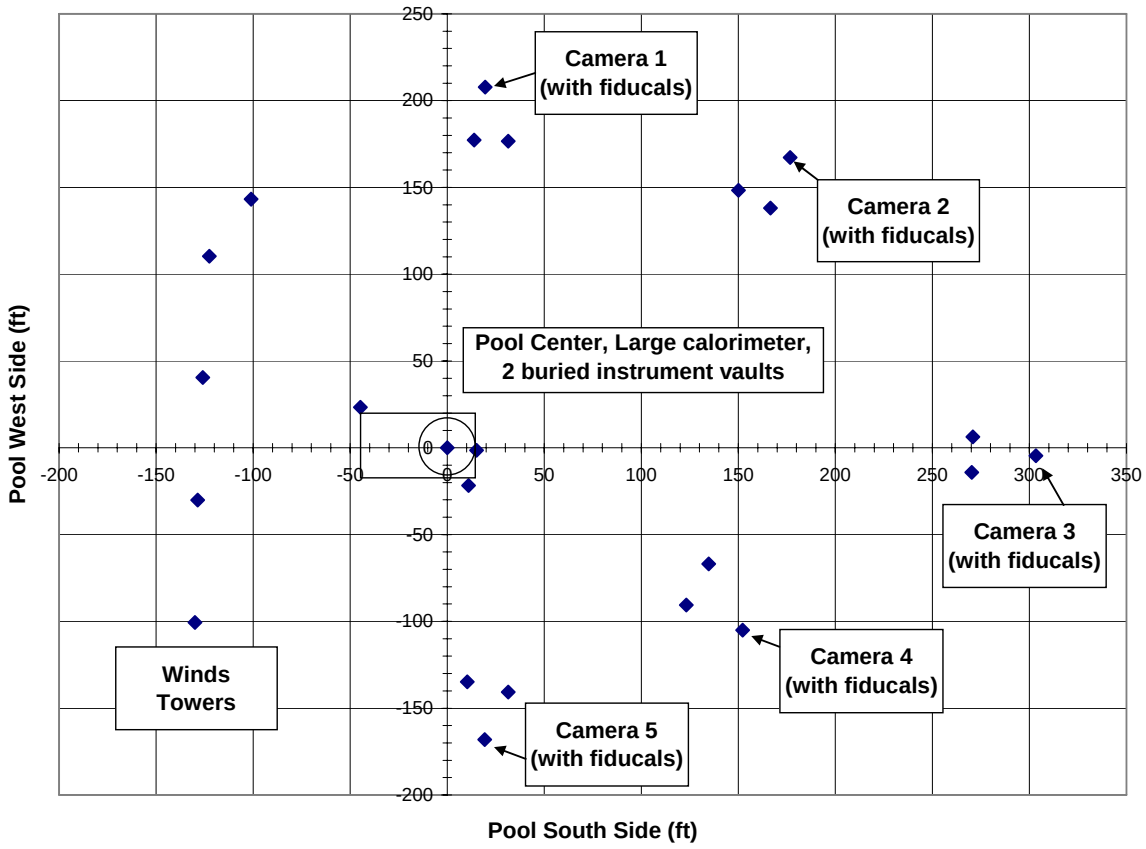

Figure 1. Camera Layout in the Large Open Pool Experiments.

Forcing the digitization process to reformat the image into 480 vertical by 640 horizontal pixels gives square pixels (when tied to the 3:4 image). Because of the parallax, distances are not the same in the FOV. However, common angles are the same across the FOV. This gives the opportunity to calculate linear measurements by use of a concept instantaneous field of view (IFOV). IFOV is the angular degrees per pixel calculated by dividing the extent of the FOV in the image by the total pixel count.

The analyses used the pixel location of a common point on the left and right fiducial with the measured angle between the camera and the fiducials (using the law of cosines). If the range to a point is known, then it is simple trigonometry to calculate to the distance off bore sight. To obtain the range, two nearly orthogonal cameras view a common point from whence triangulation is calculated. Since the ground zero of the fire (the middle of the circular pit) or any other point in the field of view from the survey is known, the distance from that point to any other point in the field of view can be obtained from trigonometric calculations.

In Test 1, the East and South cameras were used for the triangulation, although the images were excellent from the other two sets available (North and East pair and Northeast and Southeast pair). The geometry is shown in Figure 2. As an example of how to measure an angle to point Y, select the difference in pixel count of Y to X in the horizontal and multiply by the IFOV for Camera B. Since the triangle ABX is known from the survey, triangle ABY is easily calculated.

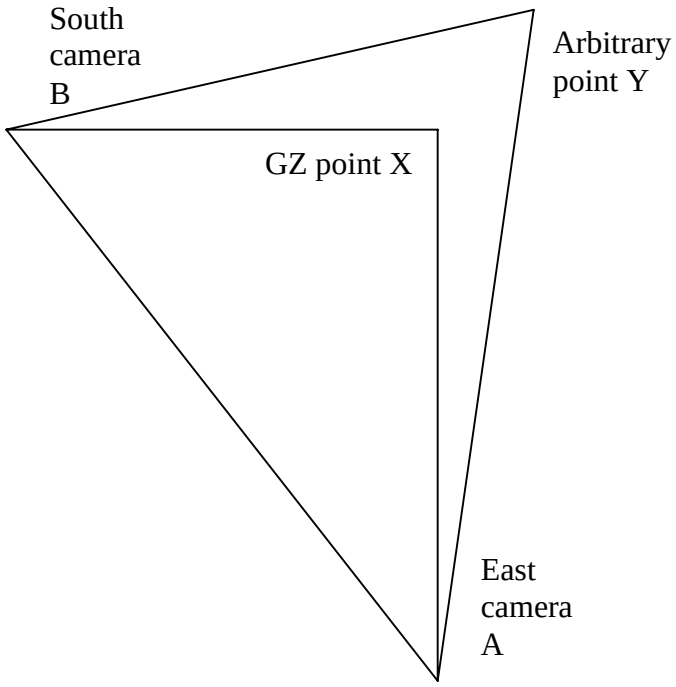

Figure 2. Geometry of Triangulation.

Next, note that the cameras are not at the same relative heights as ground zero and their bore sights are tilted. Therefore, the perceived vertical distances need to be corrected. Fore these tests, both cameras were higher than ground zero and had positive (upward looking) bore sights.

A typical geometry is shown in Figure 3. Using the Law of Sines as shown in Figure 3, variance due to the tilt for each camera is adjusted.

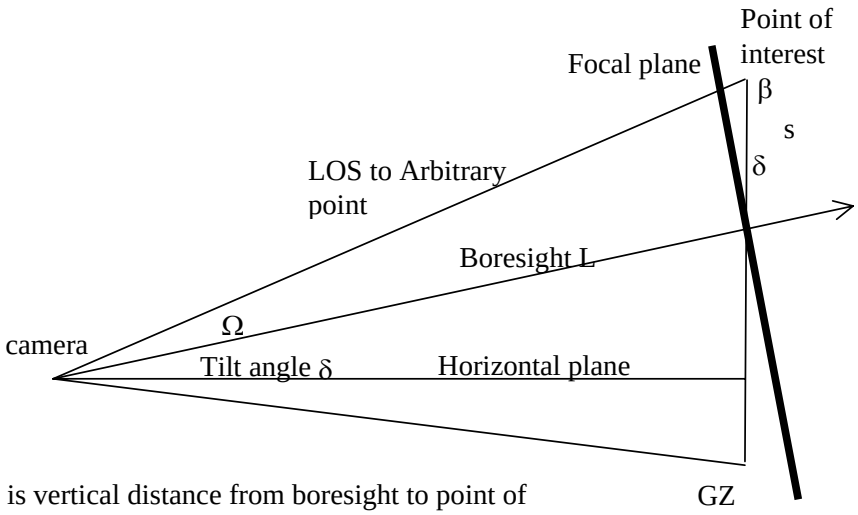

S is vertical distance from boresight to point of interest. Total distance adds the distance the boresight is over the GZ to GZ

For $\Omega>0$, $\beta = 180-(90+\delta)-\Omega$

$\sin\beta/L = \sin\Omega/s$ or $s = L \sin\Omega/\sin\beta$

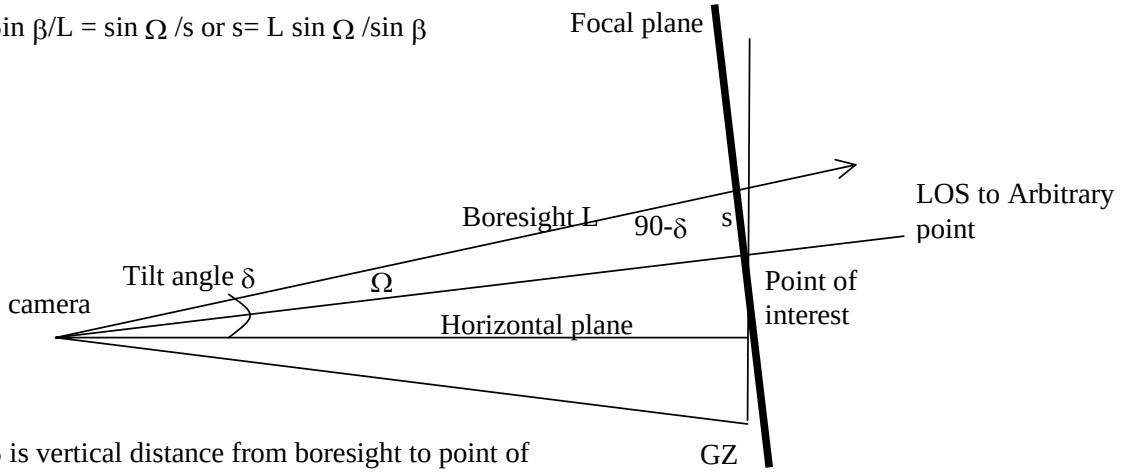

S is vertical distance from boresight to point of interest. Total distance subtracts S from the distance the boresight is over the GZ to GZ

For $\Omega<0$, $\beta = 180-(90-\delta)-\Omega$

$\sin\beta/L = \sin\Omega/s$ or $s = L \sin\Omega/\sin\beta$

Figure 3. Geometry for the Law of Sines.

One of the goals of the following analyses was to determine the flame plume height. This was assumed to be the height vertical position where glowing combustion products can be seen. Note that glowing carbon particles have a temperature of at least 900ºC.

Furthermore, it is difficult to get an exact common location between the two cameras even though the common time frames (when the plume is viewed from two orthogonal locations) is easily obtained. The skill of the analyst skill is important in picking the common location as seen from two views. There is some error associated with this process but the trigonometry helps the analyst get the common height and then he can estimate the location on the height plane where the two views see the same point based on the structure seen in the camera frame. Therefore the error typically is no more than a few inches. The measurements are reported to the closest half foot from the computer calculation to account for the uncertainty).
The first frame was chosen to be the frame immediately prior to pool ignition. The time for each frame is calculated as $1/30^{th}$ of a second times the number of the frame. For example, frame F4C4000030 is Test 4 Camera 4 (SE camera) and is the frame 1 second after the first frame.

For the timing studies to obtain the puff frequency, a duration of 15-25 seconds was chosen (starting at 1 minute 30 seconds after the movie clip began). However, the movie clips did not start at ignition. For Test 1, Camera 3 had a 20 second delay to ignition; Test 1, Camera 5 had a 21 second delay; Test 3 Camera 2, a 27 second delay; and Test 3 Camera 4, a 27 second delay. Since the puff count was sampled on the half minute (based on the movie clip timer), the samples overlap, but are not necessarily for the exact same time span.

A puff occurs when the rising combustion products roll and form a torus. Sometimes that occurred near the fire base and at other times the fire seems to almost jet up the smoke plume and only form tori higher and slightly later in time. The estimates from two cameras for the same test may not give the same exact number of puffs over the same time because the plume looks different from different angles, thus a puff generated on one side may not be seen from the other side until much later. The chaotic nature of a puff introduces uncertainty in the measurement. For these analyses, an average and a standard deviation were determined based on all the data from two cameras.

The precision of this technique can be calculated by using a common location located in the fields of view of each camera. The 4-foot round, 15-foot long large calorimeter next to the burn pool (with a known distance of 7 feet from ground to the calorimeter top) was ideal for this purpose. Precision is a function of the distance from object. Note that the pixels in the data files have been recast from a 480 by 512 format by computer software to a 480 by 640 pixel count, yielding a limit of precision of 1-2 pixels. For Test 1 the East camera data suggested the length of the calorimeter was 15.1 feet and the height was 6.69 feet to the top from the ground. Adding one pixel to the height and length resulted in a height of 7.08 feet and a length of 15.53 feet, yielding a precision of about 0.4 feet in each direction. The South camera data suggested the width of the calorimeter was 3.56 feet and a height of 6.72 feet; adding one pixel resulted in a height of 6.97 feet and a width of 3.8 feet for a precision of about 0.25 feet. The reason for the difference is the South camera is about 170 feet away while the East camera is about 300 feet away, the apparent pixel linear sizes are smaller for the South camera.

Test 1

For Test 1, there were three parameters to be determined from the camera data. The first was the plume formation that includes the puffing frequency (or formation of tori). The second was the height of the flame plume. The third was to identify flame impingement time and duration on the large calorimeter near the fire pool. There winds were near-calm; the fire plume rose essentially vertically for the 20 minutes of the burn. Table 1 gives the results of the puff analysis yielding a frequency of 0.56 puffs/sec with a standard deviation of 0.1.

Table 1. Test 1 Puff Count

Camera	Time start (minutes)	Time stop (minutes)	Number of puffs	Puffs/sec
C1	1.5	1.750	9	0.60
	2.5	2.883	11	0.48
	3.5	3.783	9	0.53
	4.5	4.817	9	0.47
	5.5	5.817	10	0.53
	6.5	6.967	11	0.39
	7.5	7.833	8	0.40
	8.5	8.800	8	0.44
	9.5	9.767	8	0.50
	10.5	10.783	8	0.47
	11.5	11.767	8	0.50
	12.5	12.733	8	0.57
	13.5	13.717	8	0.62
	14.5	14.783	9	0.53
	15.5	15.750	9	0.60
C3	1.5	1.667	8	0.80
	2.5	2.683	8	0.73
	3.5	3.733	10	0.71
	4.5	4.800	11	0.61
	5.5	5.867	12	0.55
	6.5	6.783	11	0.65
	7.5	7.750	8	0.53
	8.5	8.750	8	0.53
	9.5	9.767	8	0.50
	10.5	10.767	8	0.50
	11.5	11.767	10	0.62
	12.5	12.817	9	0.47
	13.5	13.733	10	0.71
	14.5	14.767	9	0.56
	15.5	15.767	10	0.62

Many puffs formed tori that were parallel to the ground, but some had one side or the other higher. These tori were generally stable in shape for a few seconds and rose with the buoyant velocity of the heated combustion products. The tori were between 7-15 feet in vertical dimension and were about 30 ft in diameter, slightly larger than the pool fire source (26 ft diameter). Sometimes the outside of the torus would glow. In most case there tori would present as rolls of black smoke.

Following ignition, the fire took about 1.5 minutes to completely engulf the fire pool area and then it took to an additional 7 minutes before the fire achieved steady-state conditions (a constant height). However, after about 2 minutes the flame plume was about 50 percent of its final state. Figure 4 shows the peak height of the flame plume as determined from the glowing combustion products. There were occasional flaring up where the glowing products reached to a very high distance (as seen in the 14-minute observation) but on average the glow products reached about 50-60 feet high. It would vary as the turbules moved through or a light breeze interacted with the plume and moved the top of the dome. The average flame height was 63.3 ft with a standard deviation of 13.4 ft.

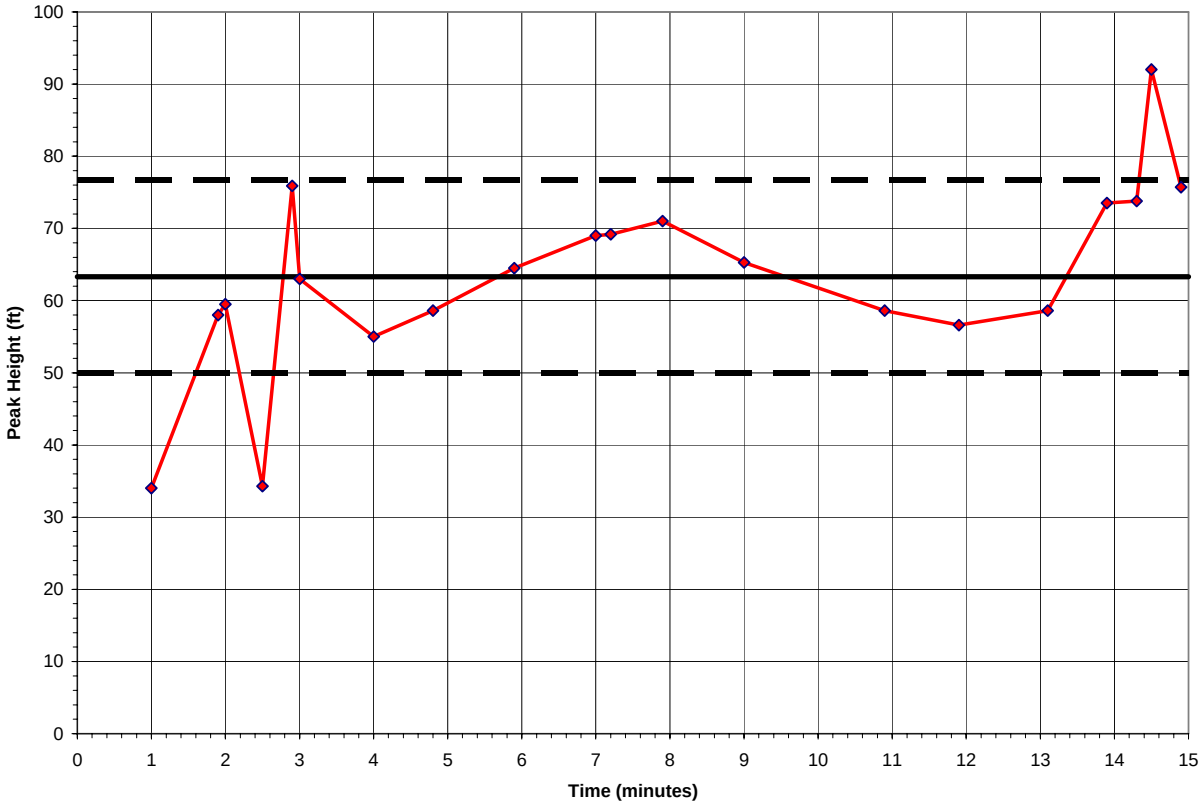

Figure 4. Peak Height of the Flame Plume from Test 1

After the pool was fully engulfed, flames could be seen impinging and engulfing the front of the large calorimeter. The MPEG file from the South camera was reviewed to determine flame impingement times in order to compare the calorimeter sensor readings with the observed time of engulfing. The time spans of the flame impingement on the large calorimeter are given in Table 3.

Table 3 Flame impingement times on the large calorimeter in Test 1

Flame impingement time span	Time in Hr:Min:Sec
Start Time	Stop Time
00:01:38	00:01:52
00:02:13	00:02:24
00:02:41	00:02:42
00:02:44	00:02:45
00:02:47	00:02:54
00:02:59	00:03:01
00:03:33	00:03:34
00:03:38	00:03:43
00:03:47	00:03:49
00:03:51	00:03:54
00:04:01	00:04:04
00:04:07	00:04:13
00:04:17	00:04:20
00:04:49	00:04:51
00:05:49	00:05:52
00:05:56	00:06:03
00:08:00	00:08:02
00:08:11	00:08:15
00:08:23	00:08:26
00:09:07	00:09:15
00:09:24	00:09:30

The following figures present some of the views from the South and East cameras. The first two images are at 1 minute after the start of the fire. It should be noted that the time on the image is from the internal timer on the cameras and they were not synced. The frame count from initial flame spark for both cameras is the same 1800 frame offset. The pool is only half engulfed. The top image is from the South camera and shows three turbules. The lowest one is the slight bulge just above the pool, the next one is measured in the image as is the third one, where only a little portion of the glowing combustion products remain. The lower image is from the East camera and shows the 15-foot calorimeter obscuring the lower portion of the flame pool. The smoke plume is and remains fairly symmetric, but it is difficult to pick exactly the same portion of the glowing cloud with the non-symmetric obscurations from the darkened combustion products. This is confirmed by the height measurements at the top of the cloud where the last glow is observed. The South and East cameras show the 34-foot height of the glowing plume.

In the 1.9-minute picture pair, a plume height of 58.5 ft was determined. The South camera view shows flame impingement on the large calorimeter.

In the 2-minute images, a well-developed flame pool with a tilted turbule is measured. It is slightly elongated in the North South direction by about 5 feet. Due to the tilt of the turbule, it is about 25-feet high on the west side and 14 feet on the northeastern side. There is an error in locating a point in a glowing dynamic cloud from two viewing points because the glow is not necessarily seen from both directions. The horizontal location of a glow feature is estimated in the orthogonal view and adjusted to equilibrate the height from both views in the analysis. If the

horizontal placement is slightly off, the error in height is only a few inches. This is the reason that the measurements are only recorded to within a half-foot.

The frames 5171 show how the dark cooled combustion products mask the glowing products from both directions. The frames 5400 highlight the difference in the two camera views. The South camera view shows more detail but only to a height of about 85 feet while the East camera can view about twice that height.

Analysis of the frames 7100 yields a flame plume height of about 55 feet at 4 minutes.

Some of the frames show a LOS, or line of sight length from the pool center to the maximum glow. Analysis of frames 13000 (~ 7 minutes) yields a height of about 69 feet. Review of the movie shows that the height has increased continuously (about 15 ft) from 4 minutes to 7 minutes.

The frame 25802 (~14 minutes) images show the flame height at 92 feet. This is the highest height recorded. The flame plume continues to rise to the same height until burn out as shown in the frame 26052 images where another glowing turbule is cooling.

Test 1 S and E cameras at frames 1800 (1 minute)

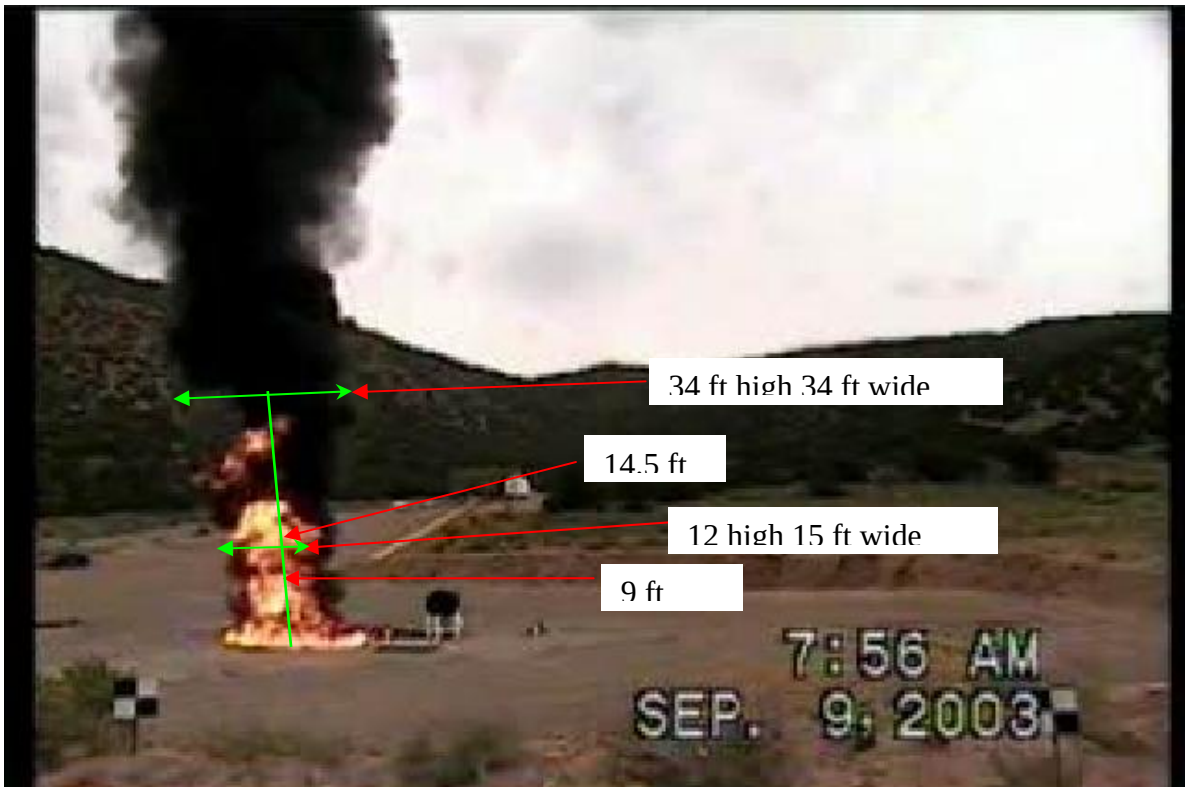

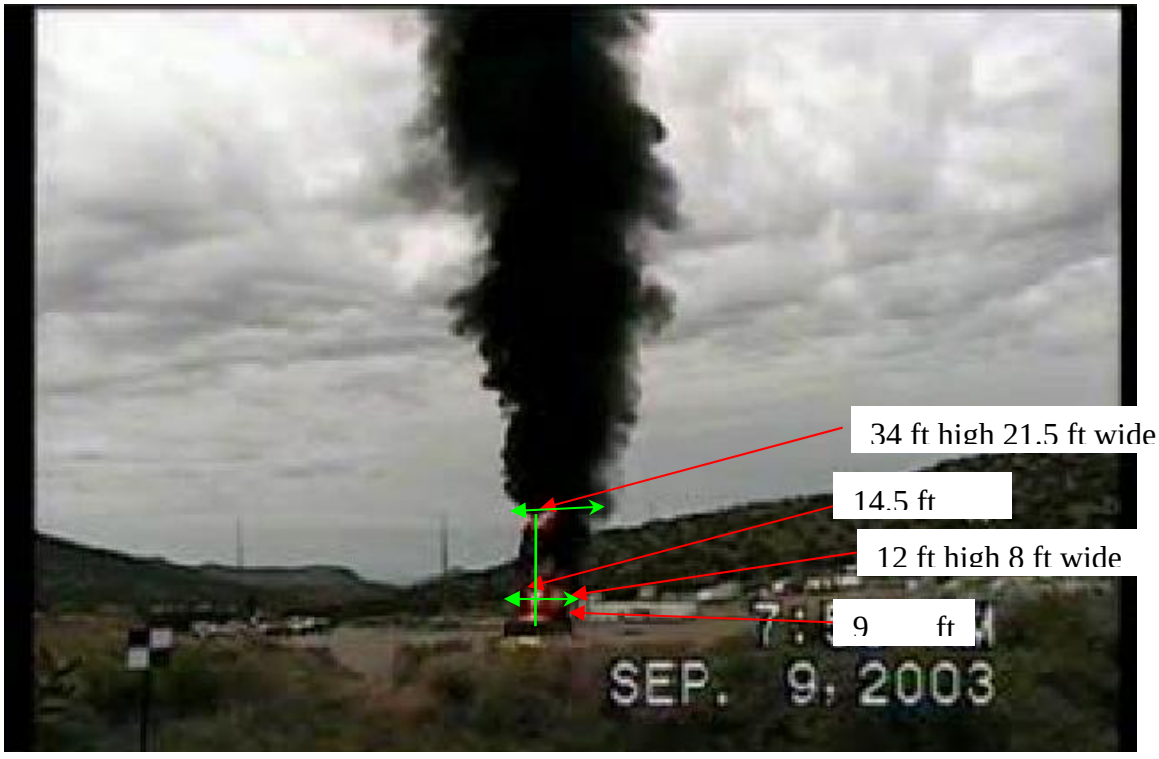

Test 1 S and E cameras at frames 3450 (1.9 minute)

Test 1 S and E cameras at frames 3600 (2 minutes)

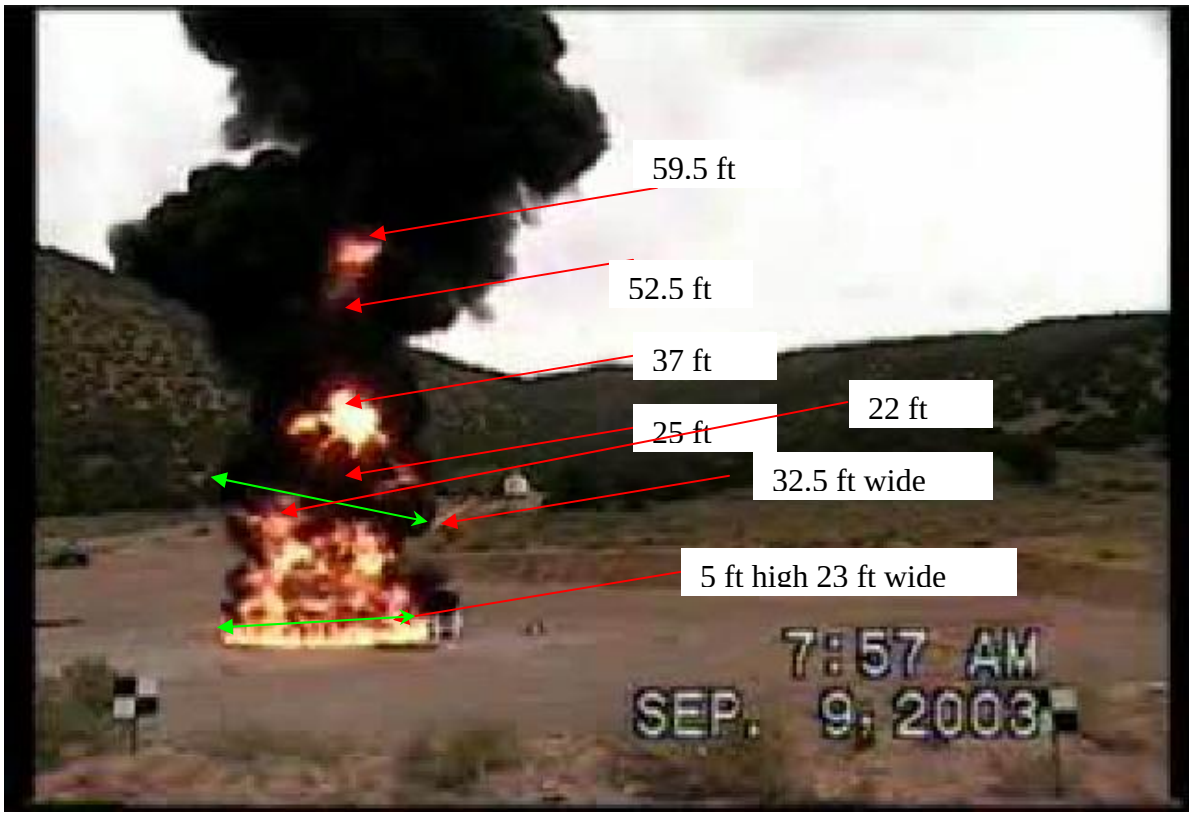

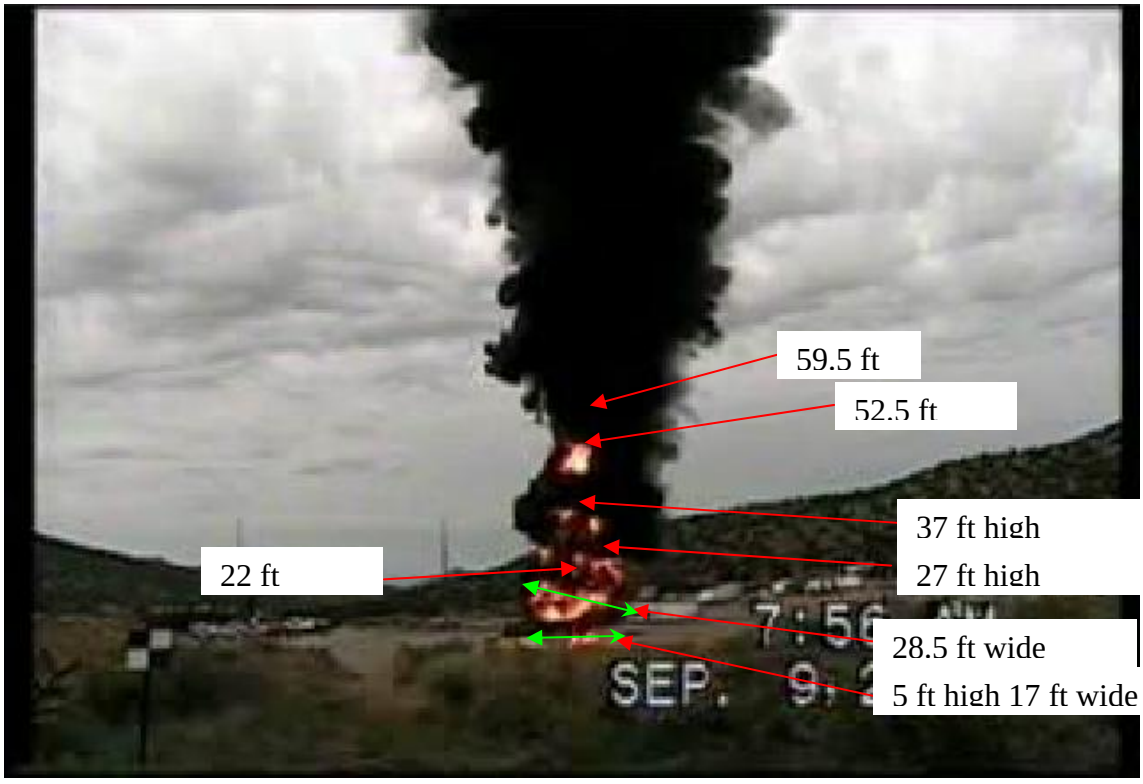

Test 1 S and E cameras at frames 5171 (2.87 minutes)

Test 1 S and E cameras at frames 5400 (3 minutes)

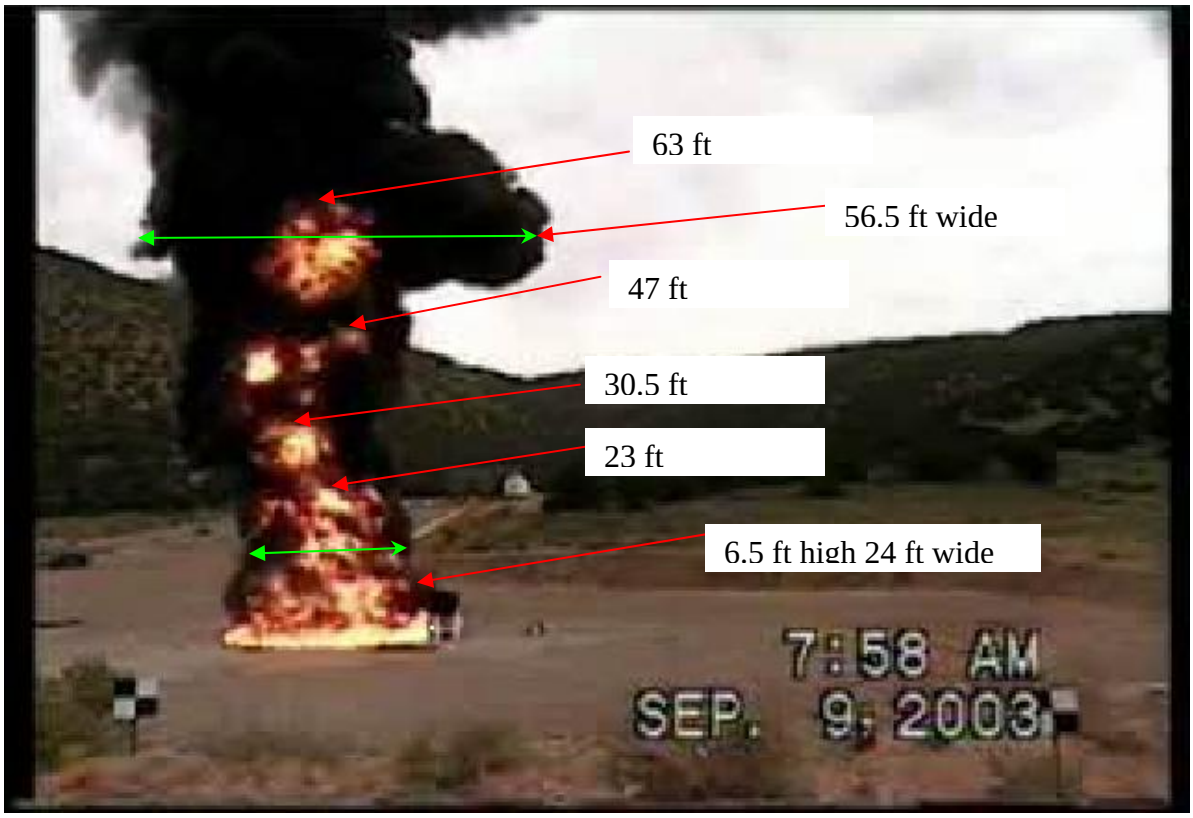

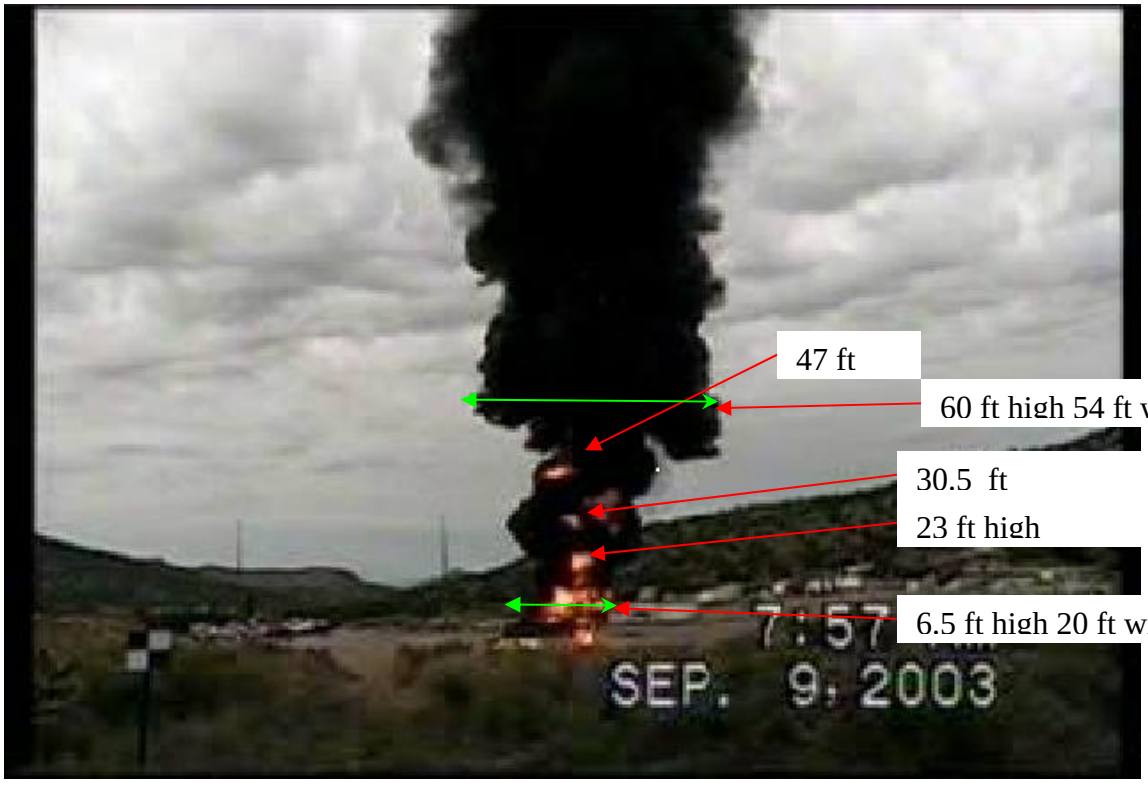

Test 1 S and E cameras at frames 7100 (4 minutes)

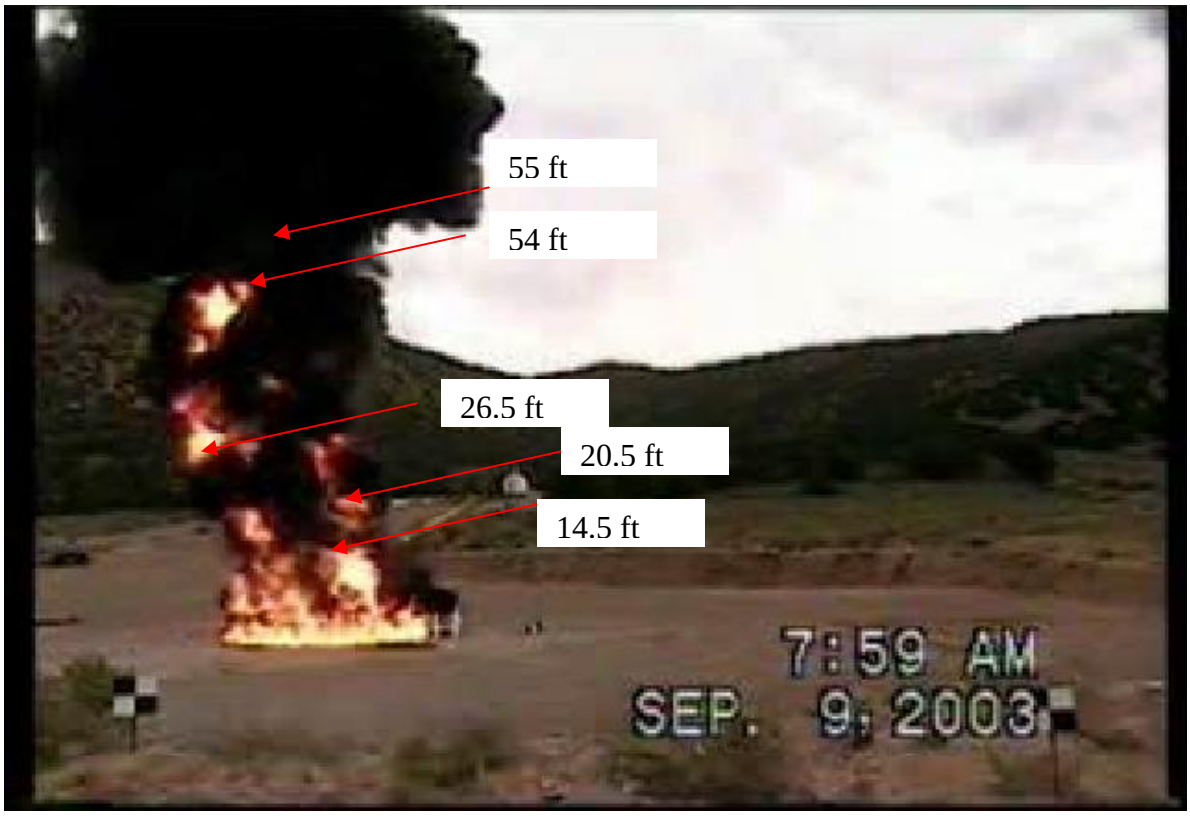

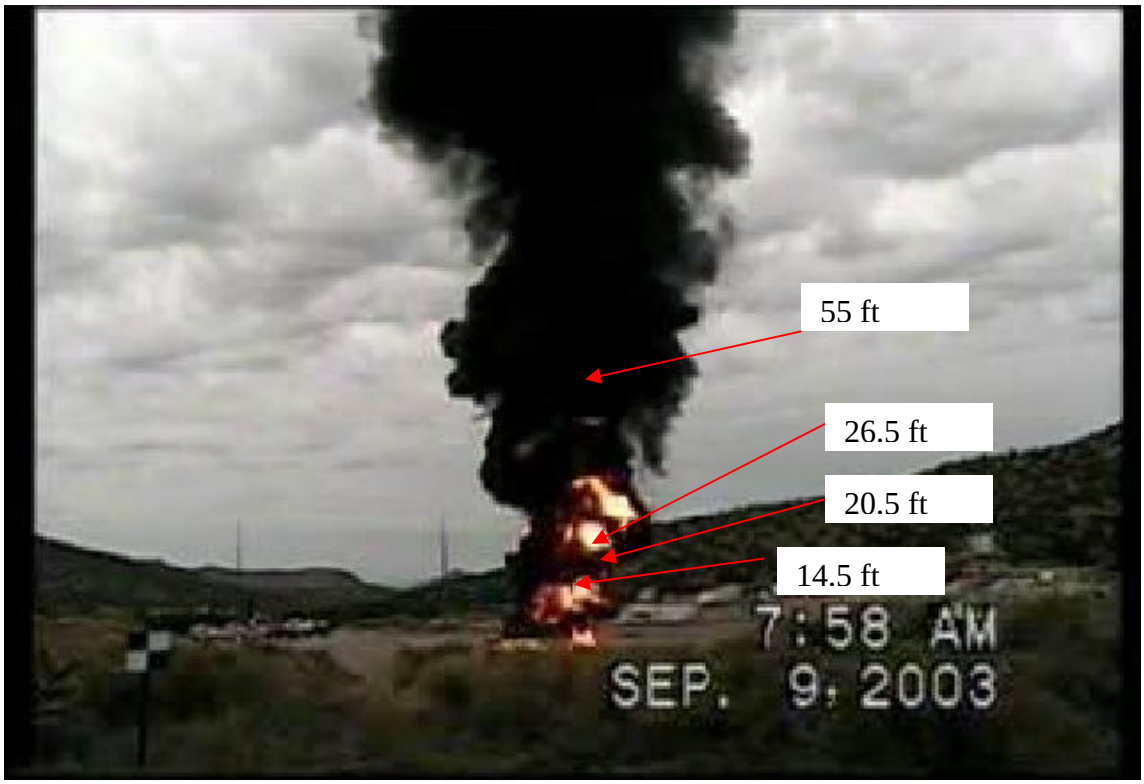

Test 1 S and E cameras at frames 13000 (7.2 minutes)

Test 1 S and E cameras at frames 25802 (14.3 minutes)

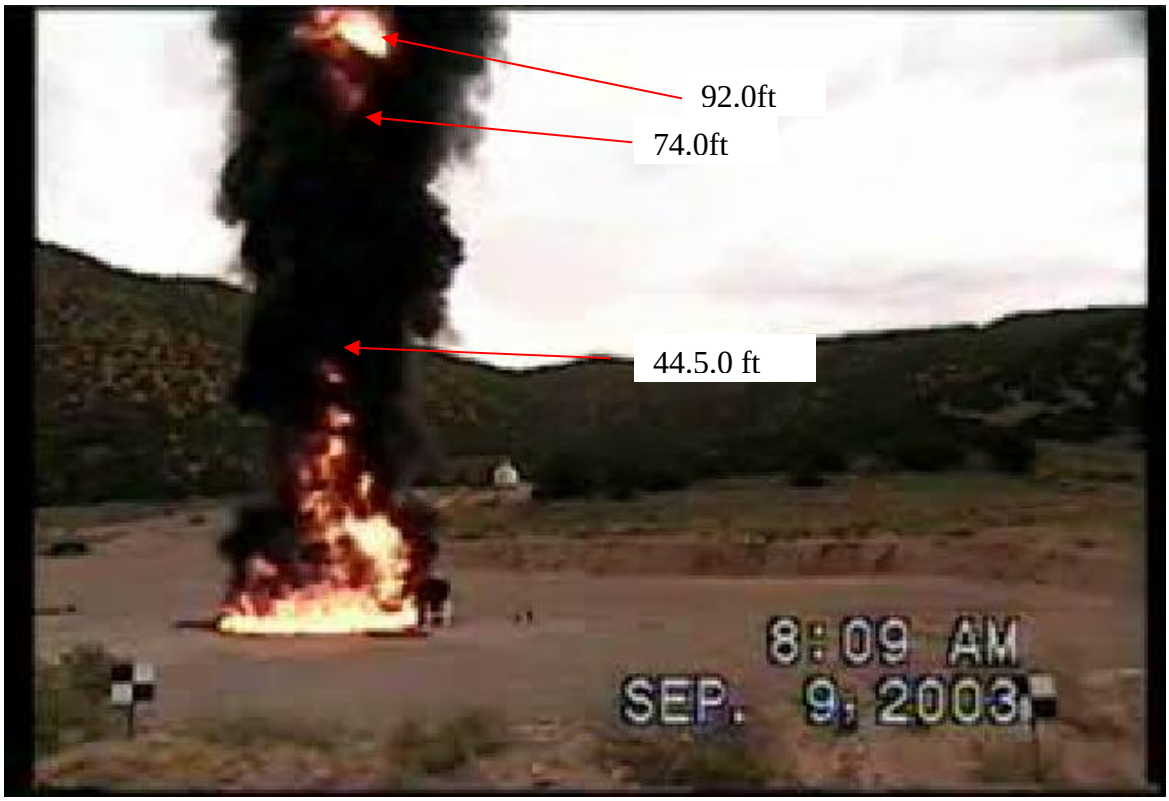

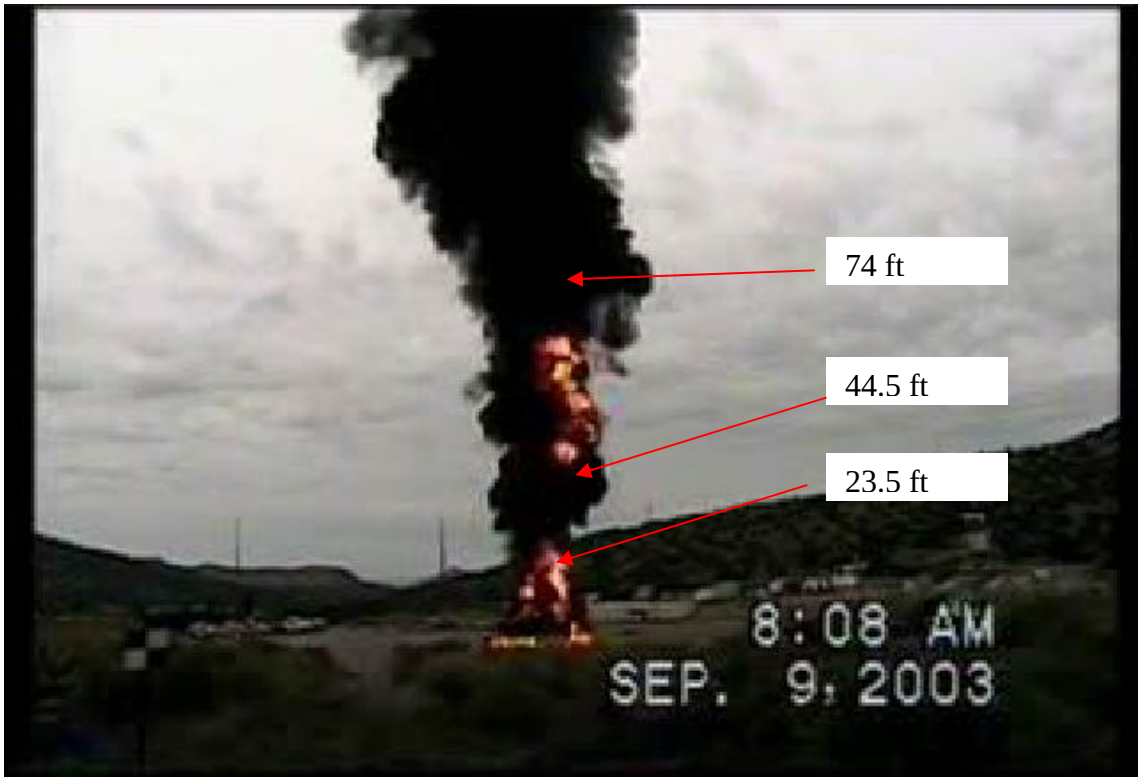

Test 1 S and E Cameras at frames 26052 (14.4 minutes)

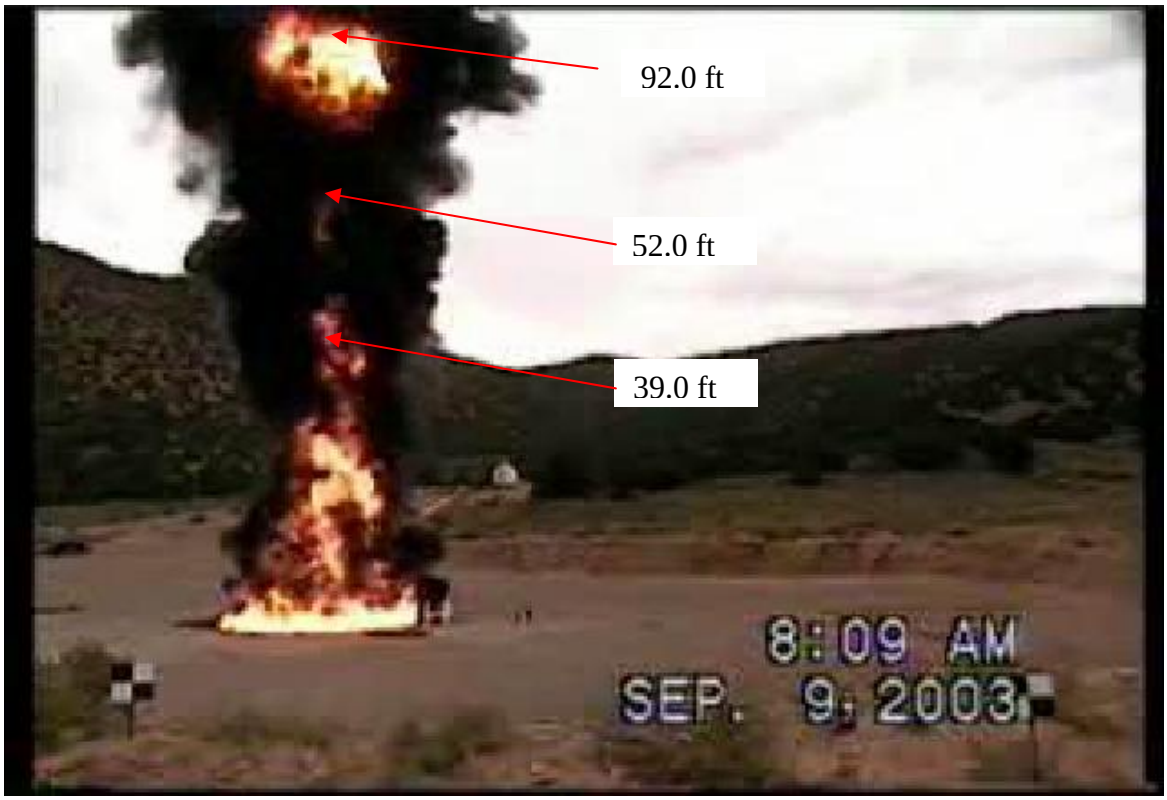

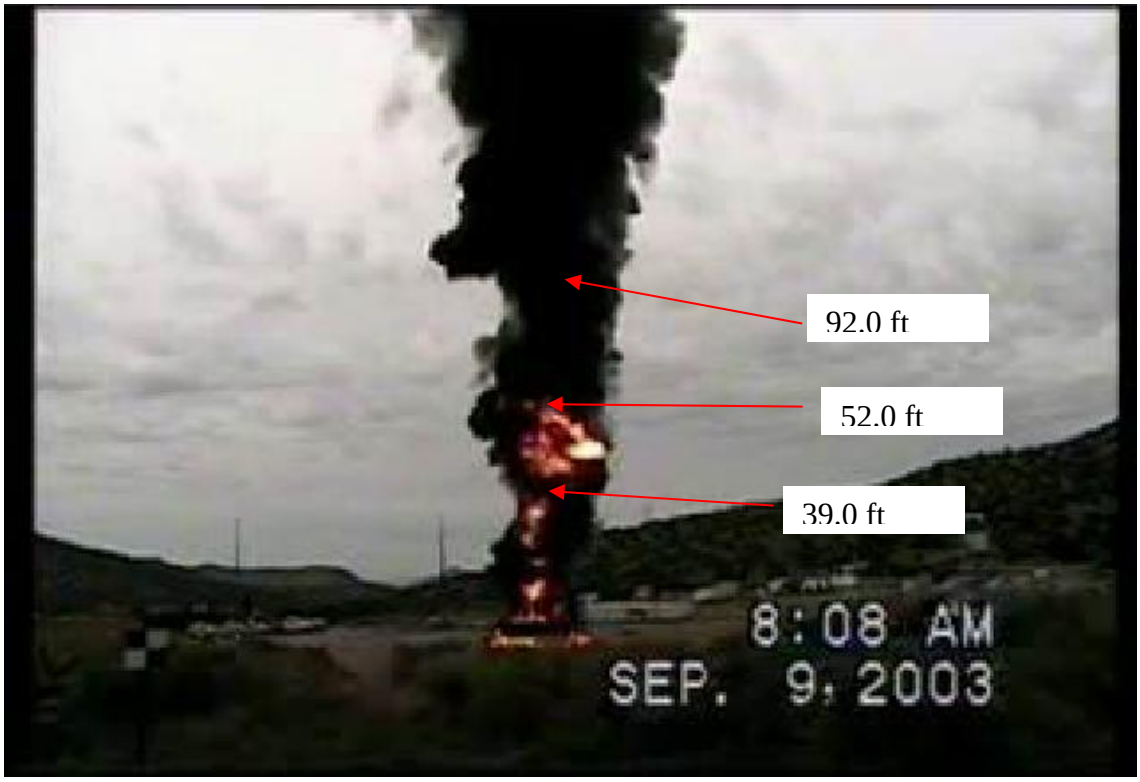

Test 1 E and S Camera views at frames 26842 (14.9 minutes)

76 ft LOS 75.5 ft high 87 deg

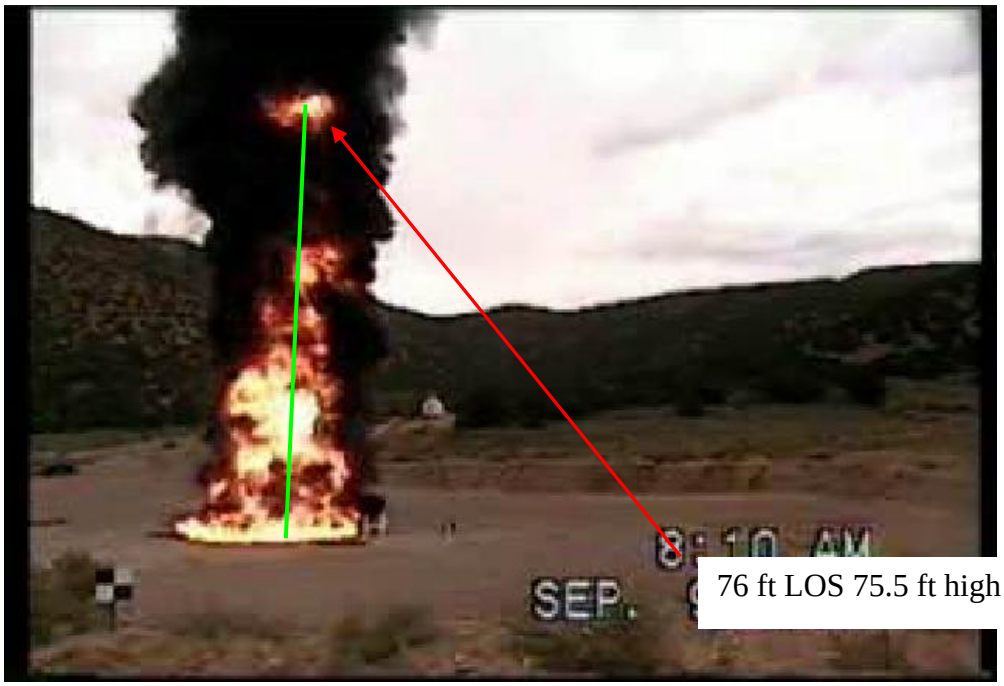

76 ft LOS 75.5 ft high 87 deg

Test 2

Test 2 included the large calorimeter. Due to the wind condition, the smoke and fire plume basically engulfed the large calorimeter for the entire 20 minutes. The fire fully engulfed the pool in 21 seconds as the spark was on the upwind side of the pool and the wind quickly carried the flame over the calorimeter area. It was in about 20 seconds that the flames began interacting with the calorimeter.

The winds were basically out of the west. The maximum shift was out of the WNW such that the plume passed over the SE camera for a few seconds (~34-degree shift); however, most of the time the plume shifted only a few degrees north or south. Normally the plume blew right over the east camera and that view could not be used for triangulation. It was critical to have the NE and SE cameras available to obtaining quantitative data.

The calorimeter was used as a benchmark for calibration of the camera data. With the cameras at a 46 and 54 degree offset, the ends of the calorimeter are in view and the length is foreshortened. Calculation of the perceived width sans end caps should be about 10.3 or 12.2 feet for the NE and SE camera respectively. The height should be 7 feet. The problem is again that the base of the calorimeter is hard to establish with the narrow legs and the calorimeter shadow on the ground. A calorimeter height of 6.9 and 7.1 feet and a width of 11.4 and 13.1 feet were obtained from the NE and SE camera views, respectively. A one-pixel shift yields a precision for both cameras in both directions of 0.3 feet. Therefore there is approximately a three-pixel error in the technique in the horizontal direction, which is not surprising, since the data was scaled by the electronics to increase the pixel size from 512 to 640 and blur of a sharp edge in the image increases the uncertainty of that edge by at least one pixel. Assuming the same amount of error on both ends yields the three-pixel error.

The following figure sets show the lengths from the center of the burning pool to the points of interest and some cross dimensions. The length (labeled LOS for line of sight from the pool center to the point) was obtained by calculation using the two camera views, the known geometry between the two cameras and the pool center, and the offset from the bore sight to the pool center and the points of interest. The lines marked as length are perceived lengths between the chosen points. They are calculated as the square root of the sum of the square of the differences in height and horizontal distance from the pool center of the two chosen points. The following figure shows the height of the farthest glow from the fire center and the distance of the line of sight from the pool center to the point.

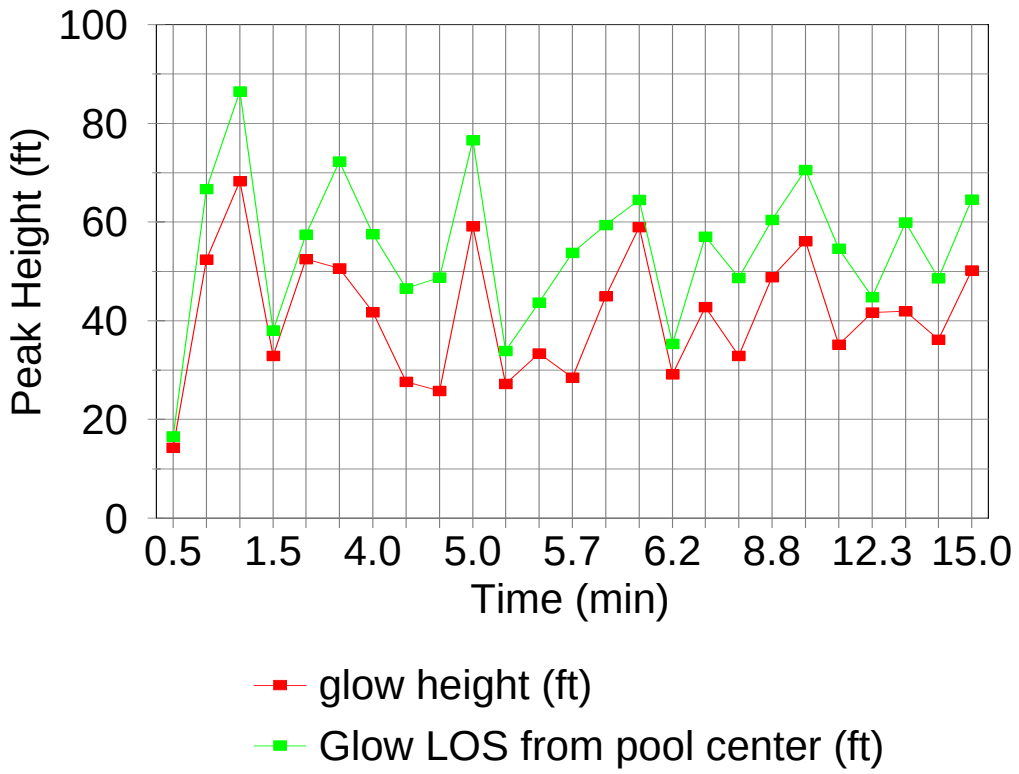

Figure 5. Test 2 Glow Heights and Distances from Pool Center

The gaseous flow of the burning vapors began as a turbulent rotation from the plume center to the outside. As the wind moved the heated and rising air to the east the shape took the form of two parallel corkscrews. The one to the south was turning in a clockwise direction and the one to the north in a counterclockwise direction. This can been best seen in the 5.7-minute set of pictures below. As the wind slightly abated, a vertical torus would form. Several angles from the ground at the pool center to various points were calculated. The smaller the average angle of the plume with the ground usually represents a larger wind velocities.

In the thirty second pair the angle of the plume is between 22 and 46 degrees with the average about 37 degrees for the first 20 feet or so. Then there is a sharp increase in angle.

The one-minute picture pair shows a well-developed plume lying over at between 0 and 41 degrees with a typical angle of about 19 degrees. It begins to rise off the ground at about 35 feet from the center of the pool. The glowing gases seem to extend about 18 feet. This compares with the first test at the same time where the glowing gases seem to risen a distance of about 34 feet vertically.

At 90.5 seconds a corkscrew rotation of the burning vapor products is seen on the north side of the plume near the ground. It has an angle of about 32 degrees while the other burning products have an angle of 60 degrees. It appears that the wind has abated slightly to allow a more vertical component of the plume to be dominant. The glowing gases seem to have extended to about 38 feet. Note in Test 1 (at about 20 seconds) the glowing part of the plume reaches about 58 feet.

At 2 minutes the Test 2 plume is about 28 feet long. The angle varies from 0 to 48 degrees nearest the pool and increase to about 66 degrees over 30 feet away. The Test 1 plume is glowing intensely at about 35 feet vertical, but a secondary glow is seen as high as 59 feet.

At 3 minutes the Test 2 plume has not changed much in length or angle. The glowing part extends about 28 feet at between 20 and 30 degrees.

The remaining picture sets of less than 6 minutes show the glowing portion of the plume extending between 35 and occasionally up to 54 feet with a tilt angle of 20-40 degrees.

The 12.3-minute picture set shows the slope of the plume at 0 to 30 degrees and a normal torus forming above 30 feet and offset by about 25 feet.

Test 2 NE and SE Camera view at frames 900 (30 seconds)

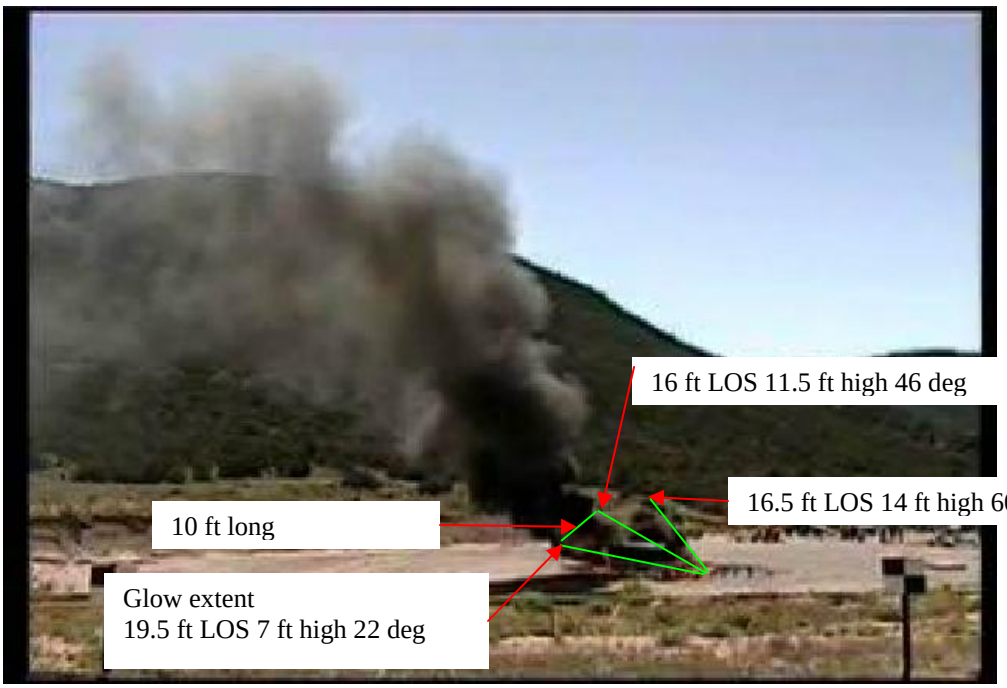

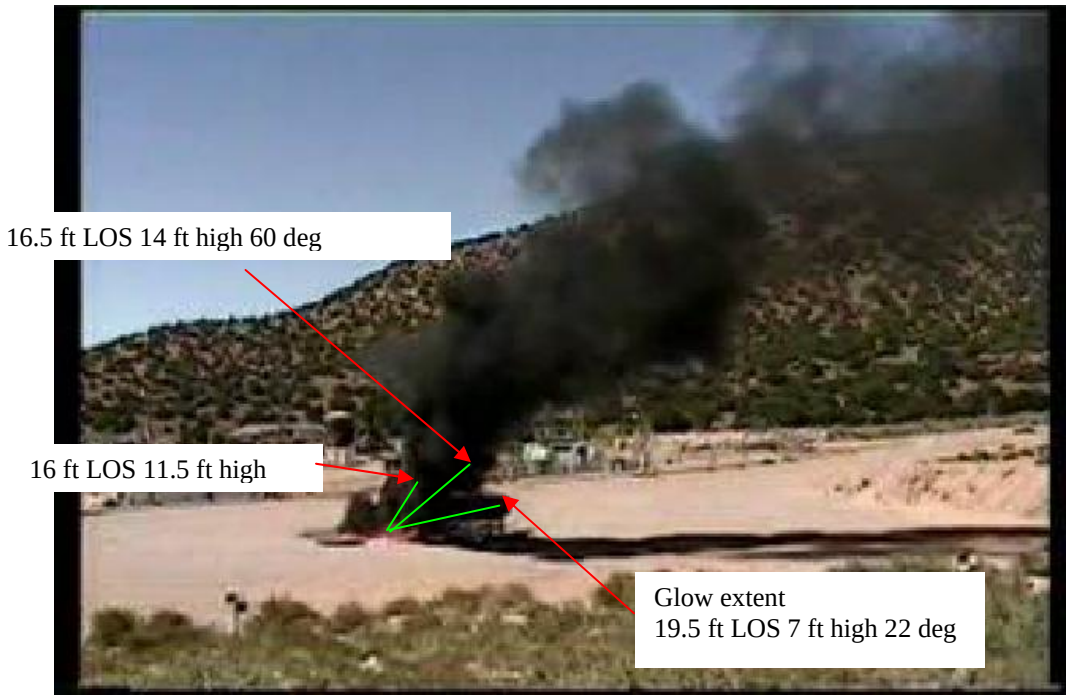

Test 2 NE and SE Camera view at frames 1800 (60 seconds)

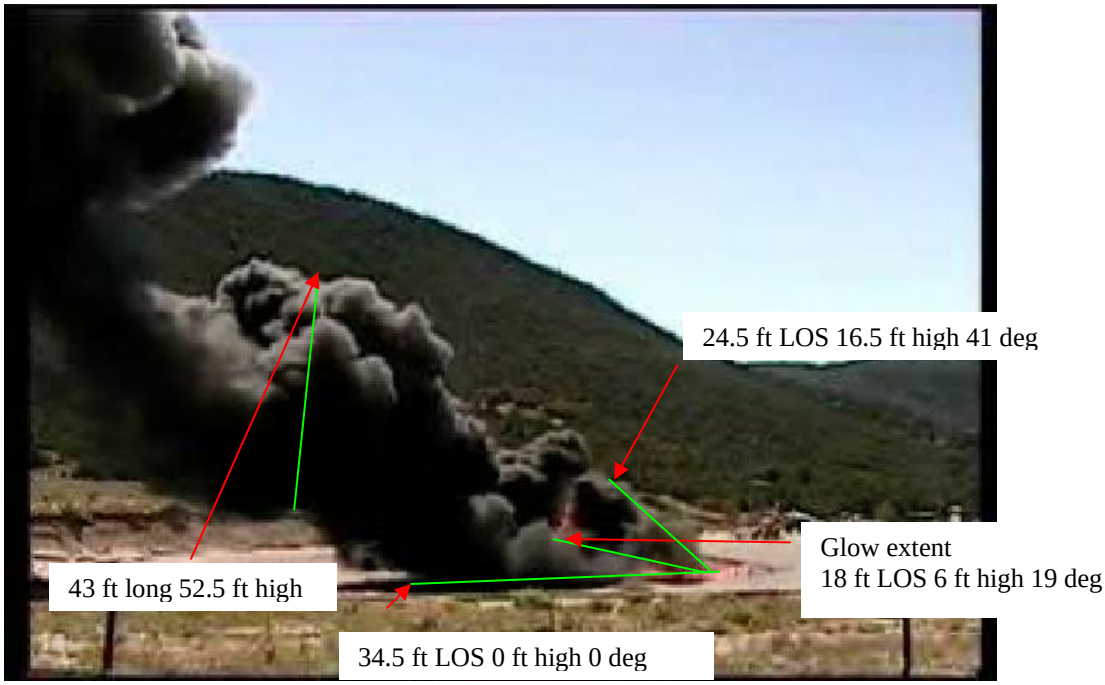

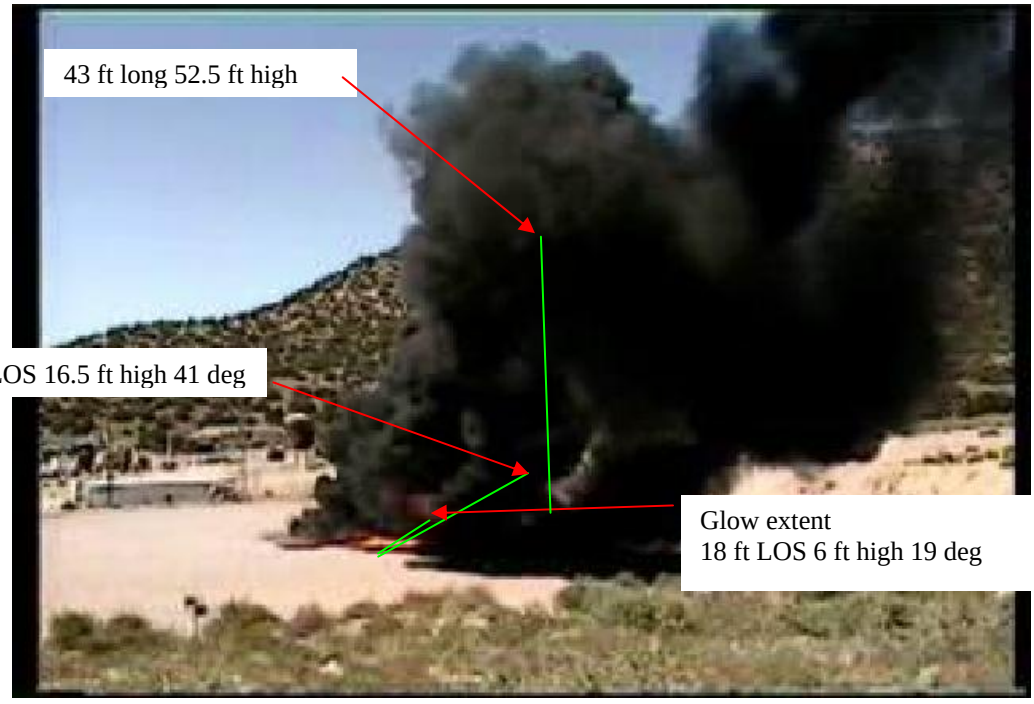

Test 2 NE and SE Camera view at frames 2715 (90.5 seconds)

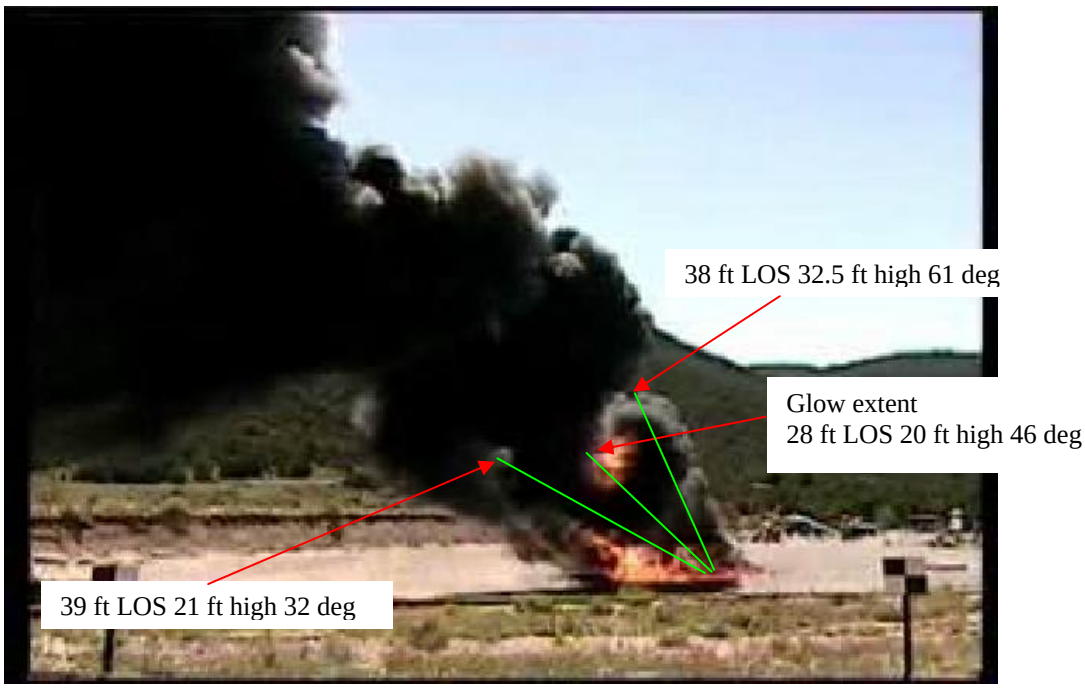

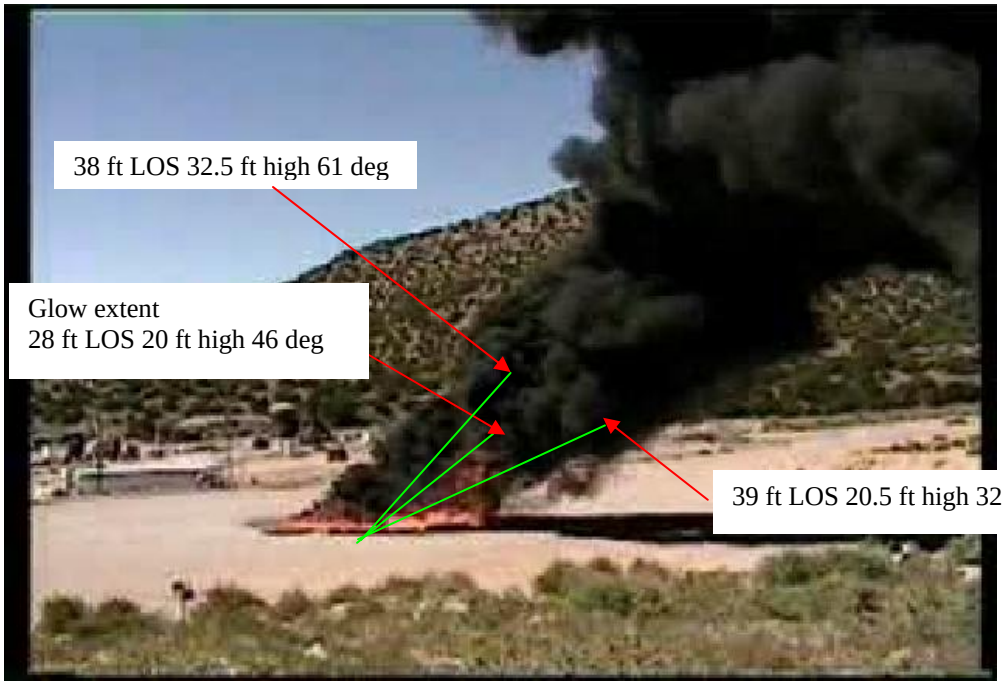

Test 2 NE and SE Camera view at frames 3600 (2 minutes)

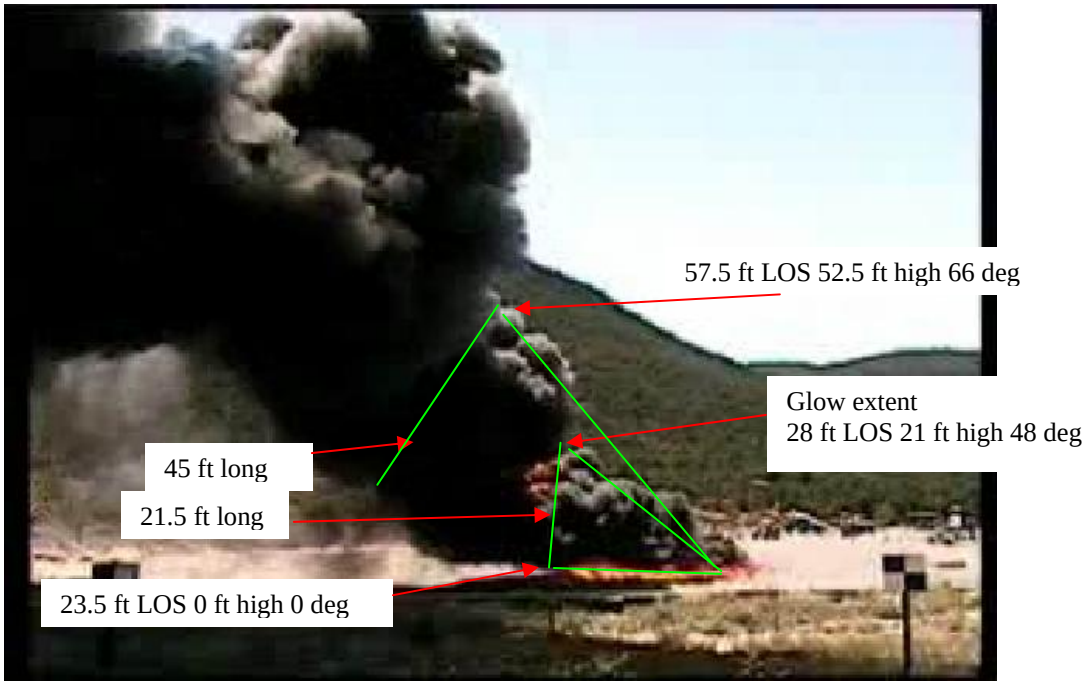

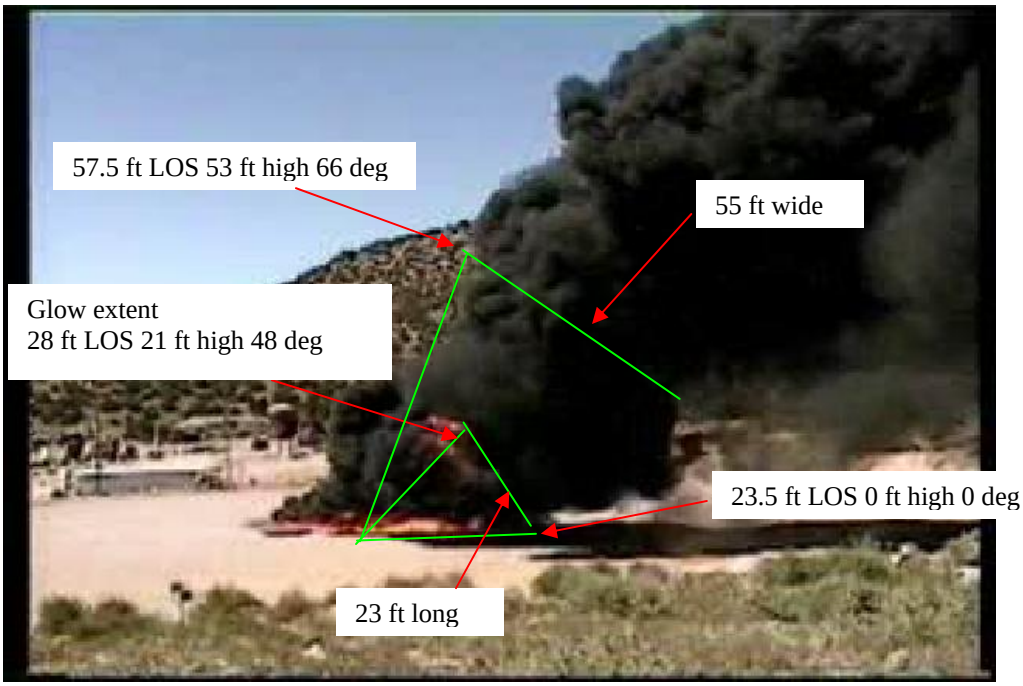

Test 2 NE and SE Camera view at frames 5400 (3 minutes)

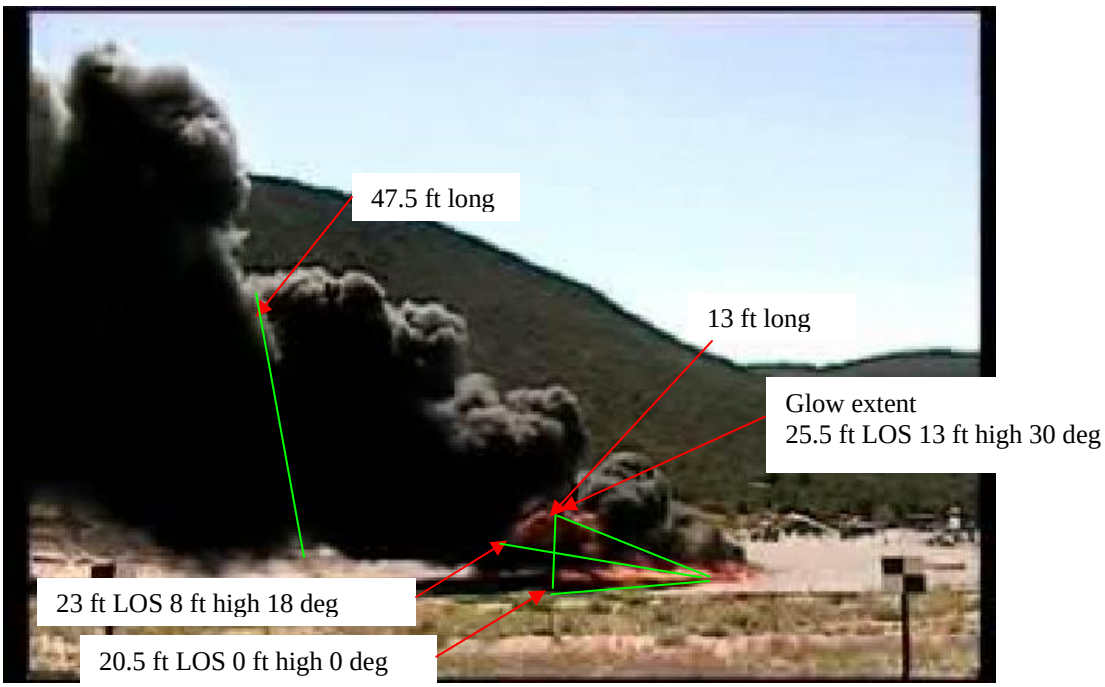

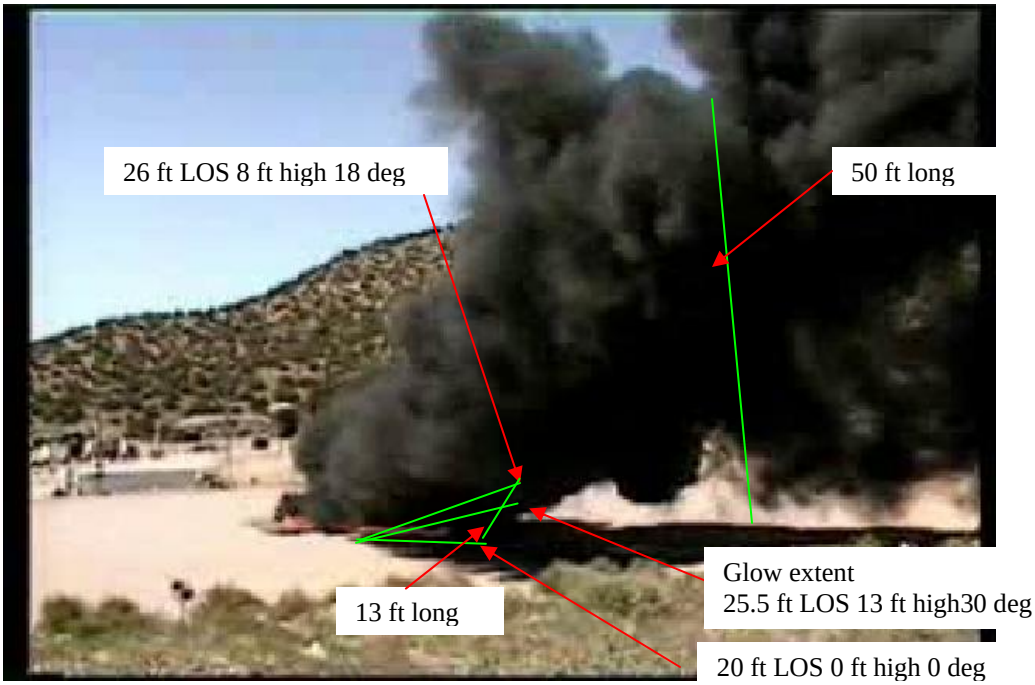

Test 2 NE and SE Camera view at frames 9000 (5 minutes)

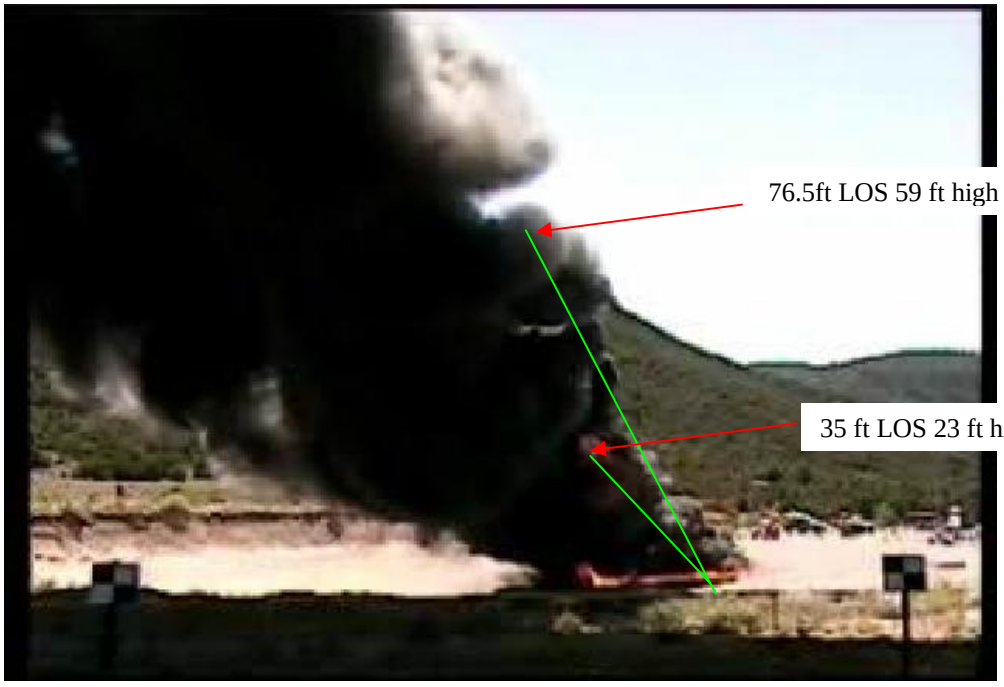

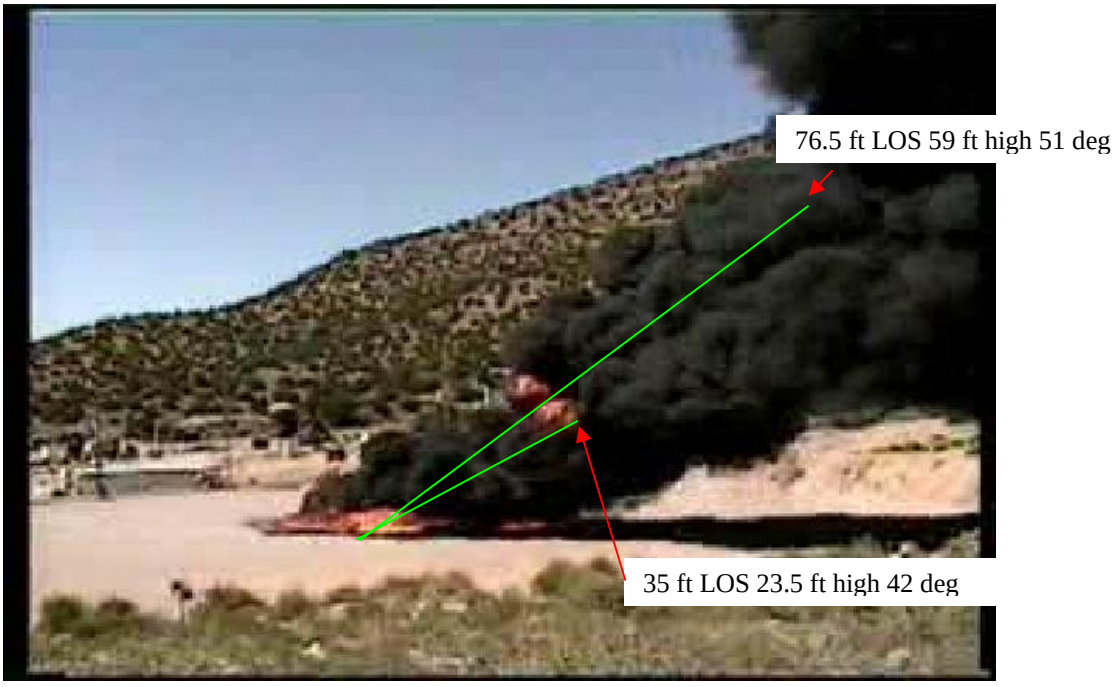

Test 2 NE and SE Camera view at frames 10257 (5.7 minutes)

Test 2 NE and SE Camera views at frames 17915 (10 minutes)

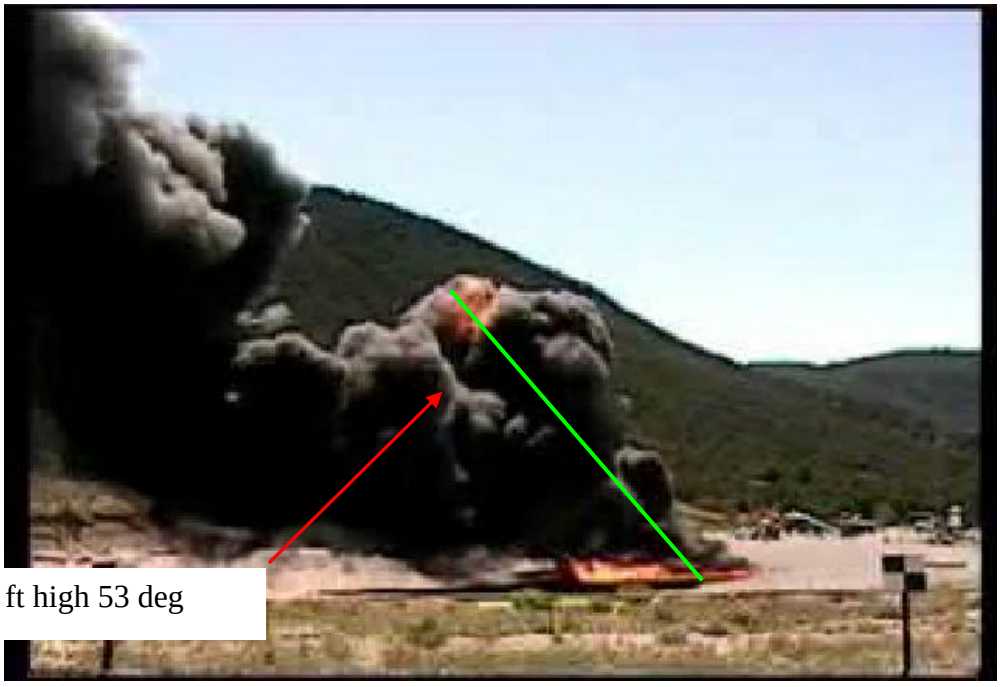

70.5 ft LOS 56 ft high 53 deg

70.5 ft LOS 56 ft high 53 deg

Test 2 NE and SE Camera view at frames 22150 (12.3 minutes)

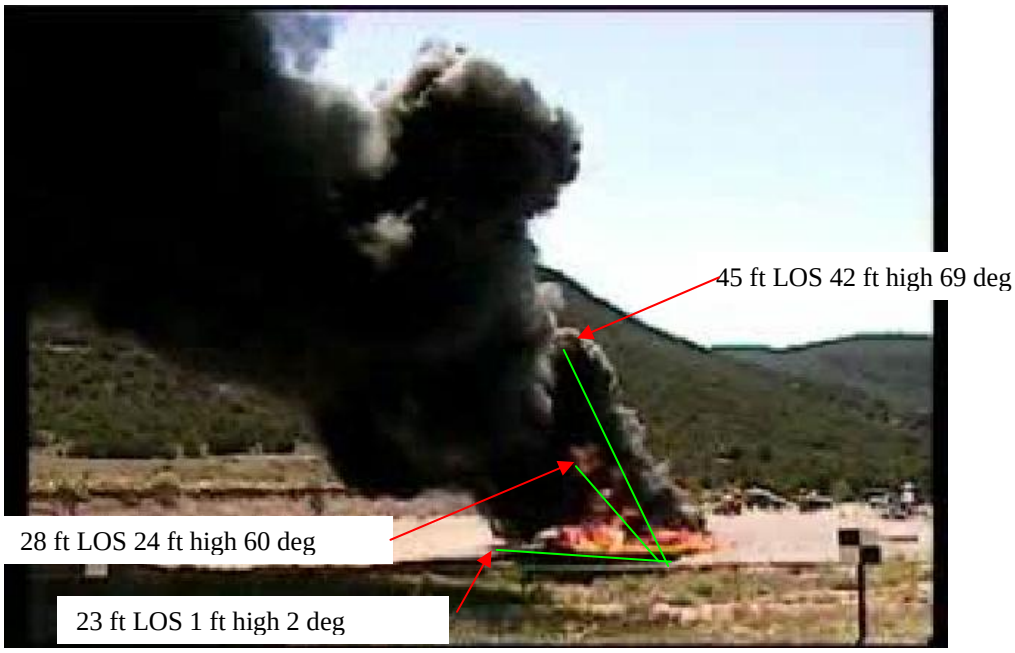

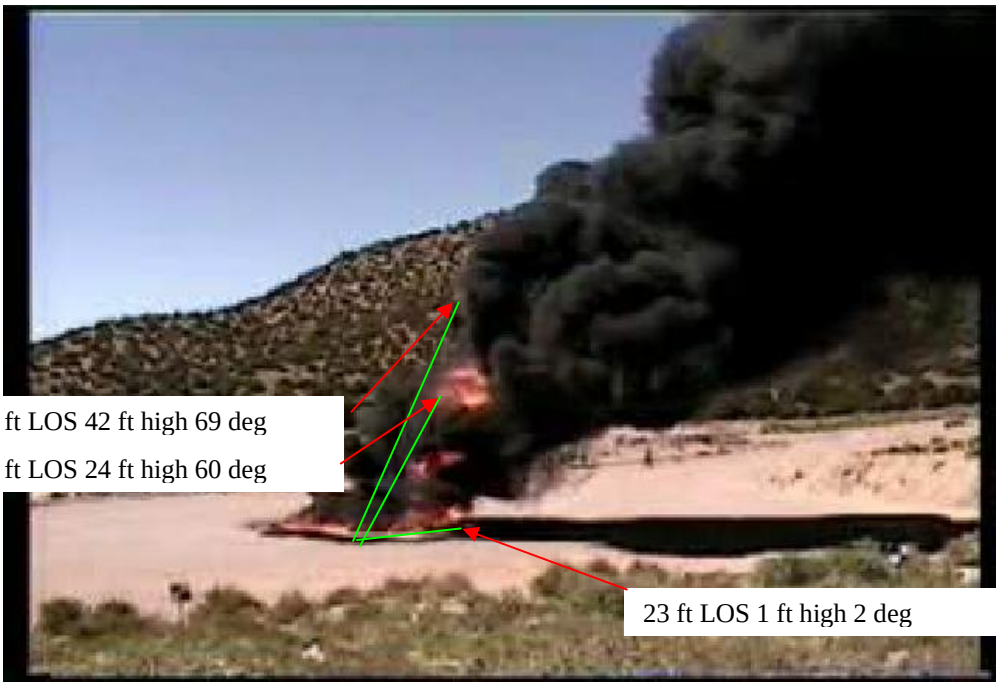

Test 2 NE and SE Camera views at frames 27018 (15 minutes)

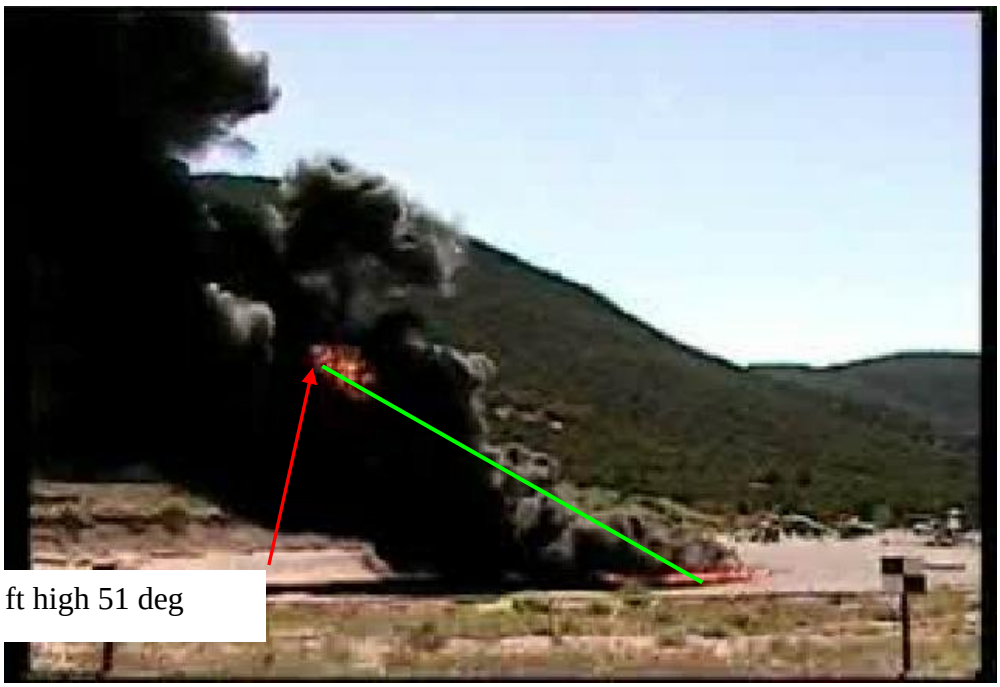

64.5 ft LOS 36 ft high 51 deg

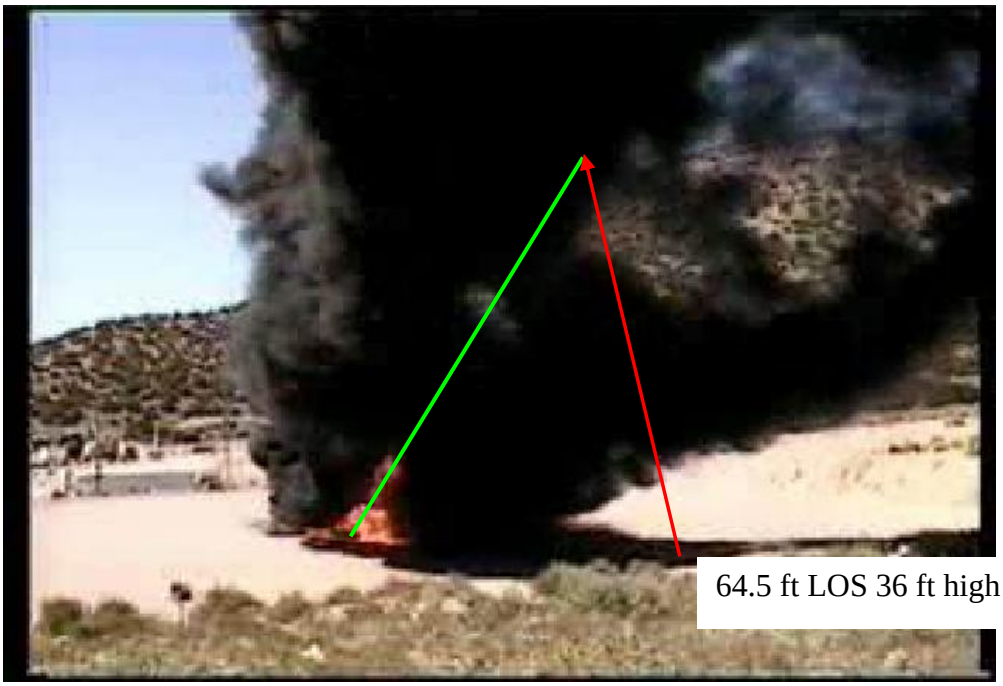

64.5 ft LOS 36 ft high 51 deg

Test 3

Because the wind, not quite calm and draining off the mountain, the plume drifted to the northwest just enough to be off the field of view of the north and south cameras. It remained enough in the field of view of the northeast and southeast to get good plume measurements. Image pairs were analyzed for every 10 seconds for the first minute of the burn and then every 30 seconds to about 11 minutes. In addition, the nearest image to the 30-second set of images that included the highest glowing point is presented. The following picture sets show the results of the measurements.

The MPEG file was reviewed for tori formation rates as with Test 1. Table 3 gives the results of the puff analysis yielding a frequency of 0.56 puffs/sec with a standard deviation of 0.09.

Table 3. Test 3 Puff Count

Camera	Time start (minutes)	Time stop (minutes)	Number of puffs	Puffs/sec
C2	1	1.283	10	0.59
	1.5	1.817	9	0.47
	2.5	2.833	11	0.55
	3.5	3.900	16	0.67
	4.5	4.850	12	0.57
	5.5	5.900	12	0.50
	6.5	6.883	13	0.57
	7.5	7.933	10	0.38
	8.5	8.833	11	0.55
	9.5	9.767	10	0.62
	10.5	10.833	12	0.60
	11.5	11.883	11	0.48
	12.5	12.867	11	0.50
	13.5	13.883	10	0.43
	14.5	14.833	12	0.60
	15.5	15.833	10	0.50
C4	1	1.267	8	0.50
	1.5	1.783	12	0.71
	2.5	2.900	13	0.54
	3.5	3.867	13	0.59
	4.5	4.850	10	0.48
	5.5	5.917	13	0.52
	6.5	6.850	14	0.67
	7.5	7.967	16	0.57
	8.5	8.783	13	0.76
	9.5	9.900	17	0.71
	10.5	10.917	13	0.52
	11.5	11.883	15	0.65
	12.5	12.833	12	0.60
	13.5	13.883	13	0.57
	14.5	14.883	13	0.57
	15.5	15.967	12	0.43

The height of the glowing portions of the cloud at the half minute and at the peak was calculated, as well as the lines of sight distance from the center of the fire pool to the point on the plume. The results for Test 3 are shown in Figure 6. The typical hot spot height increased with time.

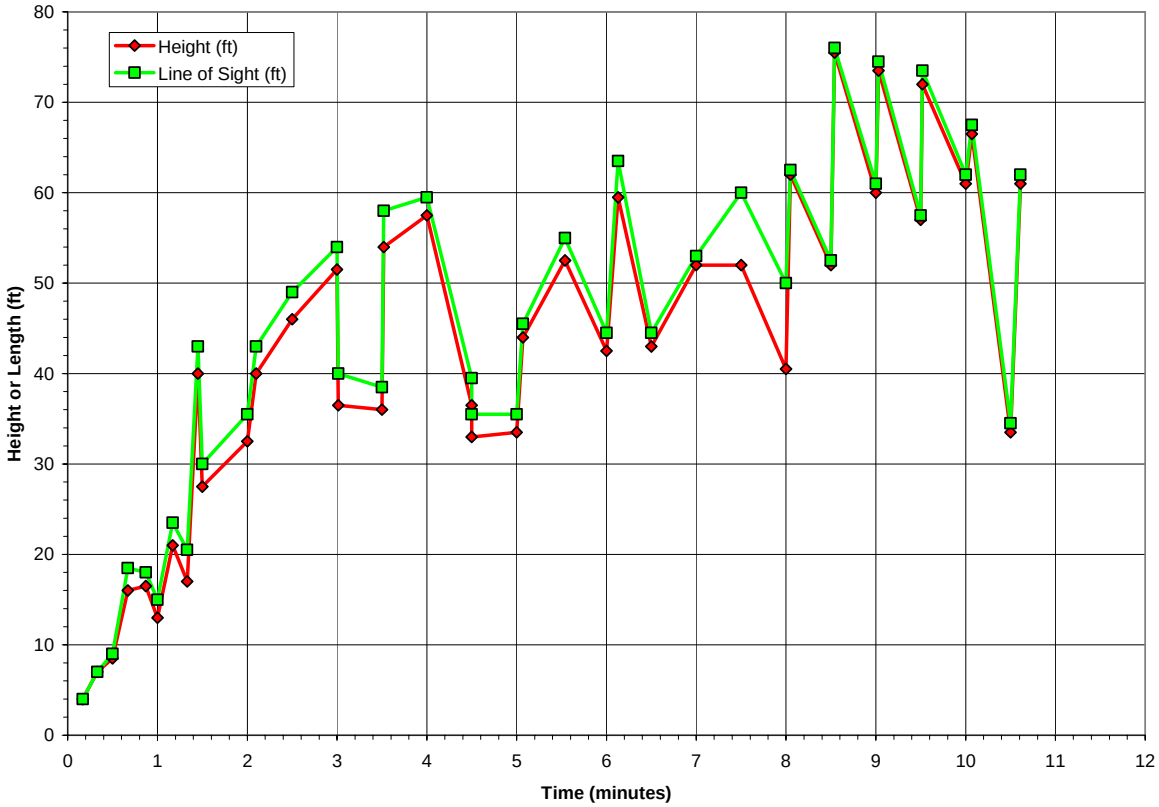

Figure 6. Test 3 Glow Heights and Distances from Pool Center.

Test 3 NE and SE Camera view at frames 1800 (1 minute)

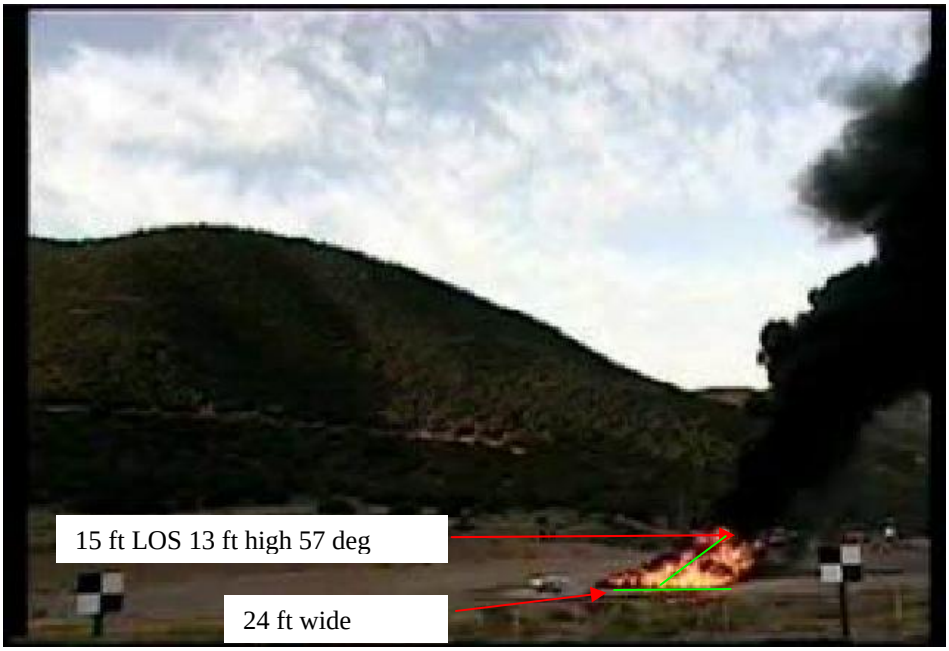

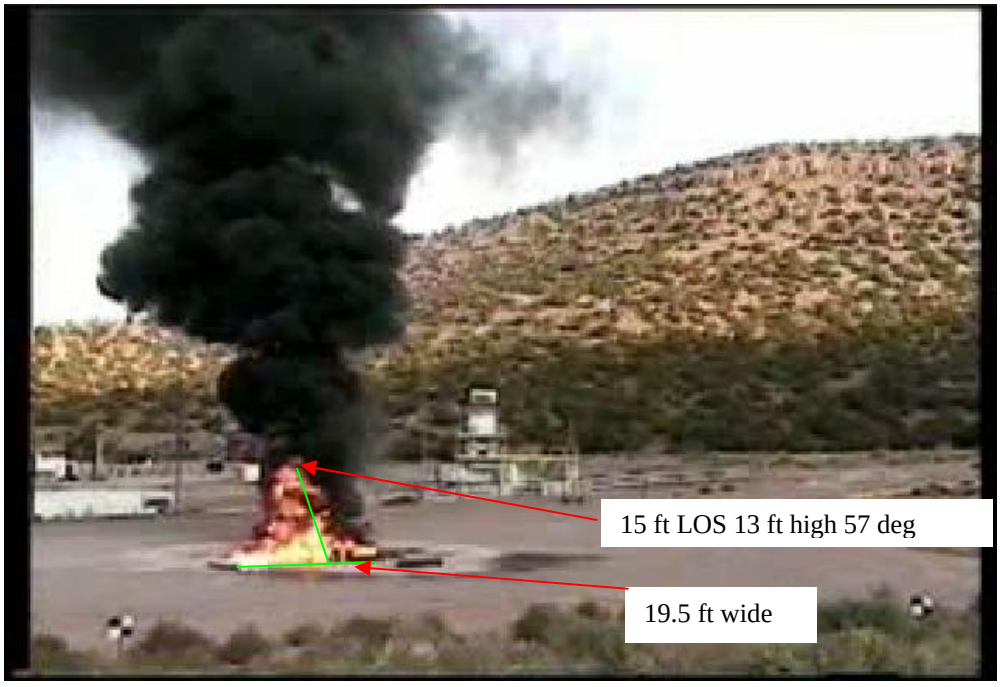

Test 3 NE and SE Camera view at frames 3600 (2 minutes)

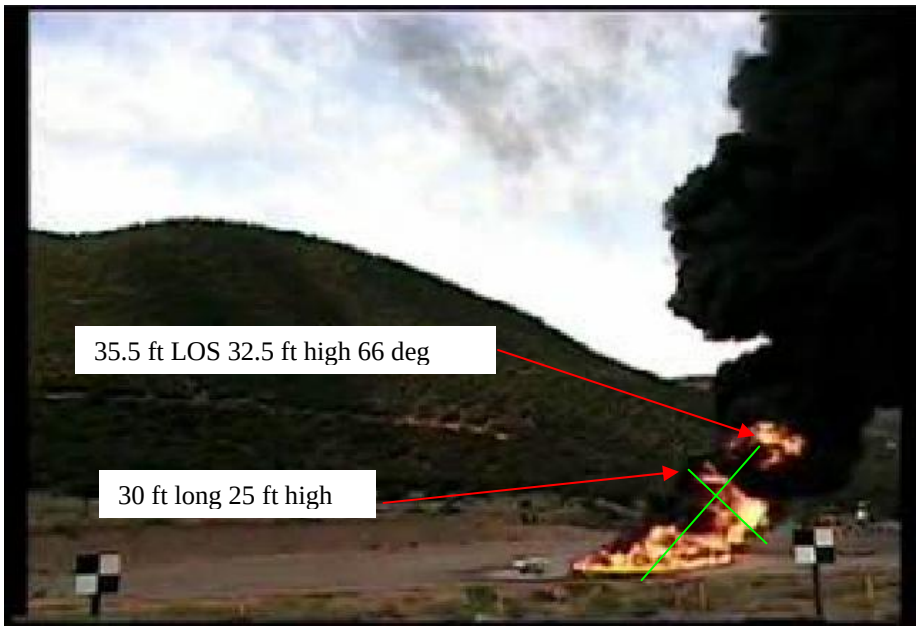

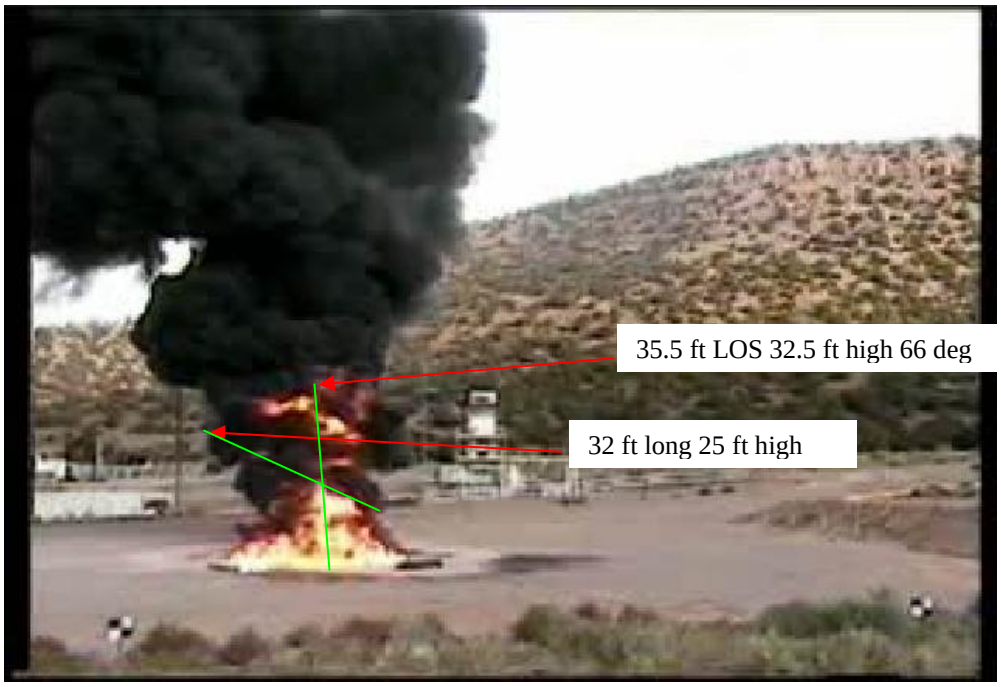

Test 3 NE and SE Camera view at frames 5400 (3 minutes)

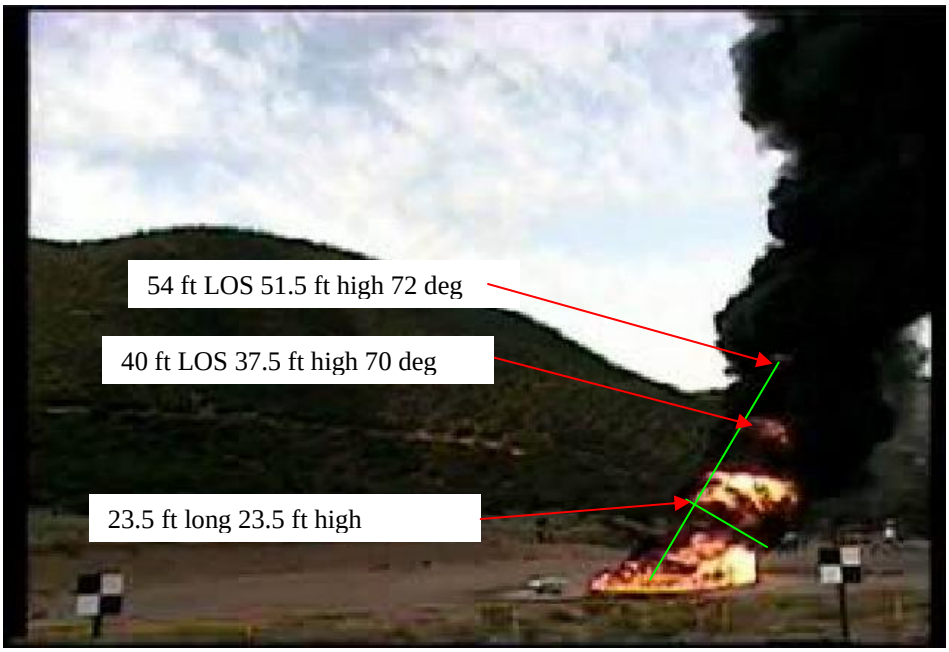

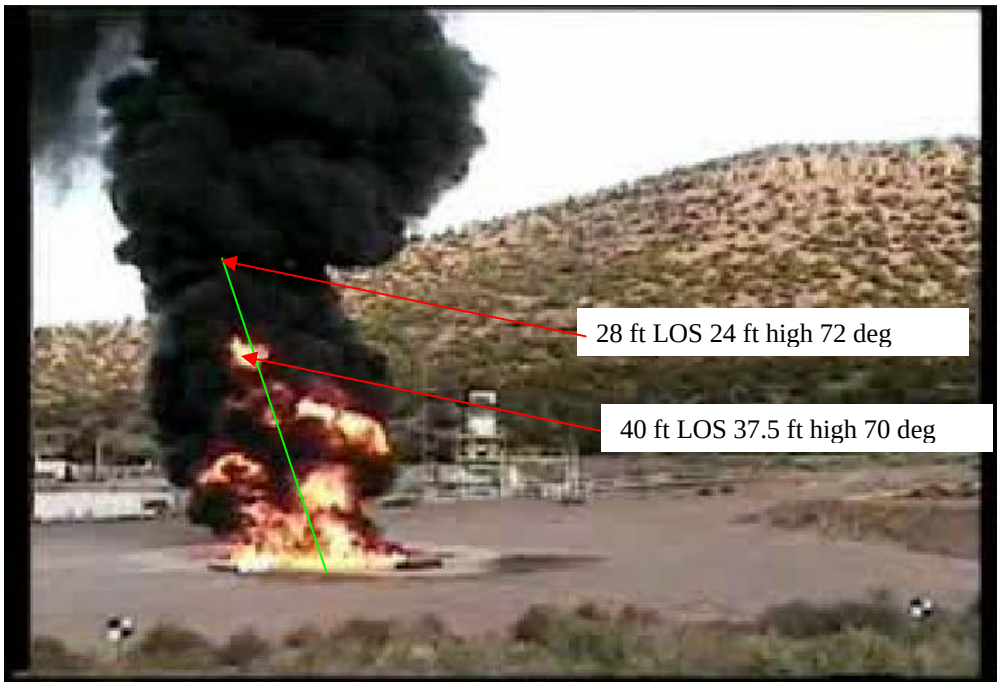

Test 3 NE and SE Camera view at frames 7203 (4 minutes)

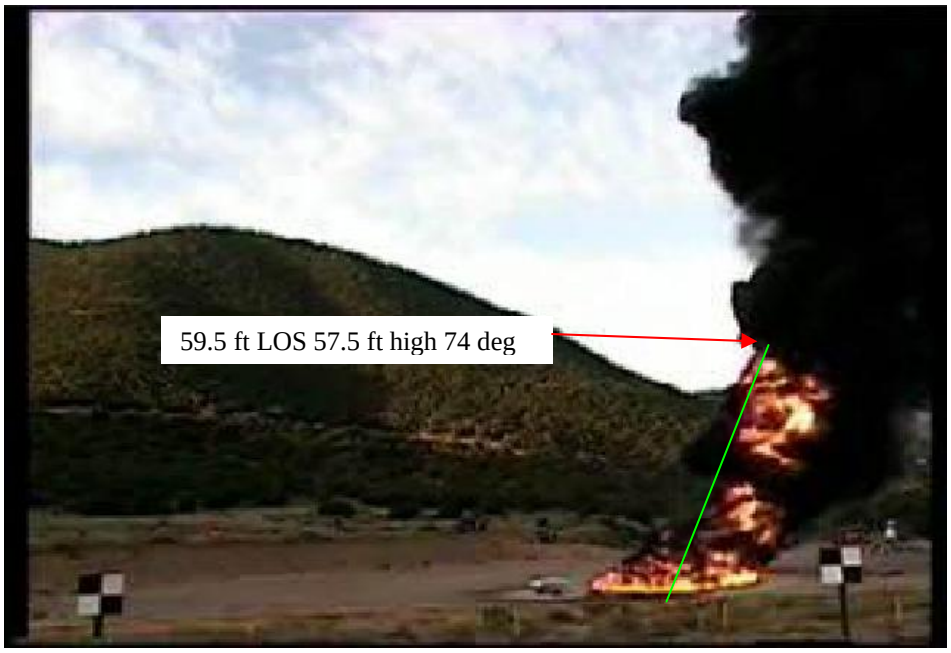

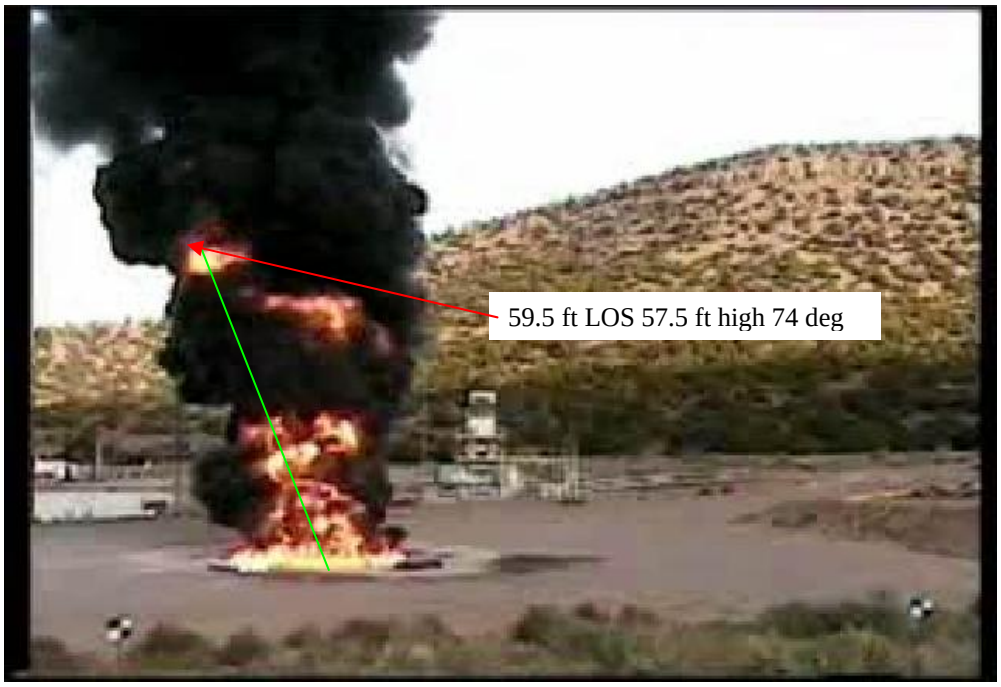

Test 3 NE and SE Camera view at frames 9000 (5 minutes)

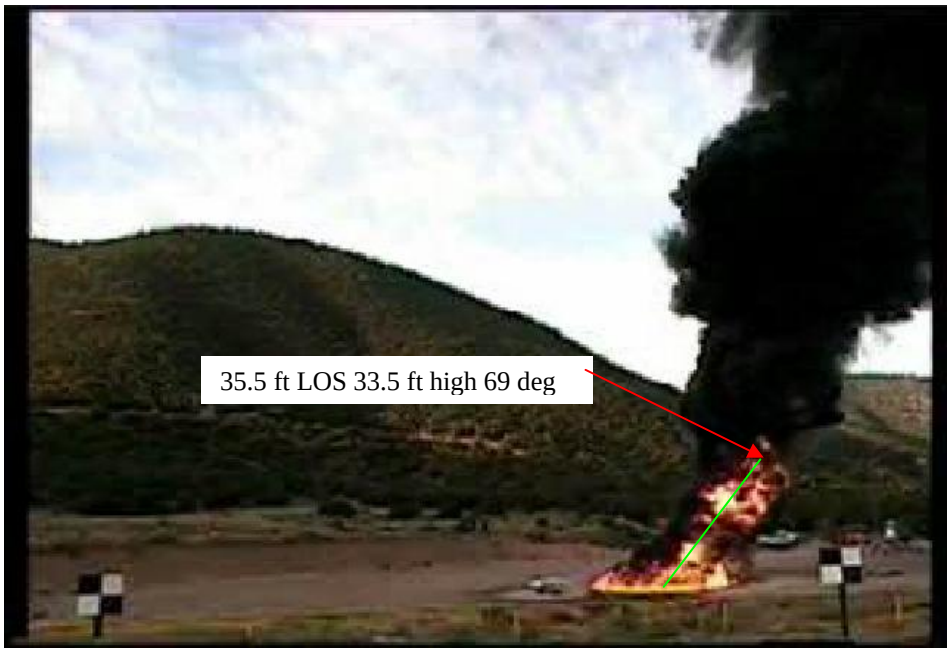

Test 3 NE and SE Camera view at frames 10800 (6 minutes)

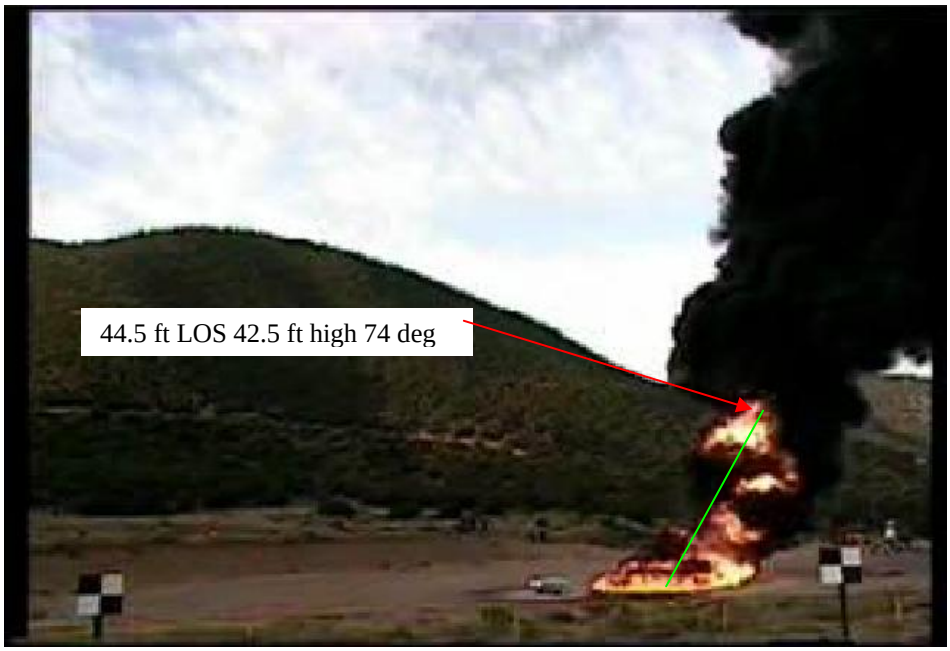

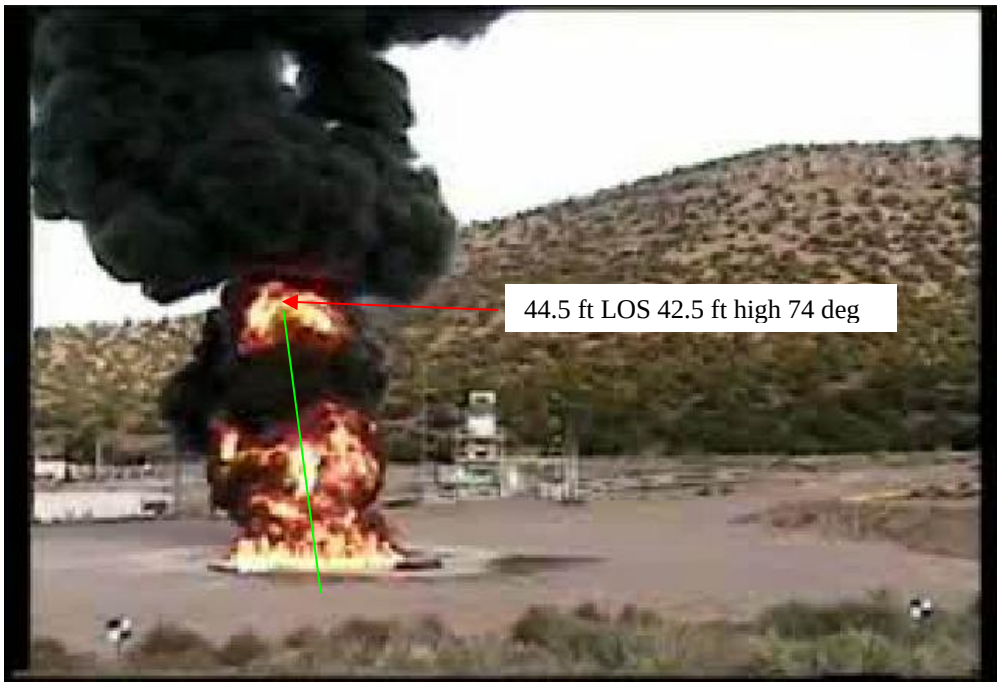

Test 3 NE and SE Camera view at frames 12600 (7 minutes)

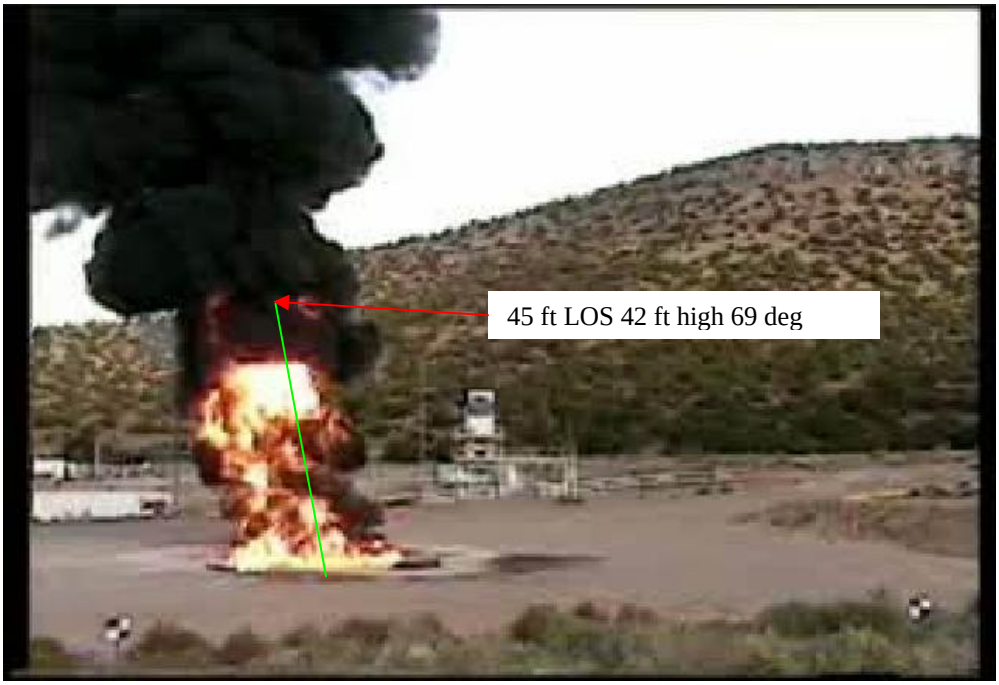

Test 3 NE and SE Camera view at frames 14400 (8 minutes)

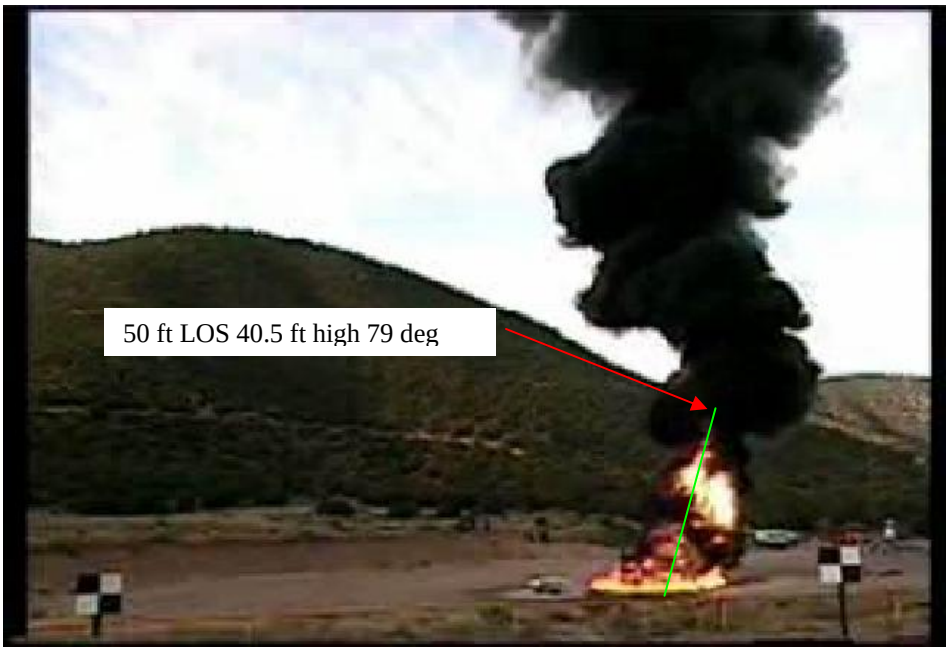

Test 3 NE and SE Camera view at frames 16200 (9 minutes)

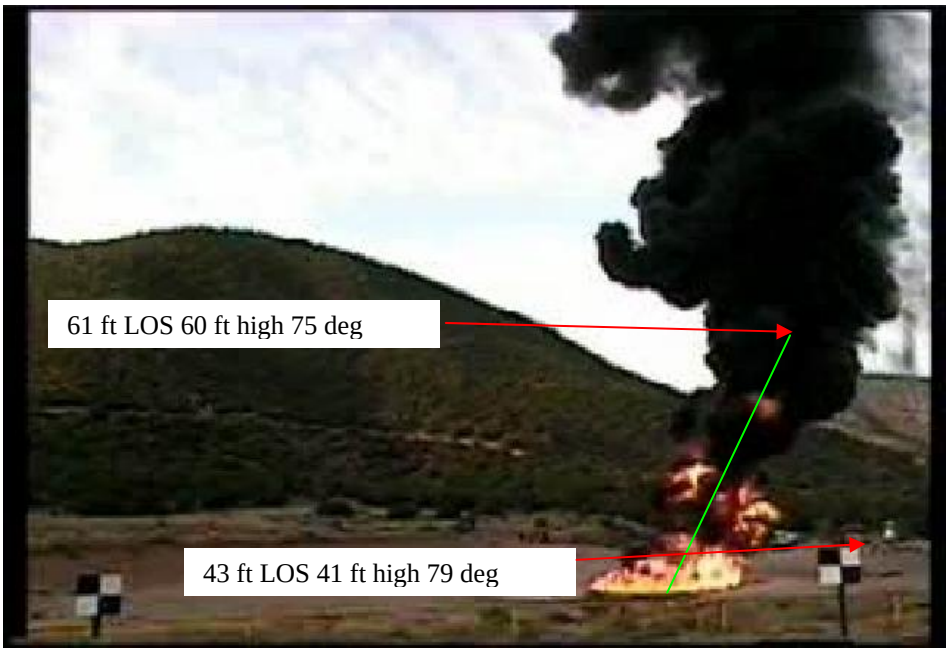

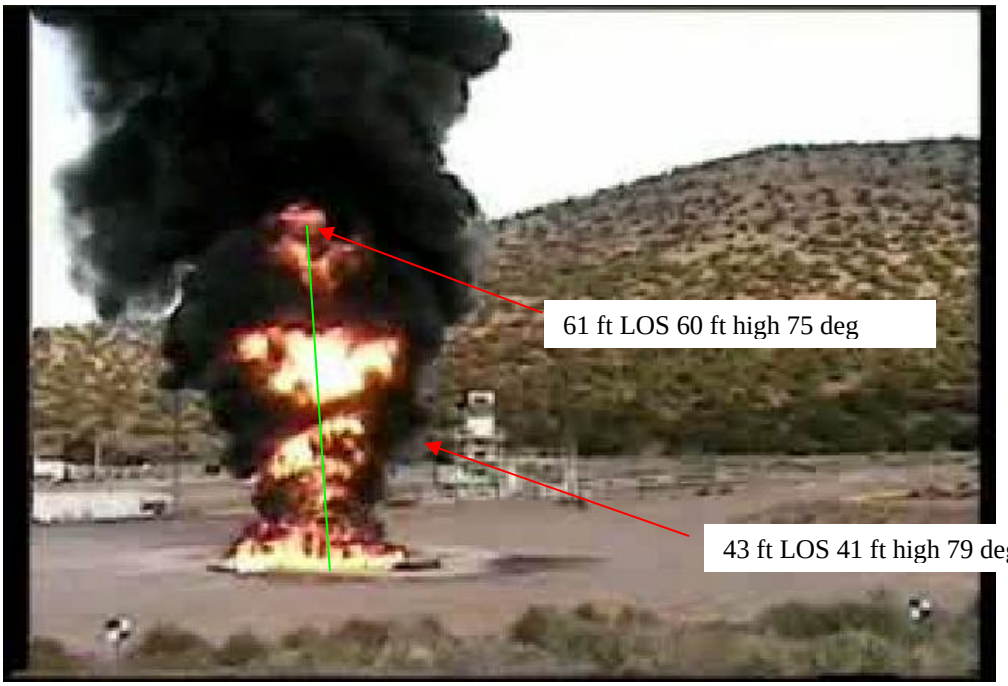

Test 3 NE and SE Camera view at frames 16255 (9.03 minutes)

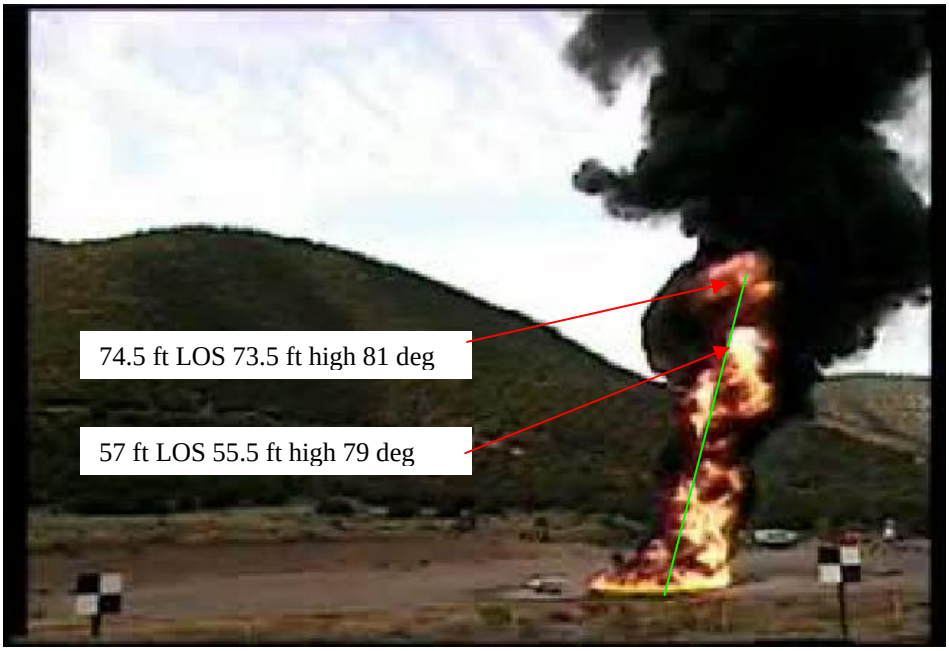

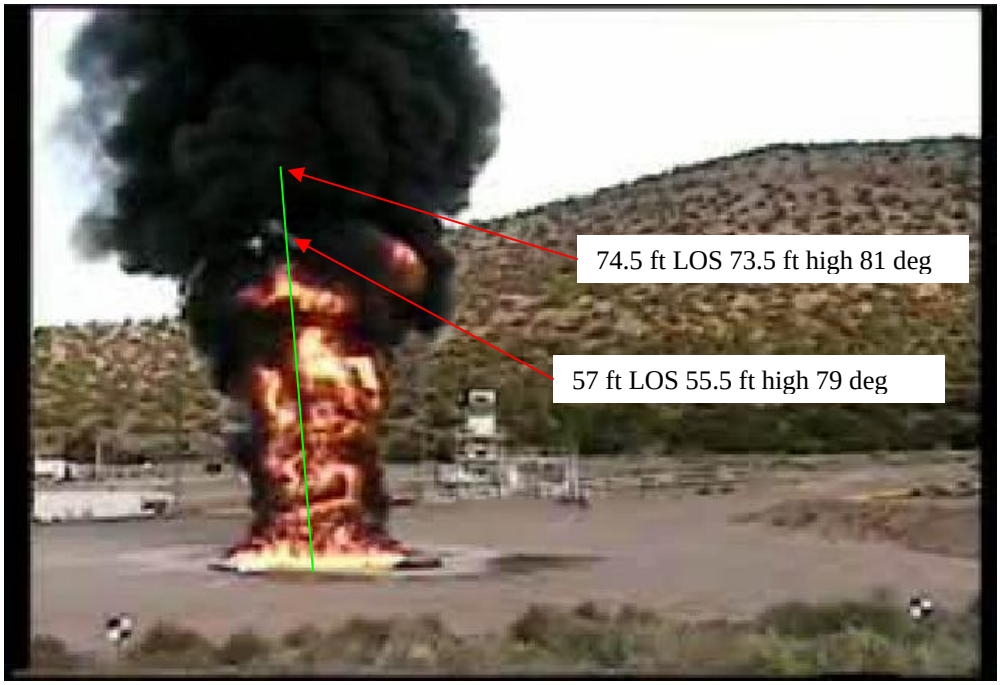

Test 3 NE and SE Camera view at frames 18128 (10.07 minutes)

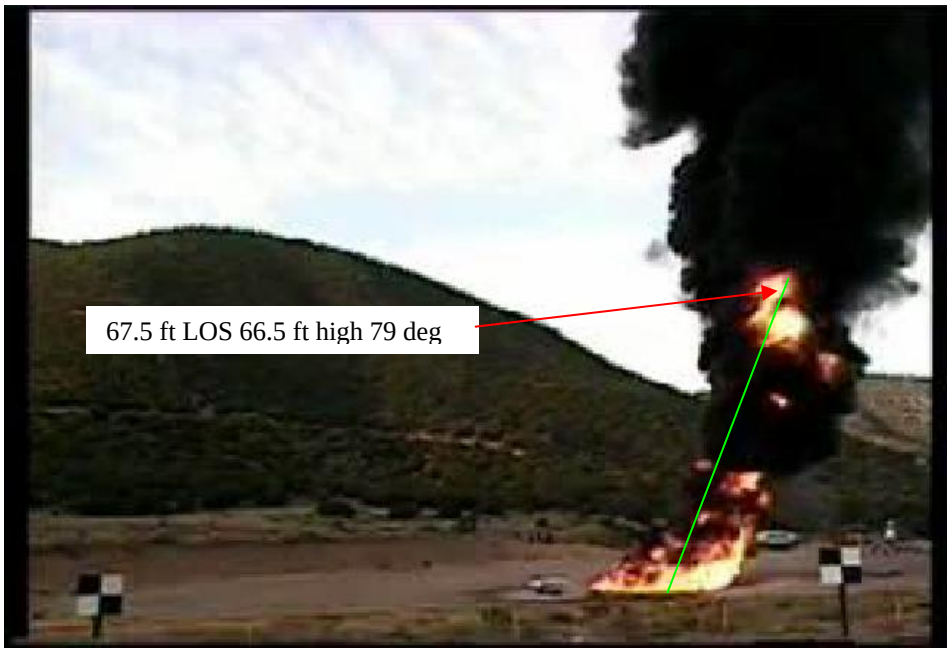

Test 3 NE and SE Camera view at frames 19092 (10.61 minutes)

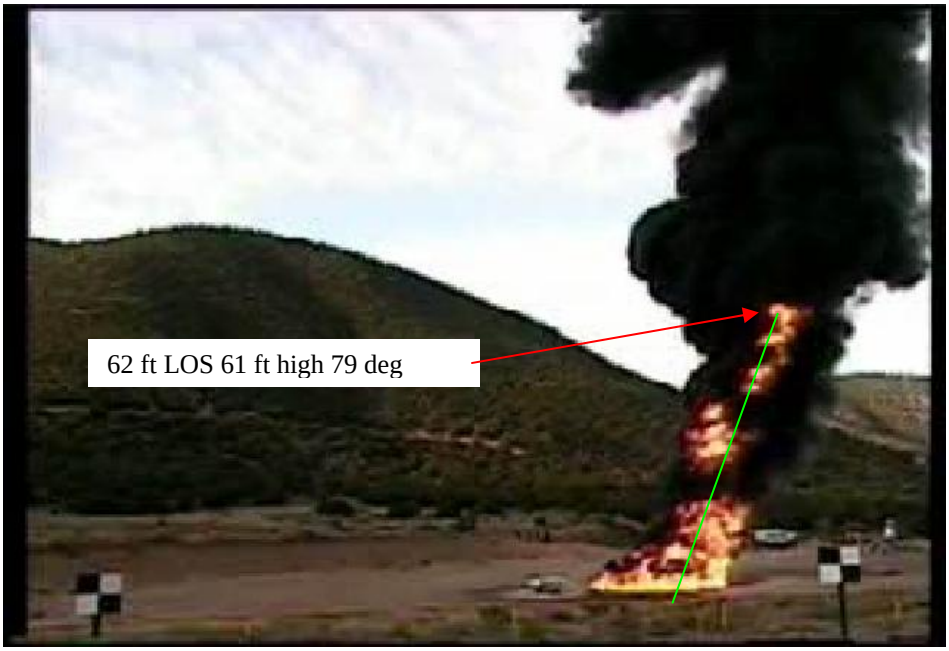

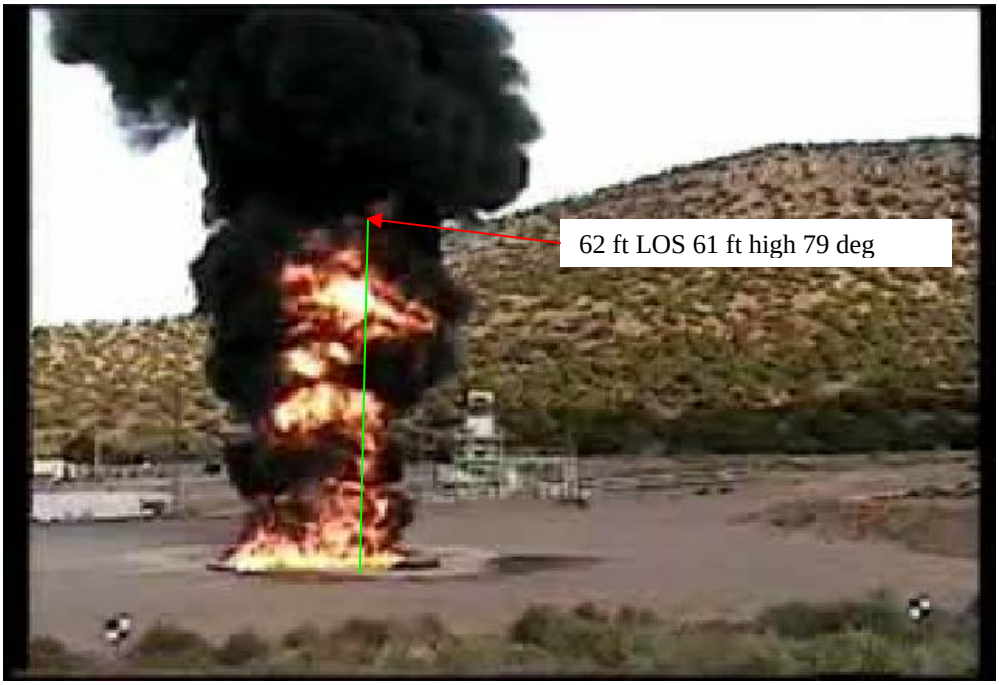

Test 3 East and South Camera views at frames 20085 (11.16 minutes),

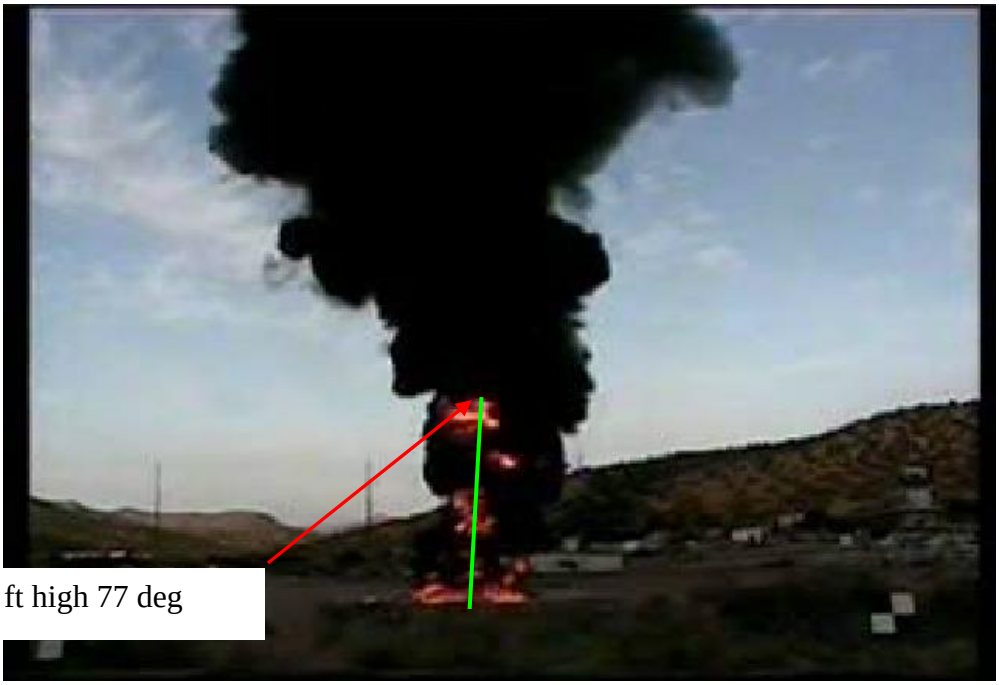

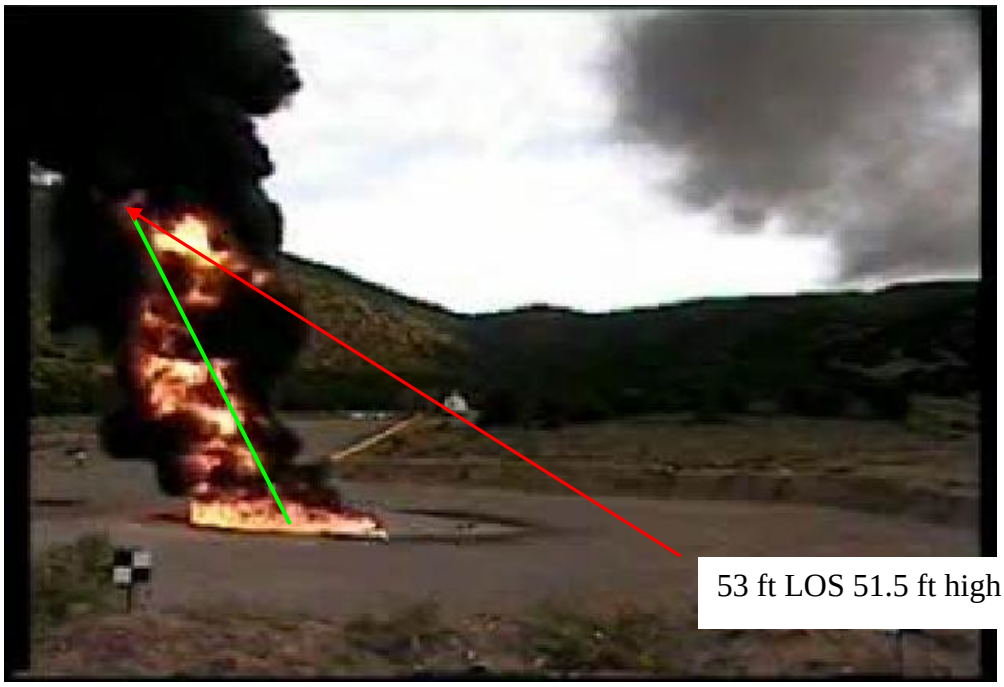

Test 3 East and South Camera views at frames 27320 (15.18 minutes)

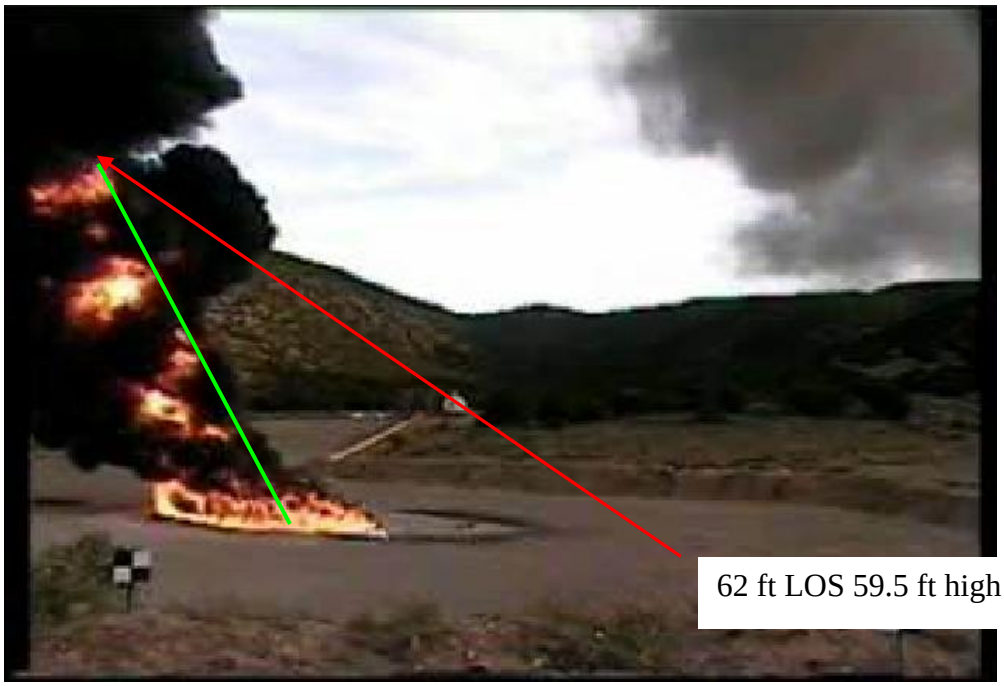

Test 4

Test 4 was conducted in the afternoon of the same day as Test 3, no changes were made in the test setup. The only difference was the wind was blowing briskly out of the west for the first minute. Then the wind shifted out of the southwest for the next 3 minutes and at minute 4 shifted out of the west again. Thus cameras 3 and 5 were used for plume analysis for the first 4 minutes, then cameras 2 and 4 were used for the center portion of the test, and finally cameras 2 and 5 were used to complete the analysis. This was necessary in order to use camera views where the plume was not moving over the top of a camera.

Since the wind was moving briskly, the plume lay over at a large angle and as a result the toroidal shape formed when the plume was vertical became two helix shaped cloud formations rotating in opposite directions that at times separated from one another.

The MPEG file was reviewed to find the peak extent of the glowing plume near the thirty-second time hacks from the start of the burn. Since the data on the disks for Test 4 was not loaded from the frame before the fire was started, the frame numbers on each disk had to be shifted for each camera to align the images to the same time. The images below for Test 4 relate to the equivalent frame number assigned to the time after start and not to the actual unshifted frame number. Figure 7 shows the height of the glowing portions of the cloud, as well as the lines of sight distance from the center of the fire pool to the point on the plume.

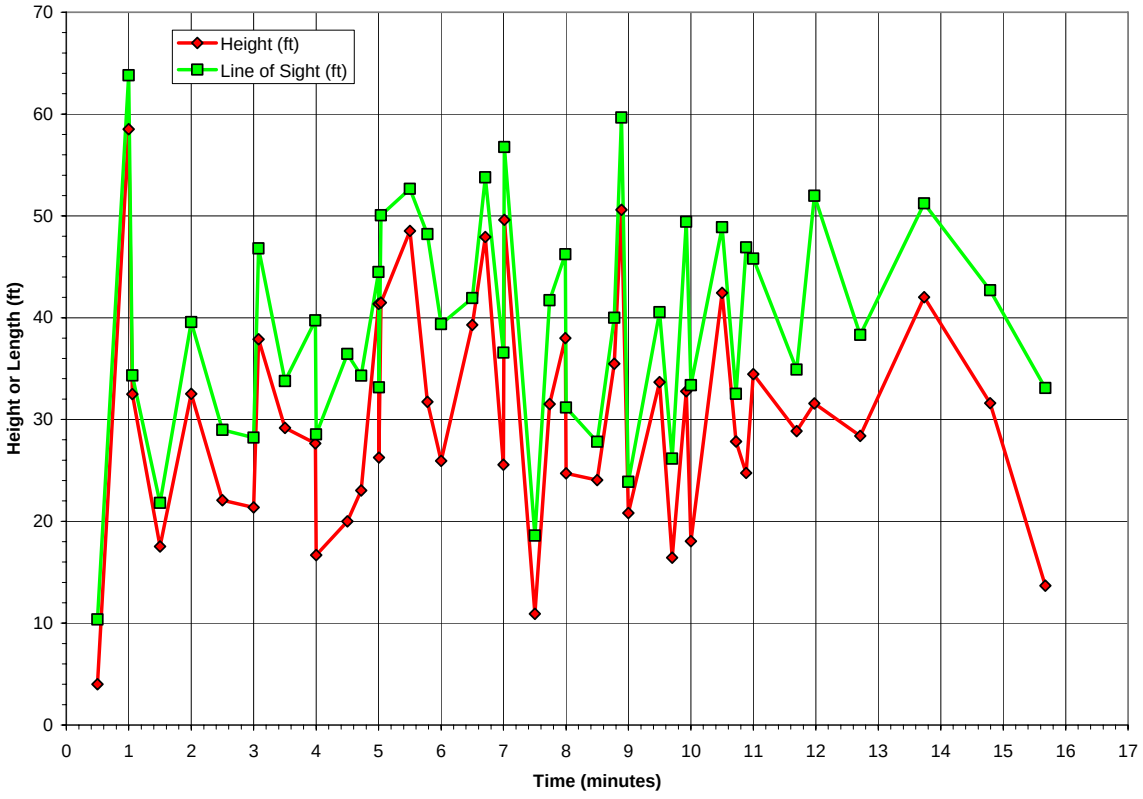

Figure 7. Test 4 Glow Heights and Distances from Pool Center.

Test 4 East and South Camera view at frames 1800 (1 minute)

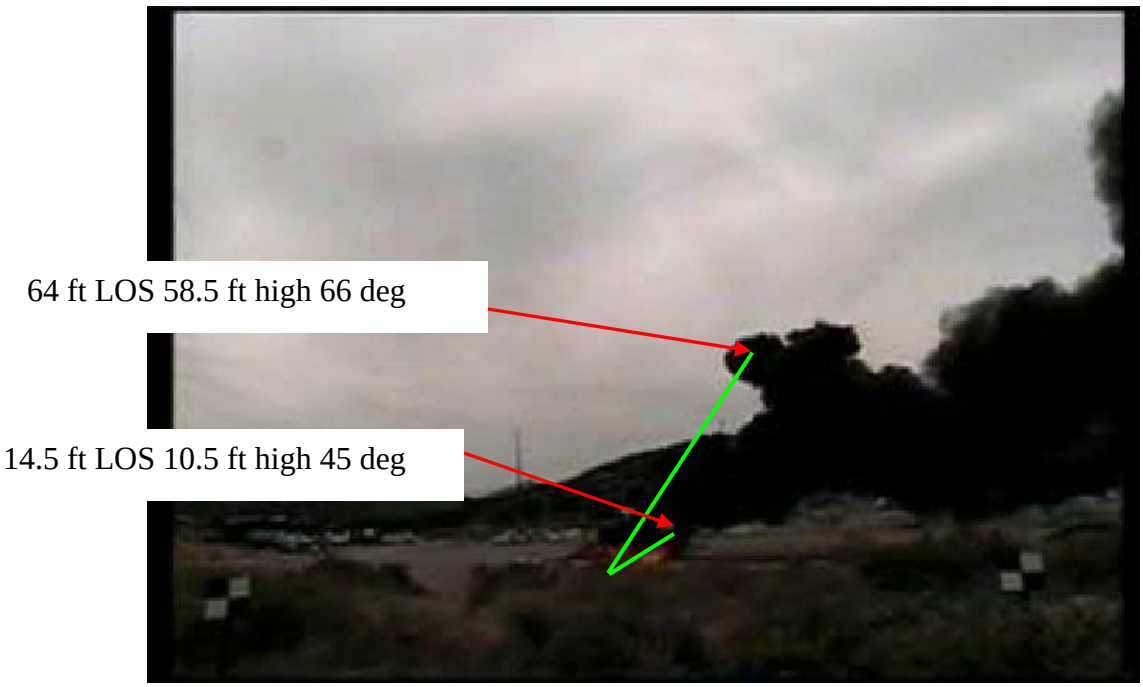

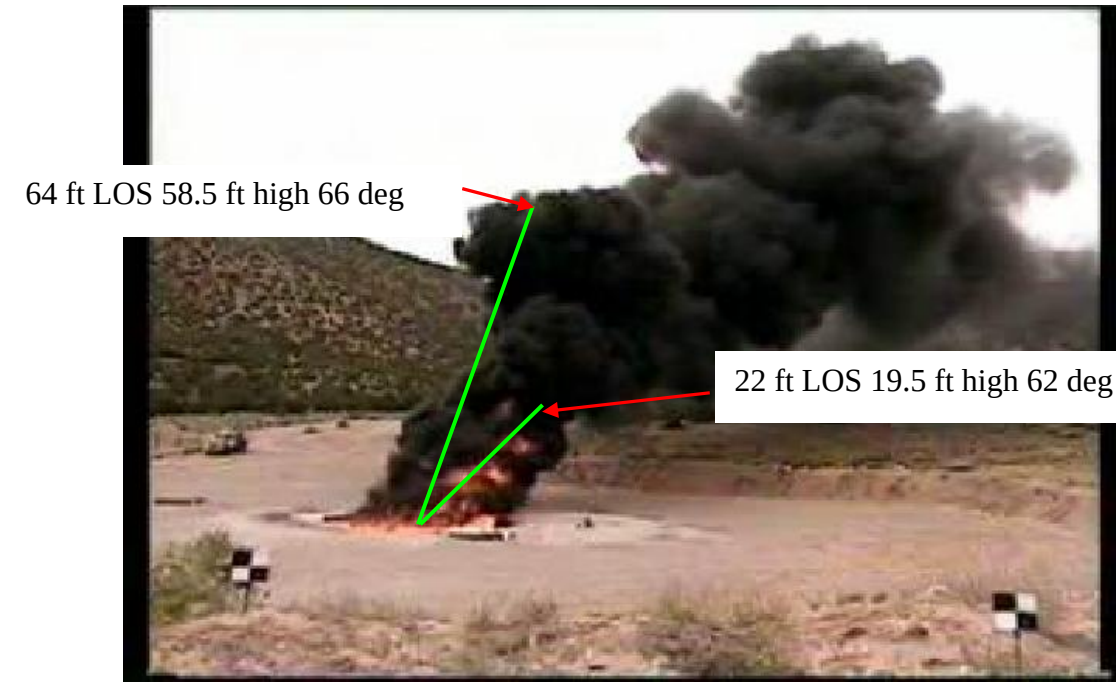

Test 4 East and South Camera view at frames 3600 (2 minutes)

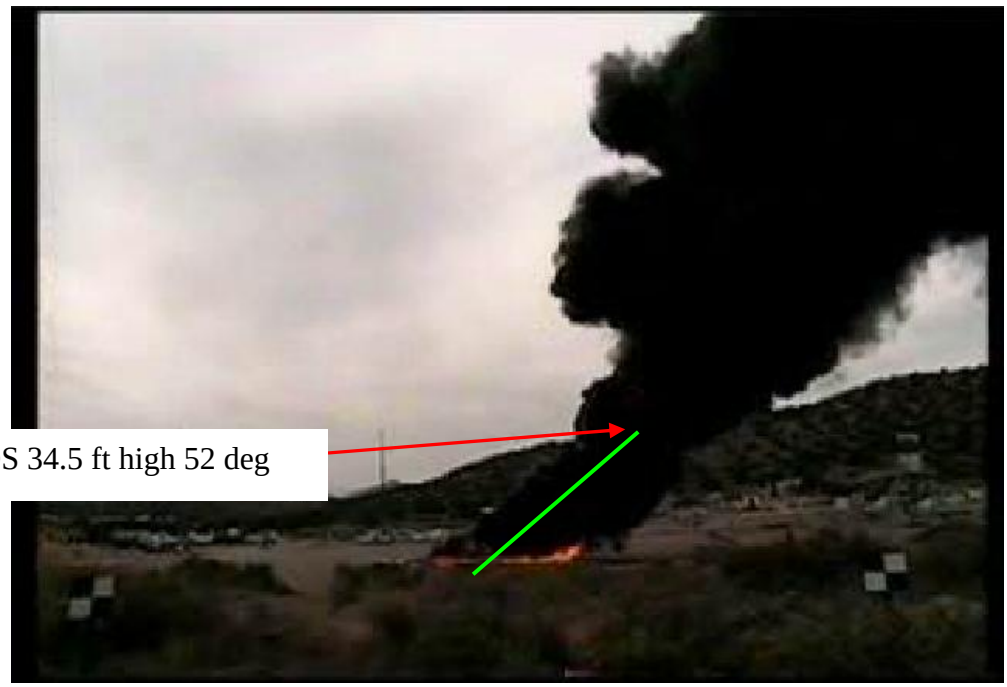

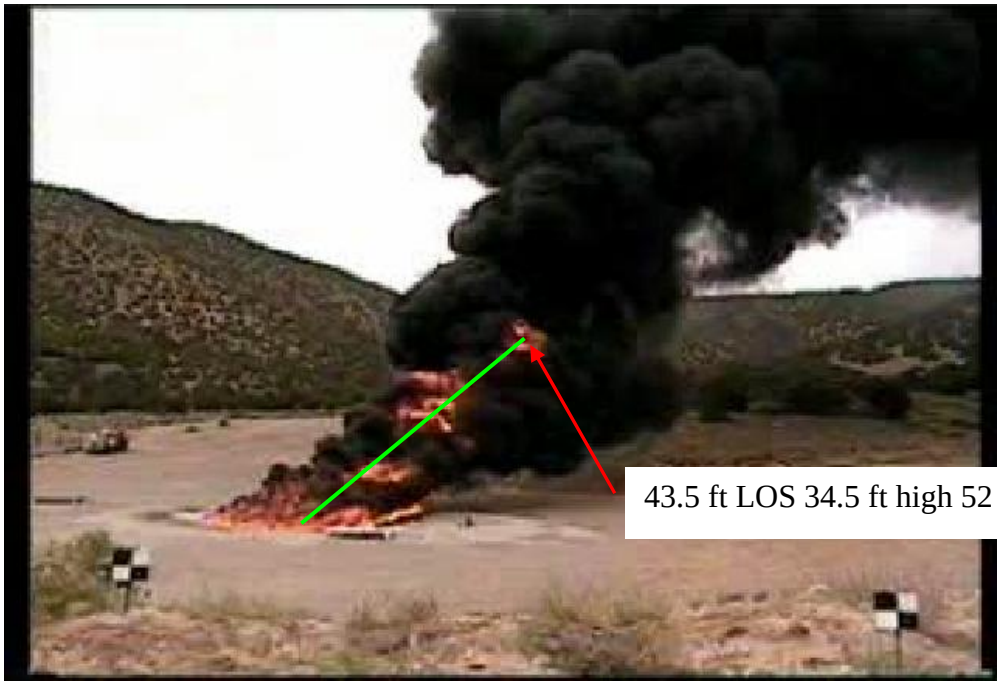

Test 4 East and South Camera views at frames 5400 (3 minutes)

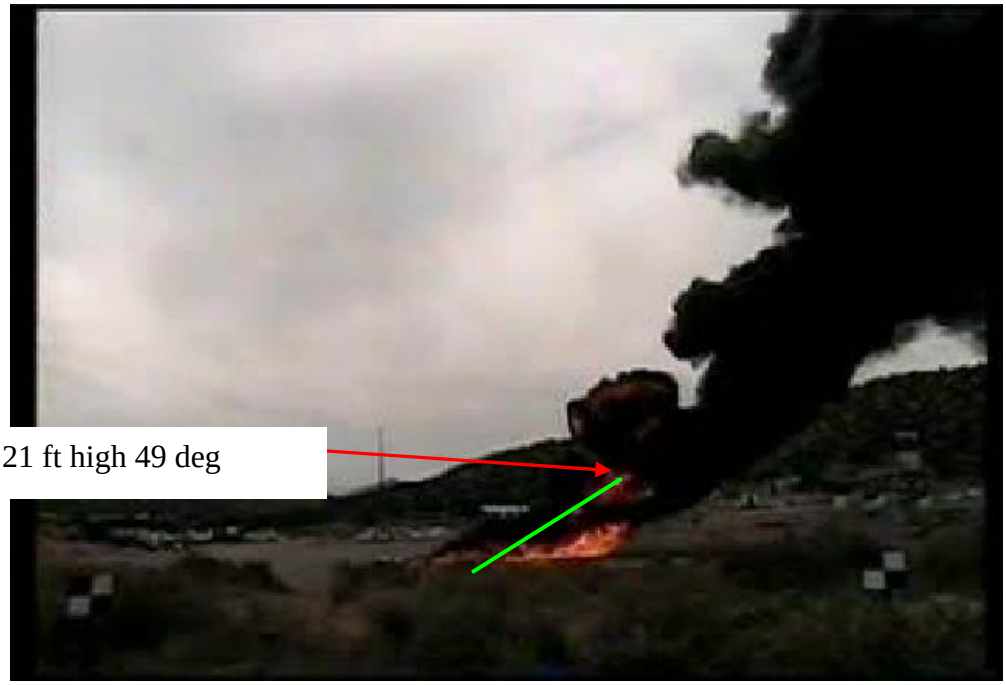

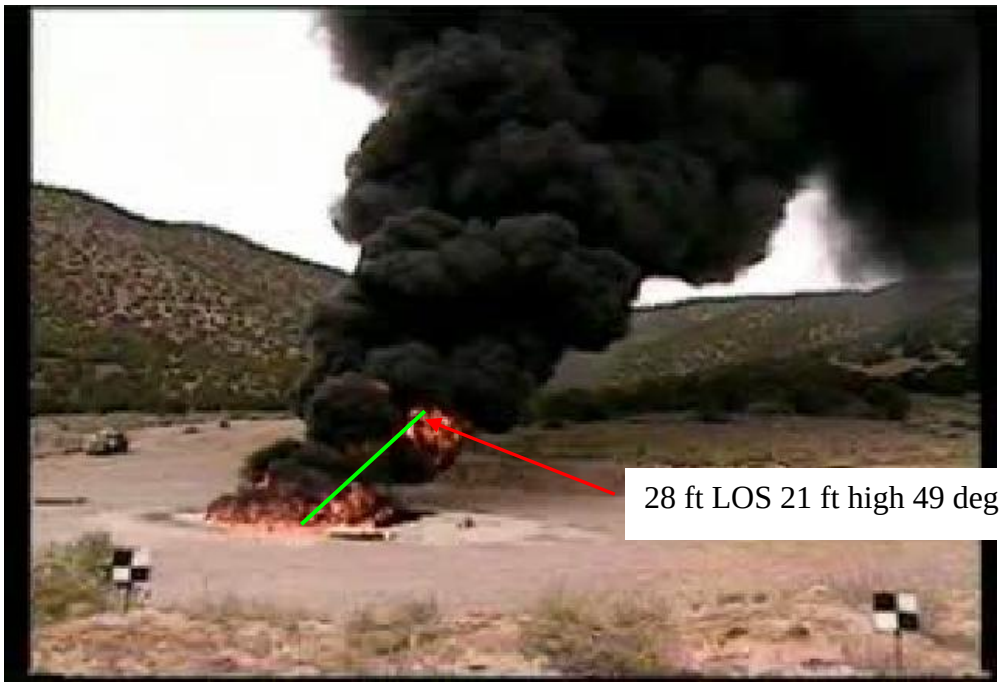

Test 4 NE and SE Camera views at frames 7200 (4 minutes)

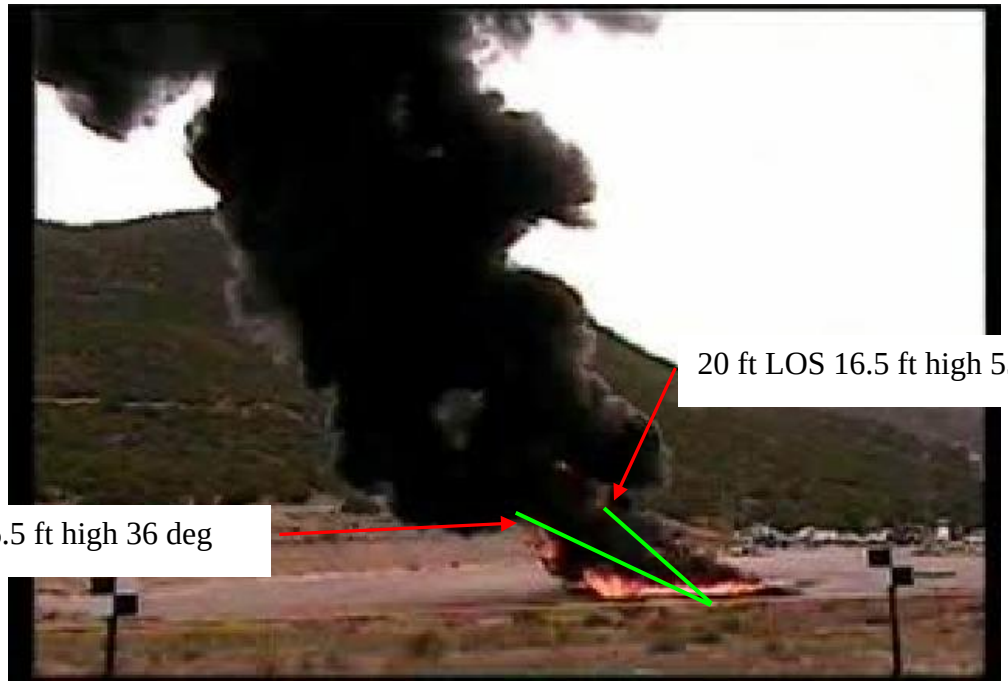

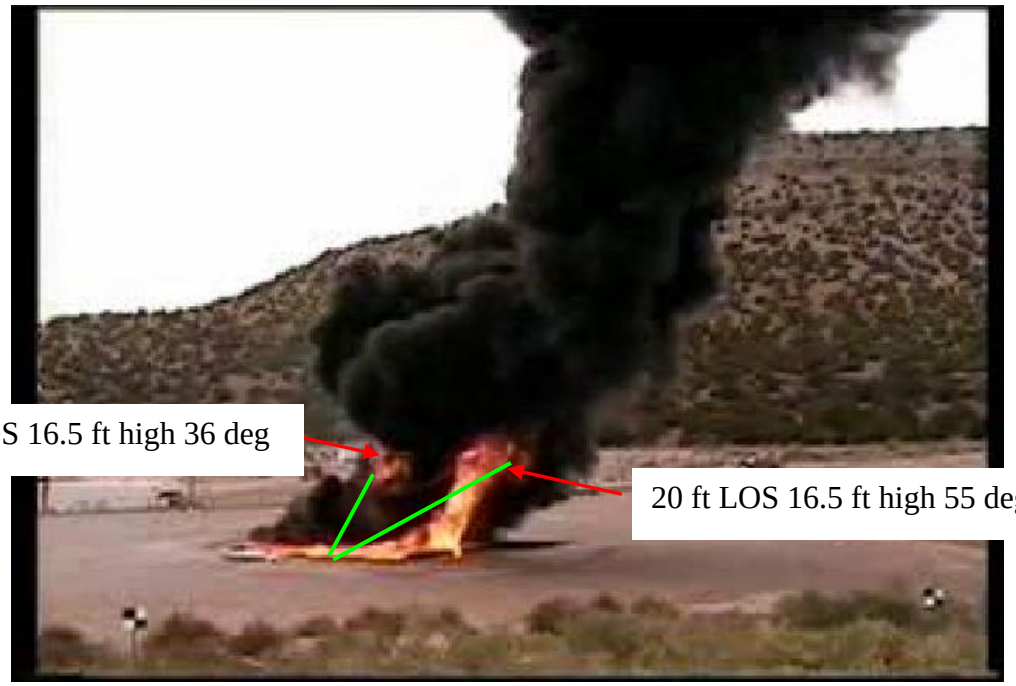

Test 4 NE and SE Camera views at frames 9000 (5.0 minutes)

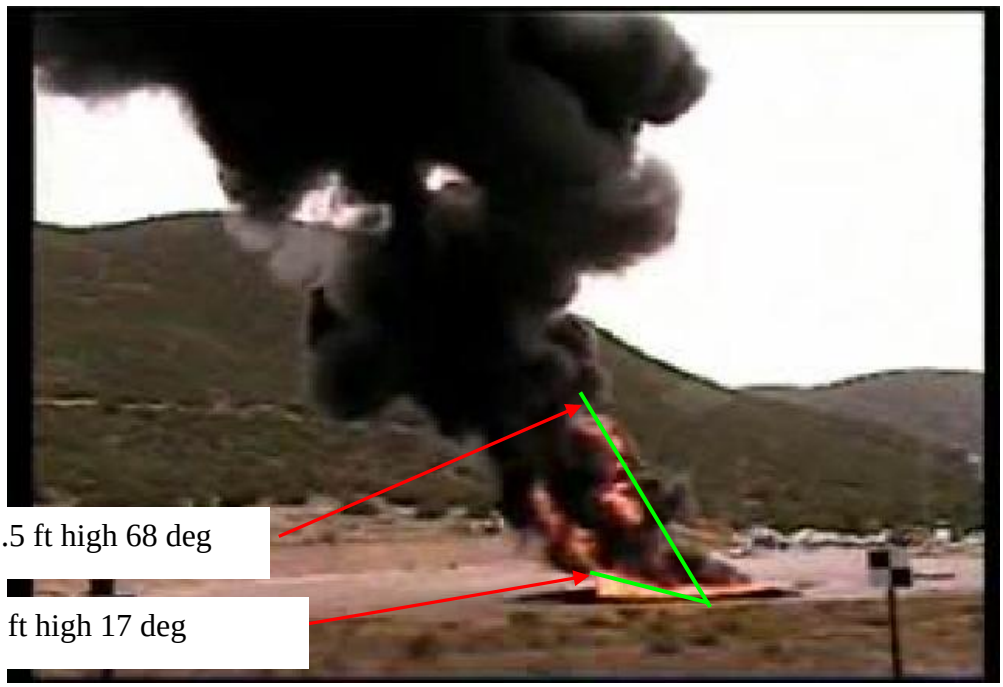

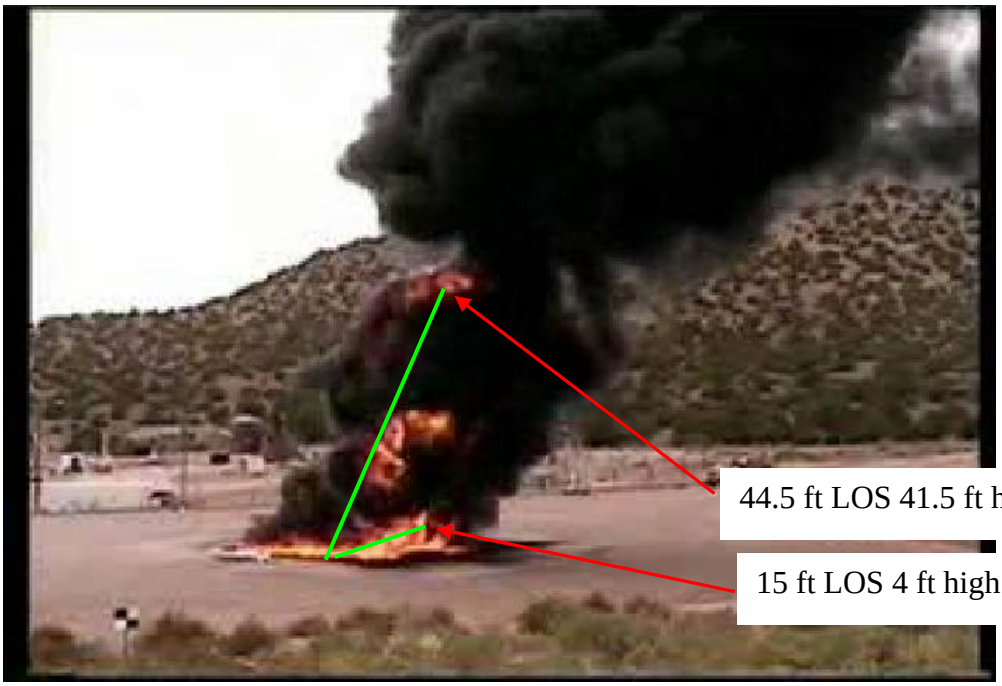

Test 4 NE and SE Camera views at frames 10800 (6 minutes)

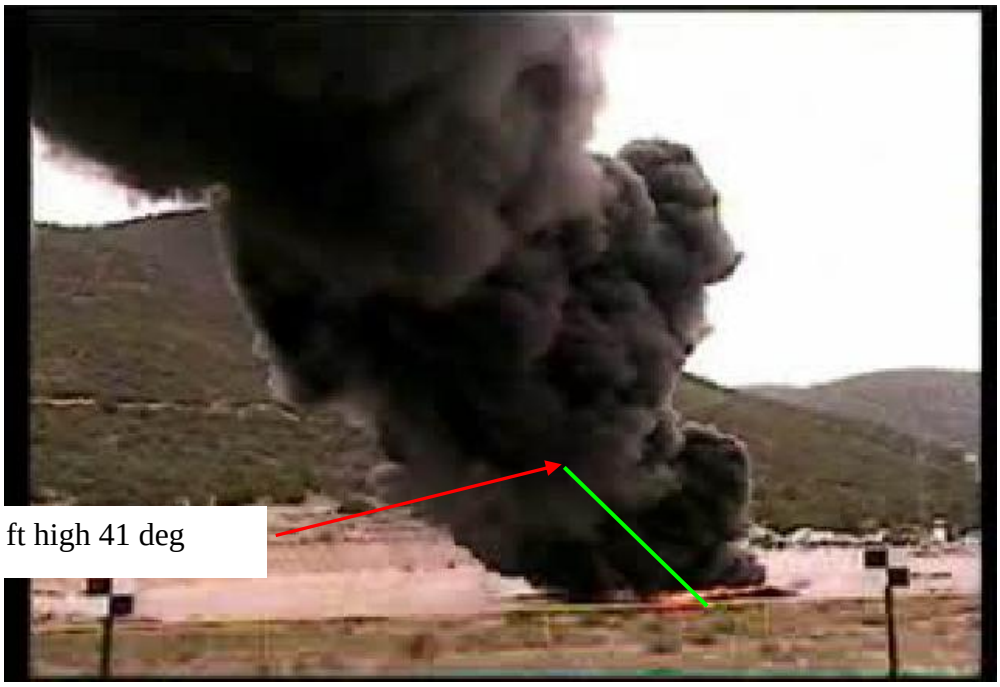

39.5 ft LOS 26 ft high 41 deg

39.5 ft LOS 26 ft high 41 deg

Test 4 NE and SE Camera views at frames 12600 (7 minutes)

Test 4 NE and SE Camera views at frames 14400 (8 minutes)

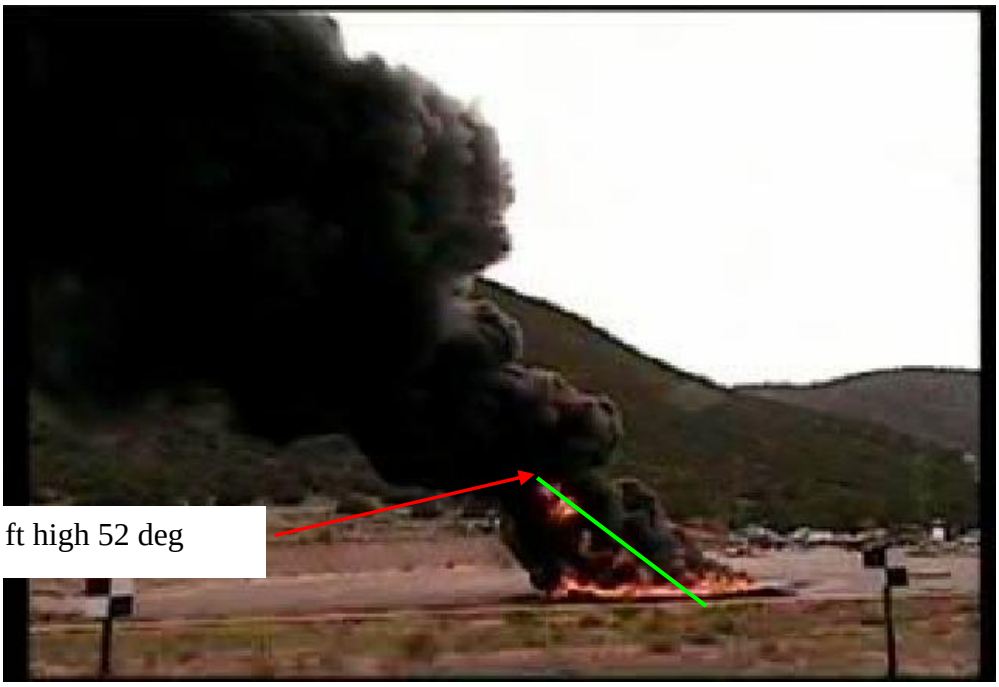

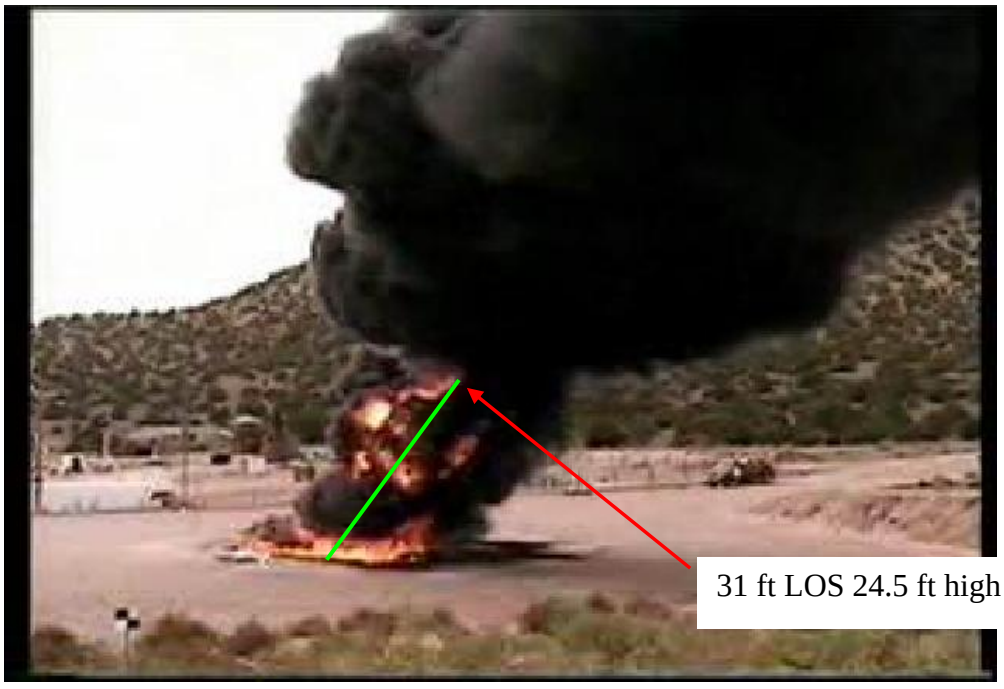

Test 4 NE and SE Camera views at frames 18000 (10 minutes)

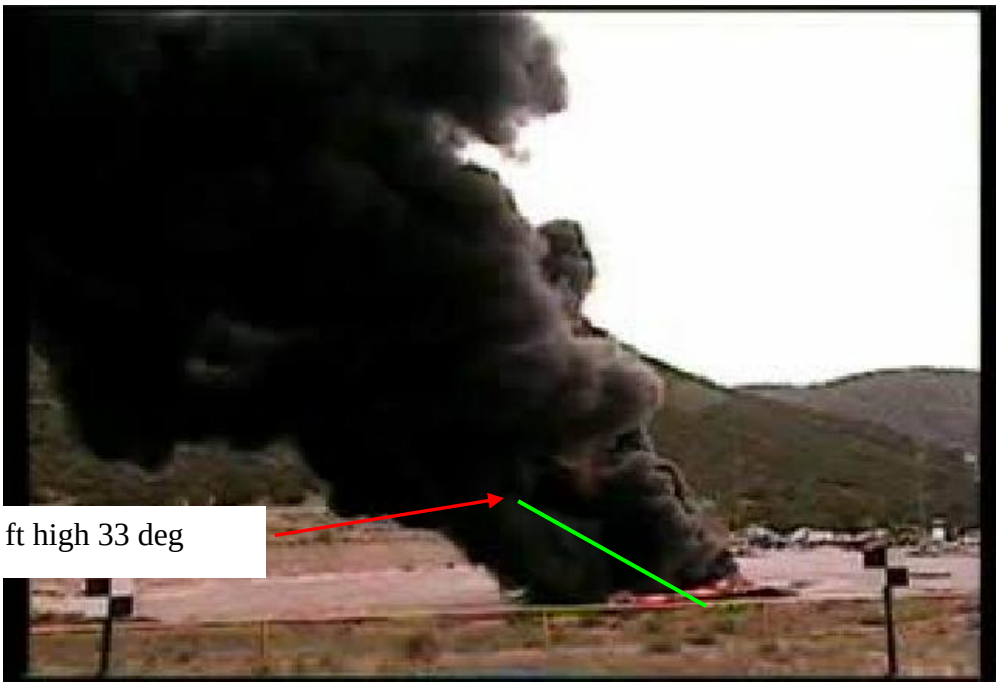

Test 4 NE and SE Camera views at frames 26624 (14.8 minutes)

Test 4 NE and S Camera views at 3602 frames (2 minutes)

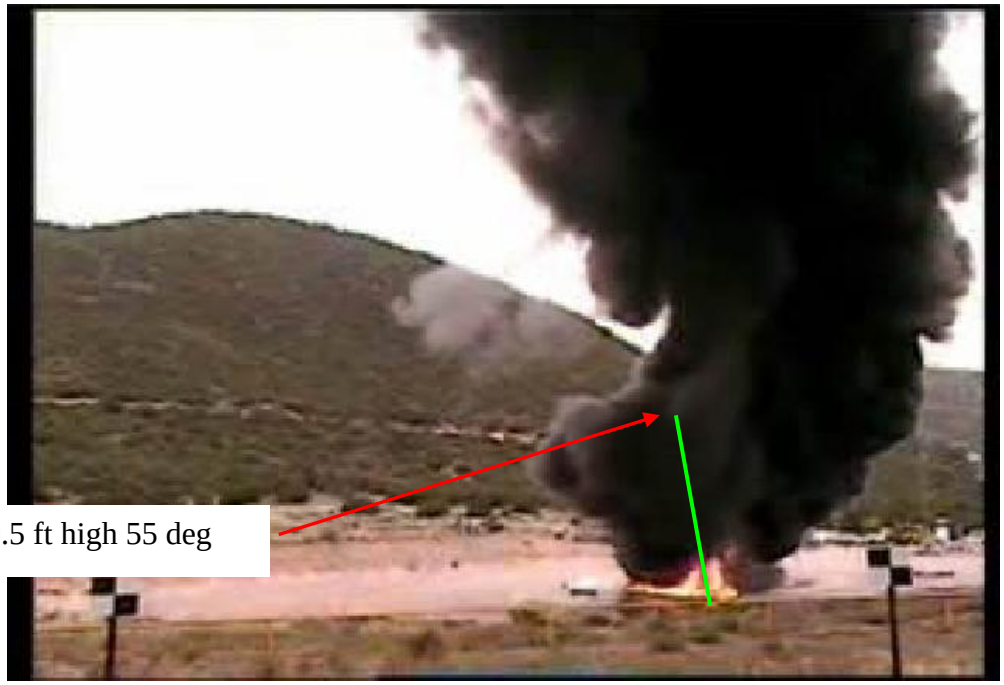

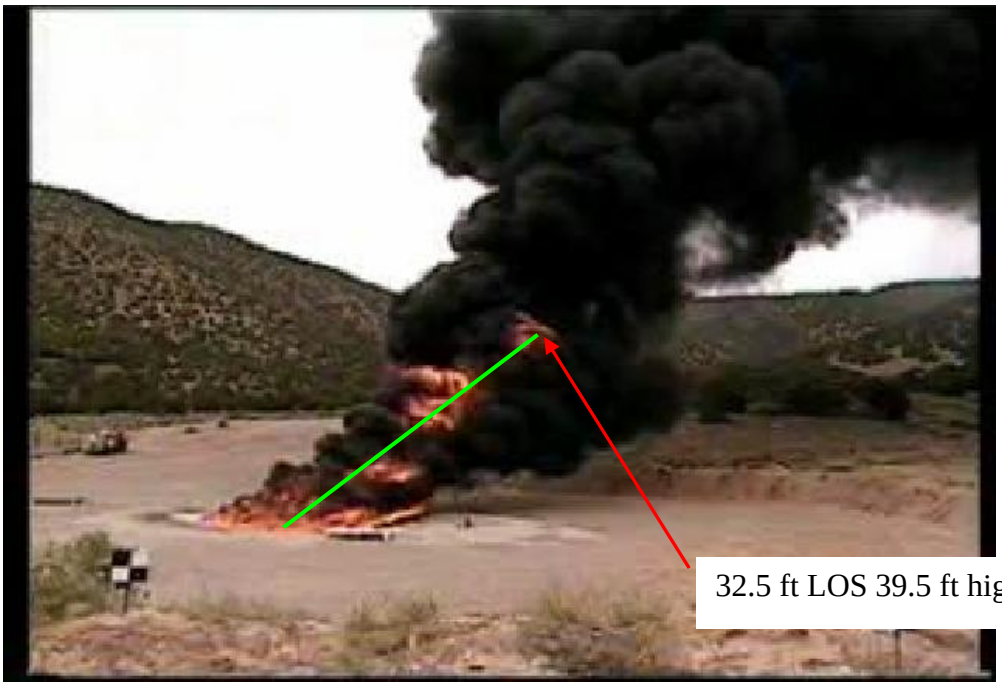

Test 4 NE and S Camera views at frames 9068 (5.04 minutes)

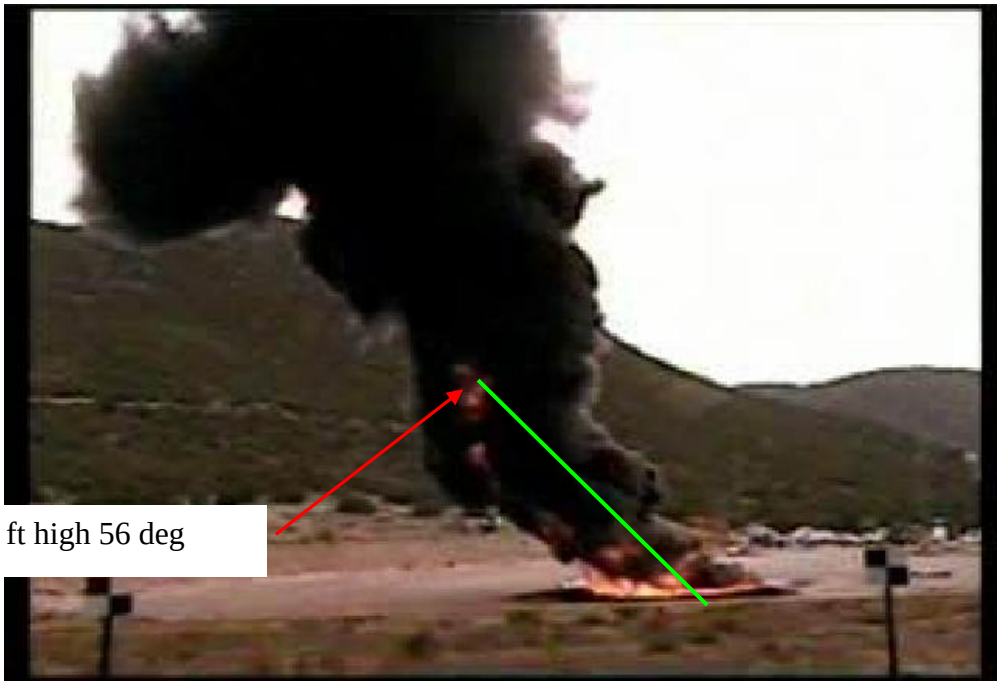

50 ft LOS 41.5 ft high 56 deg

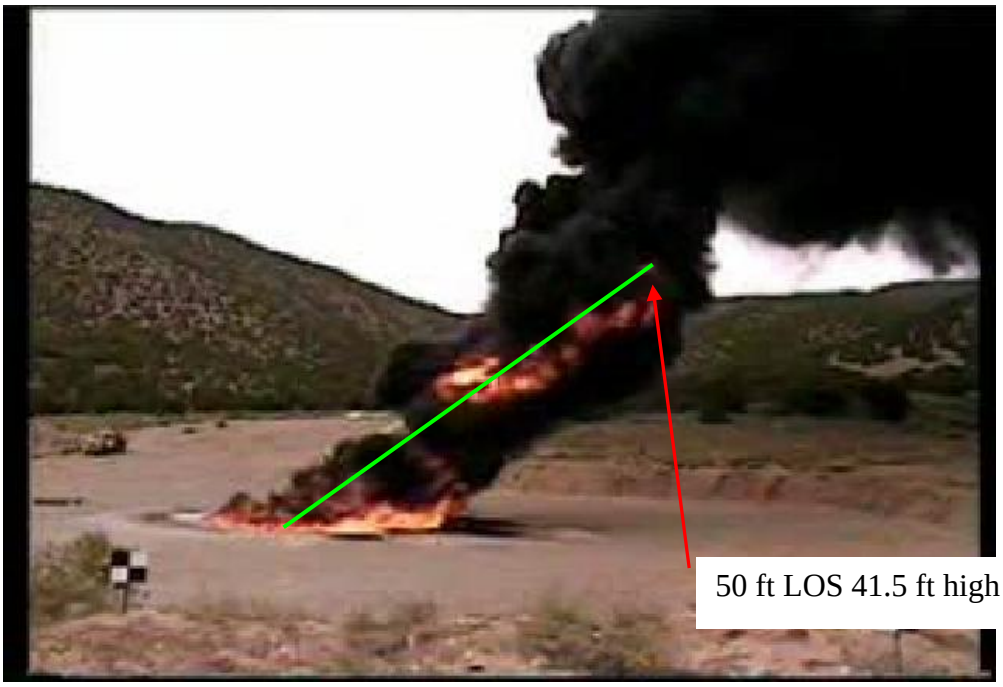

50 ft LOS 41.5 ft high 56 deg

Test 4 NE and S Camera views at frames 14384 (7.99 minutes)

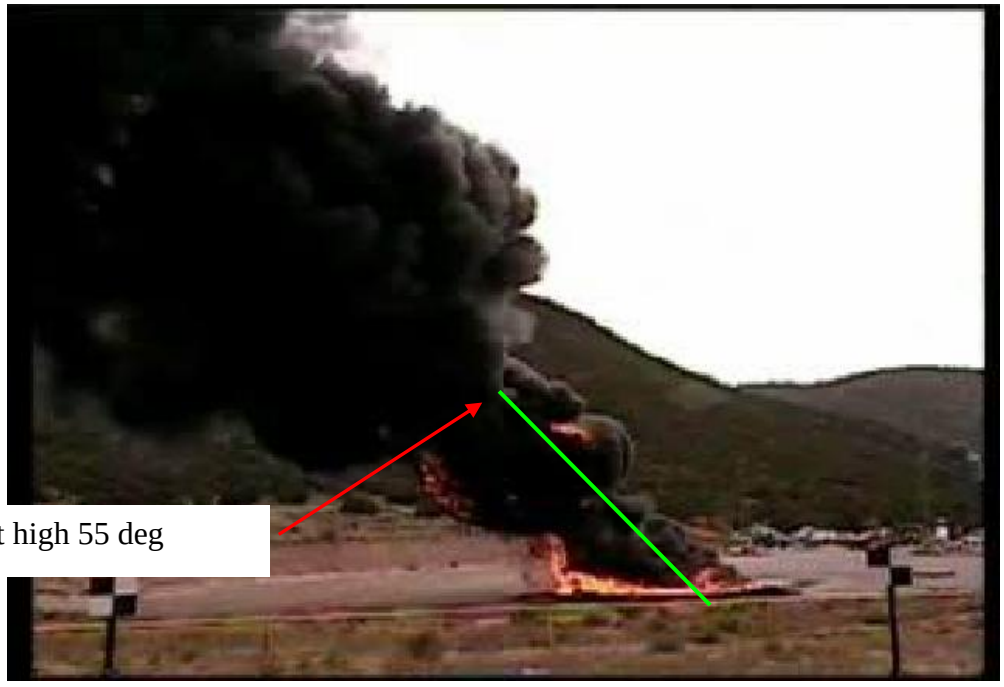

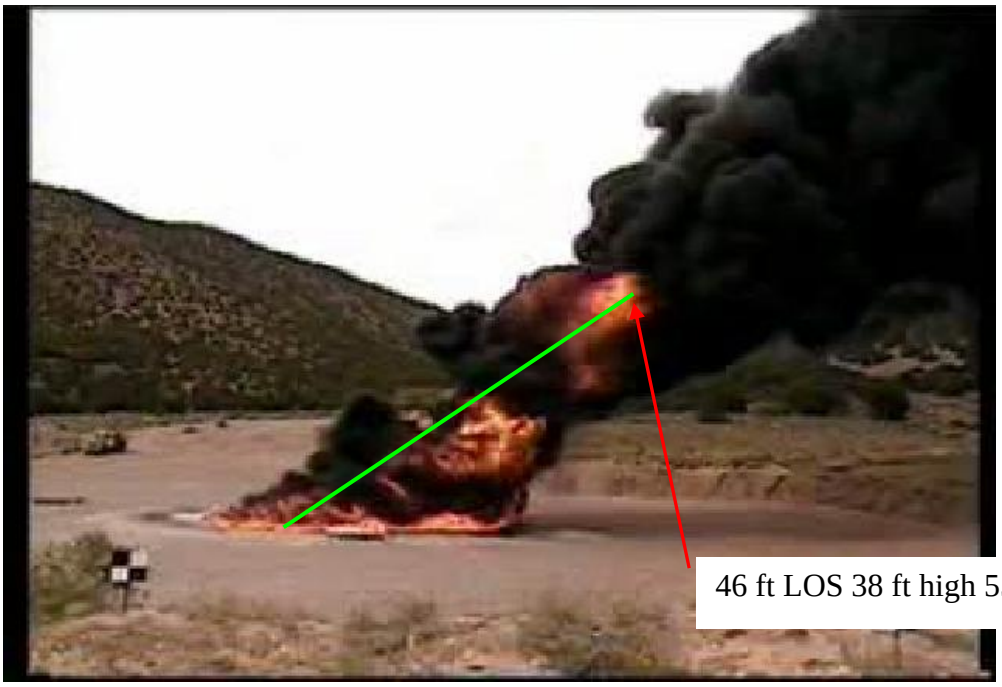

Test 4 NE and S Camera views at frames 16000 (8.89 minutes)

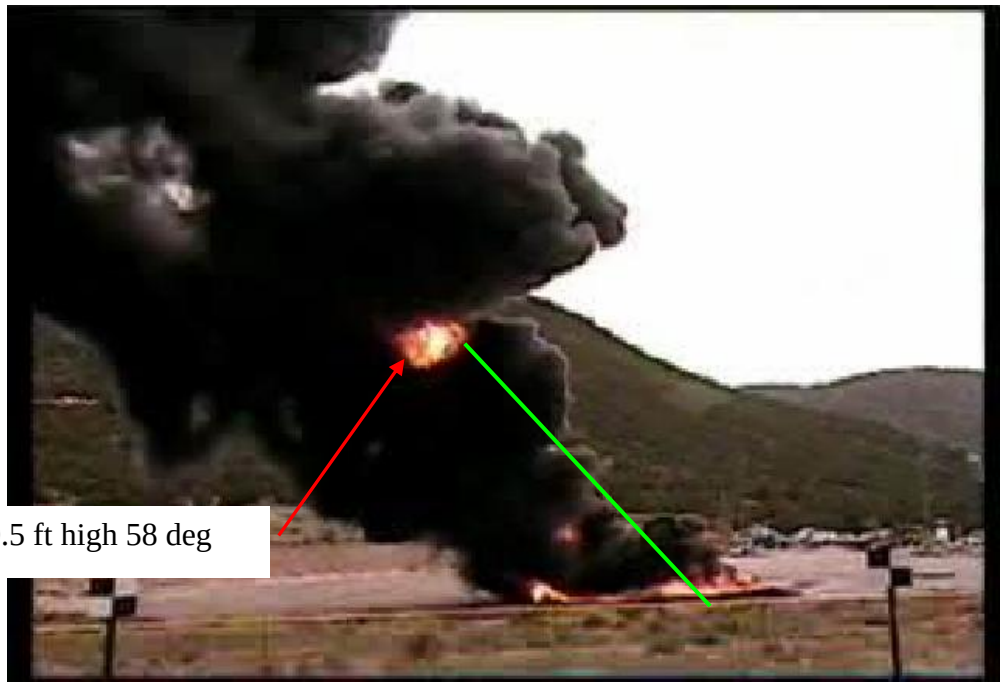

59.5 ft LOS 50.5 ft high 58 deg

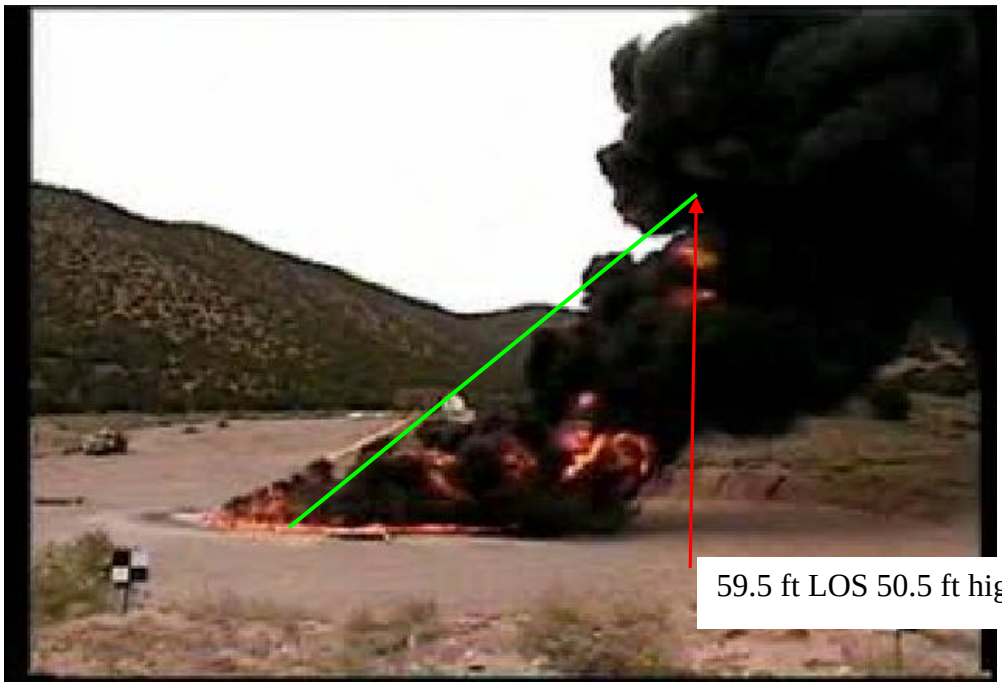

59.5 ft LOS 50.5 ft high 58 deg

Test 4 NE and S Camera views at frames 17862 (9.92 minutes)

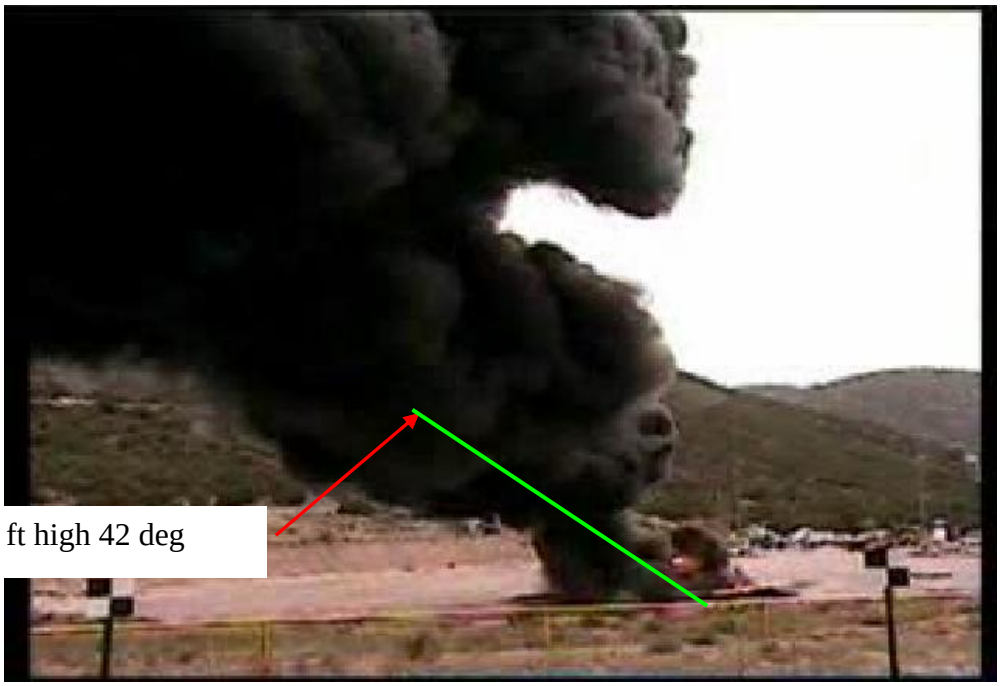

49.5 ft LOS 33 ft high 42 deg

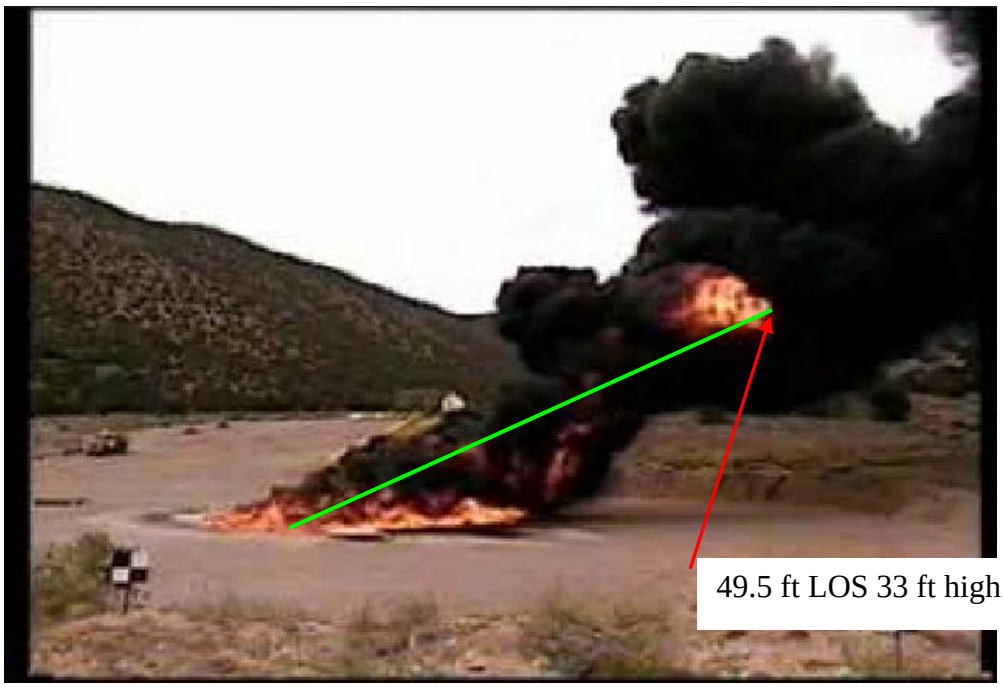

49.5 ft LOS 33 ft high 42 deg

Test 4 NE and S Camera views at frames 19590 (10.88 minutes)

47 ft LOS 25 ft high 32 deg

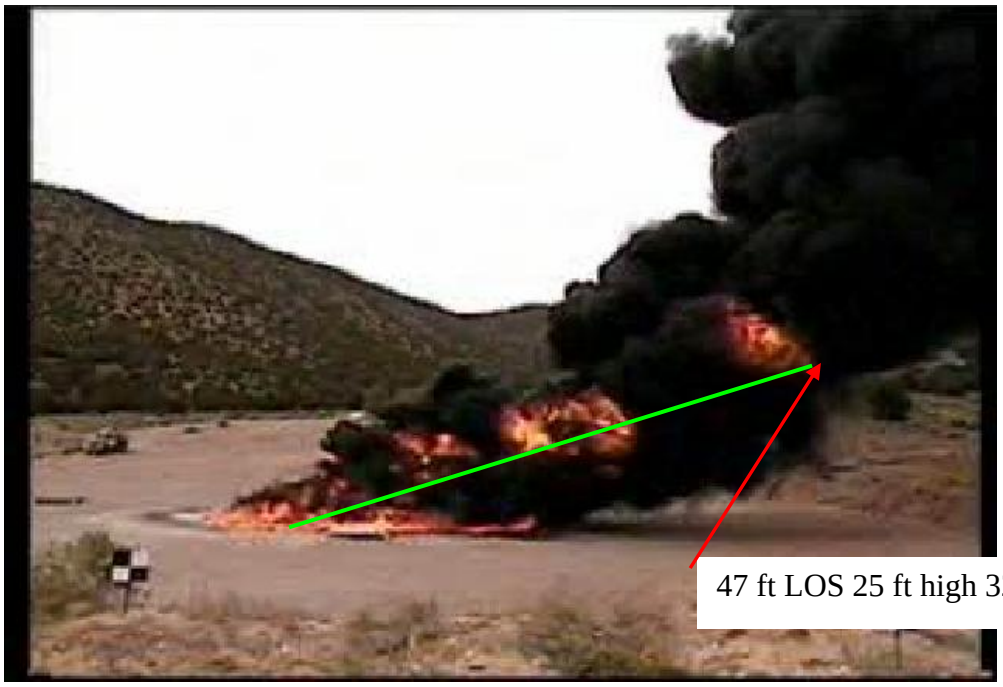

47 ft LOS 25 ft high 32 deg

Test 4 NE and S Camera views at frames 21560 (11.98 minutes)

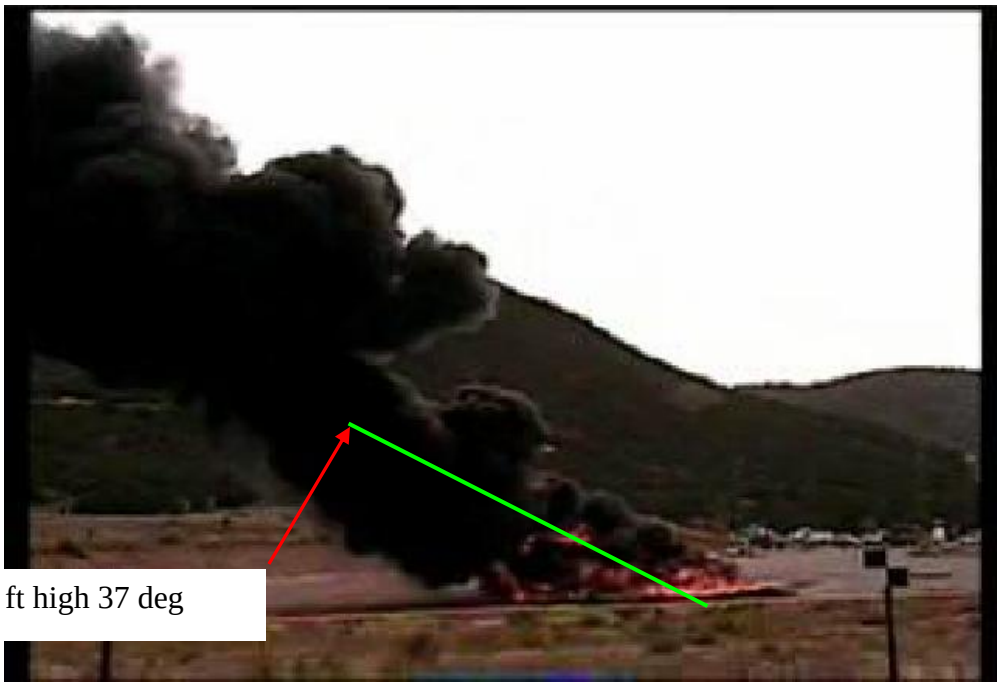

CONCLUSIONS

Tests 1 and 3 were conducted with minimal wind. However, Test 3 had a little more wind than Test1 and was more variable. Tests 2 and 4 had stiff winds, but Test 4 had motion out of several directions over the course of the test. This caused the plume to blow over the top of several cameras (2, 3 and 4) (NE, E, and SE). That in turn caused the analysis to use different sets of cameras to obtain the measurements. The resultant maximum heights of the glow are shown in Figure 7. The maximum distance from the pool center to the farthest glow point is given in Figure 8.

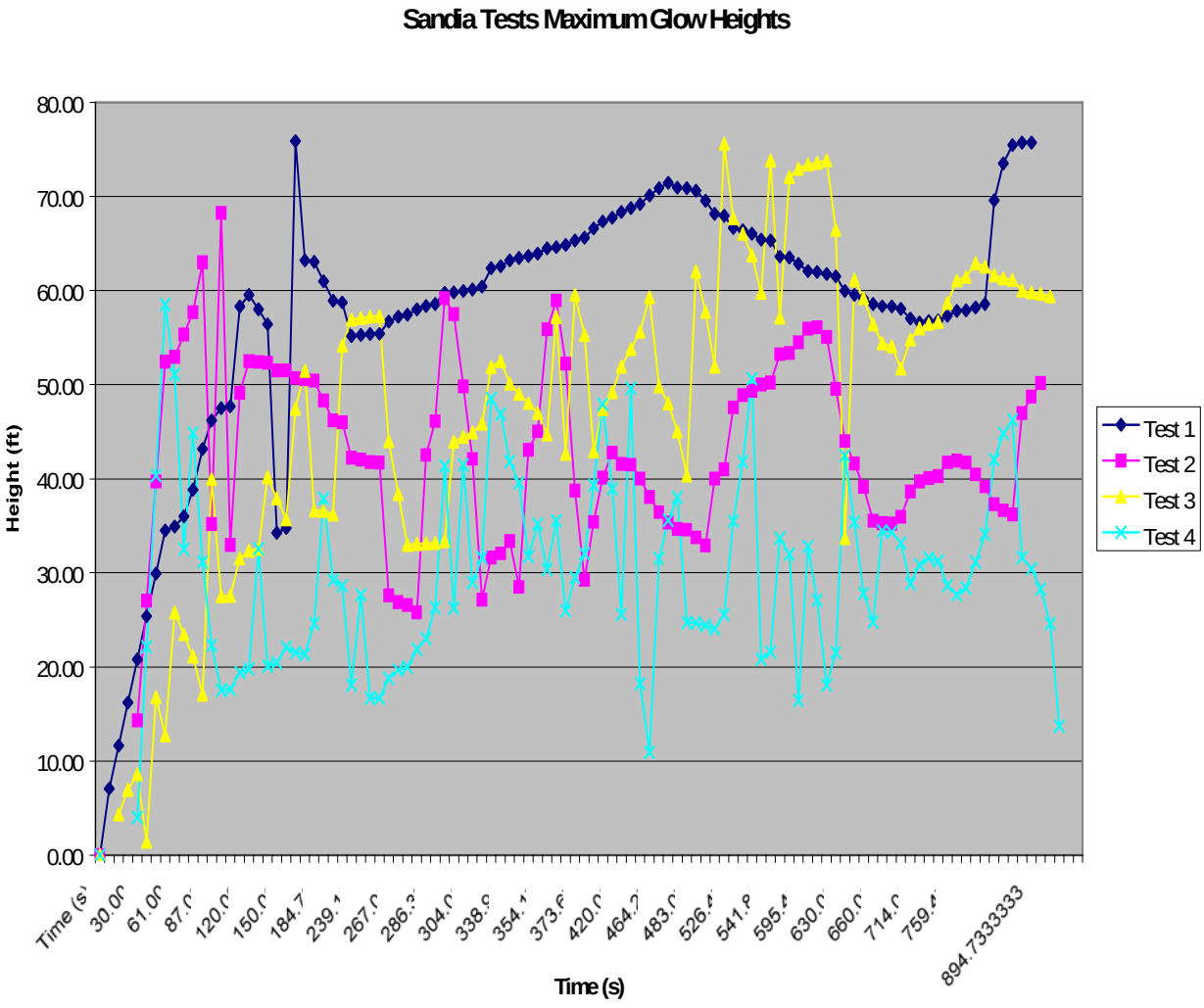

Figure 7. Sandia Tests maximum glow heights.

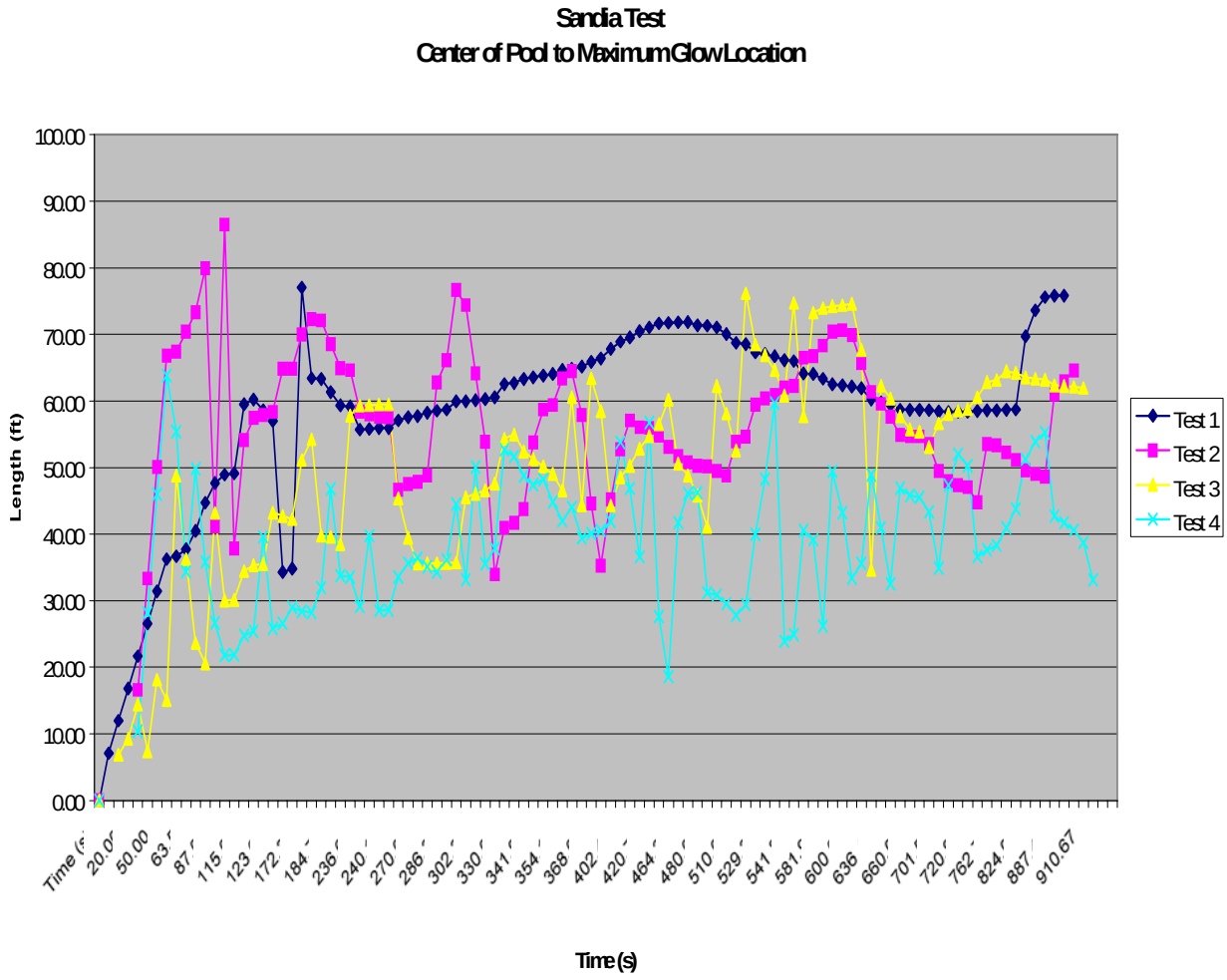

Figure 8. Sandia Tests maximum distance from pool center to farthest glow

Comparison of the vertical dome height in Test 1 with the length of the hot gases from the pool center to the perceived end of the glowing field in Test 2 show the lengths are generally within a factor of two of each other, with the Test 1 vertical length generally being the longer of the two.

Tests 1 and 3 have about the same heights and maximum distance from the pool center over time. They grew to about 60 feet and held relatively steady (both maximum height and distance from center of the pool since it was calm for these tests.). Tests 2 and 4 maximum heights varied from 30 to 50 feet depending on the intensity of the wind. A case can be made that the maximum distance from the pool center to maximum glow seems to be the same length as the hot plume would be in a calm situation out to a few hundred seconds. However, a close examination of the data leaves open the possibility that the tilted plume does not grow to the height of the calm plume. Clearly Test 4 maintains between 30 and 50 feet whereas Tests 1 and 3 vary around 50-70 feet. However, the LOS distances in vary from 40 to 80 feet.

The puffing frequency for both of the near-calm wind tests was found to be 0.56 puffs per second.

DISTRIBUTION

EXTERNAL DISTRIBUTION

2 Defense Threat Reduction Agency
Attn (CSNS/McGinnis)
8725 John J Kingman Rd Stop 6201
Fort Belvoir Va 22060-6201

1 Charles Allen
NGIT A&AS
8211 Terminal Road Suite 1000
Lorton, VA, 22079-1421

1 Miles Greiner, Associate Professor
Mechanical Engineering Department/312
University of Nevada, Reno
Reno, NV 89557

SANDIA INTERNAL DISTRIBUTION

1	MS0821	1530	A. L. Thornton
1	MS1135	1532	S. R. Tieszen
5	MS1135	1532	T. K. Blanchat
1	MS1135	1532	V. F. Nicolette
1	MS1135	1532	W. D. Sundberg
1	MS1135	1532	V. G. Figueroa
1	MS1135	1532	S. Gomez
1	MS1135	1532	D. A. Jernigan
1	MS0718	6765	C. Lopez
1	MS1146	1384	A. J. Suo-Anttila
2	MS9018	8944	Central Technical Files
2	MS0899	4536	Technical Library